

An X-ray and Optical Study of AM Herculis Systems

Thesis submitted for the degree of
Doctor of Philosophy
at the University of Leicester

by

Keith Brendan Sohl
X-ray Astronomy Group
Department of Physics and Astronomy
University of Leicester

October 1997

UMI Number: U103785

All rights reserved

INFORMATION TO ALL USERS

The quality of this reproduction is dependent upon the quality of the copy submitted.

In the unlikely event that the author did not send a complete manuscript and there are missing pages, these will be noted. Also, if material had to be removed, a note will indicate the deletion.



UMI U103785

Published by ProQuest LLC 2013. Copyright in the Dissertation held by the Author.
Microform Edition © ProQuest LLC.

All rights reserved. This work is protected against
unauthorized copying under Title 17, United States Code.



ProQuest LLC
789 East Eisenhower Parkway
P.O. Box 1346
Ann Arbor, MI 48106-1346

An X-ray and Optical Study of AM Herculis Systems

Keith Brendan Sohl

Abstract

An observational study of AM Herculis systems is presented, incorporating photometry and spectroscopy at both X-ray and optical wavelengths. Much of this thesis focuses upon one system, HU Aqr, a bright eclipsing system discovered by ROSAT. HU Aqr is unique amongst AM Hers because it has eclipses and possesses an accretion stream with significant optical flux, thus allowing detailed study of the nature of the accretion flow for the first time.

Strong constraints on the accretion stream in HU Aqr have been obtained from optical photometry and spectroscopy. Changes to the mass accretion rate lead not only to variations in the mean flux from the system, but also to changes in the number of accreting poles and to alterations to the accretion geometry. A correlation analysis of the short timescale flickering in the data reveals a strong association between the photometry and polarimetry during the absorption dip. This is interpreted as arising from density structure within the accretion stream. The spectroscopic data reveals a highly complex emission pattern arising within the stream. A model has been developed which is used to measure the brightness distribution along the stream using both eclipse and emission line data. This has demonstrated that the line and continuum emission regions are located in well-defined yet separate regions within the stream.

Further evidence for complex density structure in the accretion stream has been obtained from short timescale variations in the X-ray flux during the absorption dip of both HU Aqr and UZ For. In HU Aqr, the first detection has been made of coronal emission from the secondary star in an AM Her system. Both systems have also provided clear evidence for spectral structure within the accretion region, comprising a hard core of emission with a softer region surrounding it.

This X-ray analysis was extended to include a total of 30 systems in a study of the soft X-ray light curves and phase-resolved spectral behaviour of AM Her systems. In addition to confirming that the overall morphology of AM Her light curves is broadly consistent with most of our expectations, evidence for structured accretion regions, similar to those found in HU Aqr and UZ For, were discovered in six other AM Her systems.

Dedicated to my father,
William J. Sohl
1940-1982

Contents

| | | |
|----------|---|-----------|
| 1 | Introduction to AM Herculis systems | 1 |
| 1.1 | The Roche potential | 2 |
| 1.2 | Cataclysmic variables | 3 |
| 1.2.1 | AM Her systems | 4 |
| 1.2.2 | Intermediate polars | 5 |
| 1.2.3 | Non-magnetic systems | 7 |
| 1.3 | AM Herculis systems | 8 |
| 1.3.1 | The secondary | 8 |
| 1.3.2 | The accretion stream | 10 |
| 1.3.3 | The accretion region | 16 |
| 1.3.4 | The primary | 25 |
| 1.4 | The impact of ROSAT | 28 |
| 1.5 | Orbital periods and evolution | 29 |
| 1.5.1 | The period distribution | 29 |
| 1.5.2 | Evolution | 30 |
| 2 | Optical photometry and polarimetry of HU Aqr | 36 |
| 2.1 | Introduction | 36 |

| | | |
|----------|---|-----------|
| 2.2 | Observations | 38 |
| 2.3 | Data reduction | 40 |
| 2.4 | The photometric and polarimetric light curves | 41 |
| 2.4.1 | Description of the light curves | 41 |
| 2.4.2 | Interpretation of the light curves | 45 |
| 2.5 | Accretion stream trajectory changes | 56 |
| 2.6 | Correlated photometric and polarimetric variability | 58 |
| 2.6.1 | Linear correlation | 60 |
| 2.6.2 | Results | 63 |
| 2.6.3 | Increased variability in the dip | 66 |
| 2.6.4 | Concluding remarks | 68 |
| 2.7 | Summary | 68 |
| 3 | Phase-resolved optical spectroscopy of HU Aqr | 70 |
| 3.1 | Observations | 70 |
| 3.2 | Data reduction | 71 |
| 3.3 | Results and discussion | 73 |
| 3.3.1 | The mean orbital spectrum | 73 |
| 3.3.2 | The light curves | 76 |
| 3.3.3 | The phase-resolved RGO spectra | 79 |
| 3.3.4 | Emission line velocity curves | 84 |
| 3.3.5 | Mass estimate | 86 |
| 3.3.6 | Phase resolved FORS spectra | 90 |
| 3.3.7 | Secondary spectrum and the distance to HU Aqr | 92 |
| 3.3.8 | Magnetic field strength | 94 |

| | | |
|----------|--|------------|
| 3.4 | Modelling the accretion stream emission | 94 |
| 3.4.1 | Eclipse profile model | 95 |
| 3.4.2 | Emission line model | 98 |
| 3.4.3 | Future work | 107 |
| 3.5 | Summary | 108 |
| 4 | ROSAT observations of HU Aqr | 109 |
| 4.1 | Introduction: the ROSAT mission | 109 |
| 4.2 | Observations | 112 |
| 4.3 | Results | 114 |
| 4.3.1 | The X-ray light curve | 114 |
| 4.3.2 | Eclipse ephemeris | 117 |
| 4.3.3 | The hardness ratio of HU Aqr | 119 |
| 4.3.4 | The phase resolved spectra | 119 |
| 4.3.5 | Flux in eclipse | 123 |
| 4.4 | Discussion | 124 |
| 4.4.1 | The narrow dip | 124 |
| 4.4.2 | The broad dip | 130 |
| 4.4.3 | The soft X-ray excess of HU Aqr | 134 |
| 4.4.4 | The X-ray emission regions | 135 |
| 4.4.5 | Detection of secondary in eclipse | 139 |
| 4.5 | Summary | 141 |
| 5 | ROSAT and quasi-simultaneous optical observations of UZ For | 143 |
| 5.1 | Introduction | 143 |

| | | |
|----------|---|------------|
| 5.2 | Observations | 146 |
| 5.3 | Results | 146 |
| 5.3.1 | The X-ray light curve | 146 |
| 5.3.2 | The hardness ratio of UZ For | 149 |
| 5.3.3 | The phase resolved spectra | 149 |
| 5.3.4 | The optical light curve | 153 |
| 5.4 | Discussion | 153 |
| 5.4.1 | The narrow dip | 153 |
| 5.4.2 | The X-ray emission regions | 159 |
| 5.4.3 | The soft X-ray excess of UZ For | 161 |
| 5.4.4 | The optical eclipse profile | 162 |
| 5.5 | Summary | 163 |
| 6 | ROSAT pointed observations of AM Her systems | 165 |
| 6.1 | Selection criteria | 165 |
| 6.2 | Reduction method | 166 |
| 6.3 | Theoretical expectations | 168 |
| 6.4 | Results | 176 |
| 6.4.1 | Bright-faint systems | 183 |
| 6.4.2 | Continuous systems | 195 |
| 6.4.3 | Flaring systems | 200 |
| 6.5 | Discussion | 204 |
| 6.5.1 | Classification of the soft X-ray light curves | 204 |
| 6.5.2 | Absorption dips | 205 |
| 6.5.3 | Structured emission regions | 206 |

Chapter 1

Introduction to AM Herculis systems

AM Herculis (or AM Her) type stars are a subset of the cataclysmic variable class of binary stars. The AM Hers are unique amongst the cataclysmic variables because the white dwarf primary possesses a magnetic moment large enough to constrain the flow of material between the two stars. This magnetically confined accretion provides an excellent laboratory for the study of accretion processes and plasma-field interactions. In this chapter the characteristics of the cataclysmic variable family as a whole are briefly introduced before a detailed discussion of the AM Hers themselves is presented, in order to place the physical consequences of the strong magnetism in AM Hers into context.

There have been a number of reviews published covering both cataclysmic variables and the subclasses individually. An excellent review of the AM Her stars by Cropper (1990) is now slightly out of date given the advances that have occurred since the launch of the ROSAT X-ray satellite in June 1990. Some effort has been made throughout this chapter to address this shortfall. Patterson (1994) provides a commentary on the closely related class of intermediate polars. Frank, King and Raine (1992) discuss the details of accretion physics and the cataclysmic variables as a whole are reviewed by Córdova (1995). Most recently, Warner (1995) published a comprehensive book on cataclysmic variables that includes a sizable chapter on AM Her stars. This also covers some of the developments that have occurred since 1990.

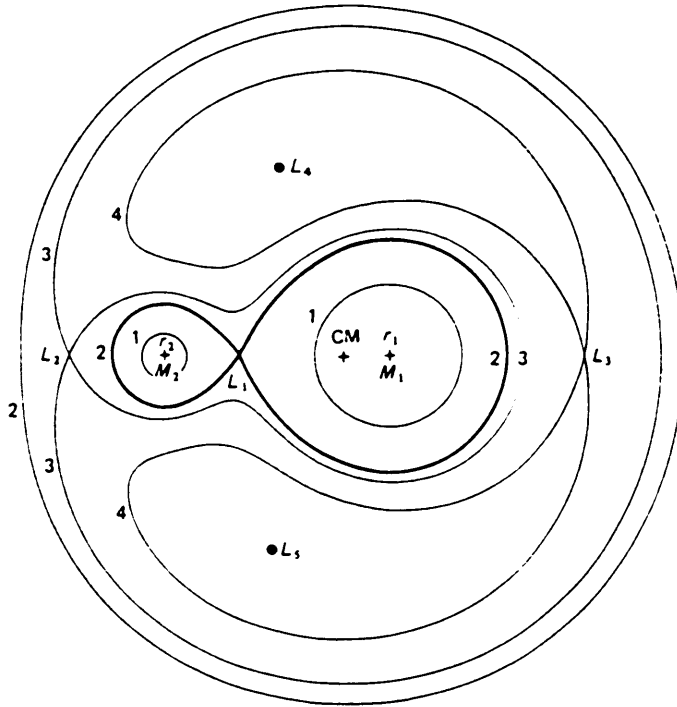


Figure 1.1: Cross-section in the orbital plane of the Roche equipotentials for a binary with mass ratio $q = 0.25$. The centre of mass (CM) is marked, along with the Lagrange points L_n . The equipotentials are labelled 1-4 in order of increasing Φ_R . See text for a full description. From Frank, King & Raine (1992).

1.1 The Roche potential

The total gravitational potential of two stars in close proximity is not just the sum of the individual stellar potentials but also includes a centrifugal force term. This solution for the gravitational potential is known as the Roche potential surface of the system. Figure 1.1 shows the intersection of the equipotential surfaces with the orbital plane for a binary system with a mass ratio $q = M_2/M_1 = 0.25$. This rather confusing diagram is more easily understood when each element of it is considered in turn. At large distances the binary nature of the system is not apparent and the equipotentials are circular, equivalent to those of a point mass seen in a rotating frame. Very close to one or other star the potentials are again circular because the gravitational potential is dominated by a single star. Further away, the potentials become distorted into a teardrop shape, and eventually the two teardrops meet between the two stars at the inner Lagrangian point (L_1). The L_1 point is a neutral position representing a saddle point between two low potential ‘wells’ (surrounding the stars) and two high potential ‘peaks’ (at L_4 and L_5).

The equipotential surrounding each star that passes through the L_1 point is known as the Roche lobe of that star (shown in bold in Figure 1.1). Each lobe represents the largest size that the individual star can reach while still remaining in equilibrium. If neither star fills its Roche lobe, the binary is known as a detached system. If one star fills its Roche lobe then stellar material can flow through the L_1 point and fall under gravity (accrete) onto the other star. These are the semi-detached systems. Finally, if both stars fill their Roche lobes then the two share a common surface and are known as contact binaries.

1.2 Cataclysmic variables

Cataclysmic variables are semi-detached binary systems comprising a white dwarf primary and a late-type companion. The companion star (or ‘secondary’) lies close to or on the main sequence with a spectral type in the range G to M. The secondary undergoes mass loss via Roche lobe overflow as described above, and this overflow material then accretes onto the white dwarf star. Because the white dwarfs have masses of the order one solar mass but have radii of only $\approx 10^9$ cm ($0.01R_\odot$), the potential well is very deep and hence a great deal of gravitational potential energy is released by the accretion process. For a body of mass M and radius R the gravitational potential energy released by the accretion of mass m onto its surface is

$$\Delta E_{acc} = \frac{GMm}{R}. \quad (1.1)$$

If the accreting body is a white dwarf with radius $R \approx 10^9$ cm and mass $M \approx 1 M_\odot$ then the energy yield is approximately 10^{17} erg g^{-1} . For a typical mass accretion rate of 1×10^{16} g s^{-1} , this translates into an accretion luminosity of the order 10^{33} erg s^{-1} . In order for the secondary to fill its Roche-lobe in this fashion the period of these systems has to be short; the orbital periods are found to lie in the range 80 minutes to several hours. The distances to these systems, determined predominantly by detections of the secondary, fall in the range 50–1000 pc.

For the purposes of this thesis, the various subclasses of cataclysmic variable can be differentiated by the geometry of their accretion flow, which is itself determined by the magnetic field of the white dwarf. The three main categories are the polars (or AM Her systems), the intermediate polars and the non-magnetic systems.

1.2.1 AM Her systems

AM Herculis systems have white dwarfs which possess a large magnetic moment ($5 \times 10^{33} < \mu_1 < 5 \times 10^{34} \text{ G cm}^{-3}$, King 1994). As the accreting material leaves the secondary it will follow a Keplerian trajectory and begin to orbit around the white dwarf. This stream is at least a partially ionised plasma and therefore a conductor, and so at some point will have its motion resisted by the magnetic field. As the material falls the magnetic field eventually penetrates the stream and the plasma flow will become dominated by the field. This is known as ‘threading’ of the stream by the field. At this point the stream will deviate from its Keplerian trajectory and start to follow the field lines, bringing the stream out of the orbital plane. Since the threading of the stream occurs only over a small range of azimuths the range of field lines threaded is small; the stream remains well collimated all the way down to the white dwarf and accretion occurs over a very small portion of the white dwarf surface. Figure 1.2 shows a schematic representation of a typical AM Her system.

The stream meets the surface quasi-radially at velocities greatly exceeding the sound speed in the plasma ($V = (2GM/R_{wd})^{1/2}$), so the material will shock before settling to the surface. The shock heats the material in the stream (its temperature will increase by a factor of four) and because all the accretion luminosity must be released before the surface is reached a bright X-ray source is found at this location. This bright source is commonly known as the ‘pole’. Therefore, magnetically controlled accretion (in both polars and IPs, see below), coupled with the rotation of the primary leads to a simple and immediately recognizable observational signature; the periodic modulation of the observed flux. This modulation can be further enhanced by beaming.

The defining features of AM Her systems are derived from the magnetic nature of the primary; they are the synchronisation of the rotation of the stellar components and substantial optical polarisation. The white dwarf magnetic field interacts with the secondary’s field and the intra-system plasma (stellar wind) to produce a braking torque. This torque forces the two stars into synchronisation. As the ionised stream falls through the magnetic field the free electrons within it will spiral around the field lines. This causes cyclotron radiation from the stream close to the white dwarf which will emerge as highly linearly and circularly polarised optical flux. The detection of significant optical polarisation is *the* defining characteristic for AM Hers. The discovery of optical polarisation in AM Her by Tapia in 1976 represents the origin of the study

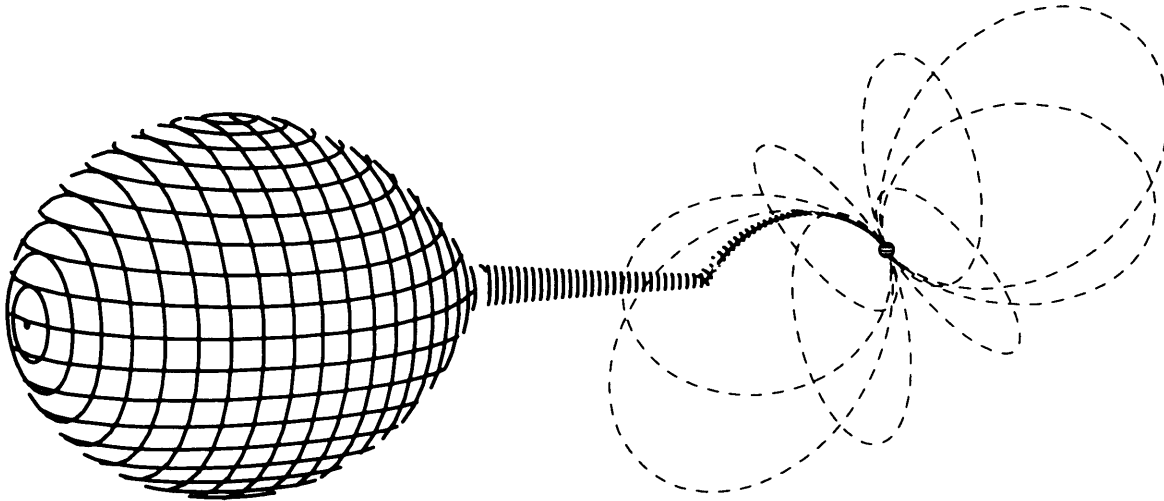


Figure 1.2: Schematic picture of an AM Her system. Shown are the Roche lobe-filling secondary, the gas stream and white dwarf primary. The dashed lines represent the inclined magnetic field of the primary.

of polars as a separate class (Tapia 1977).

1.2.2 Intermediate polars

If a system is not synchronised yet displays magnetic properties, it is classified as an *intermediate polar* (IP). As with AM Hers the white dwarf is significantly magnetised (though probably to a lesser degree), and this field channels the accretion flow onto the magnetic poles. X-ray modulations are detected at the spin period, originating from the X-ray pole on the white dwarf. These are distinct from the optical modulation which is detected at a sideband of the orbital period. This periodicity arises from irradiation by the X-ray pole, rotating at the spin period, of a region fixed in the rotating frame of the binary, rotating at the orbital period. This region could be the secondary star or an enlarged portion of the accretion disc. Variability at both the spin and orbital periods combined with hard X-ray emission is effectively the defining characteristic for IP's.

It is likely that the asynchronism in these systems arises because the magnetic moment is too low for a given separation; the field-field interaction is too weak to provide a synchronising torque. It should be noted that some systems, such as BY Cam and V1500 Cyg, are only just out of synchronism, P_{spin} is with a few percent of P_{orb} . It is likely that these are AM Her systems that have been temporarily knocked out of synchronism, by a nova explosion for example.

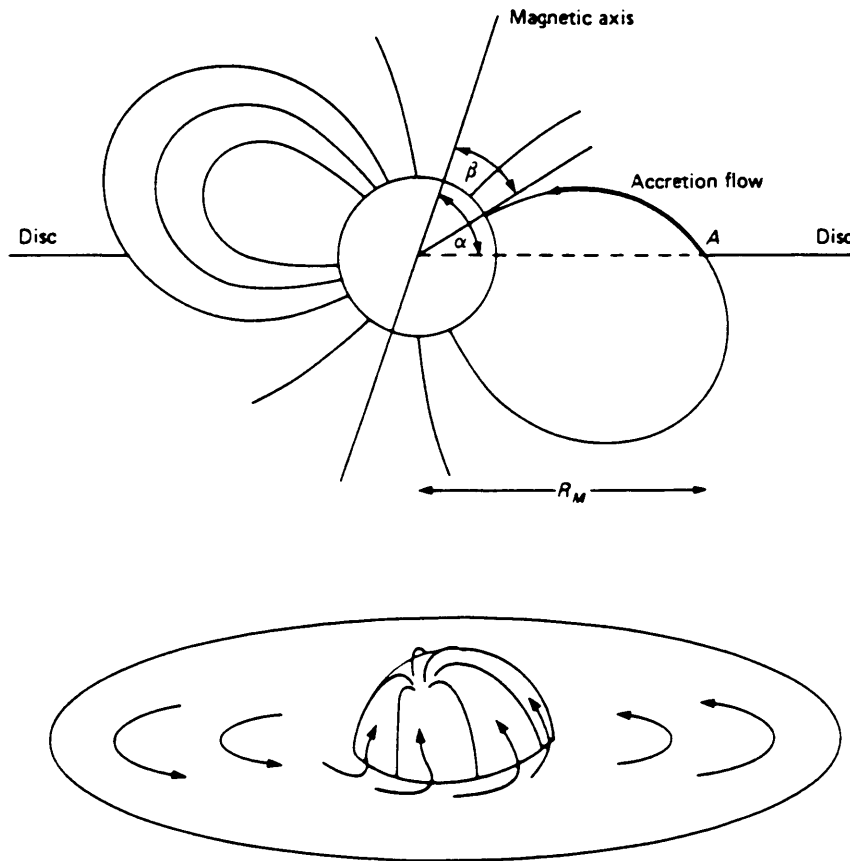


Figure 1.3: Schematic representations of IP systems. The upper figure shows a vertical section through the disc and primary, while the lower panel shows the distortion of the accretion disc as viewed from outside the system. From Frank, King & Raine (1992).

There is much debate over the accretion geometry of intermediate polars. Two scenarios have been proposed. The first suggests that the accretion flow can circularise and form a disk (see below) *before* the field disrupts the flow. The disk formed is truncated at small radii where the flow begins to follow the field lines (Figure 1.3). Evidence for this comes from emission line studies and eclipse mapping (Hellier 1991). The second scenario is a direct stream-fed geometry reminiscent of the AM Hers. This comes from the detection of an X-ray beat period between the orbital period and the white dwarf spin period that is incompatible with accretion via a disk (Wynn & King 1992). This beat arises as the flow switches from one pole to another as the white dwarf rotates.

1.2.3 Non-magnetic systems

As matter leaves the secondary star and falls along its Keplerian trajectory it attempts to form a ring around the primary at the circularisation radius:

$$R_{circ}/a = (1 + q)[0.500 - 0.227 \log q]^4 \quad (1.2)$$

where q is the mass ratio M_2/M_1 . In AM Her systems (and possibly intermediate polars) this is prevented from occurring by the magnetic field. In non-magnetic systems the stream is free to follow this path. Viscosity effects mean that the circular ring thus formed will spread both towards the white dwarf and away from it, forming an accretion disk. The outer limit of the disk is set by tidal forces and is close to:

$$R_{tide} = 0.9R_L \quad (1.3)$$

where R_L is the primary's Roche lobe radius. Therefore in non-magnetic systems the material is accreted around the equator. The greater isotropy of this accretion region means that the X-rays will not be modulated as the white dwarf rotates.

Optical and ultraviolet emission from the disk arises primarily from the centre of the disk, though there is significant optical emission from the hotspot where the accretion stream impacts the edge of the disk. The majority of the evidence for the disk structure is obtained through its optical line emission. It is straightforward to show that for disk accretion one half of the accretion luminosity arises within the disk, and so the other half must be released at the disk-white dwarf interface. This thin region is known as the boundary layer, and is the most likely location of the X-ray emission from non-magnetic cataclysmic variables.

The non-magnetic CVs can be separated into a large number of sub-categories based upon their wide variety of optical outburst behaviour. The following are the main categories, with a brief description of their behaviour.

- *Classical Novae* are systems that display a single, sudden brightness increase of ~ 9 magnitudes. The rise times for these events are of the order of hours while the decay lasts tens to hundreds of days. These violent episodes are generally accepted to be caused by thermonuclear runaway within the accreted material that builds up on the surface of the primary.

- *Dwarf novae* exhibit less spectacular outbursts that occur at quasi-regular intervals (weeks to years) and lead to a brightening of 2–5 magnitudes, or in some rare cases up to 8 mag. These outbursts are reasonably well understood as the release of gravitational energy as the accretion rate increases due to a rise in the mass transfer rate or a disk instability (in which a disk viscosity change allows the disc to move angular momentum outwards and matter in towards the white dwarf).
- *Recurrent novae* are objects that have had repeated outbursts. They are distinguished spectroscopically from the dwarf novae; recurrent novae display a substantial high-velocity shell of ejected material, dwarf novae do not.
- *Anti-dwarf novae* spend most of the time in outburst with occasional short drops to quiescence.
- *Nova-like variables* display all the typical properties of cataclysmic variables without having shown an outburst. Most seem to be dwarf novae that are permanently in outburst. Note that for historical reasons the magnetic cataclysmic variables are sometimes included in this class.

1.3 AM Herculis systems

1.3.1 The secondary

The secondary stars in AM Her systems do not display many properties distinct from the secondaries of the other classes of cataclysmic variable. The secondary is a low-mass red dwarf star with a typical spectral type between M3 and M6 (Cropper 1990). Because of its low luminosity it is difficult to observe the star directly against the background of emission from the stream, pole and primary. It is therefore necessary to study the secondary when these contributions are reduced, or in the infrared. Spectra of the secondary have been obtained during low states of accretion (Schmidt, Stockman & Margon 1981) but contamination by emission lines is still a problem. Better observations can be made during eclipses by the secondary but the number of eclipsing systems is low.

When the spectrum can be obtained, determination of the spectral type is usually straightforward by comparison with spectra from other late type stars of known spectral class. The spectral

type allows a distance estimate to be made using the tabulated absolute magnitudes of late type stars. Another means of finding the distance is by K-band photometry (Warner 1987). The surface brightness of a cool star in the K-band is only weakly dependent on its luminosity and temperature and so the distance can be determined given an assumed mass-radius relationship and orbital period for the system.

Time resolved measurements of the NaI doublet in absorption (8193Å, 8194Å) can reveal the radial velocity amplitude of the secondary. Some components of the He and Balmer emission lines are also thought to arise on the surface of the secondary and therefore provide a second means of finding its orbital velocity. For a given inclination and orbital period the orbital velocity of the secondary specifies the mass ratio of the system via Kepler's Laws. For those systems where such measurements were possible the secondary star masses have been found to lie in the range 0.10 - 0.35 M_{\odot} . Observation of absorption lines from the secondary show that the star rotates synchronously (e.g. Young & Schneider 1979), and this is also a requirement of evolutionary theory (Czerny & King 1986).

Magnetic fields have been detected for isolated M-dwarfs and M-dwarfs in detached binaries (Schrijver 1985). Since magnetic activity is correlated with rotation rate and the rate is typically higher for M-dwarfs in AM Her (given synchronism), it is highly likely that the secondaries of AM Her possess magnetic fields. Evolutionary theories also require a field of $10^2 - 10^3$ G for synchronisation in systems with periods > 3 hr (Hameury et al. 1987). Although not as strong as the primary's field, this field can become important when considering such issues as the trajectory of the accretion stream and the creation of density structure within the stream. The rapid rotation and significant magnetic field also suggest that the corona of the secondary should also be a minor source of X-rays in AM Her systems.

The primary-facing side of the secondary will be bathed in radiation from the primary and the pole. This leads to heating of the photosphere (Hameury, King and Lasota 1986) and hence causes Balmer line emission from the secondary (this is the line emission component from the secondary mentioned earlier). Recent successes have been achieved both in modelling the irradiated atmosphere (Brett & Smith 1993) and in mapping the flux distribution across the star's surface (Southwell et al. 1995, Davey & Smith 1996). An example of the brightness distribution for AM Her is shown in Figure 1.4. It is important to realise that this will non-

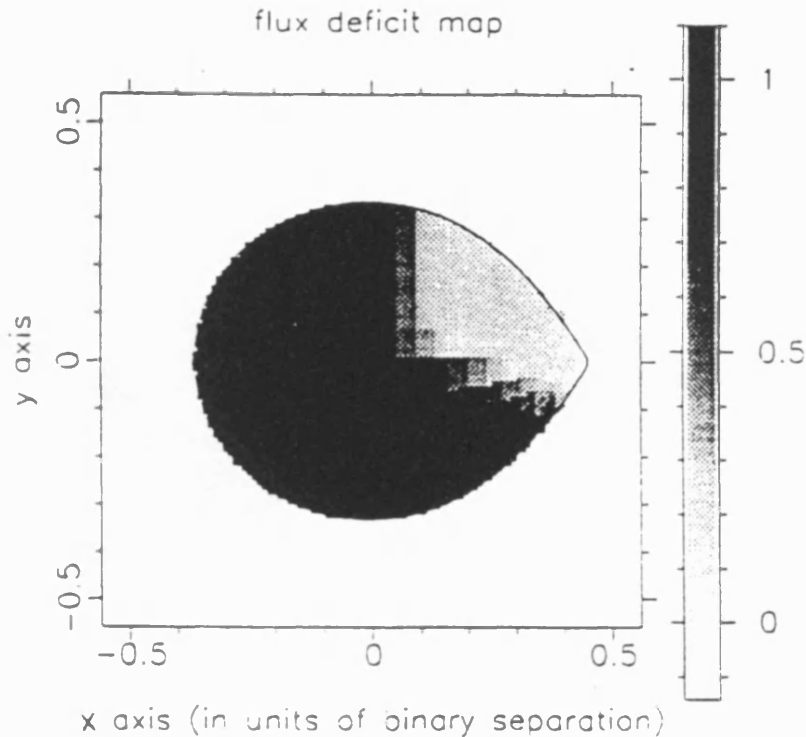


Figure 1.4: Surface map of AM Her. Shown is the strength of the Na I doublet; the light region is where the doublet is weak, and where irradiation by the pole is therefore strongest. From Davey & Smith (1996).

uniformly effect the 'centre of gravity' of the emission lines used to determine the orbital velocity of the secondary. A correction must therefore be made for this bias.

1.3.2 The accretion stream

Basic stream models

The interaction of the accretion stream and magnetic field in AM Her systems is highly complex, a fact first appreciated by Liebert & Stockman (1985). Although their ideas changed the way the stream was envisaged and were highly successful, it will be seen that even their approach is far too simplistic.

According to Liebert & Stockman, the accretion stream in AM Hers may be divided into the three regions as outlined in Figure 1.5. The limits of these regions are determined by three competing pressure forces within the stream; the ram pressure P_R , the thermal pressure P_T and the magnetic pressure P_M of the field. Both P_M and P_R increase as the stream gets closer to

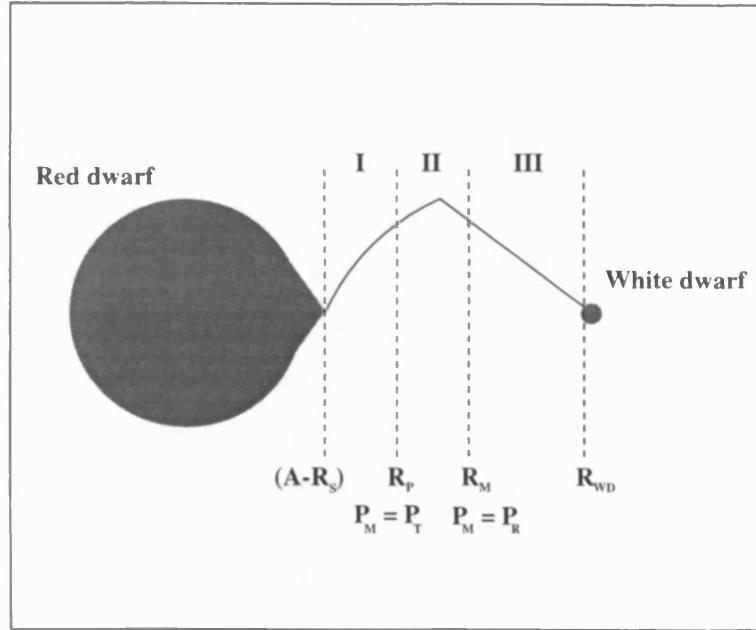


Figure 1.5: Sketch of an AM Her system, with the three main regions of the accretion stream marked. See text for details.

the primary. The magnetic pressure increases at a far greater rate so even if $P_R > P_M$ at the L_1 point, the magnetic pressure may eventually dominate over the ram pressure. If the magnetic moment of the primary is not large enough for this to occur before the minimum approach distance of the stream to the white dwarf is reached ($R_{min} \sim R_{circ}/2$) then the binary system will not be an AM Her.

The first region in Figure 1.5 runs from the secondary star's surface, at a radius $A - R_S$ from the centre of mass (COM) of the primary, to the radius R_P at which P_M equals P_T . While in this regime the stream follows a ballistic trajectory like that of a non-magnetic CV, with decreasing density as it accelerates. Only long period systems ($P_{orb} > 3$ hr) will have a region of this type because at shorter periods $R_P > (A - R_S)$, so the stream starts out in the second region.

Beyond R_P , in the second regime, P_M exceeds P_T but not the ram pressure P_R . This is the so-called threading region that lasts until $P_M > P_R$ at a radius R_M from the COM of the primary. Many processes complicate the physics of this region, for example Kelvin-Helmholtz shredding of the shocks, reconnection and X-ray heating, making this a poorly understood portion of the stream.

At radii shorter than R_M , the stream is constrained by the field and so follows the field lines down to the white dwarf surface. In most systems the stream in this regime will be raised out of the orbital plane by the magnetic field.

An immediate problem is apparent because both P_M and P_R depend upon the density of the stream material. R_M and R_P will therefore be located at different radii for streams of different densities. However, the stream is likely to possess material at a range of densities which will each want to thread at different radii causing multiple streams to form. The modelling of such a complicated flow is understandably difficult and for this reason most models to date have greatly simplified the stream (e.g. Rosen, Mason & Córdova 1987, Mukai 1988, Ferrario et al. 1989*b*), by assuming a single density, well collimated flow.

Optical line emission from the stream

Three principal methods exist for probing the stream in the region between the L_1 point and the accretion shock; by optical line emission from the stream, from X-ray and optical absorption dips and from eclipses. Phase resolved optical spectra show the strongest emission lines (H Balmer, HeII 4686Å etc.) to be comprised of multiple components, each with its own distinctive radial velocity variation. It is believed that such components arise within the accretion stream, apart from one which may also arise partially on the secondary. Greenstein et al. (1977) describe an early example of such a study of AM Her, which actually precedes the discovery of polarisation from AM Her and the ‘birth’ of polars as a class.

Figure 1.6 shows these emission line variations from AM Her (Greenstein et al. 1977). In this trailed spectrogram each component displays its radial velocity variation over the orbital cycle as an S-wave running down the plot. The superposition of these components builds up the complete line profile. Typically two components are detected (as in this case); a broad, high velocity component and a narrow, low velocity component, but up to four separate components have been found (Rosen, Mason, & Córdova 1987). The radial velocity variations are a combination of the stream and orbital velocities, while the breadth of each component is related to the spread of velocities within the emitting material. The broad component is presumed to arise within the accretion funnel close to the pole, while the narrow component comes from close to or on the secondary.

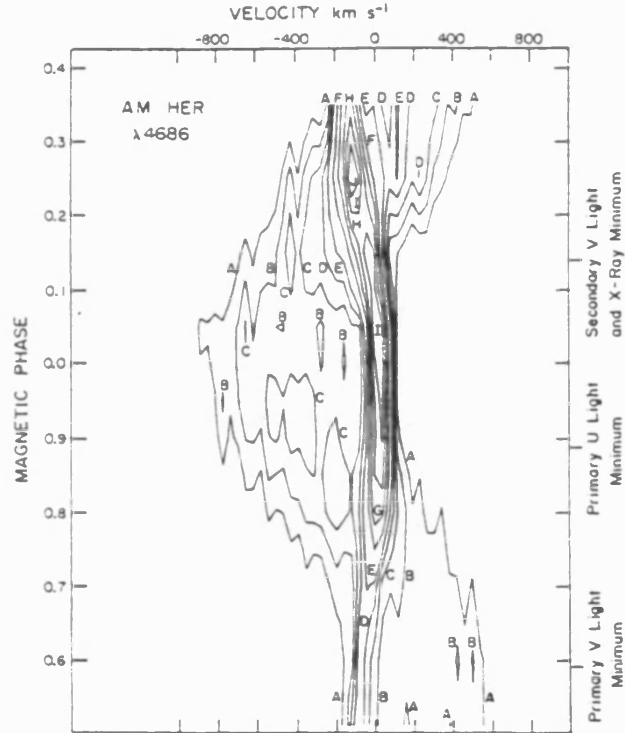


Figure 1.6: Contour representation of the trailed spectrogram of the He II $\lambda 4686\text{\AA}$ line from AM Her. Both a narrow component and broad underlying component can clearly be seen. From Greenstein et al. (1977).

The infall velocity of the material in the accretion funnel is much greater than the orbital velocity at that point, whereas the infall velocity is almost insignificant at greater distances where the narrow component arises. The orbital velocity vector will therefore dominate the narrow component, but will be undetectable in the velocity variations of the broad component, leading to orthogonal velocity vectors for the two components. This introduces a phase shift between the narrow and broad components, allowing them to be distinguished in the trailed spectrograms.

For an accretion funnel that lies directly between the secondary and the white dwarf, a 90° phase difference would be expected between the two line components. Usually the broad component leads the narrow by 10° – 60° , indicating that the pole leads the secondary in phase. It is possible to derive the phase at which the accretion region is viewed closest to face on from both photometry and polarimetry (e.g. Cropper 1987). The coincidence of this phase with the phase of maximum redshift of the broad component proves that the accretion funnel is the source of the broad component.

By modelling the equivalent widths and radial velocities of these components the location of the line emitting gas can be established. There have been some successes with this, for instance Rosen et al. (1987) find a distance of 1.2×10^{10} cm ($\sim 13R_{WD}$) between the broad component emitting region and the white dwarf surface in V834 Cen. Ferrario et al. (1989*b*) present a more sophisticated approach which provides good fits to data from V834 Cen, ST LMi and UZ For. They succeed in finding locations for the line formation regions and show the threading region to be very azimuthally extended and located 0.5–0.75 of the way between the white dwarf and first Lagrange point. However, it is probably true to say that the full potential of such techniques has yet to be realised. The convergence of good spectroscopy (spectral resolution $\sim 1-2\text{\AA}$, time resolution of a few minutes) with advances in the stream models, fitting methods and computing power should enable great advances to be made in this area over the next few years.

Absorption dips

In the optical and X-ray light curves of many AM Her systems a short reduction in the flux is detected. These ‘dips’ are believed not to arise from an eclipse by the secondary but from occultation of the polecap by the accretion stream (Mason 1985). An example of an absorption dip detected in the ROSAT soft X-ray light curve of EF Eri is shown in Figure 1.7. The occulting portion of the stream typically lies some 10^{10} cm from the white dwarf (King & Williams 1985) and therefore these dips can provide a clean diagnostic of the stream at a known location well away from the accretion funnel. Photoelectric absorption is thought to be the process causing the X-ray dips while free-free absorption is the most likely cause of the optical attenuation. Since these two processes have different dependence of optical depth on density, simultaneous optical and X-ray observations of a dip could be used to measure the density profile across the stream. Watson et al. (1989) elaborate on this method and apply it to the system EF Eri. Such measurements are difficult given the complications involved in scheduling simultaneous X-ray and optical observations, and so this has yet to be undertaken in more than a couple of systems.

A demonstration of the potential that such dips can provide to learn about the stream was given by Watson et al. (1995) for a dip detected in the light curve of RE1940-10. Phase-resolved broadband optical spectroscopy was used to compare the spectrum during the dip to that at non-dip phases. They found that the spectrum of the absorber causing the dip was flat, which is contrary to the expectations for free-free absorption. Watson et al. present a plausible explanation for

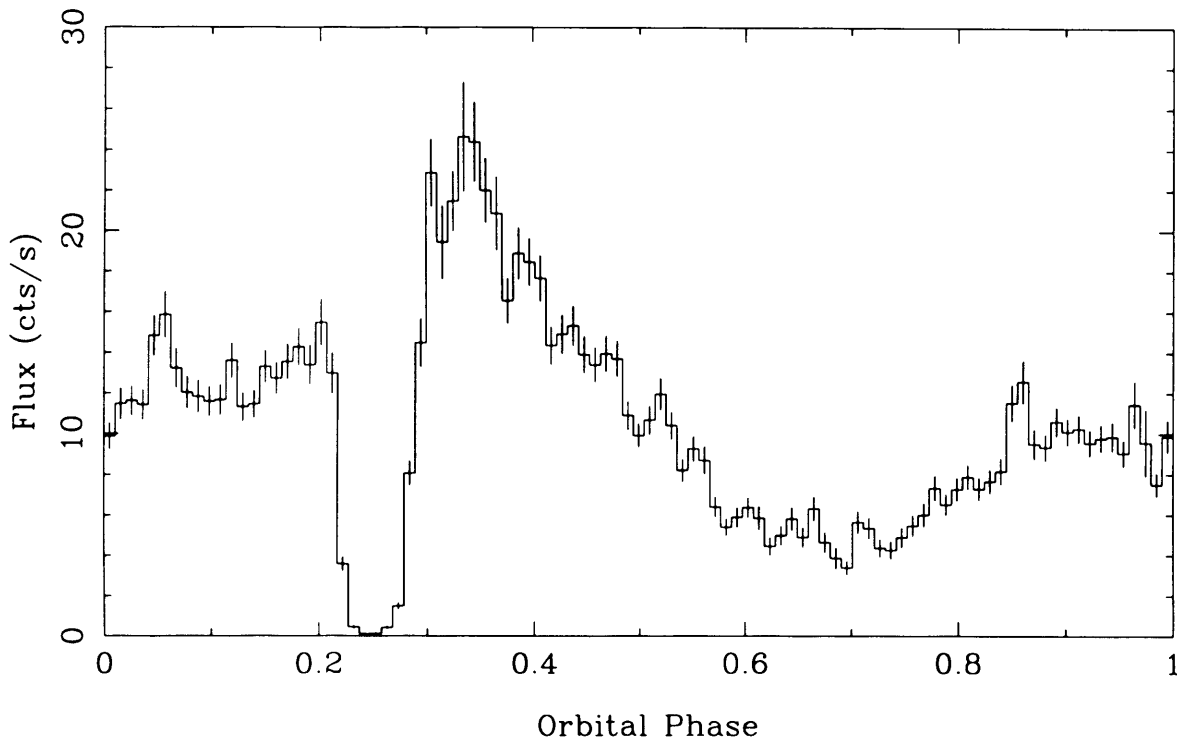


Figure 1.7: ROSAT soft X-ray light curve of EF Eri. A deep absorption dip can be seen at phase 0.25.

the lack of a spectral signature by using the idea of an inhomogeneous stream, wherein dense, optically thick filaments of gas cause complete and wavelength-independent attenuation of the flux. This structure may correspond to that associated with the accretion region (see below).

Multiple streams

The soft X-ray light curves of several AM Her systems have been seen to change substantially from epoch to epoch (e.g. QQ Vul, Osborne et al. 1987; AM Her, Heise et al. 1985). In these systems an anomalous mode of accretion is found whereby the soft X-ray modulation becomes antiphased with its earlier behaviour. This anomalous state came to be known as the ‘reversed X-ray mode’. Heise et al. (1985) concluded that the soft X-ray emission during the reversed mode arises on a second pole while the soft X-ray emission in the normal mode and the hard X-ray emission in both modes arises on the main pole. Thus two accreting poles are required which implies that two accretion streams must be present. Figure 1.8 shows one scheme for achieving this. A second stream is shown leaving the threading region on different field lines so that it impacts on the white dwarf on the opposite side to the main pole. This represents

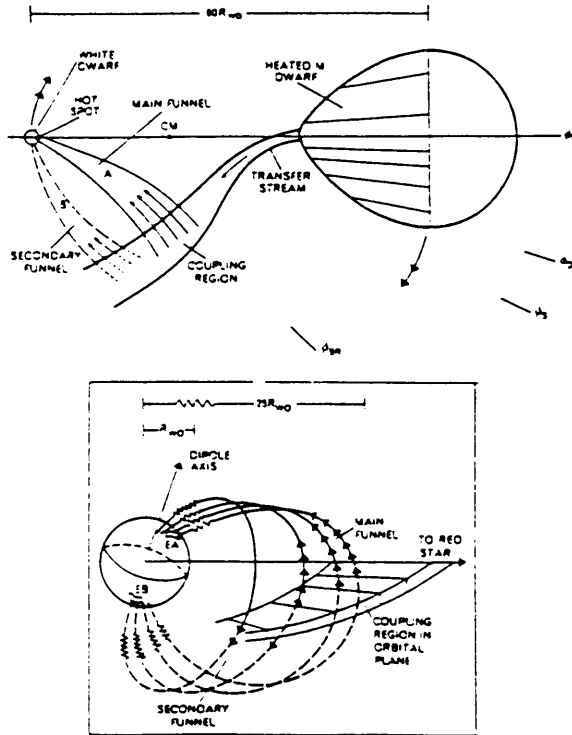


Figure 1.8: Schematic view of an AM Her system showing two separate accretion flows from the threading region to the white dwarf (adapted from Wickramasinghe 1988).

a further example of how the accretion process is not as straightforward as the initial ideas of Liebert & Stockman (1985).

1.3.3 The accretion region

The term ‘standard model’ is used to refer to the earliest models for the accretion region in AM Her systems, developed soon after the discovery of AM Her (Lamb & Masters 1979). These were highly simplistic; they were usually one-dimensional and did not include all of the physics necessary to properly describe the emission. Unsurprisingly these have since been superseded by more detailed models which try to pick up on these shortcomings. To understand current theories of accretion region physics it is necessary to understand their origins in the standard model and hence the reasons that they have been developed in the way that they have. In addition, the standard model itself still serves to introduce the basic physics of the accretion region. In this section the model and the physics behind it, its weaknesses when compared to observations and the more recent models are discussed.

The standard model

Before impacting on the white dwarf surface the gas within the accretion stream is flowing supersonically. After the impact it must assume the properties of the photosphere; temperature, density and velocity ($v_{phot} \simeq 0$). Clearly a shock will form, across which the flow changes from supersonic to subsonic ($v_2 = v_1/4$, where the subscripts ‘1’ and ‘2’ refer to the pre- and post-shock flows respectively). The shock also produces a large increase in the temperature ($kT_2 = 10 - 30$ keV) and the density ($\rho_2 = 4\rho_1$) of the gas (Frank, King & Raine 1992). The time taken for the gas to cool and decelerate to match the conditions at the top of the photosphere determines the equilibrium height of the shock. The shock plus the post-shock flow is commonly referred to as the ‘accretion column’.

The cooling mechanisms acting within the post-shock flow are bremsstrahlung emission, cyclotron emission and Compton cooling. The relative importance of these depends upon the conditions, principally the magnetic field B and the mass accretion rate per unit area (the *specific mass accretion rate*), which is related to L/f , where L is the luminosity and f is the fraction of the stellar surface covered by the accretion column. Note that Compton cooling is often left out of the calculations since it is only important for very massive white dwarfs ($M_1 \simeq 1.4M_\odot$, Frank, King & Raine 1992).

The basic geometry of the standard model and the mechanisms for dissipating the accretion energy are depicted in Figure 1.9. The flux from the accretion column comprises three components; hard X-ray bremsstrahlung radiation, cyclotron radiation and blackbody radiation at soft X-ray wavelengths. The hard X-ray bremsstrahlung is emitted from the free electrons within the column, with kT_{br} typically 30 keV. The column is optically thin to these hard X-rays. Semi-relativistic electrons spiraling around magnetic field lines emit the cyclotron radiation. This radiation is only important as a cooling mechanism when B is high or L/f is low; it is generally more important as an observable diagnostic of the accretion region. The highest harmonics of the cyclotron radiation will be optically thin, while the lowest are optically thick. Note that the presence of the strong magnetic field means that any optical emission from the column is likely to be significantly linearly and circularly polarised.

The bremsstrahlung and optically thin cyclotron flux is emitted isotropically, and hence roughly

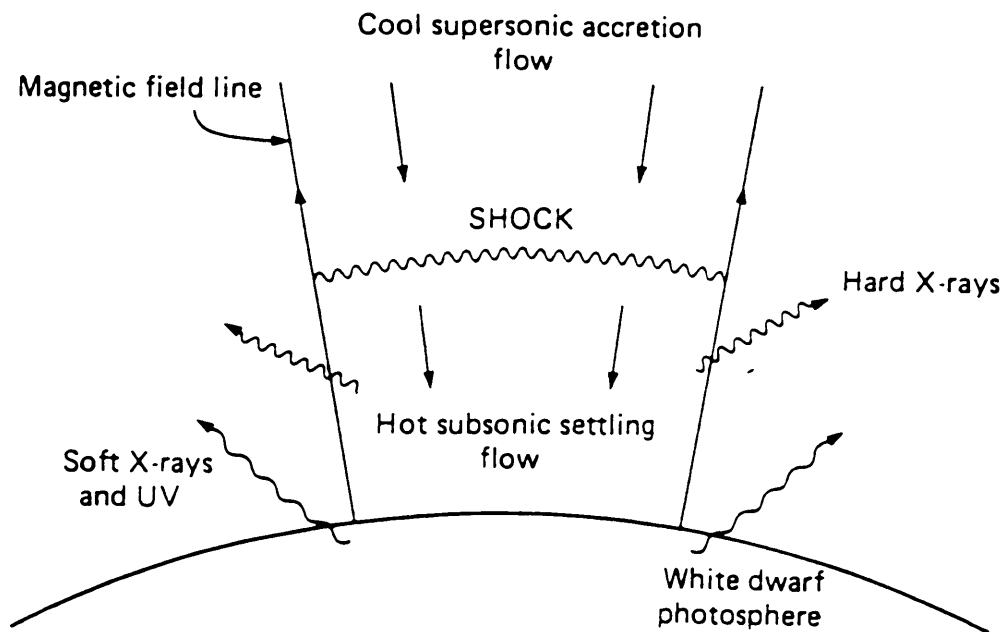


Figure 1.9: Accretion geometry according to the standard model. From Frank, King & Raine (1992).

one half of this emission will be intercepted by the primary. This flux can then be either reflected or absorbed. For energies > 30 keV the albedo of the surface is likely to be around 1 (total reflection). The lower energies (< 30 keV) will be absorbed, and this energy is then thermalised and re-emitted as a blackbody spectrum. This emission will emerge in the UV or soft X-ray regime ($kT_{BB} \simeq 40$ eV). It has been shown by King & Watson (1987) that the predicted energy balance gives the luminosity ratio:

$$\frac{L_{BB}}{L_{br} + L_{cyc}} \approx 0.56 \quad (1.4)$$

There are a number of weaknesses of the physics in this model that can already be identified. There is no consideration of the temperature and density structure of the post-shock region. No consideration of the sides of the column has been made. No other energy transport mechanisms are considered, such as electron conduction. The interaction of the radiation with the gas in the column has not been included fully. Better models were developed to make the physics more realistic by including some of these omissions (Kylafis & Lamb 1979, 1982, Imamura & Durisen 1983, Imamura 1984, Imamura et al. 1987). In spite of these refinements Equation 1.4 will always hold approximately true so long as the bulk of the emission arises in a 10–30 keV plasma.

Although these improvements made the models more realistic and reduced some of the discrepancies between the theoretical models and the data, some serious problems remained. The main limitation is that a spherically symmetric shock is assumed. In reality non-uniformities across the shock, time variability and density structure within the stream are to be expected. The observational evidence to support these is presented below.

Cyclotron Radiation

It has already been stated that cyclotron radiation is important as a diagnostic of the accretion region. This is because the cyclotron lines arise primarily in the optical, which is observationally far more accessible than the X-ray regime. Substantial labour has therefore gone into modelling the cyclotron emission from AM Her systems (Chanmugam & Dulk 1981, Meggitt & Wickramasinghe 1984, Barrett & Chanmugam 1984, Canalle & Opher 1988, Wickramasinghe 1988 and references below). Wickramasinghe (1988) and Schwope (1990) review these developments so only a summary of the predictions of the models will be presented here.

According to the standard model, most of the cyclotron flux will emerge in the UV waveband. Cyclotron radiation is detected over a range of harmonics which appear as broad humps in the spectra, but at the energy of the electrons in the accretion column little flux is found at the fundamental frequency (Warner 1995). The strongest cyclotron lines from a plasma with the parameters of the accretion column will correspond to the 4th – 7th harmonics of the fundamental frequency. Cyclotron radiation from the column is subject to a strong beaming effect and so the flux peaks at 20° from the perpendicular to the magnetic field lines (Wickramasinghe & Meggitt 1985). This is distinct from the maximum circular polarisation which is seen *along* the field lines for the low order harmonics, rising to 20° away from the field lines for the higher order harmonics. The linear polarisation, present in the higher harmonics only (> 5th), is concentrated perpendicular to the field.

The soft X-ray excess

Apart from the reversed mode (§1.2.2), the X-ray light curves of AM Her systems can be reasonably well understood by the standard model alone (e.g. Imamura 1984). A serious problem

arises when the X-ray spectra are considered, and attempts to reconcile this have dominated studies of the accretion process since its discovery. Early fits to the spectrum of AM Her found that the luminosity of the soft component exceeds the hard component by a factor of ~ 50 (Tuohy et al. 1978, Raymond et al. 1979, Fabbiano et al. 1981). Equation 1.4, from King & Watson (1987), predicts that this ratio should be around 0.5 if the contribution of the cyclotron flux is insignificant (as it is for AM Her). This discrepancy was first noted by King & Lasota (1979) and came to be known as the soft X-ray ‘problem’, while the unexpected soft X-ray flux is known as the ‘soft X-ray excess’.

This discovery was followed by a period of confusion where the cause and even the presence of the soft X-ray excess was under debate. For example both Patterson et al. (1984) and Lamb (1985) stated that the soft X-ray problem might have disappeared based on observations of VV Pup (Patterson et al. 1984) and EF Eri (Beuermann, Stella, & Patterson 1987). This confusion stemmed from the difficulty of getting good luminosity estimates from the hard tail of the soft component which was the only portion observable at that time. It was not until grating spectrometer results from EXOSAT that the identification of the soft excess became secure. For example QQ Vul (Osborne et al. 1987) and AM Her (Heise et al. 1985) were found to have $L_{bb}/L_{br} \sim 4.5$ and 10 respectively. It is now almost certain that the excess is real (see Watson 1986, Osborne 1988, Paerels, Heise & Teeseling 1994 for example). Indeed, the debate has now progressed to the point where a soft excess is actually a theoretical requirement. King & Watson (1987) show that the mass transfer rate inferred from the hard X-ray flux is an order of magnitude too low to allow AM Her systems to evolve on a realistic timescale (less than the Hubble time). The extra accretion implicit in the presence of a soft excess implies a mass transfer rate comparable to that predicted.

The soft X-ray observations by ROSAT have provided a new opportunity to search for soft X-ray excesses in AM Her systems (see Watson 1994 for a summary). This has been possible because ROSAT spectra are able to constrain the parameters of the soft component better than in previous missions. Ramsay et al. 1994 carried out a study of ROSAT observations of a number of systems in which fits to the well-resolved soft and hard components were used to define the spectra. This demonstrated that most AM Her systems (12 out of 16 in this study) do possess a large soft X-ray excess.

Inhomogeneous accretion models

Kuijpers & Pringle (1982) proposed two solutions to the problem of the soft X-ray excess which have remained the favoured explanations since that time. The first is the bombardment solution, which does away with the assumption from the standard model that the shock is thin. If the shock is thick, some energy can be radiated away from the accreting material as it passed through. If this cooling is strong enough the top of the post-shock region will become cooler than for a thin shock solution. Less time is required to cool the plasma within the post-shock and so its height will decrease. It may be possible to extrapolate this to the point where the shock touches the surface and no post-shock region exists at all. If the gas thermalises in a thin layer in this manner then an excess of soft X-rays will result.

The question that has to be answered is whether the shock can radiate efficiently enough for this to occur. Thompson & Cawthorne (1987) considered this problem and concluded that another source of cooling is required, and that cyclotron cooling might provide this. Frank, King & Lasota (1988) denounced such a possibility for any shock temperatures above 10 keV. Low shock temperatures require material with a low density, so the bombardment solution will only work where the specific mass accretion rate is low ($10^{-3} < \dot{m} < 10^{-1} \text{ g cm}^{-2} \text{ s}^{-1}$ for $B = 5 - 70 \text{ MG}$). Woelk & Beuermann (1992) have developed further bombardment models which they contend may apply in some situations.

The alternative solution to the soft X-ray problem is to use an inhomogeneous flow model for the stream, in other words by invoking the density structure within the stream. If the density of a given blob of material is high enough that it penetrates the photosphere by a distance greater than the optical depth, then the X-rays generated from the accretion energy will be thermalised by the photosphere. This will give rise to an excess of soft X-ray flux. Note that while the use of the word ‘blob’ evokes an image of a spherical object, any material within the stream is stretched by tidal forces and increasingly constricted by the converging field lines as the stream approaches the primary. Density enhancements of any shape will therefore become distorted into long filaments of material following the field lines.

Frank et al. (1988) present the model in a more quantitative way. An individual blob’s ability to penetrate the photosphere and thereby contribute to the soft excess is determined solely by its

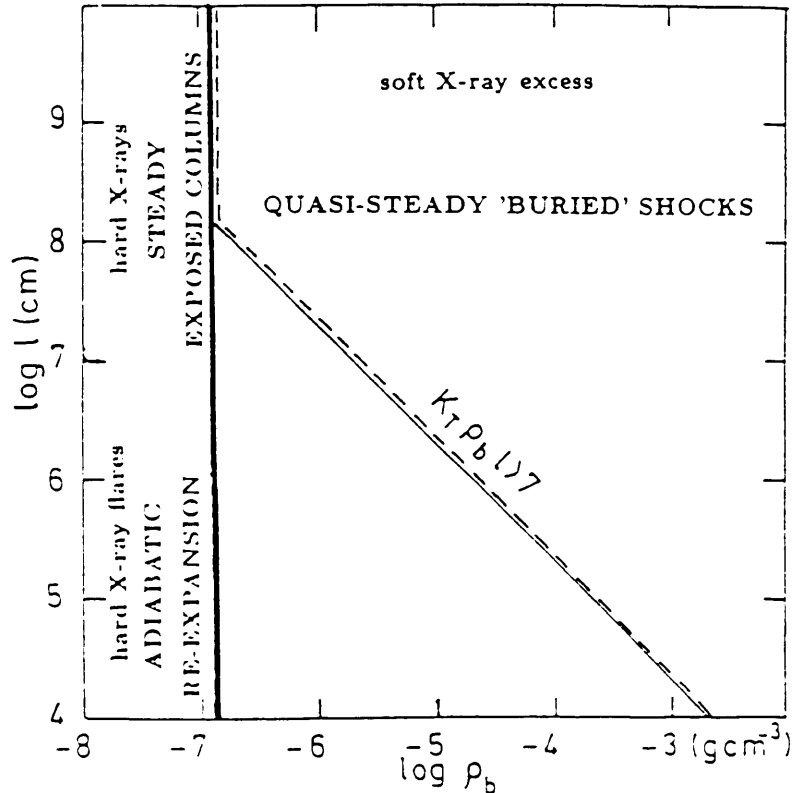


Figure 1.10: Dependence of accretion shock type on accreted blob size (length) and density. The different regions shown are discussed in the text. From Frank et al. (1988)

density and length. Figure 1.10 shows the different emission characteristics of the blobs based on their position in the density/length plane. Buried shocks will arise if the density exceeds the minimum density marked by the vertical line. If the density is not high enough for penetration, but the length of the blob is high enough for a steady shock to form then hard X-rays plus a small quantity of soft X-ray flux will be produced. If the length is too short then hard X-ray flares result. Hameury & King (1988) expand upon this by considering the distribution of blobs across the accretion region and deduce that only 10–15 individual blobs accreting at any one time is enough to account for the observed phenomena. It is anticipated that many accretion regions would comprise a mixture of dense blobby accretion with more tenuous ‘standard’ accretion. By altering the properties and proportions of each it is therefore possible for a single model to fit a range of soft excesses. The issues associated with blobby accretion are neatly summarised in King (1995).

There is further evidence for inhomogeneous accretion in AM Her systems. At optical and X-ray wavelengths flickering and flaring has been observed on timescales of 10 s to 5 min (e.g. VV Pup, Cropper & Warner 1986). These flares are only evident when the main accreting pole is in view. Flickering has also been seen in the polarisation which is correlated with the intensity

(Priedhorsky, Krzeminsky & Tapia 1978). This flickering is usually a stochastic process and only in some cases have quasi-periodic oscillations (QPOs) been detected (Middleditch 1982). Hydrodynamic instabilities can cause the height of the shock to vary and this may affect the luminosity of the post-shock region. However, the longest flares cannot be caused by this process because the time-scale becomes too long for the predicted luminosity variations (1-100 s). The more likely solution is that the accretion flow itself is variable. The flares in the light curve could then be caused by denser blobs of material impacting the surface. In the case of VV Pup, the shortest flares indicate blobs of length $\sim 1 \times 10^{10}$ cm.

It is unclear exactly where the blobs would arise; King (1989) notes that the gas flow through the Lagrange point will be modulated on approximately the correct timescale to create blobs but other possibilities such as breakup of the flow in the threading region cannot be ruled out. Recently Wynn & King (1995) have outlined a process whereby the stream breaks up into individual blobs via a continuous interaction with the magnetic field (see also King 1993). This process has been successfully used to predict the $P_{spin} = 0.1P_{orb}$ relation seen in many IP systems. This technique has also been extended to predict the stream trajectory in AM Her systems (see Chapter 3).

Additional modifications to the standard model

There exists further observational evidence which is not consistent with the standard model, but cannot be solved directly by the use of blobby accretion models. This requires other changes to accretion column models which are outlined with the supporting evidence below.

The standard model predicts the peak of the cyclotron flux to be located in the ultraviolet waveband. Bailey et al. (1985) and Bailey (1988) have undertaken polarimetric observations from the optical U-band through to the infrared. This work contradicts the standard model by finding the peak cyclotron flux at red wavelengths. To force the peak of the cyclotron flux down to such low frequencies requires a size parameter Λ for the emission to be 3-4 orders of magnitude larger than that determined directly from observations. The size parameter is a length given by the ratio of the optical depth to the opacity of the plasma (or, more simply, a length normalised by the optical depth of the plasma). The underestimate of Λ is an indication that the surface properties of the column (the measured optical depth) do not correctly represent

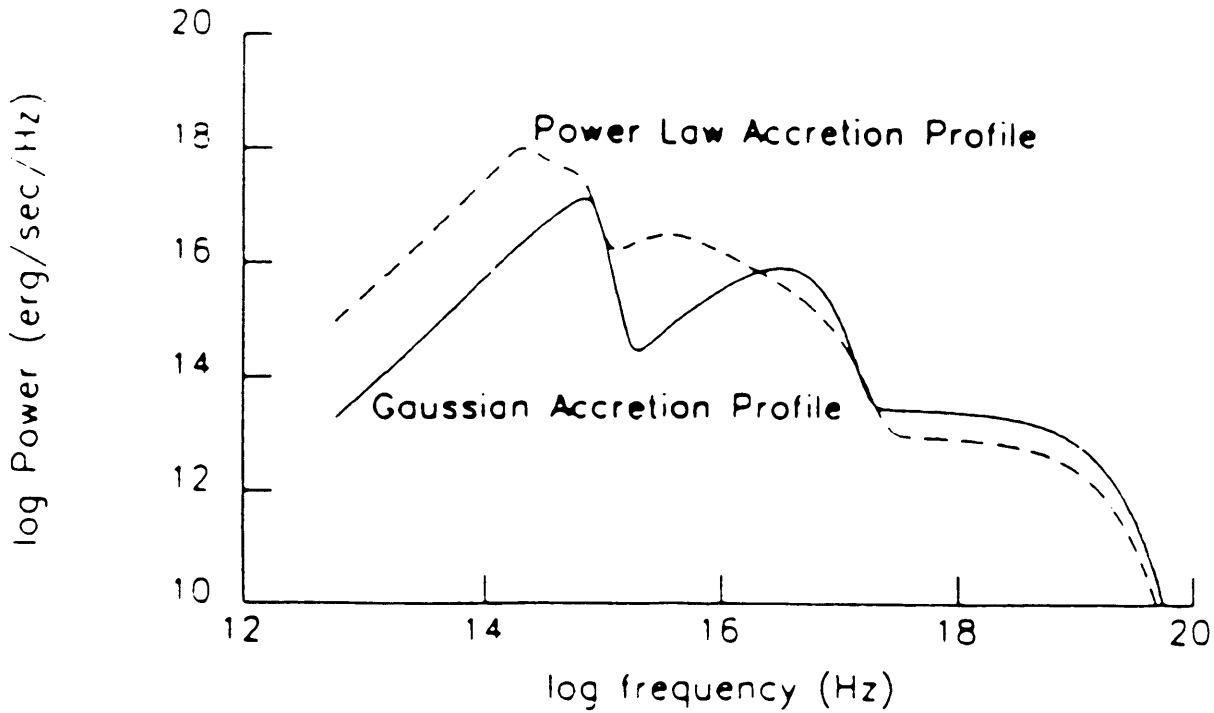


Figure 1.11: Cyclotron emission spectrum derived using non-linear accretion profiles. The peak of the flux now lies in the far red/near infrared ($\sim 9500\text{\AA}$). From Stockman & Lubenow (1987).

the properties of the core. Hence there is a need to change the structure of the emission region in the models to account for this whilst retaining the measured size parameter.

Early attempts to model this structure using ideal accretion profiles such as Gaussians and power-laws had an immediate effect upon the cyclotron spectrum. Figure 1.11 shows a model (with $L = 10^{33} \text{ erg s}^{-1}$, $L/f = 10^{38} \text{ erg s}^{-1}$, $M_1 = 0.8$ and $B = 20 \text{ MG}$) in which the cyclotron emission now peaks in the red or infrared (Stockman & Lubenow 1987). Although the model has been optimised to agree with the observations of Bailey et al. (1985) the potential of this method is still apparent. One drawback with these models is that a *reduction* in the soft X-ray luminosity is predicted, which would clearly increase the magnitude of soft X-ray problem. The blobby accretion model described above must therefore still be applied.

Another problem with early accretion models has already been raised in relation to the accretion stream; the reversed X-ray mode in AM Her, QQ Vul and other systems (Osborne et al. 1987, Heise et al. 1985). The need for two accreting poles with vastly different emission properties (hard and soft X-rays from one pole, soft X-rays only from the second pole) is a clear indication that accretion is not following the lines laid out by the standard model, at least for the second

pole. This can probably be explained by differing density spectra within the two streams (i.e. different blob sizes and numbers). However, the presence of two streams implies a quite extended threading region away from the magnetic pole, which in turn suggests that the accretion zone will be arc-shaped (or elongated, at least) and that the field lines will not meet the surface orthogonally (non-radial accretion). Some of these elements have been incorporated into the models of Ferrario & Wickramasinghe (1990).

The optical and X-ray light curves of some AM Her systems display alternate bright and faint intervals (one each per orbit) as the main emission region rotates into and out of view on the white dwarf. For a number of these systems (e.g. ST LMi, Cropper 1986; RE1149+28, Howell et al. 1995) the bright phase is not symmetric about its centre; the decline to minimum flux is shorter than the rise to peak flux. This further suggests that elongated emission regions or accretion arcs are present in some AM Hers.

1.3.4 The primary

Like the secondary, observing the white dwarf in AM Hers is not easy because the primary contributes relatively little flux at optical and X-ray wavelengths. Therefore one must look for epochs where the contributions from other sources are reduced; during low states and at orbital phases when the pole is occulted by the white dwarf. For some systems (e.g. UZ For, Bailey & Cropper 1991, and this thesis, Chapter 5), the white dwarf can be detected as the limb of the secondary sweeps across it during the eclipse ingress and egress, though useful measurements can only be made if the white dwarf is luminous enough.

The mass of the primary is difficult to obtain since there is no volume constraint on a star that is not filling its Roche lobe. The standard method for determining the mass of the components in a binary system is to obtain the inclination and orbital velocity of both stars. However, the orbital velocity of the primary is hard to establish because of the observational difficulties outlined above. It is therefore customary to assume the mass-radius relationship of the secondary which removes one of these required parameters. The range of primary masses is found to be $0.38 - 0.99 M_{\odot}$ with a mean of $0.60 - 0.64 M_{\odot}$ (Cropper 1990). This compares well with the mean mass of isolated white dwarfs; $0.6 \pm 0.1 M_{\odot}$ (Koester & Weidemann 1980).

A new method for obtaining the primary's mass has been developed by Fujimoto & Ishida (1997), see also Ishida & Fujimoto (1995), Fujimoto & Ishida (1995). This is based upon determination of the temperature of the accretion column just below the shock and at the white dwarf surface from X-ray line spectroscopy. Theoretical models of the column (see references in Ishida & Fujimoto 1995) predict the accreting matter to be heated to

$$kT_S = \frac{3}{8} \frac{GM_{WD}}{R_{WD}} \mu m_H \quad (1.5)$$

but temperature distributions within the column complicate the calculation, requiring both base and shock temperatures to be found. The ratio of H-like to He-like lines of a given element can be used to obtain these temperatures; Fe is most sensitive to T_S , other elements such as Mg, Si, Ar and S are sensitive to T_B . To make such measurements requires X-ray detectors with high spectral resolution, and hence have only been possible since the launch of ASCA in February 1994. The mass of the primary may routinely be found in this way in the future, as missions such as XMM and AXAF will prove to be even more suited to the task of observing the X-ray lines.

The field configuration of the white dwarf does not necessarily have to be dipolar. On occasion, the detection in some systems of two accretion sites that are not diametrically opposite to each other has been taken as evidence for quadrupoles and/or off-set dipoles. However, such a non-diametric configuration in a centred dipole field can occur when the stream threads closer to the white dwarf, onto field lines whose footprints lie far from the magnetic poles.

The magnetic field on the primary in AM Her stars is typically 7–61 MG (Beuermann 1995). The field strength can be found by measuring cyclotron harmonics or Zeeman split spectral lines. Zeeman splitting can usually only be seen during low states of accretion where the white dwarf photosphere is detectable directly. It is important to remember that the Zeeman spectrum and hence the field measurement obtained from it is a flux weighted mean over the whole white dwarf photosphere. Estimating the field in the accretion region itself on this basis is unreliable, but the cyclotron harmonics, arising within the accretion region, provide a means of measuring this field directly.

The fundamental cyclotron frequency is determined by the field strength in the accretion region.

A simple approximation gives the frequency of the n^{th} harmonic:

$$\omega_n = n \times \frac{eB}{m_e c} \quad (1.6)$$

where e is the charge on an electron, B is the magnetic field strength, m_e is the mass of an electron and c is the speed of light. By measuring the spacings between the cyclotron harmonics the magnetic field strength can therefore be found, and an estimate of the temperature of the region can be obtained from the width of the harmonics. For a field strength of 30 MG, typical of AM Her primaries, this places the $4^{\text{th}} - 7^{\text{th}}$ harmonics between 5100Å and 8900Å, in the red-infrared region. Recently Schwöpe & Beuermann (1990) have developed a more detailed method for deriving the field strength by modelling the wavelength shift of the harmonics as the system rotates during an orbital cycle, which also provides important information on the geometry of the system. The shift arises due to the changing position angle of the field lines. The model has been successfully applied to the phase resolved wavelength dependence of the cyclotron features of RX J0453-42 (Burwitz et al. 1995).

The synchronicity of the primary was established early on by the lack of modulation of radial velocities, flux or polarisation at anything other than the orbital period. The observations do not exclude very long slip periods, and the best candidate for finding such is the longest known eclipsing system, DP Leo. Robinson & Córdoba (1994) have found the rotation of the white dwarf in this system to be $(5.3 \pm 1.1) \times 10^{-3}$ s faster than the orbital period. Such a small deviation may simply represent oscillations of the main pole about an equilibrium position. Two systems, RE1940-10 and BY Cam do display evidence for asynchronicity which has been attributed to a recent nova explosion which has temporarily altered the primary's rotation rate.

The synchronicity of AM Hers is surprising because accretion provides a torque which will tend to spin up the primary. A balancing torque must therefore exist. It is believed that the interaction of the white dwarf's field with the conducting material between the stars sets up a magneto-hydrodynamic torque which counters the accretion torque (Lamb & Melia 1988). This dissipative torque only acts when the system is asynchronous by greater than one part in one thousand (King, Frank & Whitehurst 1990) and hence is likely to be the force which drives the system to synchronism. Another force must act to maintain synchronism.

The most plausible candidate for locking the white dwarf spin to the orbit is an interaction between the primary and secondary dipole moments. The magnetic field strength of a late-type

star is typically 10^3 G, so we would anticipate the magnetic moment of the secondary, μ_2 , to be $\sim 10^{33} - 10^{34}$ Gcm³. This is of the same order of magnitude as the dipole moment of the primary, μ_1 . Consequently, a strong dipole-dipole torque will exist which both locks the orientations of the two dipoles and locks the rotation of the stars to the orbit.

1.4 The impact of ROSAT

AM Her systems are strong emitters of EUV and soft X-ray radiation arising due to reprocessed bremsstrahlung and thermalised subphotospheric deposition (§ 1.2.2). Indeed it should be noted that most polars are poor sources of hard X-rays, only a few have enough flux above 2 keV to have produced a usable spectrum with current detector technology (Cropper 1990). Over the past six years ROSAT has had an enormous impact on our understanding of AM Her systems. Through its all-sky survey and serendipitous detections the ROSAT mission has more than doubled the number of known systems to 43 with an additional 20 ‘suspects’. The study of AM Hers has now passed from studying the systems as a group of individuals towards investigation of the properties of the population as a whole. A prime example of this are the evolutionary issues discussed below.

The strength of soft X-ray observations of AM Her stars is that the accretion region represents the primary source of soft X-ray flux. This allows a clear distinction to be made between the accretion column and other regions within the binary. It can also provide a useful tool for probing the other portions of the system, the best example being the accretion stream which can be studied through soft X-ray absorption dips. Other examples exist as well, for instance the eclipse duration can be used to measure the size of the stellar components of the system, which then enables mass ratio measurements to be made.

Longer duration, pointed ROSAT observations have enabled high resolution timing measurements to be made and X-ray spectra to be generated simultaneously, especially useful when studying the soft X-ray emission from AM Her systems. For an example of the impact of ROSAT on our understanding of AM Her systems one need only look at the recent recognition of the existence of the soft X-ray excess, which was still an unresolved issue only five years ago. The focus has changed over the last few years from debate over the existence of the excess in

the AM Her population to a debate on the accretion mechanism that causes this excess, and this shift is largely due to the detection by ROSAT of a soft excess in so many systems.

1.5 Orbital periods and evolution

1.5.1 The period distribution

In order for steady accretion to occur in a close binary, the secondary must maintain contact with the Roche lobe, and so the orbital period of the system must decrease as mass is transferred. To maintain this situation, the system must therefore lose angular momentum, but this process will only be stable for a limited range of mass ratios. The evolution of cataclysmic variables towards shorter periods means that the proportion of systems at different periods, the period distribution, is an indicator of the different phases of evolution. Figure 1.12 shows the period diagram of the non-magnetic cataclysmic variables, intermediate polars and AM Her systems for systems detected prior to the launch of ROSAT. The features that appear common to all types of CV are the short period cut-off at $P_{orb} = 79$ min. and an interval ($2 \text{ hr} < P_{orb} < 3 \text{ hr}$) where few cataclysmic variables are found, known as the ‘period gap’. Features peculiar to the AM Her subclass are the concentration of systems around $P_{orb} = 114$ min., known as the ‘period spike’ and the upper limit on the period around $P_{orb} = 4$ hr (although this has now moved out to 8 hr since the discovery by ROSAT of RE0515+01). There is an especially strong contrast between the polars which appear clustered at lower periods, and the intermediate polars which possess mostly long periods.

ROSAT has had a large effect on the period distribution, for the reasons outlined in Section 1.4, and is now far clearer as can be seen in Figure 1.13. Several changes to the distribution are apparent; there are no new AM Her systems within the period spike and many more systems within the period gap. The period spike is now far less significant and it is unclear whether this is a real feature anymore. The presence of additional polars within the period gap has raised the question as to whether the period gap actually exists for the AM Hers or not.

This issue was addressed by Wheatley (1995*a*). Recent arguments that the period gap did not exist for polars were based on the period distribution as a whole (e.g. Wickramasinghe &

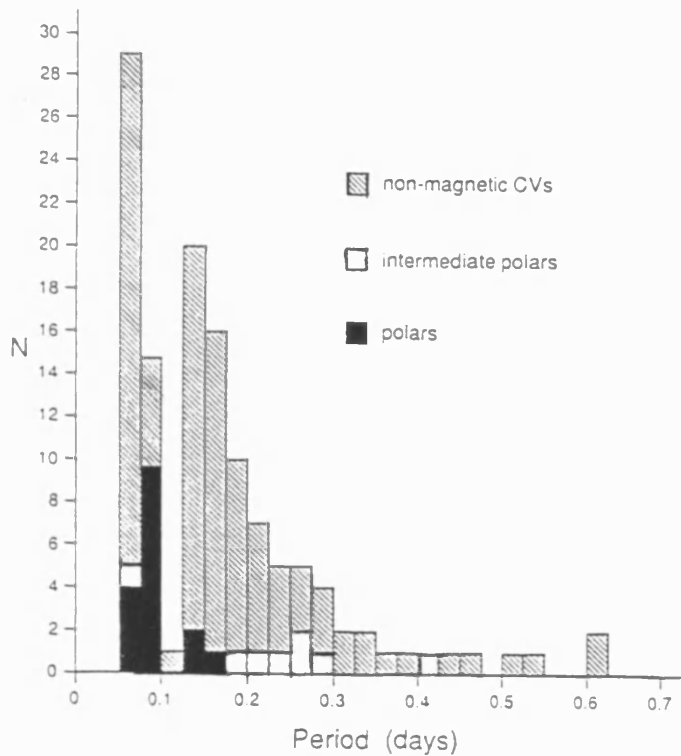


Figure 1.12: Period distribution of cataclysmic variables from the pre-ROSAT era. Taken from Cropper (1990).

Wu 1994). Wheatley suggests that to compare the systems with a period greater than 5 hr is incorrect because of the known lack of long period AM Her systems. By considering only the systems below and within the period gap, Wheatley has found no difference in the distribution of AM Hers and cataclysmic variables as a whole. Figure 1.14 reproduces Wheatley's cumulative period distributions and there is clearly no demonstrable difference between the two; the period gap is still present.

1.5.2 Evolution

The two angular momentum loss processes that are believed to be important in AM Her systems are magnetic braking and gravitational radiation. Magnetic braking occurs due to the interaction of the magnetic field of the secondary with stellar winds within the system, and will therefore only be important if the secondary's magnetic field strength is high enough. Gravitational radiation, arising from the constant acceleration of the stellar components of the binary, carries away energy and thereby reduces the angular momentum of the system. It will have an effect at all binary periods but will be strongest when the acceleration is greatest, at short periods.

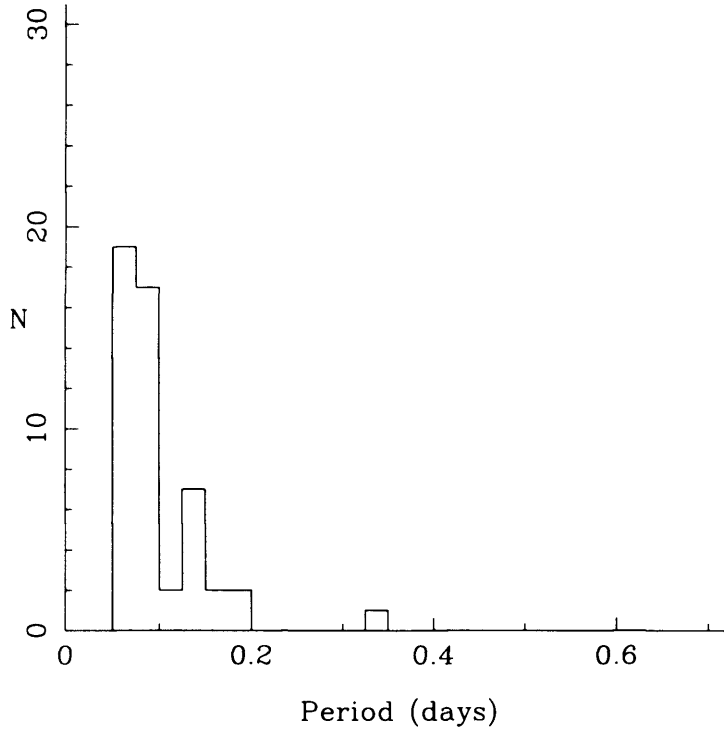


Figure 1.13: Period distribution of all known AM Hers. Compiled from the current Ritter catalogue of cataclysmic variables (Ritter & Kolb 1997).

The presence of a cut-off at short periods is surprising given that gravitational radiation is stronger at low periods. From Kepler's laws and the Roche geometry the orbital period is related to the radius and mass of the secondary (R_2 , M_2) by $P_{orb}^2 \propto R_2^3/M_2$ (King 1988). Clearly M_2 is decreasing due to mass transfer, hence for the system to evolve to lower periods the radius must also decrease. This can be easily satisfied if the secondary is on the main sequence because $R_2 \simeq M_2$ (expressed in solar units) for a main-sequence star. This relation between mass and radius arises due to the balance of gravitational and thermal (gas) pressures within the stellar atmosphere. The short period cut-off occurs as a result of the deviation of the secondary from the main sequence, so that $R_2 \neq M_2$.

At all periods, mass loss drives the secondary out of thermal equilibrium and so the star will be slightly over-sized and over-luminous for its mass for most of its lifetime. The timescale for the stellar radius to readjust is determined by the thermal timescale t_{th} . If the mass loss timescale, $t_{\dot{M}}$, is longer than t_{th} then the star remains close to the main sequence. The mass loss timescale is equal to the magnetic braking timescale when $P_{orb} > 3$ hr and is equal to the

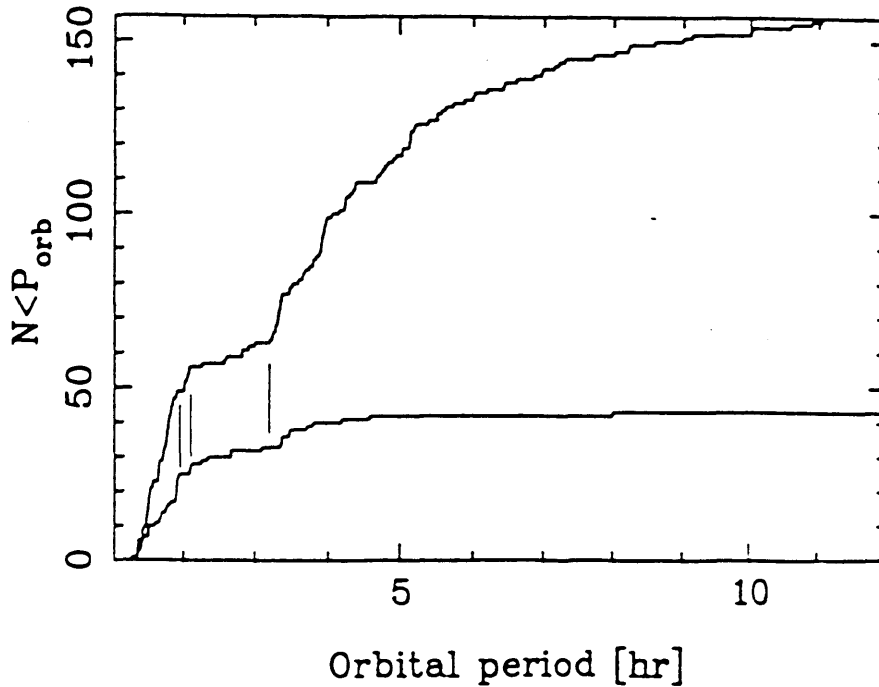


Figure 1.14: Cumulative period distribution for all cataclysmic variables (upper line) and for the AM Herculis systems (lower line). From Wheatley (1995a).

gravitational radiation timescale when $P_{orb} < 3$ hr (the reason for this will become apparent from the explanation for the period gap, given below). Figure 1.15 shows these three timescales as a function of the orbital period. Clearly the secondary will only be in thermal equilibrium above a period of ~ 1.5 hr.

Mass loss for $t_{th} > t_M$ (below the period gap) makes the star even more over-sized and over-luminous for its mass. Increased energy transport reduces the core temperature and thereby reduces the rate of nuclear burning. Eventually the secondary leaves the main sequence as hydrogen burning ceases: the star becomes degenerate. Now the mass-radius relation becomes $R_2 \propto M_2^{-1/3}$ so that further mass transfer increases the orbital period. This is believed to occur at a period of about 80 min, though it depends upon the exact luminosity of the star leaving the main sequence. When this happens the CV becomes very hard to detect because the mass transfer rate is greatly reduced.

To understand the period gap it must be remembered that an absence of systems at a given period indicates that either there are no systems at that period or that they do exist but mass-transfer is not occurring. A drop in the angular momentum loss rate at a period of 3 hr could

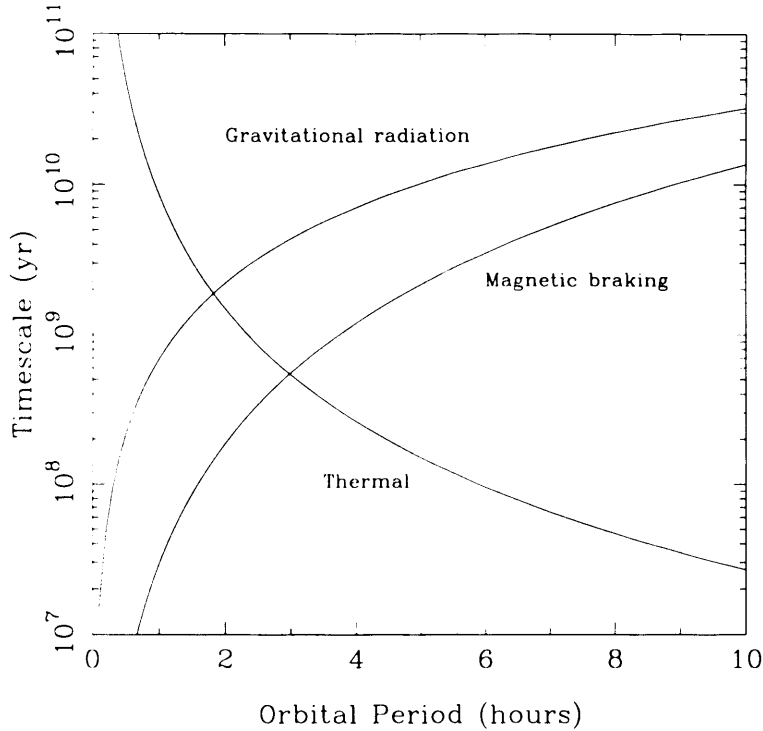


Figure 1.15: The gravitational radiation, magnetic braking and thermal timescales as a function of orbital period.

reduce the rate of mass transfer and thereby make the system undetectable. Magnetic braking requires a substantial secondary star magnetic field; to generate such a field from a stellar dynamo requires a convective zone/radiative zone boundary within a star. The secondary in cataclysmic variables is predicted to become fully convective at a period of about 3 hr which could lead to the collapse of the field and an end to magnetic braking. Magnetic braking would only dominate at periods longer than 3 hr. Another way magnetic braking could cease is if a reduction in the stellar wind occurs.

Once magnetic braking ceases, the secondary will continue to shrink as it returns to thermal equilibrium. The radius will therefore decrease to a value determined by the mass of the secondary when angular momentum loss ended; the star is said to detach from its Roche lobe and mass transfer stops. Gravitational radiation continues to reduce the angular momentum and hence the period, so the system evolves through the period gap and mass transfer will only resume once the Roche lobe ($\propto P_{orb}$) again touches the star's surface.

It was just below the period gap that a spike in the pre-ROSAT period distribution was seen (Figure 1.12). Many explanations were put forward to explain this, usually involving a radius increase when mass transfer resumes that leads to a temporary increase in P_{orb} . This would cause AM Her systems to dwell at a period of 2 hr. These ideas have become less relevant as the significance of the spike has been reduced.

The long period cut-off for cataclysmic variables as a whole lies at ≈ 13 hr and arises from the condition that the secondary mass cannot exceed the primary for stable mass transfer. The long period cut-off for AM Her systems at 4–8 hr therefore cannot be explained in the same way since the AM Hers must obey the same condition. In addition, the mass transfer phase would not be long enough for the secondary to become fully convective if mass transfer only started at $P_{orb} \simeq 4$ hr.

The period diagram of the magnetic cataclysmic variables suggests that the IP's might evolve into polars by synchronising at lower orbital periods. For this to occur, the magnetic moments of the two stars must satisfy the following relation:

$$\frac{\mu_1 \mu_2}{a^3} > (GM_1 R_a)^{1/2} \dot{M} \quad (1.7)$$

where a is the stellar separation and R_a is the Alfvén radius. The expression to the right of the inequality is the accretion torque. It was initially believed that the primary field strengths of IPs (which are difficult to measure) are too low to cause synchronisation, based on the fact that the accretion flow was able to circularise and form a disc. This belief was later brought into doubt by the discovery of IPs with field strengths greater than some polars, an indication that IPs *could* evolve into polars. On the other hand, Equation 1.7 shows that systems with a strong primary field can remain non-synchronous if the magnetic moment on the secondary is low. The relationship between the IPs and polars is complicated and will only be resolved once the field of the primary can be accurately determined in more IPs.

Since the all-sky surveys by ROSAT, the number of AM Her systems within the period gap ($P_{orb} = 2 - 3$ hr) has increased to between 4 and 8 systems. While Wheatley (1995a) has shown that this is not significant and therefore does not require a separate evolutionary scenario for the AM Her stars as a whole, the presence of the individual stars still needs explanation. Most stars in the period gap are now believed to have been 'born' within the period gap, in other words they emerged from the common envelope stage of evolution and started mass transfer at

a period of between 2 and 3 hours. If the AM Hers are not born in the gap they must evolve into it. One way of achieving this is if the secondary star has a structure such that $t_{\dot{M}} > t_{KH}$; it must be a nuclear evolved star. This leads to the testable prediction that $M_2 > 0.8M_{\odot}$ and hence $M_1 > M_2 \gg 0.8M_{\odot}$. By measuring the primary mass in the polars in the gap it is therefore possible to determine if they evolved into the gap or were born there. This may also provide a constraint upon the birth rate of AM Her systems.

Chapter 2

Optical photometry and polarimetry of HU Aqr

2.1 Introduction

Much of the work presented in this thesis focuses upon the AM Herculis system HU Aqr. This system was first detected by the all-sky surveys of the Wide Field Camera (WFC) and X-ray Telescope (XRT) aboard the ROSAT satellite (§ 4.1). The optical counterpart was discovered independently in two separate identification programmes based on WFC (Hakala et al. 1993) and XRT detections (Schwope et al. 1993). Hakala et al. followed the discovery of a candidate star showing a rich emission line spectrum with optical photometry and polarimetry obtained at the Nordic Optical Telescope. They reported significant circular polarisation which was seen to vary on a period of 125 min., thereby providing confirmation that the source was an AM Her system. A 590 s eclipse was detected and good time-resolution photometric measurements of the system revealed a complex shape to the profile of this eclipse. The profile was interpreted as the sequential eclipse of both the polecap on the white dwarf and the accretion stream. An unexpected and important discovery was the large contribution to the optical flux by the accretion stream in this new polar.

Broad-band spectroscopy was also carried out by Schwope et al. (1993). Fortuitously, the spectrum obtained included a portion of the eclipse which allowed the spectral type of the secondary star to be identified as dM4.5 in the Boeshaar (1976) system. From this the distance to HU Aqr was estimated to be 245 ± 25 pc (note that the error on the distance was an admitted underes-

timate). The spectrum also possessed cyclotron line emission with intensity maxima at 7800Å, 6300Å and 4600Å corresponding to the 4th-7th cyclotron harmonics of a $B = 37$ MG field. The complex eclipse profile found by Hakala et al. was also seen by Schwöpe et al. and an accurate eclipse ephemeris with a period of 125.021 min. was established from their photometry. This placed HU Aqr within the 2-3 hour period gap of cataclysmic variables. The width of the eclipse placed an upper limit upon the mass of the primary in this system of $M_1 < 0.95 M_\odot$.

The first extensive optical study of this new AM Her system was conducted by Glenn et al. (1994). They presented time-resolved spectra of HU Aqr with both high and low spectral resolution. The low resolution spectra allowed the magnetic field to be estimated at 36 ± 1 MG, confirming the earlier results of Schwöpe et al. The high resolution spectra revealed radial velocity variations within the H α emission line compatible with two (or possibly more) separately varying components. The phasing of these two components with respect to the eclipse was consistent with accretion funnel emission and line emission from the heated face of the secondary star. Polarimetry of HU Aqr enabled the co-latitude of the accretion spot on the white dwarf and the inclination of the system to be estimated. These were $40^\circ \pm 10^\circ$ and $80^\circ \pm 5^\circ$ respectively. The accretion spot was found to lead the secondary in longitude by $+23^\circ \pm 6^\circ$. High-speed photometry of the eclipse showed a change to the portion of the profile associated with the accretion stream from one orbital cycle to the next. This was interpreted as a change to the trajectory of the accretion stream, perhaps involving a displacement as large as $1 R_{WD}$ in a 2 hr. interval. Further results from this study included a refined distance estimate (191_{-115}^{+189} pc), a more reliable spectral type for the secondary (M4V), a measurement of the mass ratio, $q (= M_2/M_1) = 0.36_{-0.15}^{+0.41}$ and an improved ephemeris.

Most recently Schwöpe, Mantel & Horne (1996) reported the results of a detailed photometric and time-resolved spectroscopic study of HU Aqr.¹ Their work concentrated upon the emission line profiles which were found to be made up of three separate components. By fitting a Gaussian to each component, details of the flux and radial velocity variations on the orbital period were revealed. The components were further investigated using a Doppler tomogram technique known as filtered backprojection, from which the authors were able to estimate the location of these components. One component was located on the primary-facing side of the secondary, another

¹The observations of Schwöpe et al. constitute a very similar dataset to the data presented in Chapters 2 and 3 of this thesis, the spectroscopic observations were even conducted on the same night! As a result, the work of Schwöpe et al. represents a parallel but independent study of HU Aqr.

in the portion of the accretion stream lying in the orbital plane and the third in the vertical accretion funnel.

It was realised very early on that the unique properties of HU Aqr would make it an ideal target for investigating many aspects of AM Her systems (Hakala et al. 1993). One important attribute is that HU Aqr is the brightest known eclipsing AM Her system. It ought to be possible to obtain the mass of the white dwarf from the duration of the eclipse (which limits the radius of the white dwarf). It is doubly important to obtain a good mass estimate for this system because of its location within the period gap of cataclysmic variables. Hameury, Lasota & King (1988) predict on evolutionary grounds that systems found within the period gap should have higher mass white dwarfs and it would be useful to confirm this for HU Aqr. The other unique characteristic is the large contribution of the accretion stream to the optical flux which may provide the key to mapping both the brightness profile of the stream and the complex line emission from an AM Her system for the first time. This would require both photometry and phase-resolved spectroscopy with high time-resolution. It was in an effort to exploit these properties that this study was initiated.

2.2 Observations

The photometric and polarimetric observations of HU Aqr presented in this chapter were conducted on the Anglo-Australian Telescope in Siding Springs, Australia, at the South African Astronomical Observatory and on the Nordic Optical Telescope at the Observatorio de la Roque de los Muchachos, La Palma (see Table 2.1 for a log of these observations). The largest dataset consists of photometry and circular polarimetry acquired on the 3.9m Anglo-Australian Telescope (AAT) on the nights of 18 and 19 June 1993 (these observations were conducted by Jeremy Bailey, Pasi Hakala and Mike Watson). The instrument used to obtain the polarimetric data was the Faint Object Polarimeter (FOP, Cropper et al. 1990), which was fitted with a Tektronics CCD detector. The FOP is a Taurus II instrument (Unger et al. 1990) modified by replacing the Fabry-Perot etalon with a quarter wave plate and Wollaston prism. Circular polarisation is converted into linear by a $1/4$ wave plate which transforms the positive and negative contributions to the circular polarisation into orthogonal linear components. A Wollaston prism splits the linearly polarised light into its orthogonal components, which emerge as two rays, the

| Observatory | Date | Type | Filter | Coverage | Res. |
|-------------|-----------------|------------|-------------|---------------|------|
| AAT | 18/19 June 1993 | Phot + Pol | BG39/R-band | 1.7/1.3 cycle | 3 s |
| SAAO | 1 November 1994 | Phot | White light | 1.1 cycle | 10 s |
| NOT | 28 May 1995 | Phot + Pol | R-band | 1.05 cycle | 80 s |

Table 2.1: Log of the optical photometric and polarimetric observations presented in this chapter.

ordinary ray (or *o*-ray) and the extraordinary ray (or *e*-ray). Each of these rays is focused onto the detector, and the fractional polarisation is calculated from the difference of the two image intensities divided by their sum. The sum of the two spots represents the flux from the object and hence photometric measurements can be made at the same time as the polarimetric.

The FOP has been optimised for maximum throughput by using a straight-through focal reducer design. One of the great advantages of the instrument setup used was its ability to undertake integrations with very little dead-time between them. This is possible due to the fast time-series CCD readout mode developed at the Anglo-Australian Observatory, on-chip binning and windowing of the chip output. A very small window size was possible due to the small area on the CCD required by the FOP. For the purposes of this observation the dead-time was only 1.18 s, and coupled with the 1.82 s integration time this produced an overall time resolution of only 3 s.

Observing on the first night was badly affected by clouds and cirrus so the majority of the data from that night is unusable. On the second night a total of 3.0 cycles of good data were obtained using a BG39 filter (1.7 cycles) giving a broad blue band (from the atmospheric cut-off to about 6000 Å), and an R-band filter (1.3 cycles). Flux calibrations were made by comparison with observations of the standard star G93-48 (Landolt 1983) in both filters, but as the BG39 band is much broader than the standard B-band, the flux calibration of the BG39 observations will only be approximate.

Photometric observations of HU Aqr were conducted with the South African Astronomical Observatory (SAAO) 1 m telescope on 1 November 1994. The SAAO CCD camera was employed, using the Peltier cooled UCT CCD. The CCD was operated in frame transfer mode in which one half of the chip is masked from starlight. After each exposure is finished, a frame transfer takes place (in a few milliseconds) and while the next exposure is accumulating in the images

section, the previous exposure is read out from the frame store (in about 5-6 s). There is thus no dead time for readout. A 10 s exposure time was selected. These observations were intended to coincide as close as possible with the ROSAT HRI observations described in Chapter 4, and were kindly provided by Darragh O'Donoghue, who also performed the data reduction.

A further simultaneous photometric and circular polarimetric observation of HU Aqr was made at the Nordic Optical Telescope (NOT) on 28 May 1995 by Pasi Hakala and the author. Again, a Wollaston prism and quarter-wave plate setup were employed to obtain the simultaneous data. The polariser unit is an unnamed private instrument owned by Vilppu Piirola. The detector was an Astromed CCD camera equipped with a P88100 chip. Just over one cycle of continuous observations were made in the R-band. The exposure time and readout times were both 40 s for a total time resolution of 80 s.

2.3 Data reduction

The following procedure was used for the reduction of both the AAT and NOT light curves. The data arrives as a series of CCD frames each representing a single exposure (1.82 s/40 s for the AAT/NOT respectively). The frames each contain two images of the object; from the o - and e -rays of the polarimeter. The reduction software works by integrating the source flux over a circular region and obtaining the background from an annulus of the same radius around the source region. Prior to the reduction of the data the optimum aperture size for good signal-to-noise was found. This was done by measuring the flux and background manually for a range of source radii. As the radius increases the signal to background ratio increases until a maximum is reached. For larger radii, the increased aperture size serves only to include more background within the source area. This optimum radius was selected as the source radius and was found to be stable through most of the orbital cycle. A fixed aperture was therefore used for all the frames.

In reducing the data two operations are performed for each frame; the first uses an approximate source position and finds the centroid of the image. The centroid position is then used as the start position for the second iteration, which measures the sky-background subtracted flux. This is done for both images in each frame and the total signal is output as the flux, the difference

as the circular polarisation. Once all the frames have been analysed, the flux data are corrected for atmospheric extinction and the frame times are heliocentrically corrected and converted to an orbital phase using the ephemeris quoted in Equation 4.3.

The SAAO data were reduced in a different manner; the bias was subtracted and flatfielding was performed using white light flats taken of the twilight sky. Magnitudes were extracted using profile fitting in the DoPHOT programme (Schechter, Mateo & Saha 1993). Finally, differential photometry was undertaken using a bright star to the southeast of HU Aqr as the comparison star.

Polarimetric observations are usually accompanied by observations of polarimetric standards, which allow the absolute polarisation level to be assessed in a manner similar to that used to determine an absolute brightness scale from photometric standards. Polarimetric standards are stars with known, non-variable polarisations; the observed polarisation from these stars is used to calibrate the polarisation data from the target star. For both the AAT and NOT observations, separate polarisation standards were not observed because circular polarisation data only requires the zero polarisation point to be fixed, which can be done using the photometric standards.

2.4 The photometric and polarimetric light curves

2.4.1 Description of the light curves

The photometric and polarisation light curves for both filters used in the AAT observations are shown in Figure 2.1. The data have not been folded and are shown at the raw resolution of 3 s. As with most of the light curves presented here, the data have been normalised to allow for easier comparison of the flux contributions from the different emission regions within the system as they change from one observation to the next. The light curve in both the BG39 and R-band data display the same features. There are two intensity peaks separated by half an orbital cycle, at $\phi = 0.15$ and 0.65 . The peak at 0.65 is better defined than the earlier peak in both filters and both peaks are slightly more distinct in the BG39 data. The light curve is dominated by a very deep eclipse lasting about 750 s which is preceded by a shallower dip feature 0.15 orbital cycles

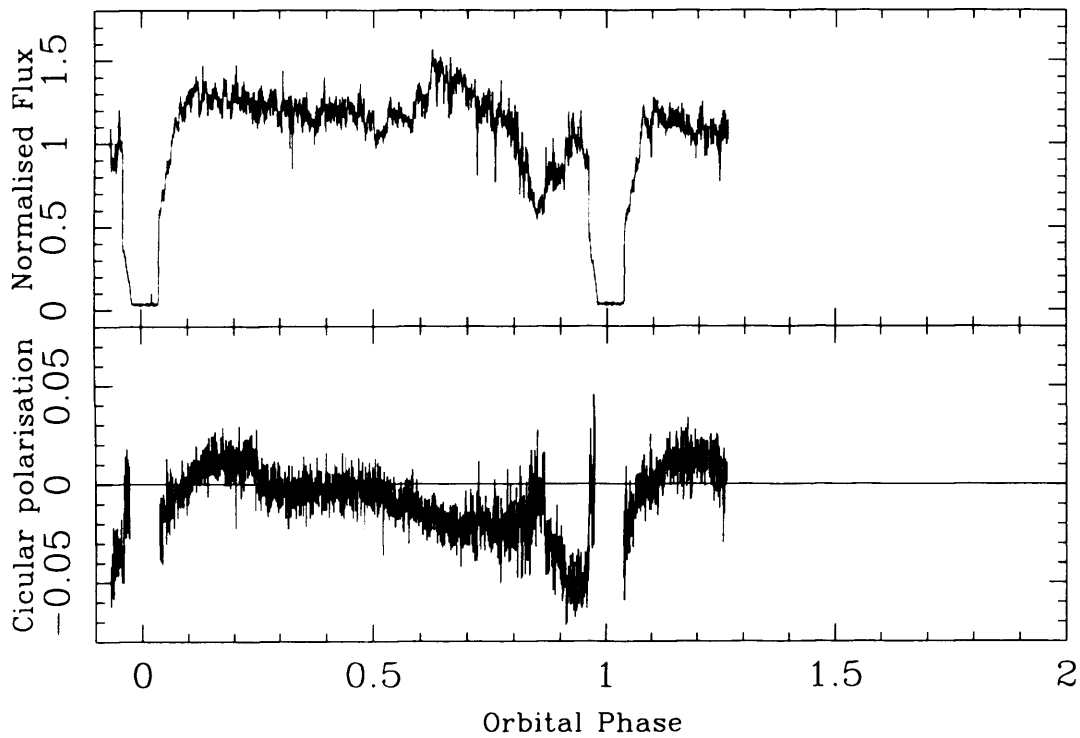
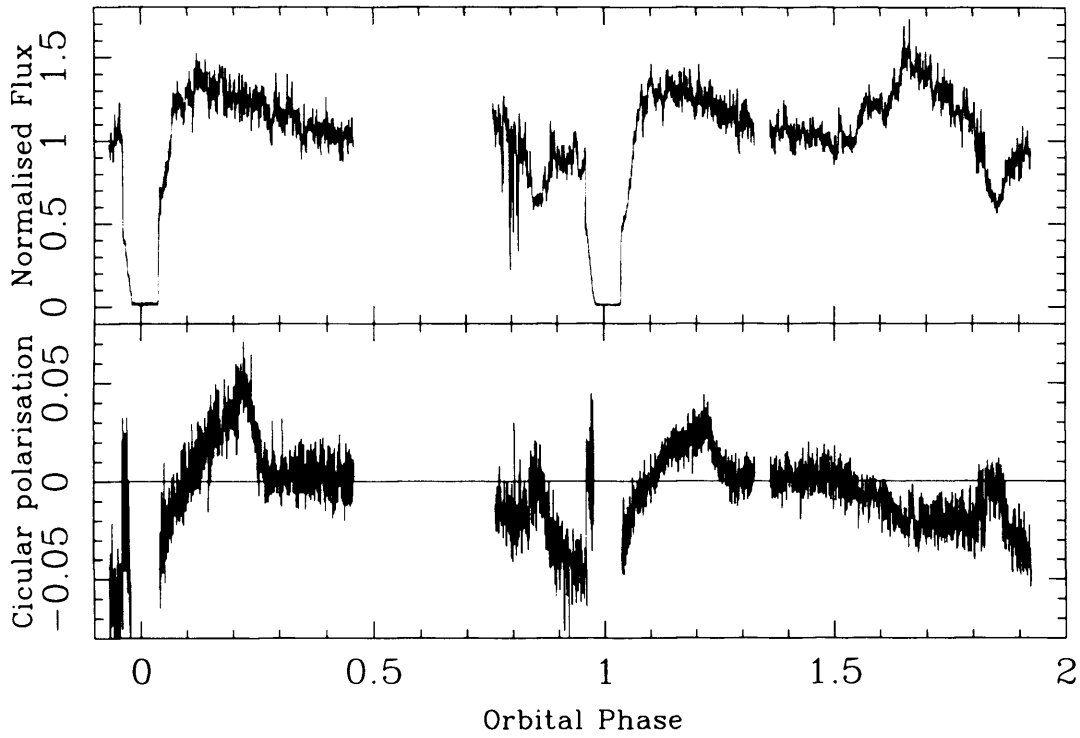


Figure 2.1: Flux and polarisation light curves from the AAT observation, (a) shows the data from the BG39 filter, (b) shows the data from the R-band filter. The upper and lower panels of each display the flux and polarisation data respectively. The time resolution of these observations was 3 s.

before it. This light curve morphology is in reasonable agreement with the earlier light curves of Hakala et al. (1993) and Schwöpe et al. (1993), but is of much higher quality. One notable difference is the absence of the prominent dip in either of the earlier observations.

The first four panels of Figure 2.4 show a detail of the flux light curve from each of the four eclipses that were observed. The eclipse profile is essentially the same for each. Both the ingress and the egress can be divided into a rapid transition lasting ~ 10 s followed by a slower transition lasting ~ 150 s. Both transitions account for approximately 50% of the out-of-eclipse flux. For comparison, the two eclipses detected in the SAAO and NOT observations are also shown in Figure 2.4 with the same time axis scaling. An ephemeris based upon these optical eclipses plus the eclipses seen in the X-ray data is presented in Section 4.3.2. It is also possible to estimate the mass ratio of the system from the width of the eclipses. This work is presented in Section 3.3.5, in conjunction with mass estimates based upon optical spectroscopy of HU Aqr.

During the AAT observations both the BG39 and R-band fluxes returned to a higher level than they were prior to the eclipse. This did not occur for the SAAO and NOT observations. It is likely that such an increase in the flux after eclipse may be associated with preferential emission from one side of the accretion stream. A stream that is shaped roughly like that shown schematically in Figure 2.9 (below) will tend to suffer more X-ray irradiation on the right (lower y -value) side than on the left. This side is in view after the eclipse and so the flux detected then is greater. This is the same conclusion as that drawn from the equivalent width light curves presented in Section 3.3.2.

The AAT circular polarisation light curve can be described as follows. The mean polarisation is flat and close to zero (within the errors) between phase 0.26 and 0.53. At $\phi = 0.53$ it starts to increase to a maximum negative polarisation of -5% just before the eclipse at $\phi = 0.93$. This increase is interrupted by a brief return to zero polarisation which coincides with the dip in the flux light curve. The polarisation value is undefined during the eclipse itself. After the eclipse, the polarisation decreases until $\phi = 0.1$ where it crosses zero and becomes positive. Maximum positive polarisation is then reached at $\phi = 0.22$, before dropping back to zero at $\phi = 0.26$.

Short timescale (10–15 s) flickering occurs at all orbital phases outside of the eclipse in both the photometric and polarimetric light curves. The absence of the flickering during the eclipse

demonstrates that it is a true property of the source, not statistical or detector noise. Apparently the luminosity of one or more of the sources of optical flux is varying on these timescales. The cause of this variation and the relationship between the photometric and polarimetric flickering are discussed in Section 2.5.

Rather surprisingly there is little difference between the red and blue light curves in the AAT data. Understandably, the residual flux from the late-type secondary during the eclipse is considerably less in the BG39 filter than in the R-band filter. The peaks in the photometric and polarimetric light curves associated with the optical bright phase are also somewhat stronger in the BG39 filter.

The SAAO light curve shown in Figure 2.2 appears similar to the AAT light curves obtained 18 months previously and only differs in a number of subtle ways. The dip which precedes the eclipse is now much narrower than in the earlier observation and also somewhat deeper (the dip depth is 56% compared to 35% in 1993). Another alteration to the dip is a shift in its phase; mid-dip was at $\phi = 0.85$ in June 1993 but by November 1994 the dip had moved to $\phi = 0.87$. These differences are quite apparent in Figure 2.4. The second distinction between the light curves is in the eclipse profile as the relative contributions of the steep and gradual portions of the ingress and egress have altered. The gradual ingress now accounts for only 40% of the out-of-eclipse flux. This change becomes even more evident in the egress where the contribution is even lower.

The flux and polarisation light curves obtained at the NOT in May 1995 are displayed in Figure 2.3. Despite the poor time resolution, these data still provide a valuable look at the system at this epoch. A substantial increase in the amount of circular polarisation from HU Aqr has been detected. The maximum circular polarisation is now -13% which is the largest polarisation fraction seen so far from HU Aqr. The shape of the polarisation light curve after the eclipse has also changed markedly. Instead of the interval of positive polarisation seen in the AAT observation, there is a gradual return to zero polarisation. The phase at which no polarisation is detected has also been brought forward from phase 0.26 to 0.20, so that the polarisation matches the optical bright phase in the flux light curve.

The second major change is that the dip is no longer present (Figure 2.4). The absence of a dip

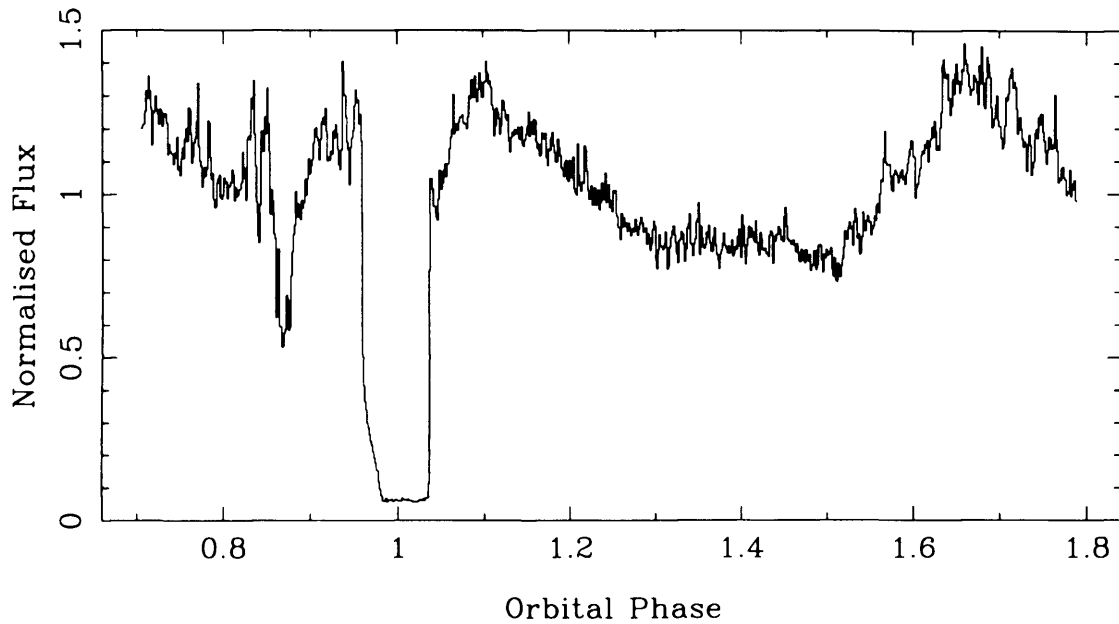


Figure 2.2: SAAO optical flux light curve from 1 November 1994. The time resolution of the data is ten seconds.

indicates a return to the light curve morphology found in the observations of Hakala et al. (1993) and Schwöpe et al. (1993). This is coupled with a change to the eclipse profile. The gradual transitions in the ingress and egress are hardly apparent at all; the contribution by the accretion stream to the out-of-eclipse flux has dropped to only 20%. But this is not all, the duration of this gradual transition has increased to $\sim 0.05 \phi$ which means the ingress lasts beyond the mid-point of the eclipse.

From this set of three observations alone it is apparent that the morphology of the light curve of HU Aqr changes markedly on timescales that range from a few orbital cycles to months.

2.4.2 Interpretation of the light curves

The dip

In the AAT and SAAO observations of HU Aqr a dip is present that precedes the eclipse. This decrease in flux occurs at the same time as a decrease in the circular polarisation to less than 1%. Such dip features are common in both soft X-ray and optical light curves of AM Her systems, and are usually attributed to absorption by the accretion stream as portions of it cross the line of sight to the polecap.

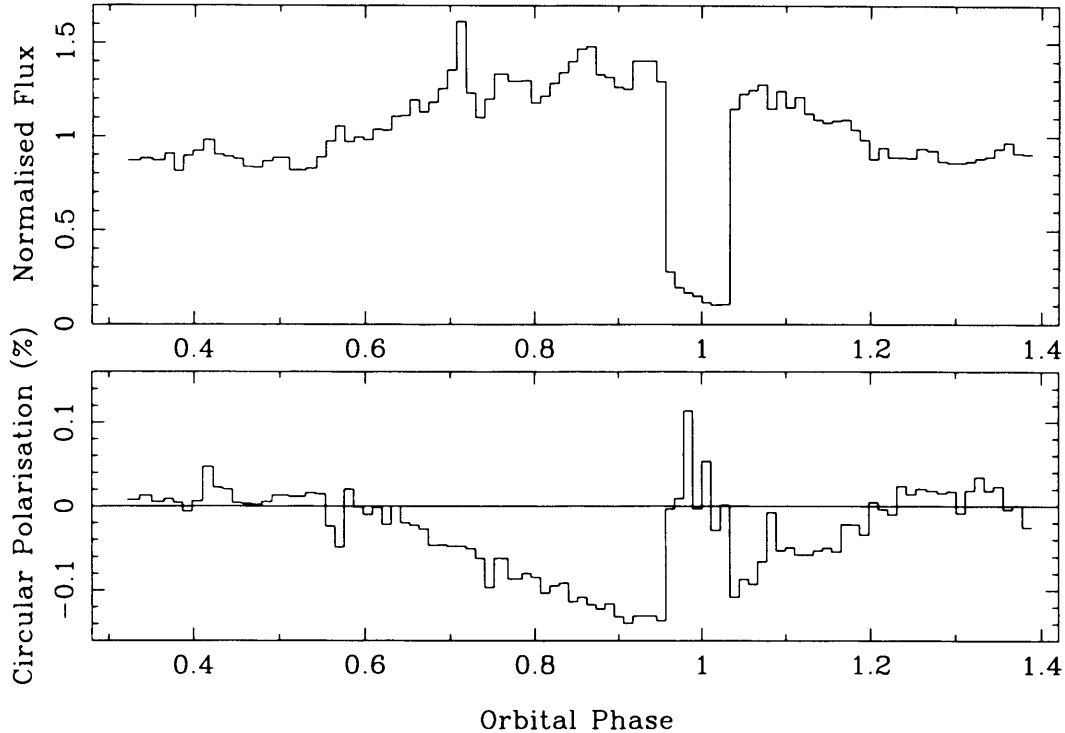


Figure 2.3: Flux (upper panel) and polarisation (lower panel) light curves from the NOT observation. The time resolution of the data is 80 s.

There are several pieces of evidence which support this interpretation for the dip in HU Aqr. The phase at which the dip occurs is that expected if a portion of the accretion stream rising out of the plane is to cross the line of sight. This point is demonstrated by Figure 2.5 which shows HU Aqr at various phases through the eclipse; between plots 2 and 3 the stream could pass in front of the pole and account for a dip in flux. The object which causes the dip cannot be fixed in the binary frame because the dip disappears at times and because its phase is not constant. The accretion stream is the only object that is large and dense enough to cause the occultation and yet still vary on the timescales at which the dip is seen to vary. This dip has also been observed at X-ray wavelengths and the results from these observations are presented later in this thesis (§4.4.1).

The eclipse profile

The rate at which the secondary sweeps across the rest of the system during the eclipse is essentially constant. This means that the duration of any flux change associated with the

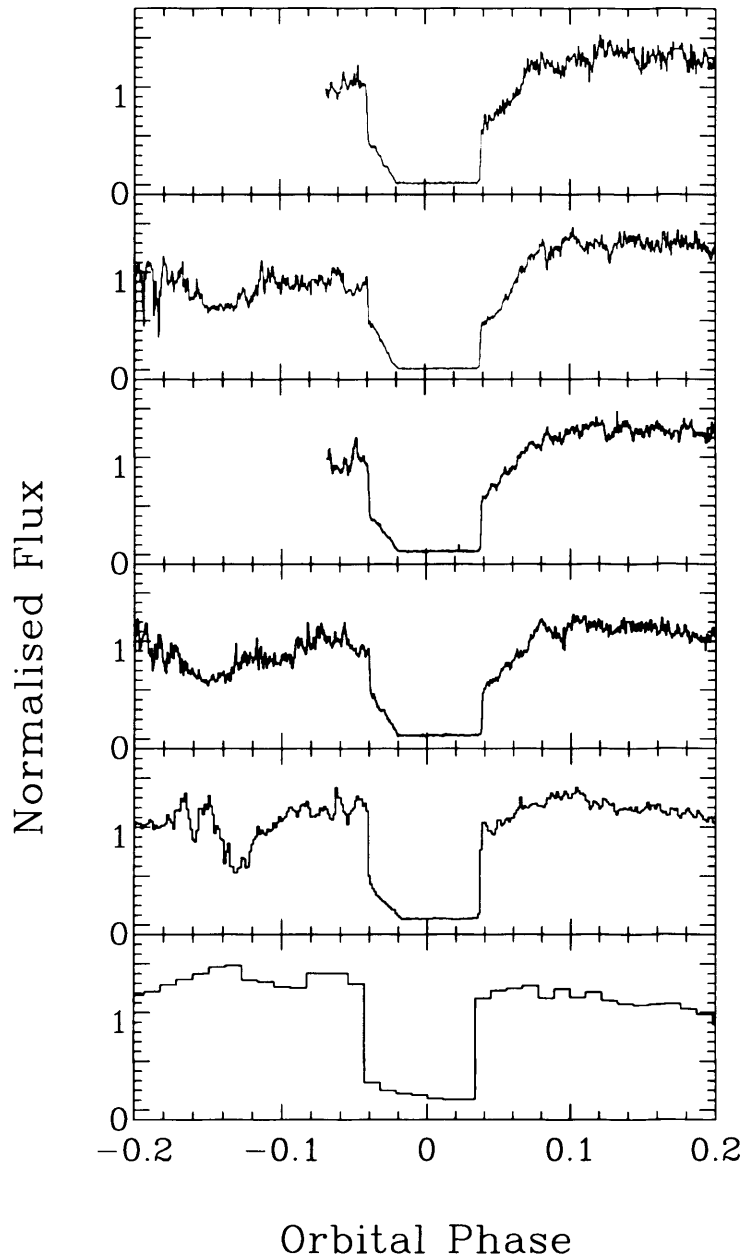


Figure 2.4: Details of the optical eclipses. The first two panels represent the AAT eclipses with the BG39 filter, the second two with the R-band filter. The eclipse profile remains essentially the same throughout the AAT observation. The fifth panel shows the SAAO results. Note the substantial change to the character of the dip between the AAT and SAAO observations. The lower panel shows the NOT eclipse which displays no dip and a very different eclipse profile.

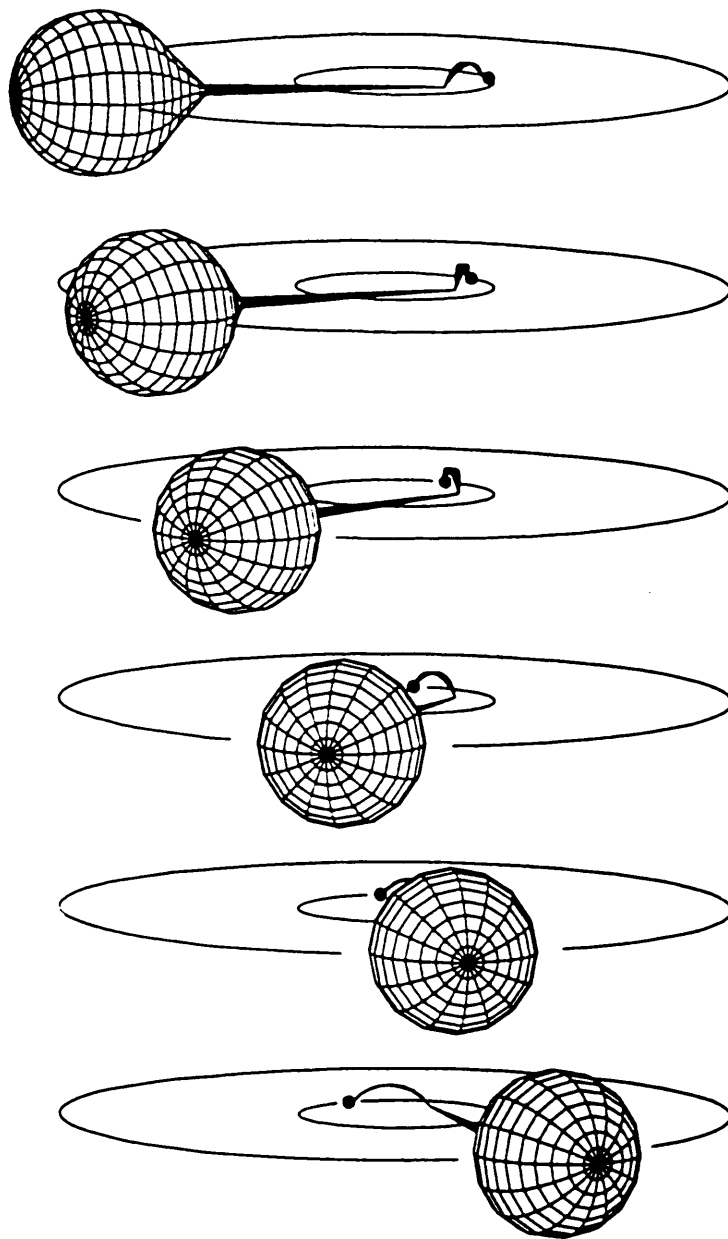


Figure 2.5: The eclipse sequence of HU Aqr. The projection of the components of the system are shown as seen by the observer. Between Plot 2 and Plot 3 the vertical portion of the accretion stream crosses the line of sight to the white dwarf and causes an absorption dip. Plot 4 shows the system as the limb of the secondary makes its first contact with the white dwarf (rapid ingress). The gradual eclipse of the stream follows this. Plot 5 shows final contact with the primary. Egress of the stream then follows until Plot 6. Adapted from Glenn et al. (1994).

eclipse is an indicator of the size of the body that has been occulted, while the amplitude of the flux change is an indicator of the brightness of that object. The ingress profile of HU Aqr signifies that a small, bright object is encountered by the limb of the secondary first, followed by a very large object of about the same brightness (the brightness depending on the epoch of observation). This sequence is then the same at egress. The small size of the first object means it can only be accounted for by the polecap on the white dwarf, the larger object is identified as the accretion stream.

This interpretation can be confirmed by inspection of a series of projections of the system as it moves through eclipse. Such a sequence is shown in Figure 2.5 and clearly shows white dwarf and pole being eclipsed and emerging before the accretion stream.

The accretion stream in HU Aqr appears to account for at least 45% of the out-of-eclipse flux during both the AAT and SAAO observations. A similar proportion of flux from the accretion stream was noted in Hakala et al. (1993) and Glenn et al. (1994). The important contribution that the accretion stream makes to the optical flux from polars was not fully appreciated until the recent observations of HU Aqr and UZ For (Stockman & Schmidt 1996). During the NOT observation in 1995 the stream brightness drops to only 20%. The changes from epoch to epoch that occur to both absorption dip and the gradual eclipse transitions are clearly associated with changes to the accretion stream. As a result there is likely to be a correlation between the changes seen in these two portions of the light curve. Such a correlation is indeed seen and is discussed in Section 2.4 below.

The optical bright phase

A significant portion of the optical flux from HU Aqr must arise at or near the polecap on the white dwarf in the form of cyclotron radiation (Cropper 1990). At first sight the AAT light curve appears to display two peaks separated by a deep eclipse and is highly reminiscent of the optical light curves of EP Dra (Schwope & Mengel 1997). Such double peaks could arise due to the strong beaming effect on cyclotron radiation. However, the NOT light curve (Figure 2.3) clearly shows only a single peak which is interrupted by a deep eclipse. This forces a re-interpretation of the AAT light curves; it is plausible that a single peak is present, interrupted by both a dip and an eclipse. Two sketches of the light curve are given in Figure 2.6, demonstrating how both

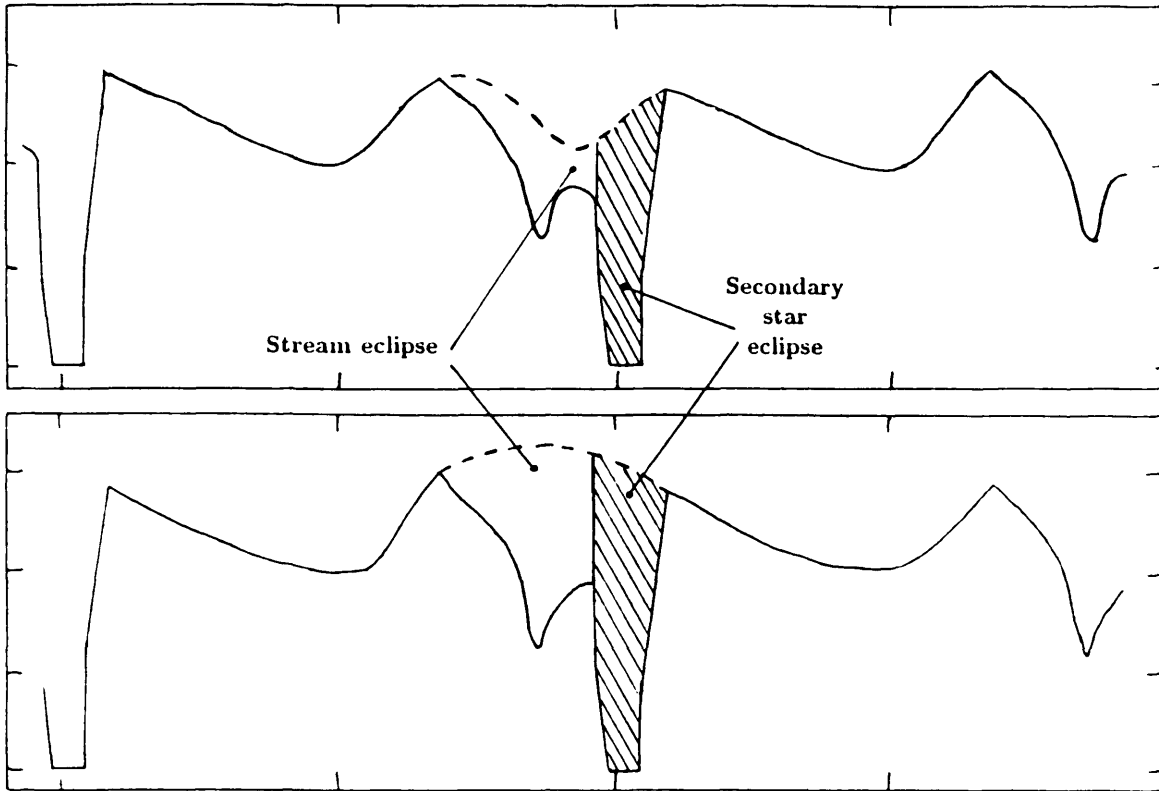


Figure 2.6: A sketch of the AAT blue light curve, showing how both a single- or double-humped shape may be masked by the dip and the eclipse. The dotted lines are the presumed shape of the light curve in the absence of occultation.

double peaked and single peaked shapes might be masked by the dip and eclipse. An indication of the possible shapes of the light curve in the absence of the dip and the eclipse are given by the dashed line. The occultations attributed to the stream and the secondary star are indicated by the blank and shaded space beneath this dashed line respectively. From this figure alone the single peak profile looks the more plausible.

The peak represents the optical bright phase, when the main accreting pole is in view. Between phase 0.26 and 0.55 (0.20–0.55 in the NOT observation) there is a flux minimum which is nearly flat. This is the optical faint phase during which the polecap is being occulted by the white dwarf. The polarimetry data support this interpretation because the polarisation detected from HU Aqr drops to zero during the faint phase. The large flux contribution from the accretion stream means that the flux during this minimum is much higher than during the eclipse (this point is discussed later).

Comparison should also be made to the X-ray light curve from HU Aqr, presented in Figure 4.3.

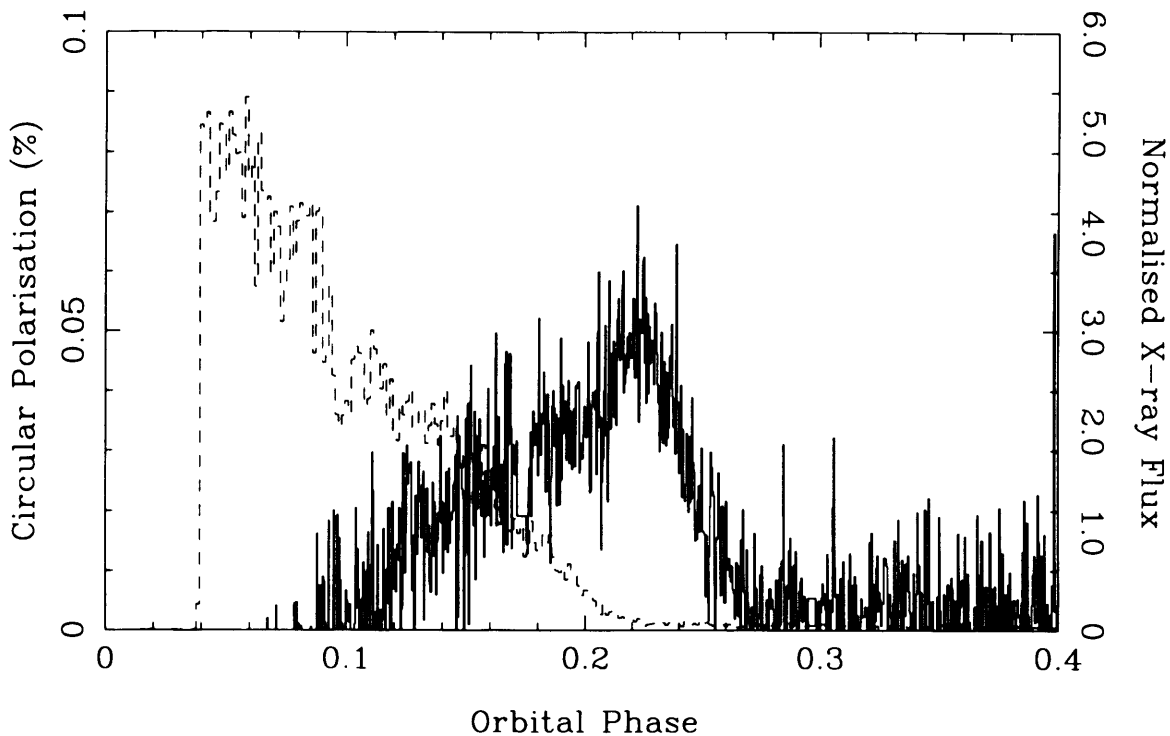


Figure 2.7: The circular polarisation (solid line) overlaid onto the X-ray flux (dashed line) from the latter portion of the bright phase. A clear discrepancy between the start of the optical and X-ray faint phases can be seen.

There is negligible X-ray flux between phase 0.21 and 0.53 because the X-ray emission region has rotated behind the white dwarf. This region is expected to be at, or close to, the location of the cyclotron emission region. An overlay of the optical and X-ray light curves from the region of the ingress to the faint phase is shown in Figure 2.7. A 0.05ϕ delay in the optical ingress with respect to the X-ray ingress is apparent.

Two simple explanations for the phase difference between the X-ray and optical ingress are (i) that the emission regions have moved between the observations (the X-ray observations take place 5 months after the optical) or (ii) that the trailing edge of the optical emission region lags behind the X-ray emission region. In (ii) the leading edge of the optical and X-ray regions are still co-incident and hence the egress occurs simultaneously. The existence of emission regions with complex shapes and which move over time have been inferred from observations of other AM Her systems (see Wickramasinghe 1988, Cropper 1990 and references therein), as have systems where the X-ray and optical emission regions do not overlap perfectly (e.g. ST LMi,

Cropper & Horne 1994).

In spite of the plausibility of both arguments, the preferred explanation for the longer optical bright phase is the presence of a second accreting pole. Evidence for its existence comes primarily from the polarisation light curve as discussed below.

The phase range during which a given pole is visible can be used to estimate its location on the white dwarf (its co-latitude and longitude). If it is assumed that accretion is occurring radially at the magnetic pole then the viewing angle α can be related to the inclination i , the colatitude of the magnetic pole β and the magnetic phase ϕ by:

$$\cos \alpha = \cos i \cos \beta - \sin i \sin \beta \cos \phi. \quad (2.1)$$

Magnetic phase zero is the instant that the magnetic pole is on the far side of the rotation axis. When the emission region is at the limb of the white dwarf the field lines are perpendicular to the line of sight (i.e. $\alpha = 90^\circ$), if the X-ray emission region is at the pole and is just a spot on the surface with no vertical height. This occurs at the both transitions between the bright and faint phases. By setting α to 90° and ϕ to the magnetic phase of the beginning or end of the bright phase, the magnetic co-latitude can therefore be found.

It is not possible to estimate the location of the main accreting pole from the AAT observations directly because the presence of a second pole makes it impossible to determine the exact phase of ingress to the faint phase. However, determination of the pole's location is possible using the NOT observation. Using the faint phase interval $0.2 \pm 0.04 - 0.54 \pm 0.04\phi$ and the inclination determined by Glenn et al. (1994) from linear polarisation measurements ($80^\circ \pm 5^\circ$), the magnetic co-latitude was found to be $10.3^\circ_{-3.0}^{+9.1}$. From the mid-point of the bright phase (at $0.87 \pm 0.04\phi$), the longitude of this pole is found to be $46.8^\circ \pm 1.4^\circ$.

Circular polarisation changes

The bulk of the negatively polarised flux originates at or near to the main accreting pole. The gradual increase in the magnitude of the negative circular polarisation fraction between phase 0.53 and 0.93 arises due to the changing aspect at which the pole is viewed. In the AAT observation this is interrupted by the absorption dip, during which the polarisation falls because the pole is being occulted by the accretion stream. When the dip is not present, as in the NOT

observation, the polarisation increases smoothly to its maximum. This maximum is detected when the angle between the line of sight and the field lines in the emission region is at its minimum. As expected this occurs both at the same phase as the peak in optical intensity and close to the mid-point of the optical bright phase.

Between the rapid ingress and egress to the eclipse it is expected that the polarisation will fall to zero as it did during the absorption dip. Careful inspection of the polarisation light curves (Figures 2.1 & 2.3) show that no polarisation is detected during the gradual eclipse ingress, thereby confirming that the pole is indeed eclipsed at these phases. Because of the low flux it is not possible to measure the polarisation at eclipse minimum. The eclipse as seen in the polarisation data therefore supports the interpretation of the photometric eclipse profile presented above.

In the AAT observation the behaviour of the polarisation after the eclipse is quite complex. From the behaviour prior to the eclipse a gradual return to zero polarisation at about phase 0.2 would be expected. This is precisely what is observed from the NOT observation and the observations by Glenn et al. (1994). Instead, the AAT polarisation falls more rapidly, crossing zero at phase 0.1 to an interval of positive polarisation that lasts until phase 0.26. Figure 2.8 is an overlay of the the AAT (BG39) and NOT polarisation curves which shows these differences clearly. The AAT data have been rescaled to match its peak polarisation to that of the NOT data. Shorter reversals in the sense of polarisation have been seen in other AM Her systems, e.g. VV Pup (Cropper & Warner 1986). The usual reason put forward for this is that the accretion column is being viewed from underneath. Such an explanation seems unlikely here because the reversal is of longer duration than in most such cases and because a delay to the ingress to the optical faint phase has been found in the same observation.

The explanation preferred here is that a second emission region is present, visible between phase 0.05 and phase 0.26. This region is near the opposite pole to the main accreting region and therefore cyclotron emission from this pole is polarised in the opposite sense. In addition, it is still visible later than the main pole and so causes the optical ingress to occur at a later phase. It is quite plausible that accretion onto this pole is intermittent which would explain its absence in the NOT and Glenn et al. observations.

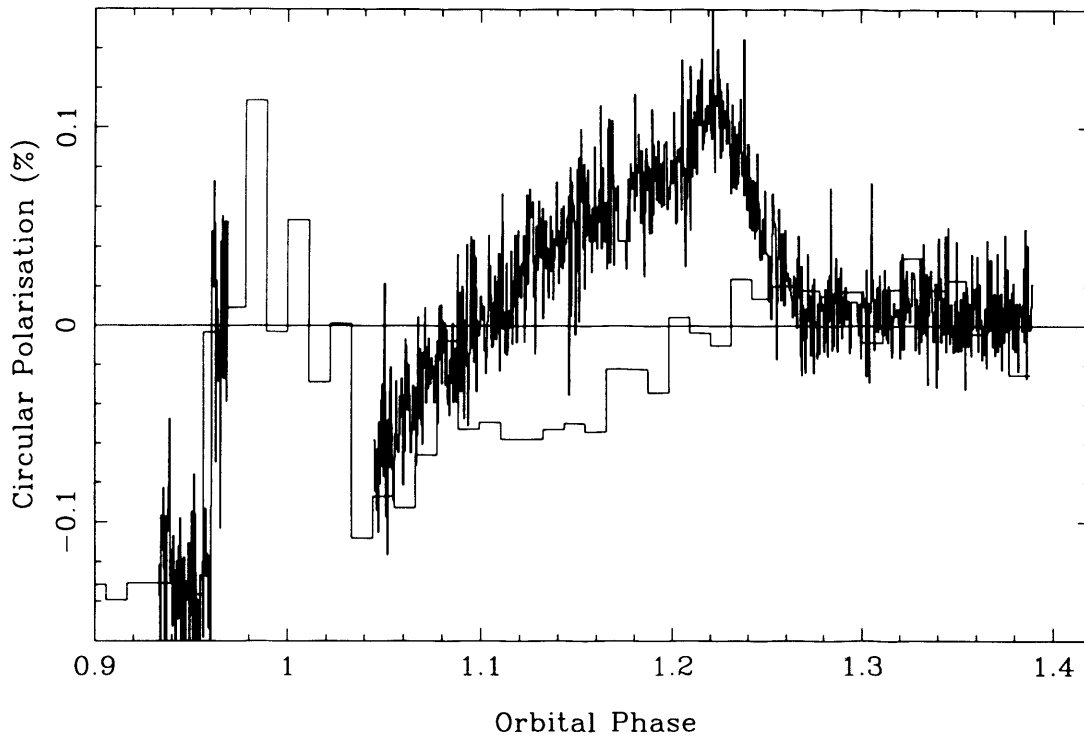


Figure 2.8: Overlay of the post-eclipse portions of the AAT and NOT polarisation light curves. The huge difference between the two curves can clearly be seen.

Figure 2.8 shows that the deviation of the AAT and NOT polarisations occurs immediately after the eclipse. This is therefore the latest phase at which the second pole could emerge from behind the white dwarf. The possibility that it emerges during the eclipse cannot be ruled out, making the earliest egress phase 0.96. If the pole is indeed on the limb of the white dwarf at phase 0.05 and at phase 0.26 then its location can be found using Equation 2.1. From this the co-latitude is found to be 174° . If the pole emerges at the very beginning of the eclipse then the co-latitude falls to 171° . The mid-point between the phase where the pole emerges and disappears constrains the longitude of the pole to be 40° to 54° behind the line of centres, for the range of allowed egress phases 0.96 to 0.05.

Optical ‘faint’ phase flux

The term ‘faint’ phase is used to refer to the phase range where the pole is self occulted by the white dwarf ($0.26 - 0.53 \phi$ or $0.20 - 0.55 \phi$). In the case of HU Aqr the optical flux during the faint phase is quite significant. This is unsurprising, as several portions of the system that are

known to be optically bright are still in view (the primary-facing side of the secondary and the accretion stream). However, is the level of flux detected in the faint phase what is expected from evidence in other portions of the light curve? The contribution to the optical flux by the stream and secondary star are fixed by the dip and eclipse to be $\sim 50\%$ and $\sim 6\%$ respectively. It may therefore be expected that the flux detected in the faint phase ought be around 56% , but it is not; the faint phase flux is close to the mean orbital flux during the AAT observation and about 80% of the mean flux during the SAAO observation.

What could the origin of this excess be? Either another component is providing the flux (the white dwarf or an additional pole), or the luminosity of the stream and secondary during the dip and eclipse must not be the same as that during the faint phase. The white dwarf flux is constrained by the eclipse profile. Were the white dwarf to contribute that much optical flux, it would be evident as an additional transition in the eclipse profile. An additional pole is discounted because there is no polarimetric evidence for another pole in this phase interval, and there is no need to further complicate the system when the workable explanation given below is provided by the components already there (by applying Occam's Razor, in other words).

The apparent brightness of the secondary star would be expected to be modulated twice per orbital period as a result of the asymmetric Roche lobe. Such effects are known as ellipsoidal modulations, and have been detected in a number of systems, particularly at infrared wavelengths (e.g. Panek & Eaton 1982). Similar modulation might be expected of the highly asymmetric accretion stream. Unfortunately, as the stream rotates the maximum flux will be detected at phase 0.25 and 0.75 , when the stream and secondary present the largest surface area to the observer. Hence this modulation cannot account for excess flux at $\phi \approx 0.5$.

The solution favoured here is related to the ellipsoidal variations, but depends upon asymmetric *heating* of the stream and secondary. It is likely that the primary-facing side of the stream is being heated by the X-ray flux from the pole, since the secondary star in HU Aqr is already known to be brighter on its primary-facing side due to X-ray heating (§3.4). Similar heating has been detected by Southwell et al. 1995 for AM Her. The flux detected from the stream and secondary would therefore be greater at $\phi = 0.5$ than at $\phi = 0.0$. The scale of this modulation is large (the flux may almost double) and is a further demonstration of how important the accretion stream is to understanding the optical behaviour of HU Aqr.

2.5 Accretion stream trajectory changes

As noted earlier, the profile of the eclipse and absorption dip change during the course of these observations. These changes can be seen in Figure 2.4 and are summarised in Table 2.2 for all photometric observations of HU Aqr. This table highlights a possible link between the presence of an absorption dip and the duration and depth of the gradual eclipse of the stream. Such a relationship is not entirely unexpected if both features are associated with the stream. In 1992 the brightness and duration of the stream eclipse are both large and the dip is not present. By the June 1993 observations, the dip is present but the duration of the gradual eclipse decreases to 0.02ϕ . At some point between November 1994 and May 1995, the dip disappears again and the duration lengthens to 0.05ϕ , but the brightness of the stream is at its lowest value of only 20% of the out-of-eclipse flux.

The absence of an absorption dip indicates that either the stream density is too low to cause attenuation of the flux or that the trajectory is such that the stream no longer crosses the line of sight to the polecap. Changes to the stream density might be accompanied by other observable effects, such as changes to the accretion luminosity, the optical brightness of the stream or to the column density obtained from fits to the soft X-ray spectra. Unfortunately it is impossible to compare the nature of the optical dips with X-ray spectral fitting results because of a lack of simultaneous data. The optical magnitude of the system does not correlate with the presence of the dip, nor do the changes to the brightness of the stream summarised in Table 2.2.

On the other hand, there is evidence for a correlation between the dips and stream trajectory changes. If the eclipse of the stream lasts longer at a given epoch, it follows that the stream has become more extended in the direction perpendicular to the line of centres (the y -direction, see Figure 2.9). The presence of a dip is accompanied by a shortening in the y -direction (Table 2.2) which suggests that the stream is threading onto a field line earlier. This could cause the stream to be brought further out of the plane and into the line of sight, thereby producing the dip. This strongly suggests that trajectory changes alone could account for the occasional disappearance of the dip.

Material within the stream will thread onto a field line when the ram pressure of the gas ($\propto \rho_{gas}$) is exceeded by the magnetic pressure, which increases as the material falls. Clearly any low

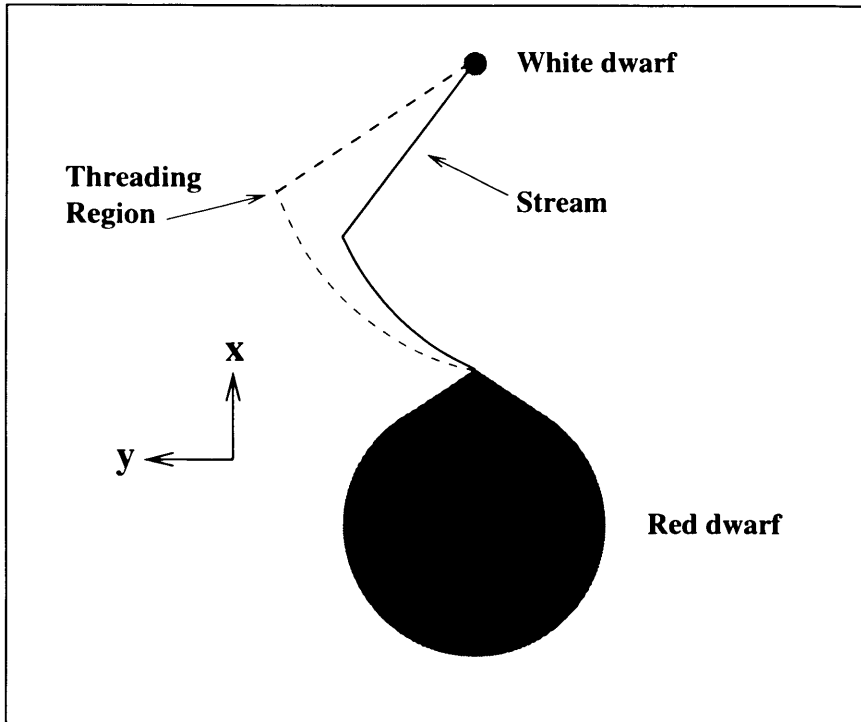


Figure 2.9: Schematic of an AM Her system, showing the axis convention used in this thesis. The dashed line shows a different stream trajectory to the solid line, with a larger y -extent and consequently with a longer gradual eclipse.

density material will thread before the higher density material, producing an ‘accretion curtain’ effect. Evidence that the stream threads at a range of azimuths in HU Aqr has been obtained from the X-ray data, see Section 4.4.1. One can speculate that in 1992 the stream material was at high density and so was able to penetrate deep into the field. The stream would therefore have a large y -extent. The accretion flow changed in 1993 to a low density state during which the material can thread early causing the observed absorption dip and lower y -extent. In 1995 the stream became even denser than in 1992, with an even larger y -extent than in 1992. It should be emphasised that these ideas are quite speculative at the moment; the dramatic changes to the accretion stream that occur from time to time are not well understood. An explanation awaits the development of better models for the stream trajectory that can then be compared to the data.

| Observation | Absorption Dip? | Stream brightness | Stream eclipse duration |
|---------------------------|--------------------|----------------------|----------------------------|
| NOT 1992 Jun ¹ | NO | 50% | 0.04 ϕ |
| ESO 1992 Oct ² | NO | 50% | 0.04 ϕ |
| SO 1992 Oct ³ | NO | 30% | 0.03 ϕ |
| AAT 1993 Jun | YES | 40% | 0.02 ϕ |
| AAT 1993 Aug | YES | 30% | 0.02 ϕ |
| SAAO 1994 Nov | YES | 40% | 0.02 ϕ |
| NOT 1995 May | NO | 20% | 0.05 ϕ |
| ESO 1995 Oct ⁴ | NO | 25% | > 0.05 ϕ |

Table 2.2: Summary of the dip and accretion stream properties over the three years of HU Aqr observations. ESO=European Southern Observatory, SO=Steward Observatory, see text for other acronyms. The stream brightness is expressed as a percentage of the out-of-eclipse flux and the duration of the stream eclipse as a fraction of the orbital period. References: 1. Hakala et al. 1993 2. Schwobe et al. 1993 3. Glenn et al. 1994 4. Wheatley 1996, priv. comm.

2.6 Correlated photometric and polarimetric variability

Priedhorsky, Krzeminski & Tapia (1978) were amongst the first to observe flickering activity in the optical light curve of AM Her. This flickering occurred on a timescale of minutes and was detected throughout the orbital cycle. The authors concluded that it was caused by the actual flickering of the source and not by partial covering or other factors. This conclusion was based primarily upon comparison of the flickering in the optical flux to that in optical polarisation obtained simultaneously. By measuring the correlation between these two variables they observed that an increase in the flux was associated with an increase in the absolute value of the polarisation (in the V-band). From this they further concluded (i) that a substantial part of the observed flux is associated with the source of the polarisation, (ii) that a polarised source is the cause of the flickering, and (iii) that the correlation is in the sense expected for a variable source of polarisation which is diluted by light from an unpolarised source.

Figure 2.10 shows the flux and polarisation light curves from the AAT observation of HU Aqr in the BG39 and R-band filters. A detail of each light curve is shown from regions close to the absorption dip. The individual flares in the flux light curves can clearly be seen, as can flickering in the polarisation light curves which appears to correspond to the flares in flux. Each flare and the associated polarisation change have been labeled to highlight this correlation. The link between the flux and polarisation matches that seen in AM Her by Priedhorsky et al.

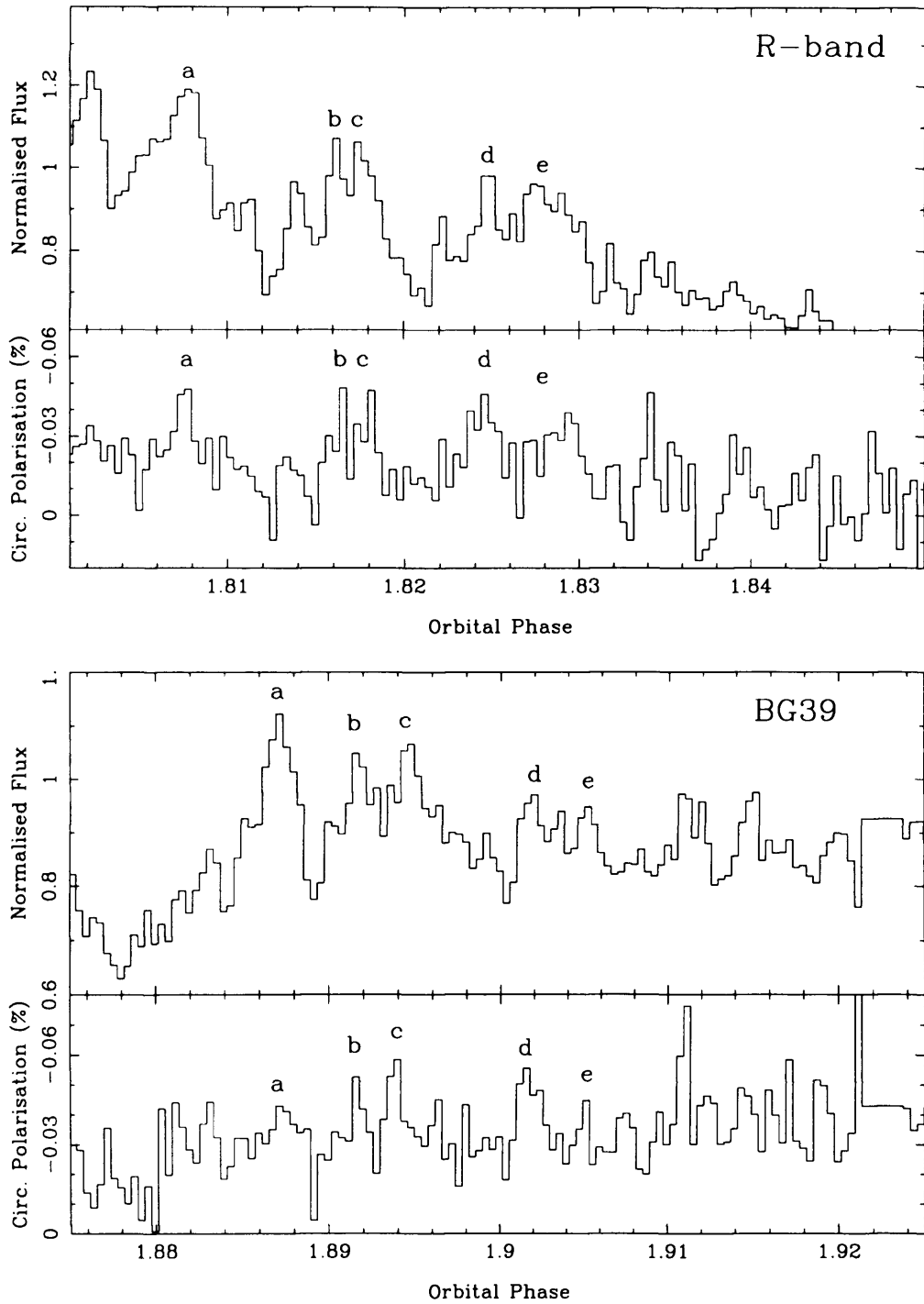


Figure 2.10: Detail of the BG39 and R-band light curves in regions close to the absorption dip. A number of flaring events are evident and have been labeled in both the flux (upper panels) and polarisation (lower panels) light curves.

An analysis of the correlation between the flux and polarisation changes in the optical light curves of HU Aqr was therefore undertaken. The initial intention was to confirm that the features observed by Priedhorsky et al. in the optical emission from AM Her can be also be found in HU Aqr. A further motivation for repeating this analysis was to understand the flickering in the context of the inhomogeneous models of AM Her accretion which had not been developed at the time of the earlier analysis. If the flickering is associated with blobs impacting upon the white dwarf surface, can the flickering be used to measure the blobs? HU Aqr provides an additional opportunity because it possesses an optical absorption dip. This enables the accretion stream to be studied at large distances from the white dwarf, and hence provides a way of sampling the blobs in a different part of the system.

2.6.1 Linear correlation

The basic question that a correlation analysis attempts to answer is; given that each point in a dataset has two or more different quantities associated with it, does knowledge of one quantity provide an advantage in predicting the value of another? In this case the data points are time (or phase) and the quantities associated with them are the optical flux and polarisation. There are actually two values to be determined for each data point; what is the strength of the association and how significant that association is. The difference between the strength and significance is simple; given enough data two distributions can have a significant association even is it is weak.

A linear correlation provides the best method for calculating a correlation between two continuous distributions. The linear correlation co-efficient is given by:

$$r = \frac{\sum (x_i - \bar{x})(y_i - \bar{y})}{\sqrt{\sum (x_i - \bar{x})^2} \sqrt{\sum (y_i - \bar{y})^2}} \quad (2.2)$$

for pairs of quantities (x_i, y_i) , $i = 1, 2 \dots N$. This is also known as the *product-moment correlation co-efficient*, or *Pearson's r*. The values for r obtained from this range between -1 and 1, where 1 represents complete positive correlation, -1 represents complete negative correlation and 0 represents uncorrelated variables, and therefore r provides a measure of the *strength* of any association between the variables. It is a poor statistic for deciding upon the significance of the correlation because r is ignorant of the distributions of x and y . There are methods available

for assessing the significance, but none of these are valid in this case because the two quantities that are being compared are not fully independent. This is not a serious problem as it will be possible to measure the correlation in a number of different phase bins in each orbital cycle. Confidence in the individual correlation measurements can be improved by the comparison of different orbital cycles with each other and by observing trends in the correlation co-efficient that can be associated with features in the light curve, such as the absorption dip. As a further aid to assessing the significance, an estimate has been made of the potential error on the correlation co-efficient. This is described below.

Before it was possible to apply Equation 2.2 to the data, it was necessary to remove the large-scale trends from the data to leave only the short-timescale flickering. This was done by finding and removing the running mean from the data; for each phase bin the mean over the interval of $\pm 0.005 \phi$ was subtracted from the flux and polarisation data. When rapid changes to the data occur this method was not appropriate because it introduces false signals into the data. For the light curve of HU Aqr this is really only a problem during the rapid ingress and egress to the eclipse. The false residuals have been corrected for in the data, but the safest approach is to treat any results within one bin of the eclipse with suspicion.

For the purpose of measuring the correlations the light curve was divided into 25 phase bins. Each bin therefore contains some 100 data points which is enough to reliably determine the correlation co-efficient. The zero point for this binning was selected to be phase 0.87, to match the bins to the end of the absorption dip.

To estimate the error on the correlation co-efficient, a ‘control’ experiment was performed. This was done by measuring the correlation between the flux from one filter and the polarisation from the other filter over the same phase range. No real correlation can occur between these datasets and so this provides a method of finding the typical random correlation between the flux and the polarisation. As expected, there was no variation of the co-efficient with phase and the standard deviation of the co-efficient about the mean value of zero was 0.10. This estimate of the error is marked on Figures 2.11, in which the results of the correlation analysis are presented.

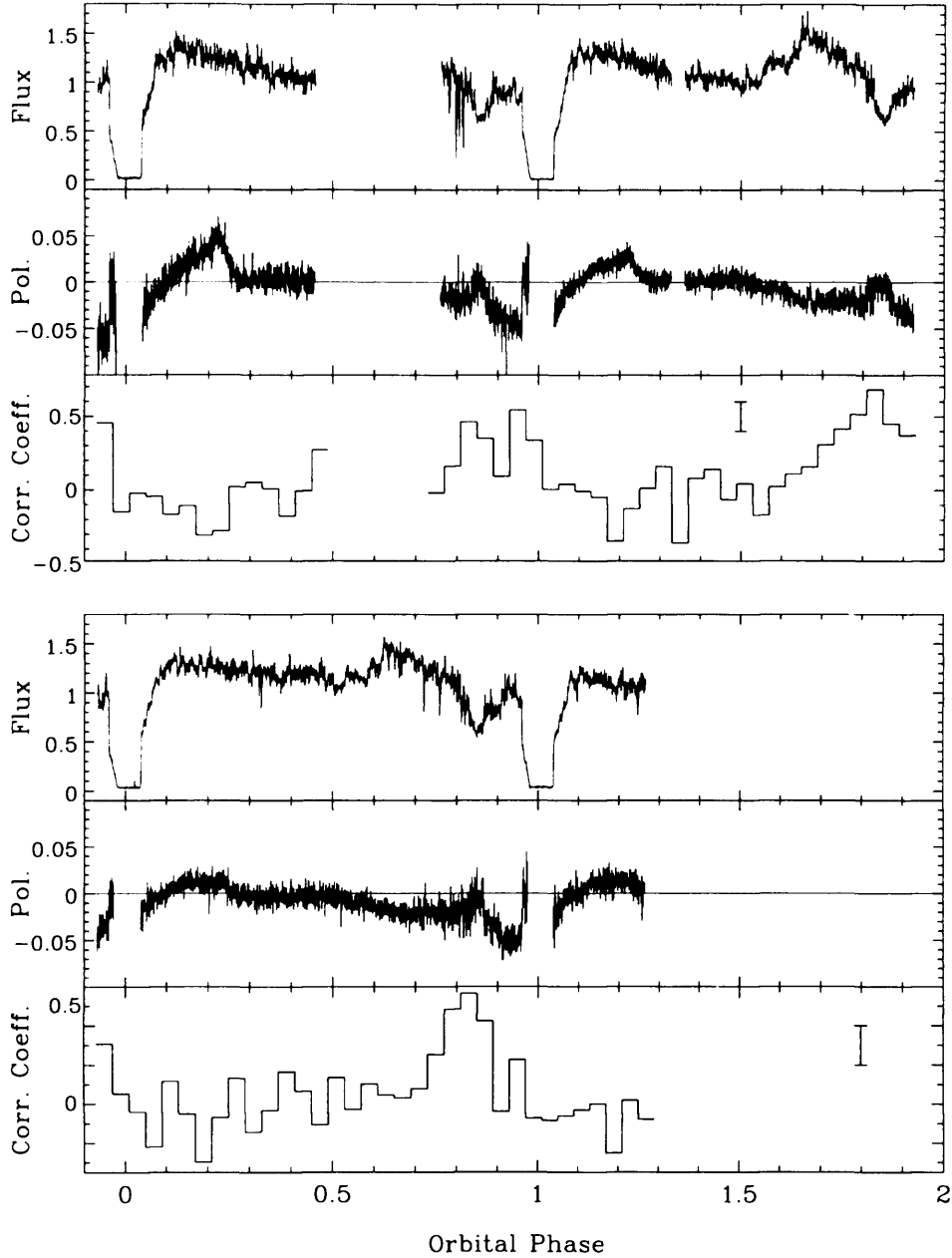


Figure 2.11: Linear correlation between the flux and the percent circular polarisation. The upper frame shows the BG39 data, the lower frame the R-band data. For each frame the flux light curve, polarisation light curve and the correlation of the flux with the circular polarisation are shown. The error bars at right show an approximate error for the correlation coefficient (see text). Note that the linear correlation values have been plotted such that values above zero represent positive correlation and values below zero represent negative correlation, regardless of the sense of the circular polarisation.

2.6.2 Results

During the faint phase ($0.26 < \phi < 0.53$) there is no correlation evident between the flux and the polarisation. This is unsurprising since the interpretation of this segment of the light curve provided in Section 2.3.3 stated that the main accreting pole is not in view at this phase. As a result there is no net polarisation and hence the residual flickering in the polarisation is not expected to correlate with flickering of the flux.

In the early portion of the optical bright phase ($0.53 < \phi < 0.70$) there is little correlation seen in the BG39 data and none in the R-band data. At these phases the main emitting pole is visible and according to the results of Priedhorsky et al. (1978) for AM Her a positive correlation between the flux and polarisation is expected. How can this lack of correlation in the HU Aqr data be explained? Two possible scenarios can be envisaged. It may simply be that there truly is no correlation between the variations in the flux and polarisation from the main pole. Such a lack of correlation is contrary to the results of Priedhorsky et al. and to the expectations of current theory. Alternatively, there may be correlated flickering in the photometry and polarimetry that is not detected. This only occurs if the signal-to-noise of the observation is low, such that the flickering amplitude is less than the noise. However, the signal-to-noise of this observation is known to be very good, as can be seen by the lack of noise during the eclipse minimum.

The flickering seen in HU Aqr between 0.53ϕ and 0.70ϕ is therefore probably not associated with the pole but with some other source instead. There is support for this idea in the fact that the character of the flickering is the same when the pole is known to be out of view during the faint phase. The accretion stream in HU Aqr is a good candidate for the source of this flickering, since the stream flux in this system is already known to be high, higher than AM Her in which the correlation *was* seen.

In the middle of the bright phase ($0.70 < \phi < 0.96$), which could also be considered the ‘dip phase’, there is strong correlation between the flux and the true polarisation. The correlation is strongest in the deepest part of the dip, therefore the correlation must be associated with the dip and hence with the occulting portion of the accretion stream. It could be suggested that the increased correlation is the result of an increase in the (unabsorbed) brightness of the main pole. The segment of the data between phase 0.90 and 0.96 discounts this possibility because

the correlation at this phase is low, but the flux is at its highest.

The positive correlation between the flux and polarisation during the dip can be explained as follows. The optical flux from HU Aqr can be considered to be dominated by two sources of light; the polarised flux from the pole and unpolarised flux from the rest of the system, which will dilute the polarisation from the pole. The photometric light curve shows that the unpolarised flux comes primarily from the accretion stream itself, and so will not be significantly occulted. The flux *emitted* from both sources can be considered to be effectively constant (small variations in flux will not matter to the argument as long as the occultation contributes the strongest modulation). As denser portions of the stream cross the line of sight to the pole they will obviously cause a reduction in the flux from the pole, and hence a reduction in the total amount of polarised flux. Since the diluting flux is unocculted the fractional polarisation decreases as well and so the flux and polarisation are correlated. What this demonstrates is that the dominant flickering during the dip is caused by the variable covering of the pole by the inhomogeneous accretion stream.

At the end of the bright phase ($0.05 < \phi < 0.26$) there is marginal evidence for a negative correlation (this is more noticeable in the BG39 data). This correlation is strongest when the mean polarisation becomes positive. Thinking again in terms of a polarised source that is diluted by an unpolarised source this suggests that the flux from the diluting source increases while the polarised source remains approximately constant (or vice-versa). The effect is that the flux increases while the percentage polarisation decreases, creating the anti-correlation.

This has to be explained in the context of the second pole which is suspected to be present at this phase. There does not appear to be a substantial amount of *flux* from the second pole (f_2), most of the evidence for another pole comes from the polarisation. It is still possible to produce the 5% positive polarisation detected at phase 0.2 with little flux if the second pole is highly polarised. For example, if the diluting flux f_d exceeds f_2 by a factor of eight then the polarisation on the second pole would have to be 40% to produce 5% net polarisation. This is not an unreasonably high value for the pole itself. To explain the negative correlation it is suggested that f_2 varies less than f_d , i.e. the flickering of the diluting source is dominant. This is likely to be true if f_d exceeds f_2 by something like a factor of eight. Therefore as f_{tot} ($= f_d + f_2$) increases the fractional polarisation will decrease and thereby create the observed

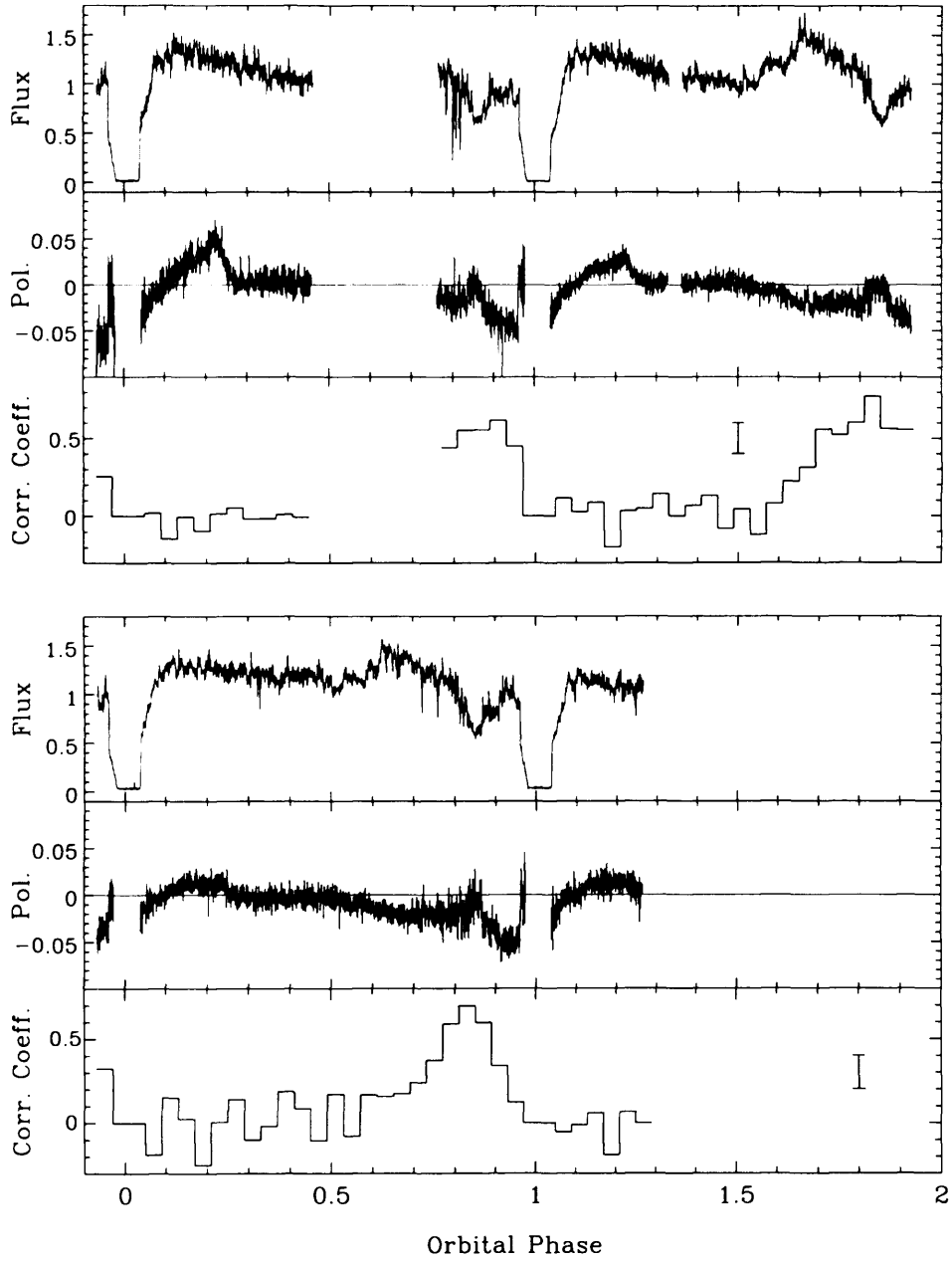


Figure 2.12: Linear correlation between the flux and the measured value for the circular polarisation. The upper frame shows the BG39 data, the lower frame the R-band data. For each frame the flux light curve, polarisation light curve and the correlation of the flux with the circular polarisation are shown. The correlation results shown here confirm the results shown in Figure 2.11.

anti-correlation. What is not clear in this interpretation is what causes the variations in the diluting flux, since there was no correlation detected in the the early bright phase.

To confirm that the results obtained are real and do not arise from an intrinsic relationship between the flux and *percent* polarisation, a second correlation is shown in Figure 2.12. In this case, the correlation between the flux and the real value of the circular polarisation (in counts) was calculated. The correlation in Figure 2.12 is in fact stronger than that seen in Figure 2.11, particularly during the dip phase, and thereby demonstrates that a real effect in the data has been detected.

2.6.3 Increased variability in the dip

By eye, there appear to be changes in the character of the flickering from one portion of the light curve to the next. In particular, the structure in the flux and polarisation light curves is far more noticeable during the dip than at other phases. This is obviously consistent with the strongest correlations being detected in this region. In order to confirm this in an objective manner, the RMS values were calculated about the mean flux and polarisation in 0.04ϕ segments of the light curve (the same bins used for the correlation analysis). Once again the linear trend within the data was removed, as were the false signals this introduces to the data, before the RMS was calculated. The results from this are shown in Figure 2.13.

As suspected the RMS increases in the interval $0.60 < \phi < 0.85$ in both filters. The mean RMS value in this region is 9% for the flux and 10–14% for the polarisation, but both fall to the same value of 6% at other phases. These RMS values are the same in both filters. Once again a change is occurring that is associated with the dip and this leads to the conclusion that the increased variability must arise due to the inhomogeneity of the stream. The RMS of the polarisation is somewhat higher than the RMS of the flux during the dip. This may arise because the variable covering effects the pole more than the diluting flux from the stream. The polarised flux is therefore more strongly attenuated than the total flux from the system.

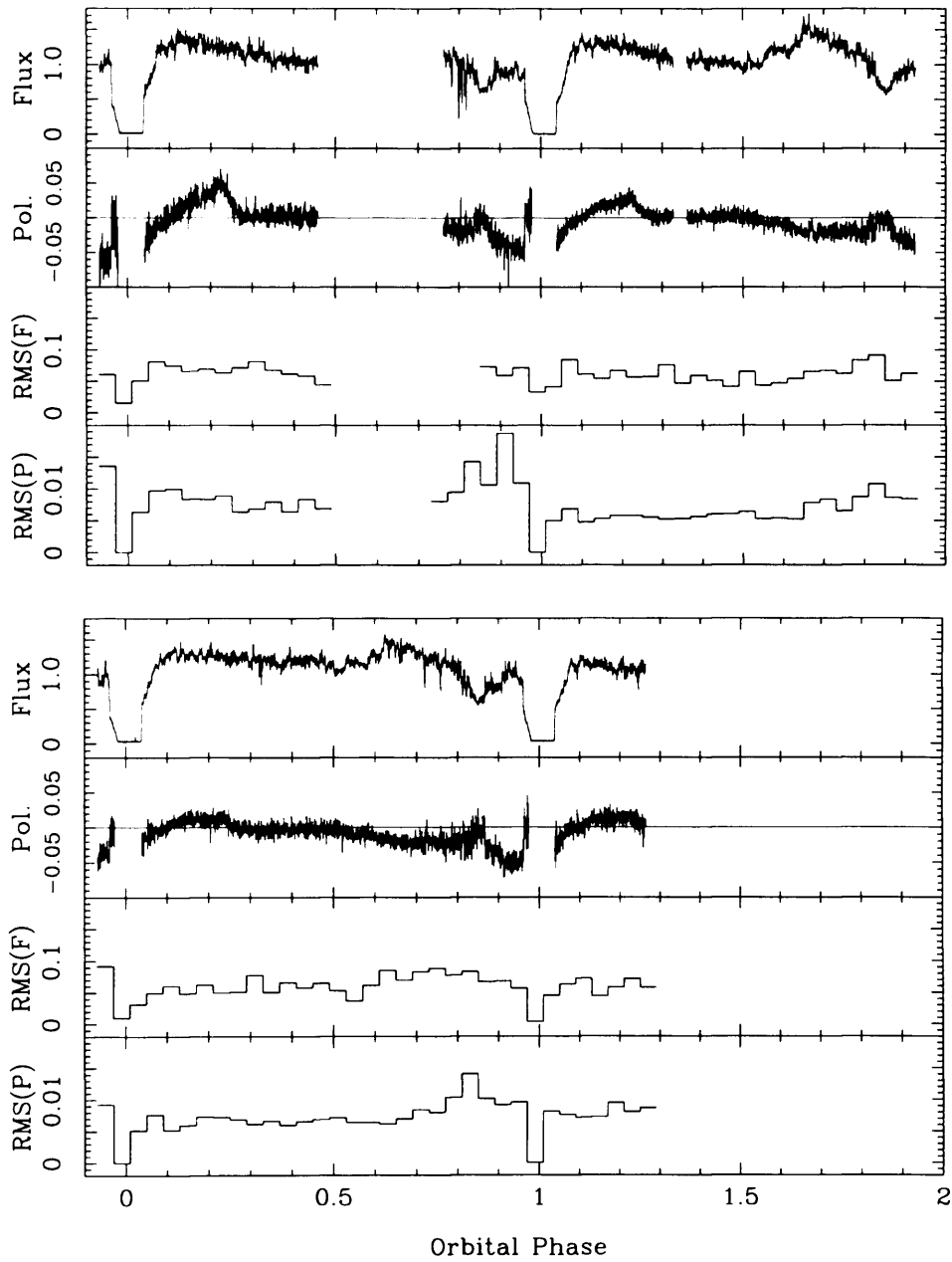


Figure 2.13: RMS values for the flickering in the data. The upper frame shows the BG39 data, the lower frame the R-band data. For each frame, the upper two plots show the flux and polarisation and the lower two plots shows the RMS value for the flux and polarisation respectively.

2.6.4 Concluding remarks

Throughout this section (§ 2.6) the term ‘variable covering’ has been used to label the cause of the structure detected within the dip by the correlation and RMS analysis. This was done without properly stating what causes the variable covering itself. It will be shown from the X-ray data presented in Section 4.4.1 that attenuation of the X-ray flux by the accretion stream continues after the dip right up to the beginning of the eclipse. This happens because the stream has broken up into a number of separate streams as treading occurs over a spread of azimuths. Similar arguments have also been used in Section 2.4 above when discussing the changes to the trajectory of the stream. The image of the stream as a single, well collimated rod of material clearly must be discarded in favour of a stream that breaks up when it encounters the magnetic field and follows a number of field lines. In this way the stream forms a kind of accretion curtain. This leads to variable covering of the pole emission as the non-uniformities of this curtain cross the line of sight to the pole. The detection of an increase in the RMS does not allow the scale of structure across the accretion curtain to be found, but it does show that the effect on the light curve is real. Further work to study these light curves and thereby parameterise the structure of the stream is therefore required.

2.7 Summary

The optical light curves of HU Aqr presented in this chapter have been obtained when the system was in a range of different states. Many details of the constituents of the system have been inferred from the light curves, the accretion stream in particular. The optical flux is dominated by the pole and, surprisingly for an AM Her system, by the accretion stream. Strong evidence for the presence of a second pole on the white dwarf during the AAT (and probably the SAAO) observations has been found. This feature seems to be associated with epochs of high accretion rate in this system. The locations of the main and second pole have been estimated from the relative phasing of the bright phases and the eclipse. The optical flux at various parts of the light curve shows that the accretion stream emits optical flux in a non-isotropic manner, probably because of uneven heating by X-ray flux from the pole. The stream is revealed to be a tenuous object, able to change its position within the system on timescales as short as a few hours. Epoch to epoch changes to the accretion stream trajectory that can be inferred from the

absorption dip and the eclipse profile appear to be correlated; a dip is seen when the gradual stream eclipse is short.

There is also compelling evidence for a great deal of density structure within the stream. This was shown best by the correlation analysis, which demonstrated that for HU Aqr; (i) the majority of the optical flux is associated with the source of polarisation, as expected; (ii) there is a lack of correlation outside of the absorption dip, which suggests that the polarised source is not the dominant cause of the flickering at these phases, (iii) the correlation detected during the absorption dip is consistent with variable covering of a polarised source in the presence of a diluting (and non-covered) optical flux.

Chapter 3

Phase-resolved optical spectroscopy of HU Aqr

In this chapter the results of a phase-resolved spectroscopic study of HU Aqr are presented. The results of this work focus mainly upon the accretion stream, since it is an optically bright object with large velocity variations which reveal themselves in emission line wavelength changes. The high time-resolution of these data and large brightness of the accretion stream in HU Aqr combine to make this the most extensive and informative investigation of the accretion stream in an AM Her system to date.

3.1 Observations

Time-resolved optical spectroscopy of HU Aqr was obtained with the Anglo-Australian Telescope (AAT) on the nights of 17 and 18 August 1993. Observing conditions were near-photometric on the first night (seeing of ~ 3 arcsec). At the start of the second night conditions were also photometric (stable seeing of ~ 1.0 arcsec), but later degraded due to fog (seeing $\sim 2-3$ arcsec). The RGO spectrograph and 1200V grating were employed to acquire blue spectra (4370–5000Å) at a resolution of ~ 1.3 Å. A slit width of 1.3 arcsec was used. The spectra were recorded by a Tektronics CCD detector. Readout overheads were minimised using on-chip windowing and binning in the spatial direction. All of the spectra were taken under automatic software control and consisted of 30 s exposures with a total readout time of 34 s between them.

A dichroic was inserted into the light path to enable simultaneous red spectra to be obtained. Low-dispersion spectra with $\sim 16\text{\AA}$ resolution and a wavelength range of 5200–11 000 \AA were recorded by the FORS. Synchronisation of the RGO and FORS spectrographs was not possible and the FORS was run using exposures of 36 s with a total dead time of 40 s between them. A total of 7.2 and 5.0 orbital cycles were observed with the RGO and FORS spectrographs respectively.

A short service-observation of HU Aqr was conducted on the 4.2 m William Herschel Telescope (WHT) on 7 June 1993. Simultaneous high-dispersion (1.5\AA resolution) red and blue optical spectra were obtained using the ISIS spectrograph with EEV CCD detectors. The wavelength range obtained was 4150–4950 \AA on the blue arm and 5970–6870 \AA on the red arm. The CCDs were read out once every 60 seconds to allow time resolved spectroscopy to be undertaken. A total of 1.3 orbital cycles were observed by both arms of the spectrograph.

3.2 Data reduction

There are a number of effects associated with CCDs and with spectroscopy which have to be corrected for to make best use of the data. The reduction of the CCD spectra is therefore a series of procedures to carry these corrections out. When the CCD is in readout mode, imperfections at the interface between the substrate (which holds the charge) and the insulating oxide layer can remove electrons from the signal during transfer. The faintest signals will be worst effected due to the proximity of the few electrons collected to this interface. A bias is therefore applied to the CCD to partially fill each CCD element with electrons, thereby separating the signal from the imperfections. During reduction this is removed by measuring the recorded signal in a portion of the chip which is not exposed to the sky (the ‘bias strip’) and subtracting this from the data.

A cosmic ray which passes through a CCD pixel will cause a large number of ionisations and thereby produce many electrons in the pixel or pixels that the cosmic ray hit. Such events are usually apparent in the CCD frame as intense spikes or streaks. Software is available to scan the frame to identify spikes based on a number of criteria and then remove them, usually by taking the mean of the surrounding eight pixels. However, this software is not foolproof and visual

inspection of the frames for any missed cosmic ray events is still required. Individual hot-spots in the CCD frame and other defects can also be noted and (hopefully) removed at this time.

Variations in pixel quantum efficiency can cause 10–20% fluctuations in the signal over the sensitive area of a CCD chip. Flat-fielding the frame eliminates this problem; a uniform source is observed, usually at the start of the observation, to produce an image of the fluctuations in chip sensitivity. Each data frame can then be corrected by dividing by this flat-field (Kitchin 1991, pg.29). When performing spectroscopic observations the flat-field must be further corrected to remove the spectral signature of the uniform source. The usual way of dealing with this is to fit the spectral response, obtained by collapsing the frame in the cross-dispersion direction, to produce a spectrum of the source and then multiply each frame by the fitted value before dividing by the flat field (Shortridge & Meyerdierks 1996).

Removal of sky background effects can be achieved simply by subtracting the mean flux detected in the pixels above and below each element of the spectrum. The wavelength scale is determined by observing a spectral standard lamp, or ‘arc’, with spectral line features of known wavelength. The correct wavelength can then be associated with each x -element of the output spectra. Flexure of the telescope as it tracks the target star across the sky can introduce variations in the wavelength scale of the spectra. To account for this a number of arc spectra are obtained throughout the night. Each spectrum of the target star therefore has its wavelength scale set by the closest arc spectrum to reduce the errors introduced by the flexure. For the observations presented here this method showed the wavelength scale to be stable and therefore only minimal flexure errors should remain.

Corrections must be made to remove spectral features introduced by the atmosphere particularly at the red end of the spectrum. Observations are made of a star with little or no spectral features at these wavelengths (usually a B-star is chosen). A low-order polynomial or spline fit is made to the portions of the spectrum without atmospheric absorption features to model unabsorbed B-star spectrum. This is divided by the actual spectrum to obtain the inverse spectrum of the atmosphere. By multiplying this inverse spectrum by the spectra of the target star the atmospheric features are removed. Scaling of the calibration spectra is also required to account for the difference in the airmasses of the two spectra. This technique is not perfect, and in the AAT FORS spectra most of the features redward of about $10,000\text{\AA}$ arise from poorly removed

atmospheric absorption.

Once the above reduction procedures are complete, comparison with standard star observations is carried out to flux calibrate the spectra. Before this is done the source spectra and standard star spectra must be corrected for extinction. This correction is different for each spectrum because the airmass through which the spectra are measured is constantly changing. The standard star spectrum is converted into a calibration spectrum by dividing the extinction corrected spectrum into a spectrum of the standard in known units ($\text{erg cm}^{-2} \text{s}^{-1} \text{\AA}^{-1}$ for example). In some cases smoothing is required to remove spurious values associated with regions of absorption in the spectrum. The calibration spectrum is then multiplied by the observed spectrum to create the final flux-calibrated spectrum.

3.3 Results and discussion

3.3.1 The mean orbital spectrum

The mean spectra derived from both the AAT blue arm and WHT red and blue arms are shown in Figures 3.1 and 3.2 with the principal emission lines and their wavelengths indicated. No correction has been performed for the velocity variation within these lines and so the narrow peak of the lines appears to be split into two asymmetric peaks (the origin of these peaks is discussed in Section 3.3.3 below). Beneath the peaks lie the broad line wings typically found in the emission lines of AM Herculis systems.

All of the usual emission lines of AM Hers are seen; the hydrogen Balmer lines and the lines of neutral (HeI) and ionised (HeII) helium. The equivalent widths of these major lines are given in Table 3.1. Due to the quality of the spectra a number of other line features are present which are not frequently seen in other AM Hers. These lines have also been labelled in Figure 3.1*a*. The $\text{H}\alpha$, $\text{H}\beta$ and HeII lines from the WHT spectra were clearly not of such high quality as the AAT lines and therefore were used only to confirm some of the more general results from the AAT study. An inverse Balmer decrement is seen in the WHT and AAT spectra between the $\text{H}\alpha$ and $\text{H}\beta$ lines; the flux ratio $F(\text{H}\alpha)/F(\text{H}\beta)$ was found to be 0.66 and 0.743 respectively. In a 10,000 K plasma with a density $n_e = 10^6$ the predicted value of $F(\text{H}\alpha)/F(\text{H}\beta)$ for optically thin

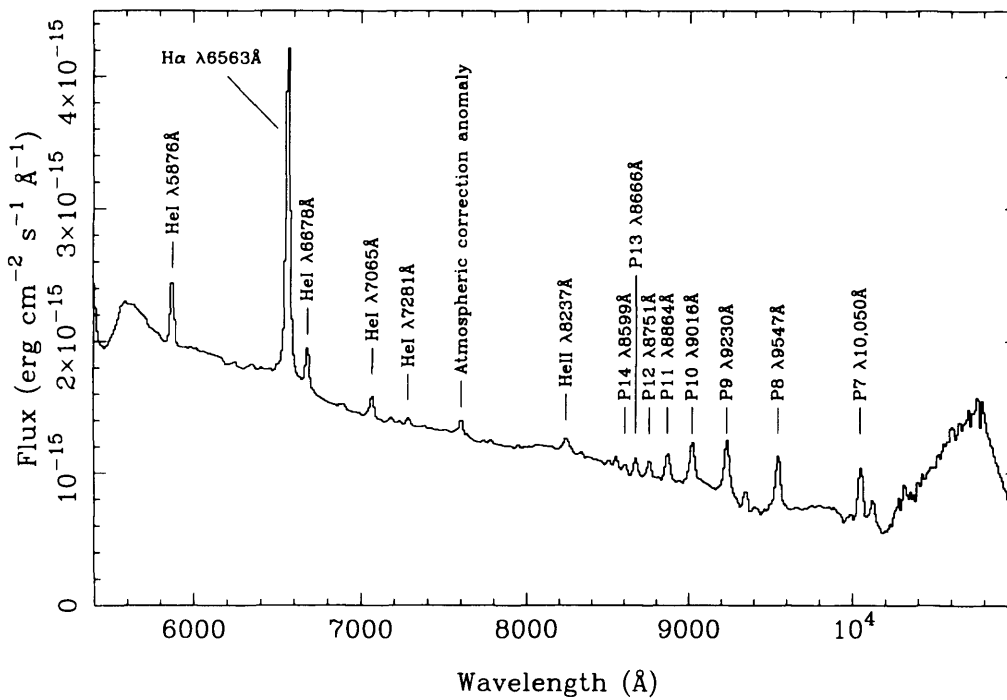
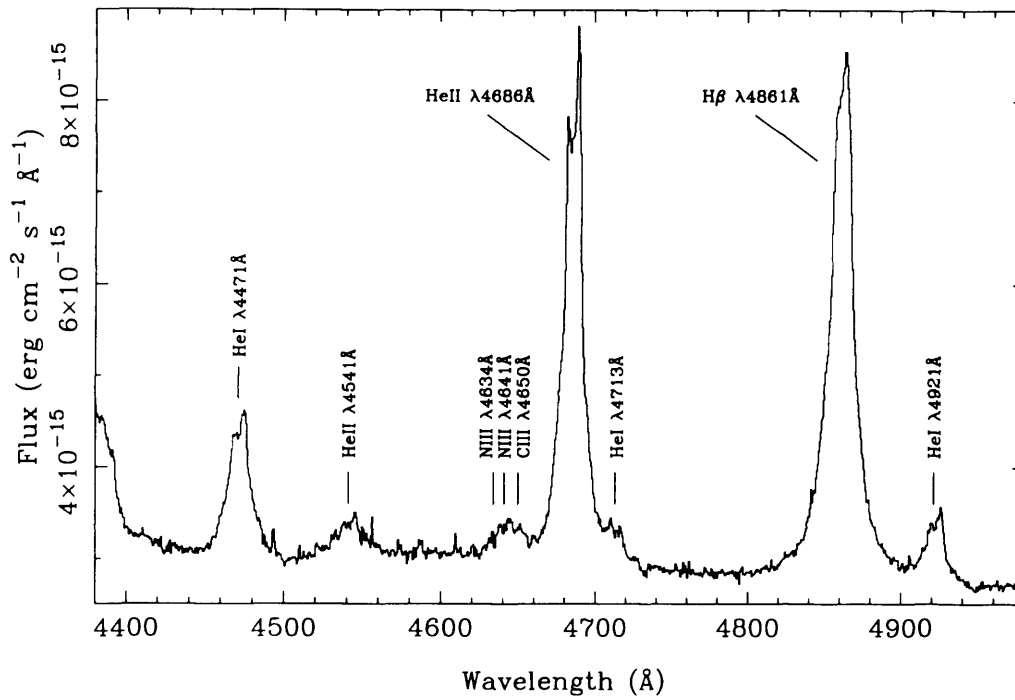


Figure 3.1: Top: Mean AAT RGO (blue) spectrum. Bottom: Mean AAT FORS (red) spectrum. The spectral resolution of these spectra are 1.3\AA and 16\AA respectively. The identities and wavelengths of the principal emission lines are marked.

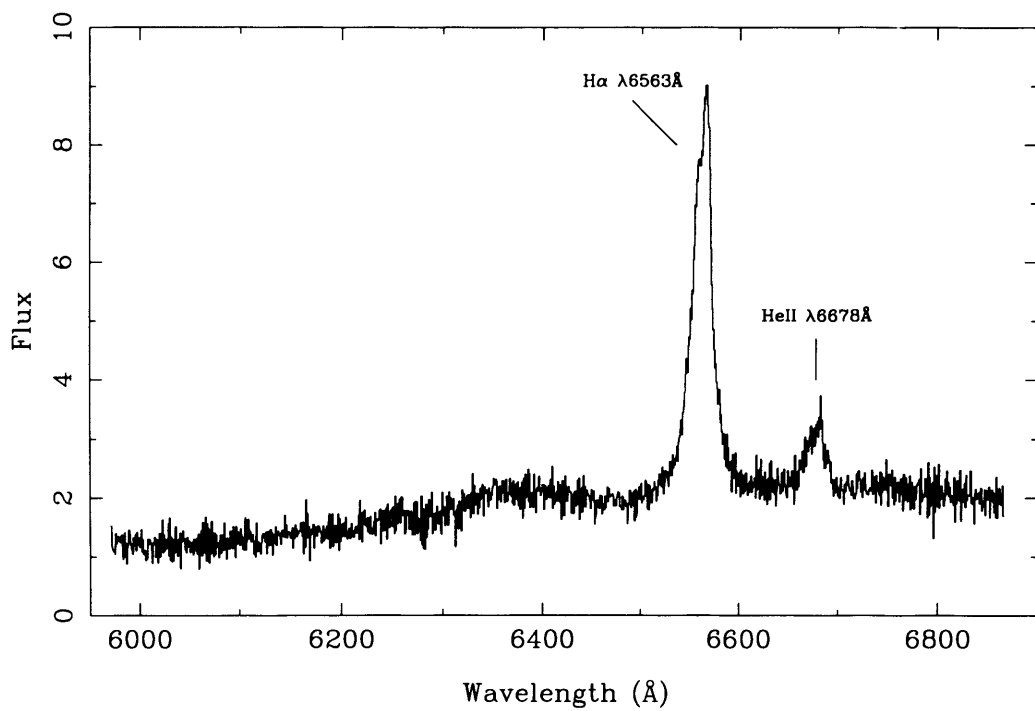
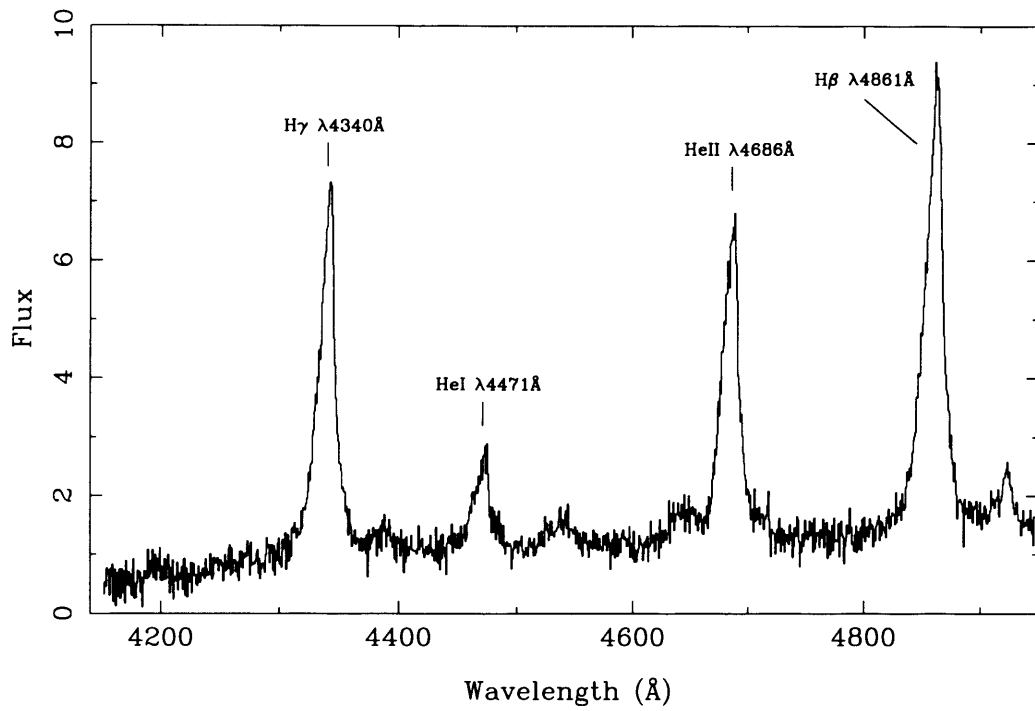


Figure 3.2: Top: Mean WHT blue spectrum. Bottom: Mean WHT red spectrum. The spectral resolution of these spectra are 1.3Å and 16Å respectively. The identities and wavelengths of the principal emission lines are marked. An arbitrary flux scale is used for each spectrum.

recombination is 2.81 (Pottasch 1984), and therefore the Balmer lines are significantly optically thick.

| | | WHT | AAT |
|------------|--------------------------|-----------------|-----------------|
| H γ | $\lambda 4340\text{\AA}$ | 30 \AA | – |
| HeI | $\lambda 4471\text{\AA}$ | 6 \AA | 9 \AA |
| HeII | $\lambda 4686\text{\AA}$ | 20 \AA | 22 \AA |
| H β | $\lambda 4861\text{\AA}$ | 34 \AA | 39 \AA |
| HeI | $\lambda 4921\text{\AA}$ | 2 \AA | 3 \AA |
| H α | $\lambda 4561\text{\AA}$ | 38 \AA | – |
| HeII | $\lambda 6678\text{\AA}$ | 6 \AA | – |

Table 3.1: Equivalent widths of the principal emission lines, derived from the mean spectra presented in Figure 3.1 and 3.2.

The mean FORS spectrum is displayed in Figure 3.1*b*. The prominent H α $\lambda 6563\text{\AA}$ line and the Paschen series redward of 8400\AA dominate the spectrum. The identities and wavelengths of these and other strong emission lines have been indicated. Above $10,000\text{\AA}$ the spectrum becomes unreliable due to poor removal of atmospheric features and below 5600\AA the spectra have been corrupted by another error in the reduction sequence (associated with sky background subtraction). Two broad humps can be seen indistinctly under the H α line at 6500\AA and at 8200\AA . These arise due to the cyclotron harmonics visible at phase 0.3 and 0.7. Similar features have been observed in two of the previous studies of HU Aqr (Schwope et al. 1993, Glenn et al. 1994). The increase in flux blueward of the HeI emission line at 5876\AA is thought to be the red tail of yet another of these harmonics.

3.3.2 The light curves

Figure 3.3 shows light curves of the continuum from the blue and red AAT spectra and equivalent width light curves of the H β , HeII $\lambda 4686$ and HeI $\lambda 4471$ emission lines. All light curves were obtained from phase-folded spectra binned to a resolution of 30 s (blue spectra) and 44 s (red spectra). The wavelength ranges $4420\text{--}4450\text{\AA}$ and $4730\text{--}4800\text{\AA}$ were used to derive the blue continuum light curve while the ranges $5980\text{--}6380\text{\AA}$ and $7675\text{--}8150\text{\AA}$ were used for the red light curve. The mean blue and red continuum fluxes (from out-of-dip phases only) were found to be $(3.2 \pm 0.6) \times 10^{-15} \text{ erg cm}^{-2} \text{ s}^{-1} \text{ \AA}^{-1}$ and $(1.8 \pm 0.4) \times 10^{-15} \text{ erg cm}^{-2} \text{ s}^{-1} \text{ \AA}^{-1}$ respectively.

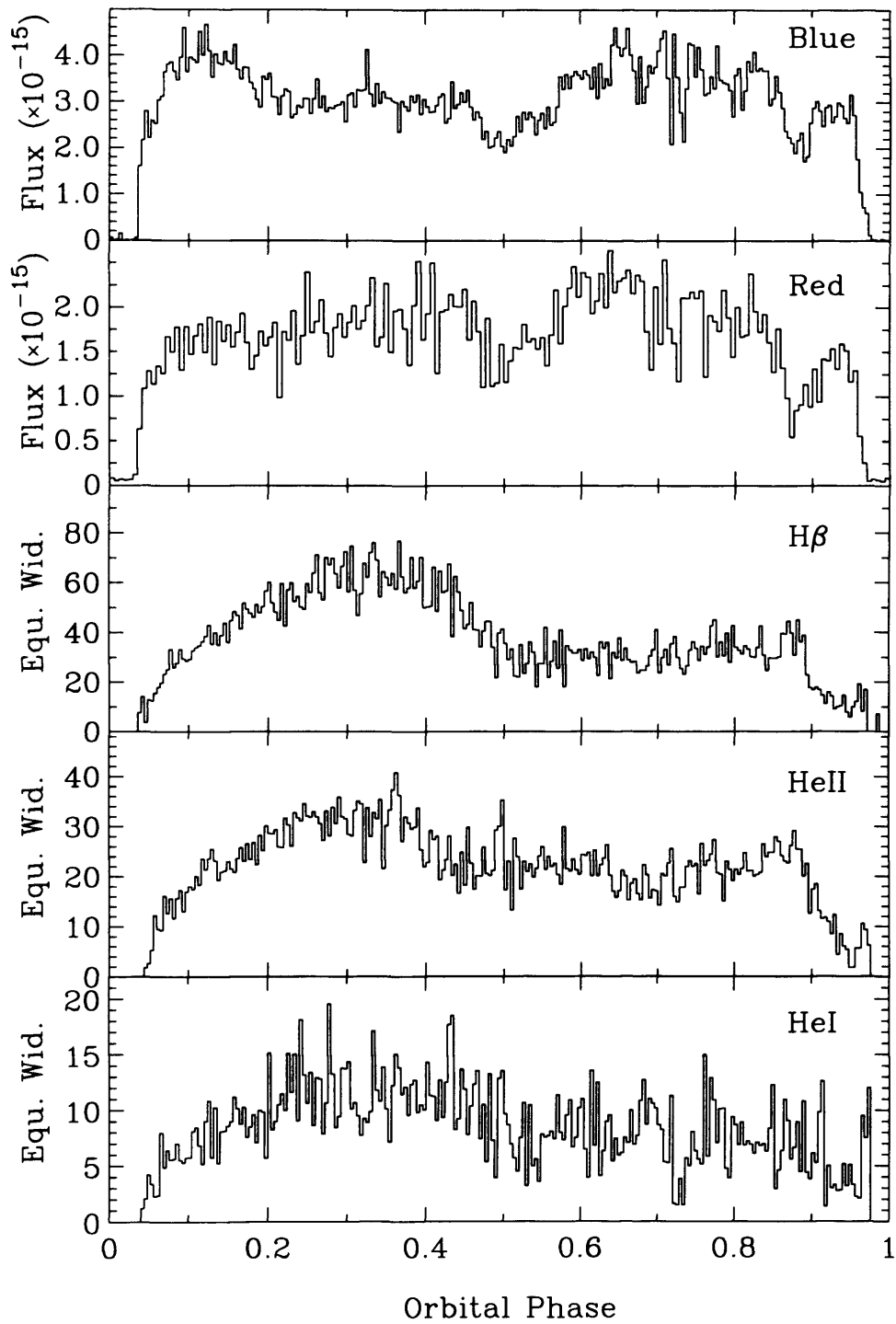


Figure 3.3: Phase-folded light curves derived from the AAT spectroscopy. The upper two panels show the blue and red continuum light curves, see text for wavelength ranges used to measure the flux. The lower three panels are equivalent width light curves for the H β , HeII λ 4686 and HeI λ 4471 emission lines. The phase resolution is 0.004 (30 s).

The continuum light curves strongly resemble those from the AAT and SAAO photometric observations presented in Chapter 2. The eclipse is obvious and a clear dip is present at phase 0.88 ± 0.02 . The minimum flux outside of the dip occurs at 0.5ϕ , associated with a short ($\pm 0.05\phi$) interval of reduced flux. The feature is discussed later, in relation to a similar feature detected in one component of the emission lines. The light curves derived from the WHT spectra (not shown) are basically identical to the AAT light curves, apart from the phase of the dip (at 0.82 ± 0.02) which was somewhat earlier than in the AAT light curves.

The dip and eclipse in the blue and red continuum possess the same profile, apart from the greater depth of the eclipse in the blue (due to the redness of the secondary star). In the red band the residual eclipse flux represents $3.6\% \pm 0.5\%$ of the estimated pre-eclipse flux, whereas in the blue band the residual flux is less than 1%. After the eclipse (around phase 0.1) there is an excess of flux at blue wavelengths when compared to the red. This must be associated with a preferential viewing angle to the pole (or poles) at that phase, leading to a larger contribution by the pole to the optical luminosity of the system than at other phases.

The equivalent width (EW) light curve of the three strongest emission lines all have the same characteristic shape. The light curve is dominated by a double-humped profile caused by projection effects as the accretion stream (which dominates the line emission) rotates. This profile is asymmetric; the equivalent width of the lines during the early part of the orbital cycle (when the secondary is receding from the observer) is almost twice that of the latter half of the orbit. This suggests that the inner surface of the curved accretion stream (see Figure 2.9) is brighter than the outer (leading) surface. This arises because the optical emission is generated by heating from the X-ray flux from the pole, and so occurs preferentially on surfaces which face the pole. This explanation is valid only if the stream is optically thick, and so this asymmetry provides independent confirmation of the result derived above that the line emission arising in the stream is optically thick.

The light curve of the HeII $\lambda 4686$ line does not match that of the other two lines. The asymmetry between the first half of the orbit and the second half is weaker in this line. The HeII line has relatively more flux in the second half of the orbital cycle because it is a high ionisation line. The stream will be less optically thick to this line and so more HeII line flux can pass through the stream than for the lower ionisation lines (Schwope et al. 1996).

Prior to the eclipse (after phase 0.88) the line light curves deviate suddenly from the smooth trend. At first the equivalent width drops rapidly ($< 0.02\phi$), then decreases slowly for a time ($0.9 < \phi < 0.96$) before brightening slightly prior to going into eclipse ($0.96 < \phi < 0.98$). The sudden drop in EW occurs at the onset of the rise from the absorption dip. The increase in the continuum flux at the end of the dip may be the cause of the EW drop, but there is no corresponding rise in EW during the ingress to the dip and the EW change is far more rapid than the continuum flux change. This feature is still not understood. The brief brightening after 0.96ϕ occurs because the cyclotron emission region is no longer visible once the pole has gone into eclipse. This drastically reduces the continuum flux and so boosts the equivalent width of the emission lines.

3.3.3 The phase-resolved RGO spectra

Figure 3.4 shows the full width of the AAT blue spectra plotted as a trailed spectrogram. The individual spectra have been folded on the orbital period and binned into 250 phase intervals. In the trailed spectrogram time (or phase) increases along the y -axis, wavelength is shown on the x -axis and flux is displayed using a colour scale. The coverage in this spectrogram is excellent; between 3 and 7 individual spectra have gone into each of the 250 phase bins, thereby providing good signal-to-noise.

In this representation, an object with a fixed velocity in the orbital frame of reference will reveal itself as an S-wave running up and down the plot. This S-shaped pattern emerges from the varying radial velocity of the object as the system rotates; the maximum amplitude gives the maximum projected radial velocity of the object. The similarity of the variations in all the all the lines ($H\beta$, HeI, HeII and the lines of N, C, Mg etc.) indicates that each line arises in similar regions of the system to the other lines. A detailed analysis was therefore undertaken of only the two strongest lines, the HeII line at 4686\AA and the $H\beta$ line at 4861\AA . Unfortunately one of the lines of the HeII-Pickering series is located at $\lambda 4859.32\text{\AA}$ and may therefore contribute to the $H\beta$ flux and radial velocity variations. Schwobe et al. (1996) estimated that the flux contribution to the $H\beta$ line was of the order 10%. The effect of this contribution may therefore need to be considered in some circumstances.

The HeII and $H\beta$ lines from the AAT observation are shown with an expanded x -axis scaling in

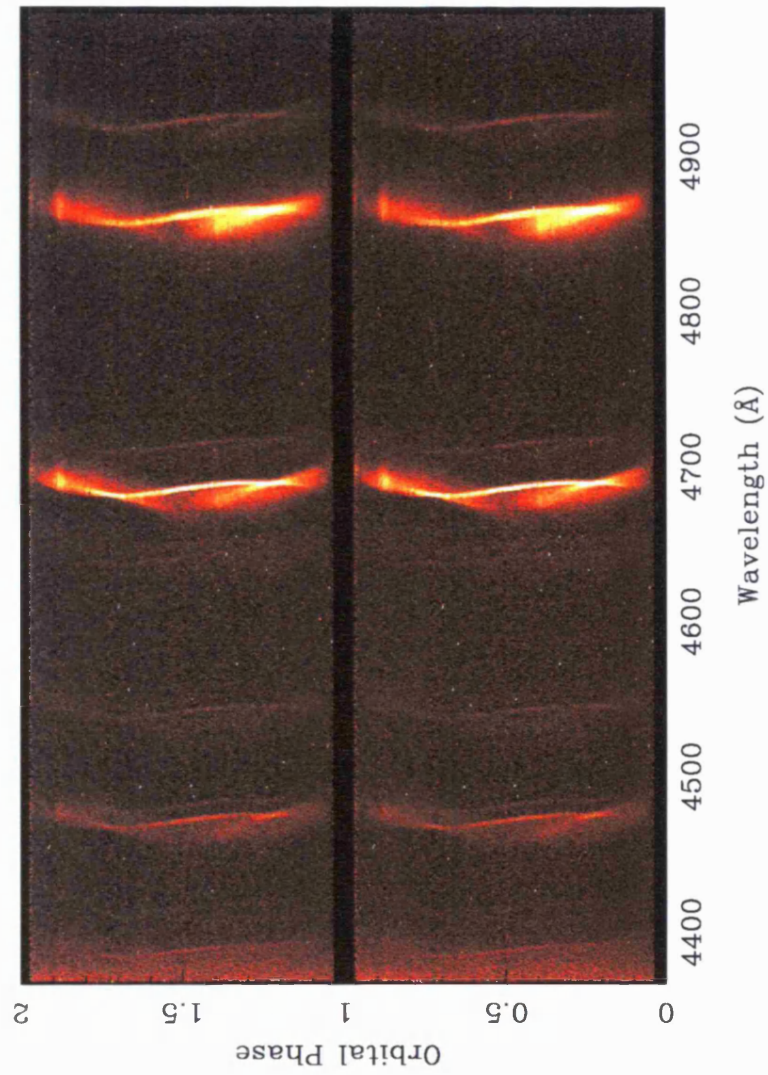


Figure 3.4: Trailed spectrogram of the AAT RGO (blue) spectra. The eclipse and radial velocity variations of eleven emission lines can clearly be seen. Two orbital cycles are shown for clarity. See Figure 3.2 for identifications of the lines.

Figure 3.5. The wavelengths on the x -axis have been converted to a radial velocity scale based on rest wavelengths of 4685.75Å and 4861.32Å respectively. The flux scale has been normalised to remove the variations in the mean continuum flux, in order to emphasise the structure of the line emission. Both emission lines are clearly separated into three components; a narrow component, a broad component and a high-velocity narrow component. Throughout this thesis these are referred to as the NC, BC and HVNC respectively. Each component is labelled in the schematic of the trailed emission lines given in Figure 3.6. An extra component has therefore been detected in addition to those found by Glenn et al. (1994). This is probably the result of the significant improvements in spectral resolution and signal-to-noise in this study over that of Glenn et al. rather than a change in the nature of the accretion process.

Modelling of the line emission presented below will provide strong constraints upon the location of the emission regions giving rise to these components. Prior to such detailed modelling it is possible to make strong statements about these locations from evidence in the trailed spectrograms themselves. The narrow component is believed to arise on or near the secondary star (e.g. Rosen et al. 1987). This idea is strongly supported by the spectra from HU Aqr because the NC has zero radial velocity close to conjunction of the secondary star and possesses a maximum velocity amplitude typical of secondary star orbital velocities ($\approx 300 \text{ km s}^{-1}$). A common explanation for this component is that it arises on the primary-facing surface of the secondary star, due to reprocessing of the flux from the accreting pole. The flux of the NC peaks around phase 0.5 which suggests this is also true for HU Aqr. The radial velocity variations of this component give rise to the asymmetric splitting of the peaks of the emission lines in the mean spectra presented in Figure 3.1 and 3.2.

A subtle difference is apparent between the NCs of the HeII and H β lines (Figure 3.5); the NC of the H β line is broader. Schwope et al. (1996) discuss the reality of this broadening and its origins at length. They consider and eliminate blending with the weak HeII-Pickering lines because the broadening caused by this is not large enough. It is most likely that the broadening represents a greater spread of radial velocities in the H β NC emission region compared to the HeII NC emission region.

The broad component reaches radial velocities of over 1500 km s^{-1} , far in excess of those seen for the NC, and is at maximum redshift close to phase 0.0. This strongly suggests that the BC

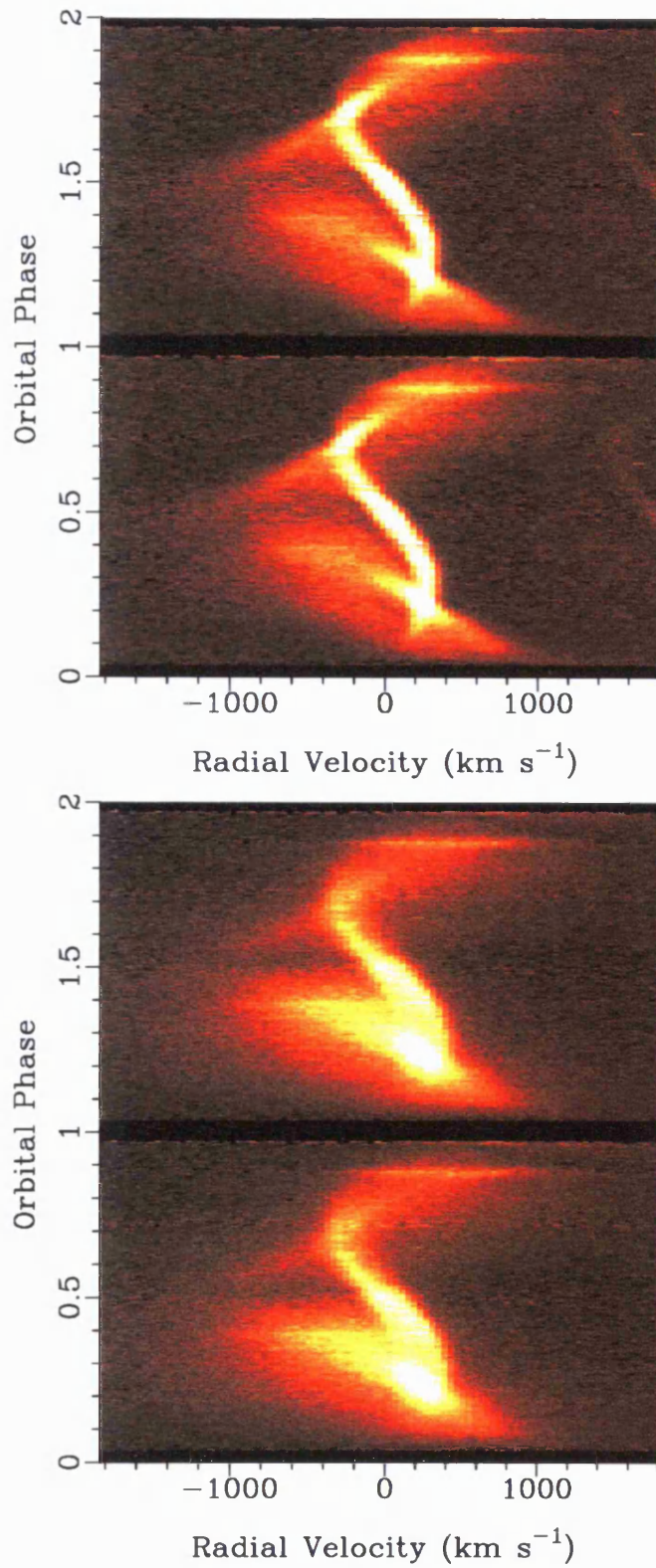


Figure 3.5: Detail of the trailed spectrogram showing the HeII $\lambda 4686$ (top) and H β (bottom) emission lines. The wavelength scale in these plots has been replaced by a radial velocity scale. Two cycles of each line are shown for clarity.

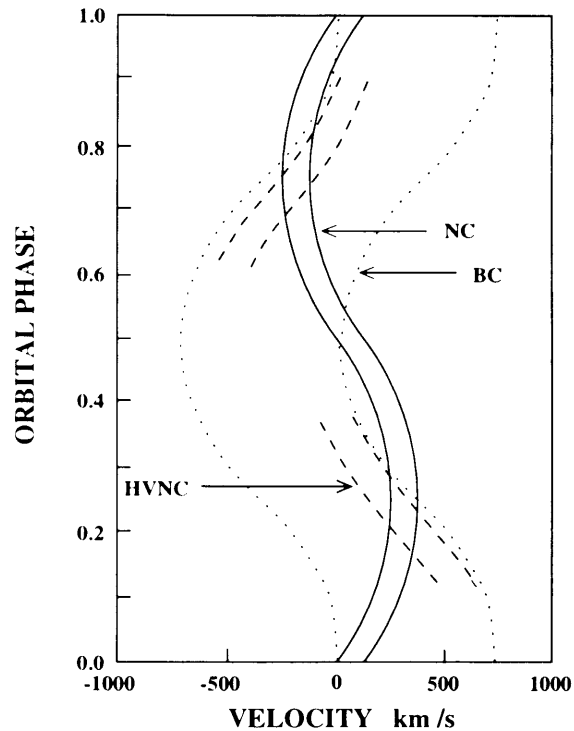


Figure 3.6: Schematic representation of the detailed trailed spectrograms in Figure 3.5, showing the location of the three components detected.

arises in the accretion funnel, where the stream material is approaching the white dwarf surface approximately radially and is travelling at velocities $\gg 1000 \text{ km s}^{-1}$ (having undergone much of its gravitational acceleration).

The high-velocity narrow component is only visible during the phase intervals $0.1 < \phi < 0.4$ and $0.6 < \phi < 0.8$. The radial velocity variations of the HVNC do not possess the smooth sinusoidal shape of the other two components. If these variations are extrapolated to the phases where the HVNC is not detected, this suggests that the maximum radial velocity of this component may be even larger than that of the BC. Such a conclusion would indicate that the HVNC arises deeper in the white dwarf's potential than the BC. A more complete picture of the HVNC will emerge from the modelling presented in Section 3.4.

A brightening of the line flux is apparent at phase 0.87–0.90 which is caused by the process of normalising the spectra to the continuum level. The light curves in Figure 3.3 demonstrate that an absorption dip *in the continuum flux* is present at this phase. When the spectra at this

phase are normalised they are therefore multiplied by a larger factor because of the reduced continuum flux. This has exaggerated the brightness of the line emission seen in Figure 3.5. It must be concluded from this that the line emission region is separate from the emission region which dominates the continuum, otherwise the line flux would be diminished as well. A similar conclusion may be drawn from the spectral behaviour as the system goes into eclipse where there is evidence for a similar brightening of the line emission once the continuum flux has dropped after phase 0.96. This leads to the further conclusion that the continuum arises close to the polecap while the bulk of the line emission arises further away from the white dwarf. These conclusions will be supported by the results of the line modelling presented in Section 3.4.2 below.

3.3.4 Emission line velocity curves

In order to investigate the radial velocity variations of the three line components multiple Gaussians were fit to the emission lines. Two steps were required to adequately fit the data. In the first stage the spectra were folded into 25 phase bins. On each folded spectrum the approximate locations of each component were marked by eye. Although this is not a very objective method, it was found that automatic Gaussian fitting routines had difficulty in producing a sensible fit when the line components cross each other. The advantage in ‘fitting’ by eye is that knowledge of the previous and following line profiles can be taken into account when unraveling a confused line profile. Automatic routines always deal with spectra on an individual basis and can therefore misinterpret a complex profile. Only the narrow component displayed a clear sinusoidal variation so the approximate positions for the narrow component were fitted by a sine curve with a fixed period of 1.0.

For the second stage the spectra were folded into 100 phase bins and fit by a multiple-Gaussian fitting routine. This routine uses a χ^2 minimisation technique to obtain the best fit to the data. The starting positions for each component were obtained by interpolating visual estimates for the BC and HVNC and the sine fit to the NC to the phase of each folded spectrum. The width of the NC and HVNC were fixed but the width of the BC was allowed to vary freely in the fit. Table 3.2 gives the limits of the regions used in fitting the HeII and H β lines, the starting width of the BC and the fixed widths of the NC and HVNC. To obtain these widths, fits in which

the widths were allowed to vary freely were made to spectra where the three components are well-resolved (e.g. at $\phi \simeq 0.1$ and 0.3). A visual inspection was made of the resultant fits to each of the 100 spectra, any for which the fit was poor were repeated manually to improve the fit. ‘Poor’ fits were obtained because the fitting was still confused by overlapping lines, because a fit to three components was made when only two were actually visible or for other reasons.

| | HeII $\lambda 4686\text{\AA}$ | H β $\lambda 4861\text{\AA}$ |
|---------------------|----------------------------------|---------------------------------------|
| Fit range | 4580–4792 \AA | 4751–4971 \AA |
| Fixed NC/HVNC width | 2.0 \AA | 3.8 \AA |
| BC start width | 11.4 \AA | 11.8 \AA |

Table 3.2: Input parameters for the multiple Gaussian fitting.

The results for the radial velocities obtained by this method are shown in Figure 3.7. The smoothest radial velocity variations are seen in the NC. A sine curve was fit to the NC radial velocities in the phase interval $0.285 < \phi < 0.665$. Outside of this phase range the radial velocity of the NC is poorly defined due to confusion with other components. The results of this fit for the two lines are given in Table 3.3. These confirm the qualitative statements made earlier; the mean velocity amplitude is 312 km s^{-1} and zero velocity is reached at phase 1.01/1.04.

| | HeII $\lambda 4686\text{\AA}$ | H β $\lambda 4861\text{\AA}$ |
|--------------------|----------------------------------|---------------------------------------|
| Semi-amplitude | $306 \pm 6 \text{ km s}^{-1}$ | $318 \pm 8 \text{ km s}^{-1}$ |
| Zero crossing | $1.01 \pm 0.01\phi$ | $1.04 \pm 0.01\phi$ |
| γ -velocity | $-12 \pm 12 \text{ km s}^{-1}$ | $-66 \pm 13 \text{ km s}^{-1}$ |
| Period (fixed) | 1.0 | 1.0 |

Table 3.3: The best-fit parameters of sine curves fitted to the narrow component radial velocities for the HeII and H β emission line. Errors quoted represent the 1σ confidence ranges.

The trailed spectrograms in Figure 3.5 clearly show that the NC is not present in the region $0.7 < \phi < 0.9$. Consequently, the Gaussian fits to the NC deviate strongly from the trend predicted by the sine fit because the fitting routine erroneously fits the NC gaussian to the HVNC, not the NC. The absence of the NC is surprising because the relative phasing of the components suggests that the NC ought to be well-resolved at these phases, without any confusion with other components. An explanation for the absence of the NC based upon modelling results is

presented in Section 3.4.

The radial velocity variations of the BC and the HVNC are not as well constrained as those of the NC. The BC still appears to follow an approximately sinusoidal shape but the HVNC does not. In the phase intervals $0.1-0.3\phi$ and $0.5-0.8\phi$ the HVNC displays the same rate of change of velocity as the BC, but with a velocity offset by $200-300 \text{ km s}^{-1}$. This suggests that the HVNC is actually just a portion of the BC, arising from increased luminosity in the fastest portions of the BC emission region. Confirmation of this conjecture can only come by modelling the line emission fully.

The orbit of the secondary star is very stable, and hence so too is the radial velocity of the secondary. The zero crossing of any line emission which arises on the secondary is therefore expected to occur at phase 0.0 (the eclipse fixes this phase very accurately with respect to the secondary). The location of the narrow components of both lines are well defined, yet the zero crossing occurs significantly later than phase 0.0. The conclusion drawn from this is that the narrow component is not symmetric about the line of centres of the two stars. Mapping of the Na line emission from the secondary in AM Her has been carried out by Southwell et al. (1995). They have also found that the line emission on the secondary surface facing the white dwarf is not symmetrical about the line of centres of the two stars. The side of the secondary which leads the orbital motion is significantly less bright than the trailing side. This probably arises due to shadowing of the leading side by the accretion stream. It is just such an asymmetry that would cause the 0.02ϕ delay in the zero crossing detected here. The modelling presented later in this chapter also demonstrates that the narrow component is not emitted evenly across the secondary star's surface.

3.3.5 Mass estimate

If the radial velocity of the narrow component can be related to the orbital velocity of the secondary it is possible to constrain the mass ratio of the stellar components. Kepler's Law can be used to derive a relation between the mass ratio and the system parameters M_1, i and P for a circular orbit:

$$\frac{GM_1(1+q)}{4\pi^2} = \frac{A^3}{P^2} \quad (3.1)$$

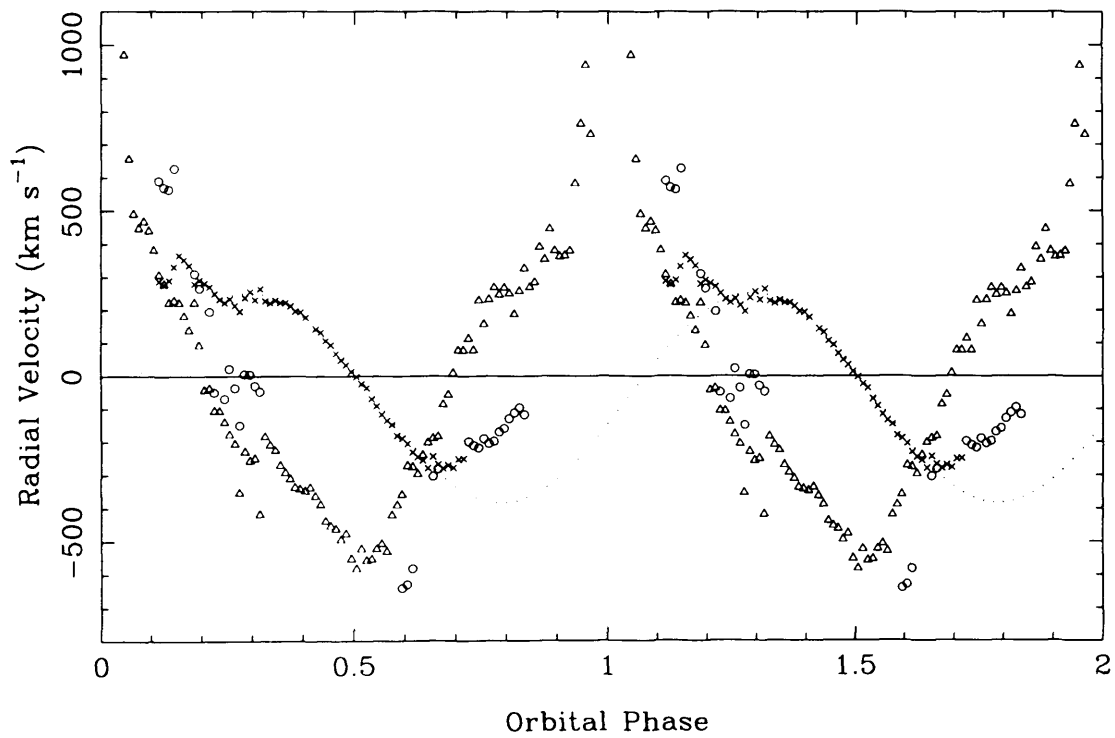
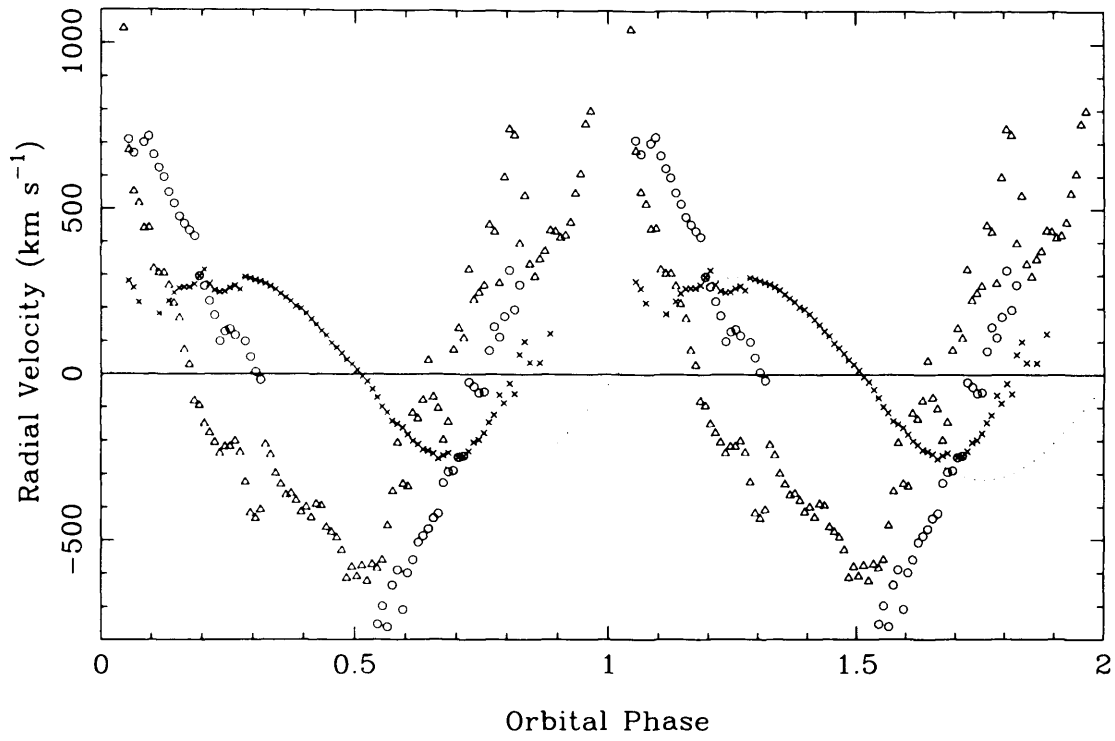


Figure 3.7: Results of the Gaussian fits to the AAT emission lines. Radial velocities for the three components detected in the HeII $\lambda 4861\text{\AA}$ (top) and H β (bottom) emission lines. Crosses represent the narrow component, triangles the broad component and circles the high velocity narrow component.

where A is the binary separation, P is the period in seconds and q is the mass ratio M_2/M_1 . The *observed* radial velocity amplitude, K'_2 , is given by

$$K'_2 = \frac{2\pi A}{P(1+q)} \sin i. \quad (3.2)$$

Combining Equations 3.1 and 3.2 gives the relation:

$$\frac{M_1 \sin^3 i}{(1+q)^2} = \frac{K'^3_2 P}{2\pi G} \quad (3.3)$$

from which the mass ratio for the system can be derived. This relation known as the ‘mass function’, having the dimensions of a mass, and is a directly observable quantity.

Unfortunately the observed radial velocity K'_2 does not represent the radial velocity of the secondary itself (K_2), because the centre of light for the narrow component is very unlikely to be at the same distance from the primary as the centre of mass of the secondary ($R_{COL} \neq R_{COM}$). To account for this a factor must be included to account for the effective distance of the emission from the centre of mass of the secondary (e.g. Horne & Schneider 1989, Rosen et al. 1987). If the narrow component emission is located at an effective distance γR_L from the secondary’s centre of mass (where R_L is the Roche lobe radius in units of the binary separation), then

$$2\pi G M_1 \sin^3 i = \left[\frac{K'_2}{1 - \gamma(1+q)R_L} \right]^3 (1+q)^2 P. \quad (3.4)$$

When γ is zero $R_{COL} = R_{COM}$, the additional term drops out and Equation 3.4 reduces to Equation 3.3. When γ is one, the centre of light is effectively at the inner Lagrangian point ($R_{COL} = R_L$). The Roche lobe radius R_L can be obtained from q using the empirical relation given in Eggleton (1983).

For given values of K'_2 , P , i and M_2 Equation 3.4 allows M_1 to be calculated over a range of values for γ . The inclination does not strongly affect the result; inclinations in the range 70–90° only alter the primary mass by 0.05 M_\odot . K'_2 and P are both well defined, so the dominant source of uncertainty will be the secondary mass. To obtain M_2 it is usual to assume that the mass-radius relationship of main sequence dwarfs holds for the late-type secondary stars in AM Her systems. Thus for a given R_L the secondary mass M_2 can be uniquely defined.

Figure 3.8 shows M_1 as a function of γ for $M_2 = 0.22M_\odot$ and $M_2 = 0.14M_\odot$, with $K'_2 = 306 \text{ km s}^{-1}$, $P = 7501 \text{ s}$ and $i = 80^\circ$. The two values of M_2 were selected to be representative of

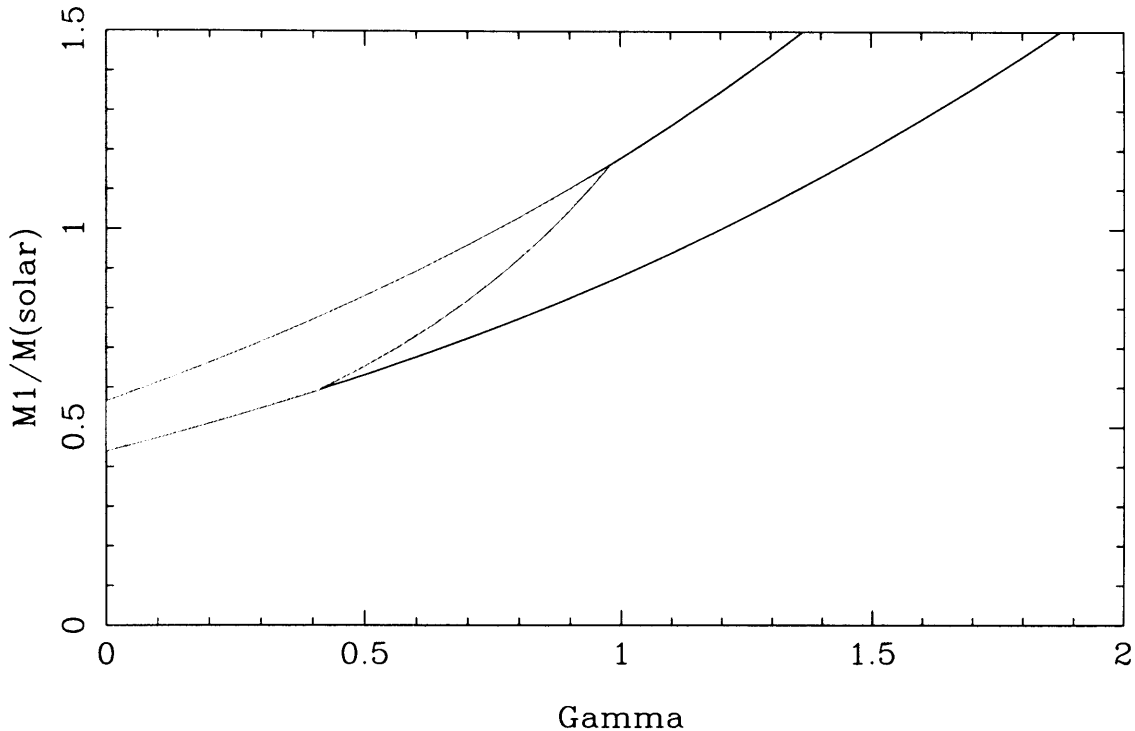


Figure 3.8: The primary mass as a function of centre of light for the narrow emission line component (γ). The two lines shown represent a secondary star mass of $0.22M_{\odot}$ (upper line) and $0.14M_{\odot}$ (lower). The region that satisfies the mass estimate derived from the optical eclipse is shaded.

the spread in values obtained by several different main sequence mass-radius relations (Biermann et al. 1985, Caillault & Patterson 1990). There are a number of additional constraints upon the allowed values of M_1 and γ . The narrow component is not detected during the eclipse and therefore must be confined to the stream or the surface of the secondary facing the primary (i.e. $\gamma > 0.0$). This gives a lower limit to M_1 of $0.45M_{\odot}$ or an upper limit on q of 0.4. The Chandrasekhar limit ($M_1 < 1.4$) implies that the emission cannot come from further than $0.75R_L$ along the stream from the Lagrange point.

Glenn et al. (1994) derive a value for the mass ratio of $q = 0.36^{+0.41}_{-0.15}$ based on eclipse duration measurements obtained from high speed photometry. The duration of totality Δt_{tot} and the first-to-last contact interval Δt_{FL} enables q to be determined by the method described in Biermann et al. (1985). The photometry obtained at the AAT in June 1993 (presented in Chapter 2) also allows the mass to be derived in this manner. To determine Δt_{tot} and Δt_{FL} a linear fit was performed to the rapid and gradual ingresses and egresses, to the flat-bottomed portion

of the eclipse and to the phase interval $0.94\text{--}0.96\phi$ for each of the four eclipses observed. The intersection of the fit to the rapid ingress with the pre-eclipse interval and the gradual ingress were taken to be the beginning and end of the ingress respectively. The intersection of the fit to the rapid egress with the eclipse minimum fit and the gradual egress was similarly taken to be the beginning and end of the egress. By this method values of $\Delta t_{tot} = 572 \pm 3.0$ s and $\Delta t_{FL} = 592 \pm 3.0$ s were obtained.

Unfortunately the error in the mass determination from this method is dominated by the uncertainty in the inclination ($i = 80^\circ \pm 5^\circ$). As a result no improvement can be made to the mass estimate obtained by Glenn et al. (1994); the estimate derived from the AAT data is $q = 0.36^{+0.41}_{-0.15}$. However, the photometric data do place tighter limits on q than the radial velocity data. The photometric constraints are represented in Figure 3.8 by the shaded area. For the mass estimates derived from the NC radial velocity and the photometry to be consistent with each other then the emission is confined to the surface of the secondary with $0.0 < \gamma < 0.85$ and $0.45 < M_1 < 1.1M_\odot$.

An independent estimate for γ would clearly be valuable in constraining the white dwarf mass in this system. It is hoped that the modelling of the emission line variations presented at the end of this chapter will eventually allow some constraints to be placed upon γ and thereby better constrain the mass. As it stands at the moment, it is not possible to confirm whether HU Aqr evolved into the period gap (in which case $M_{wd} > 0.8M_\odot$) or was born in the gap (as explained in Section 1.5.2).

3.3.6 Phase resolved FORS spectra

All of the FORS spectra obtained in the five orbital cycles of observation have been folded and binned to produce 10 phase-resolved spectra. The sequence of spectra over one orbital cycle is shown in Figure 3.9. The eclipse spectrum can be seen as the topmost spectrum. This is basically the spectrum of the secondary star, though the low luminosity and y -axis scaling makes the spectral features hard to detect in this figure. This spectrum is discussed at length in the next section.

Figure 3.9 demonstrates that the cyclotron features identified in the mean spectrum (Figure 3.1)

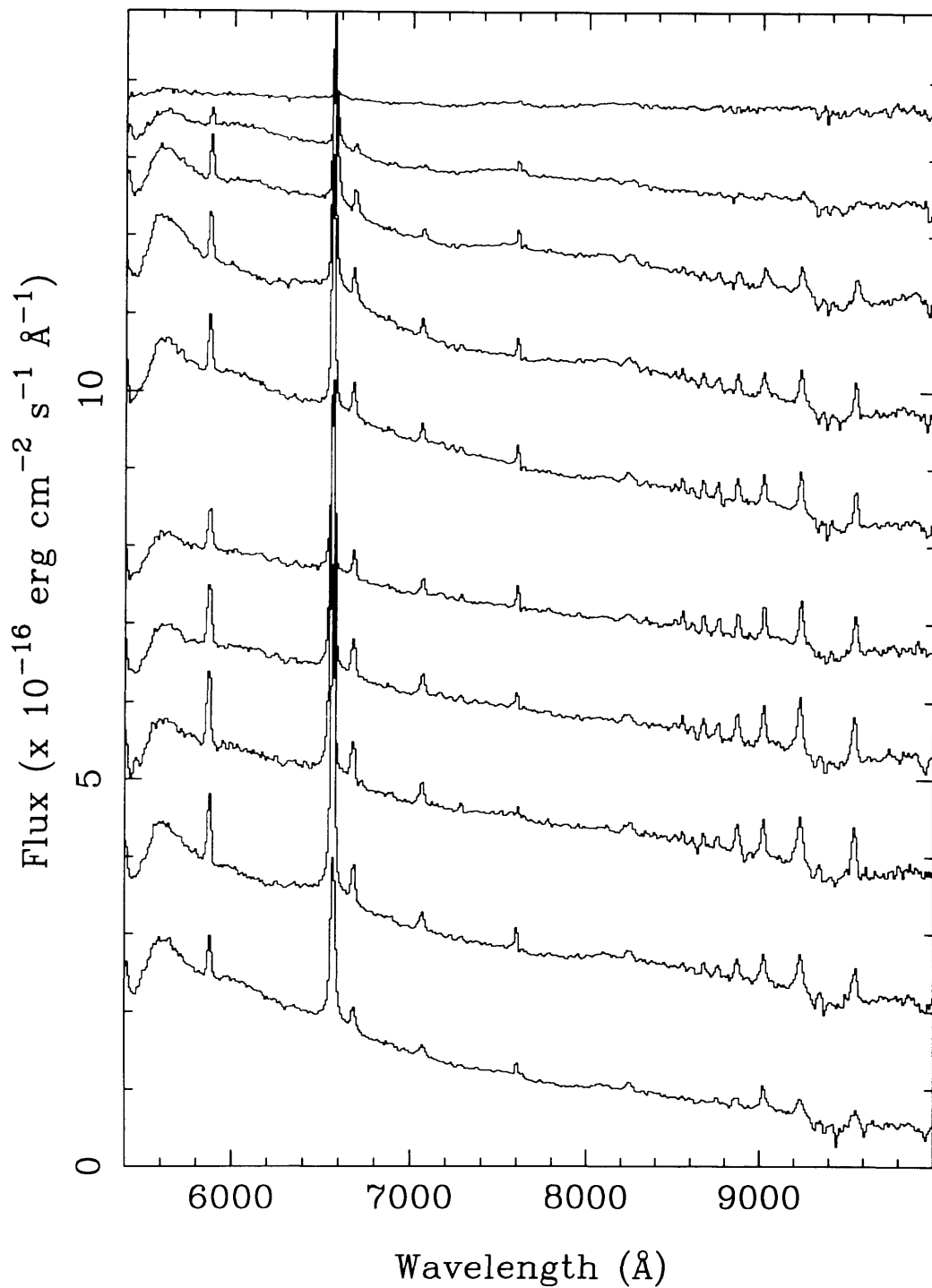


Figure 3.9: A sequence of ten folded FORS (red) spectra. Time runs down the figure, with phase 0.0 (eclipse) at the top. Each spectrum has been vertically shifted by $1.5 \times 10^{-16} \text{ erg cm}^{-2} \text{ s}^{-1} \text{ \AA}^{-1}$.

at 6500Å and 8200Å peak around phase 0.2 and 0.7. This is fully consistent with the expectations from cyclotron beaming discussed in Section 1.2.3; the cyclotron flux should peak at approximately 20° from the perpendicular to the field lines. Careful analysis of the H α line in this figure demonstrates that the radial velocity variations of the *peak* (i.e. narrow component) of the line are consistent with the results from higher resolution spectra; the peak is at maximum blueshift at orbital phase 0.25 and at maximum redshift at phase 0.75.

3.3.7 Secondary spectrum and the distance to HU Aqr

Both the photometry and spectroscopy confirm that the eclipse seen in HU Aqr is not total at optical wavelengths. It can be assumed that the mean FORS spectrum of HU Aqr from the flat-bottomed portion of the eclipse arises predominantly from the secondary star. The spectrum of HU Aqr from the phase interval $0.99 < \phi < 1.03$, shown in Figure 3.10, displays the TiO bands and steep rise to the red typical of M-dwarfs. There are no emission line features evident in this spectrum, which reinforces the belief that the secondary is the most important source of red flux during the eclipse.

In order to determine the spectral type of the secondary, comparisons with template spectra of M2 to M8 dwarf stars were performed (provided by J. Kirkpatrick, see also Kirkpatrick, Henry & McCarthy 1991). Each template spectrum was scaled to minimise the deviation between the observed spectrum and template. This deviation was measured using the χ^2 statistic. The spectral type with the smallest χ^2 value indicates the most likely spectral type for the secondary. An M4.5V spectrum was found to give the best fit to the observed spectrum, but the M5V spectrum also gave a very good fit, so the spectral type is estimated to lie in the range M4.5V–M5V. The M4.5 template spectrum is overlaid onto the eclipse spectrum in Figure 3.10 as a dashed line. The poor match to the data around 7600Å is probably due to inadequate correction for telluric atmospheric features in this region. The fits to the template spectra were repeated including an additional linear term, to crudely allow for any other sources of emission. No change to the fit was detected.

The spectral type of the M dwarf in HU Aqr was also measured by Glenn et al. (1993). They found it to be in the range M3V to M5V by a similar technique. It is possible that the slight discrepancy between their results and those presented here arises due to contamination of their

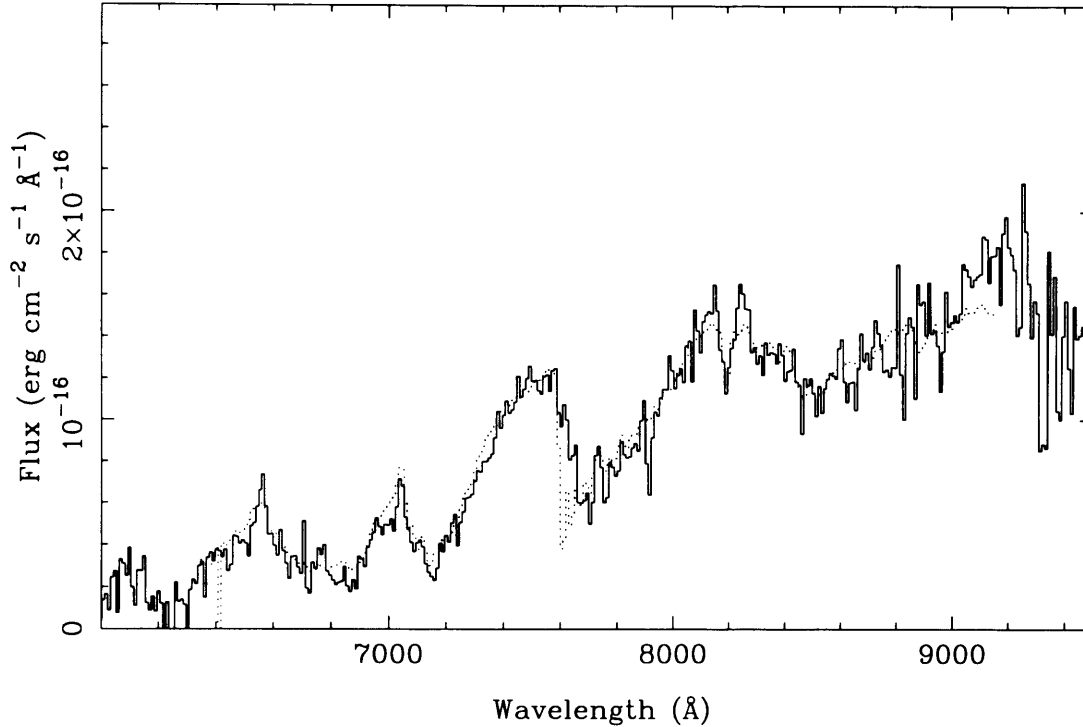


Figure 3.10: The eclipse spectrum of HU Aqr (solid line) with the best-fit M4.5 star spectrum superimposed (dotted line).

spectrum by flux from outside the phase range of the eclipse. Comparison of the spectrum in Figure 3.10 with that in Figure 3 of Glenn et al. shows their spectrum to have more blue flux and stronger hydrogen line emission. Such a difference would be expected in the presence of contaminating flux from the stream, which emits blue continuum and strong emission lines. Such contamination could account for a fit to an earlier type star.

Knowledge of the secondary's spectral type allows the spectroscopic distance to HU Aqr to be determined. The observed R-band magnitude during eclipse derived from the AAT photometric data is $m_R = 18.4 \pm 0.1$. According to Kirkpatrick & McCarthy (1994), the absolute R-band magnitude of an M4.5–M5 star lies in the range 11.9–12.5. From this the distance to HU Aqr is found to be 175 ± 25 pc. The error quoted corresponds to the uncertainty in the spectral type measurements which is expected to be the major source of error. The improved spectral type measurement allows a tighter constraint on the distance than the previous measurement of 191^{+189}_{-115} by Glenn et al. (1994).

3.3.8 Magnetic field strength

Inspection of phase-resolved FORS spectra at higher time resolution (not shown) reveals that the cyclotron features at 6500Å and 8200Å are clearly detected only over the phase ranges $\phi = 0.20$ – 0.30 and $\phi = 0.625$ – 0.775 . The peaks can also be detected during the gradual egress ($0.04 < \phi < 0.05$), just after the polecap emerges from behind the limb of the secondary. At this phase the polecap dominates the emission with little or no contamination from the bright stream. The mean positions of the cyclotron harmonics, obtained by Gaussian fitting to those portions of the spectra, were found to be $8200\text{Å} \pm 100\text{Å}$ and $6550\text{Å} \pm 100\text{Å}$.

The magnetic field strength of the accretion region can be determined from the wavelengths of the two peaks. Equation 1.6 gives the relationship between the line frequency ω_n , harmonic number n and field strength B :

$$\omega_n = n \times \frac{eB}{m_e c} \quad (3.5)$$

From this equation it is found that the peaks are consistent with the 4th and 5th harmonics of the cyclotron emission from a 34 ± 1 MG field.

These results have been used to predict the location of the 3rd and 6th cyclotron harmonics from HU Aqr. The 3rd harmonic is located at 11,000Å and therefore becomes lost in our spectra due to the atmospheric distortion beyond 10,000Å. The 6th harmonic should be located at $5500 \pm 200\text{Å}$. Reduction errors distort the spectra below 5600Å, but the red wing of the peak appears to have been detected between 5600Å and 5700Å. This wing shows flux variations with phase which are identical to the flux variations seen in the 4th and 5th harmonics (peak flux around phase 0.2 and 0.7). A Gaussian fit to this feature shows it to be consistent with a peak centred at 5500Å. The field measurement of 34 ± 1 MG derived from these three cyclotron peaks is fully consistent with the 7–50 MG observed range of strengths for accretion regions in AM Her systems (Bailey 1995).

3.4 Modelling the accretion stream emission

The past few years have seen the development of improved models for the accretion stream by the inclusion of more complex and physically realistic plasma-field interactions. One such model,

developed by G. Wynn, A. King and K. Pearson of the Astronomy Group at the University of Leicester, has successfully been applied to several intermediate polars (see Wynn & King 1995 and King 1993). The high signal-to-noise photometric and spectroscopic data from HU Aqr provide the ideal opportunity to test these models further. In this section a method for deriving the accretion stream brightness distribution using a Maximum Entropy method and a Genetic Algorithm for optimisation are presented.

3.4.1 Eclipse profile model

The first task undertaken was to model the eclipse profiles of HU Aqr obtained during the AAT observation presented in Chapter 2. As the secondary sweeps across the stream during the gradual ingress and egress to the eclipse the brightness distribution of the stream is revealed. The accretion stream in HU Aqr contributes a large portion of the optical flux detected, as is demonstrated by the height of the gradual transitions (Figure 2.4), and thus the stream brightness structure ought to be revealed at higher signal-to-noise in this system than in any other.

The initial code for this model was kindly provided by P. J. Hakala, and consisted simply of emission from the accretion stream and pole. The stream was described as a simple arc in the orbital plane. Hakala (1995) describes the application of this model to the photometric observations of HU Aqr obtained from the NOT (first presented in the discovery paper for HU Aqr, Hakala et al. 1993). This work is extended here by including a more realistic stream trajectory derived from the particle codes of Wynn et al. and by applying the model to the better data from the 1993 AAT observation. In addition to the descriptions given below, further details of the fitting method and some of the relevant issues associated with the genetic algorithms can also be found in Hakala (1995).

The accretion flow is simulated using an amended particle code first developed by Whitehurst (1988), in which the plasma-magnetic field interaction is via a velocity-dependent drag force. This prescription assumes the accretion flow to be fragmented into large, diamagnetic blobs. There is ample evidence for the existence of such blobs in HU Aqr and other AM Her systems from the soft X-ray excess (§1.2.3, §4.4.3) and from flickering during absorption dips (§2.5, §4.4.1). These blobs experience a surface drag arising from the production of Alfvén waves as

the blobs force their way through the white dwarf's magnetosphere.

Fitting of the eclipse profile is achieved by adjusting the brightness of the stream along the path predicted by this particle code. The stream is modelled by 100 equally spaced points of variable brightness, while the pole brightness is fixed to a pre-determined value. This model is then rotated and for each phase angle the visibility of each point is found by comparing its position against that of the Roche-filling secondary. The brightnesses are changed in order to minimise:

$$F = \sum_{j=1}^k \left(\frac{model_j - flux_j}{\sigma_j} \right)^2 + \lambda \sum_{i=1}^n p_i \log \frac{p_i}{m_i} \quad (3.6)$$

where k is the number of data points, n is the number of free parameters, p_i are the brightness fractions of the individual points within the stream and m_i is the default level for p_i . The local geometric mean is used as the default level (i.e. $m_i = \sqrt{p_{i-1}/p_{i+1}}$), instead of the geometric mean of all pixel values as is conventional, to allow the appearance of brighter regions needed to fit the data (Cropper & Horne 1994). The terms $model_j$, $flux_j$ and σ_j are respectively the computed brightness, observed brightness and error for a given orbital phase. The first expression in Equation 3.6 is therefore just the χ^2 value for the fit and the second expression is the maximum entropy function. The Lagrangian multiplier λ is selected to obtain the smoothest possible fit to the data; by increasing λ the importance of the smoothness of the fit is increased, by decreasing λ the importance of the noise in the data is increased.

Genetic algorithms

The more commonly used n-dimensional optimisation algorithms often have problems with local minima in the fitness criterion within a given parameter space. Genetic algorithms, although not guaranteed to find the global minimum, do have the capability to escape from such local minima. An introduction to genetic algorithms is given in Beasley et al. (1993a, 1993b). The genetic algorithm used here works in the following manner:

1. A set of 200 random solutions to the problem is generated.
2. For each solution, the 'fitness factor' is found. In this case, that is given by F in Equation 3.6.
3. The solutions are ranked in order of 'fitness' (in order of goodness of fit to the actual data).

4. The population members that will be used to create the next set of solutions are chosen. There are a number of different ways in which each of these ‘parents’ can be selected, all based on the same principle; the parent is chosen from the population at random but weighted toward those members with a high fitness factor. In this case the rule for choosing parents is:

$$S_i = \text{INT}\left(\frac{-N_{pop}}{10} \log(\text{RND}(0, 1))\right) + 1 \quad (3.7)$$

where S_i is the rank number of the population member to be added to the mating pool, N_{pop} is the population size and $\text{RND}(0,1)$ indicates a random number between 0 and 1. Two parents are required to create one offspring, therefore this equation is evaluated $2 \times N_{pop}$ times to obtain enough pairs of parents to regenerate the population

5. The next set (‘generation’) of solutions is created. Each parameter of the ‘child’ solution is taken either from one or another of the parent solutions. This mechanism is known as ‘uniform crossover’. The effect of mutation is then included. Each parameter of the child solution is allowed to change, but only at a small probability. It is this random factor which can enable the genetic algorithm to avoid becoming trapped in local minima.

Clearly it is not possible to set a convergence limit using this process. The algorithm is simply allowed to run for a number of generations before stopping. In this case the population does not change much after 400 generations, so 500 generations was chosen for the end of fitting. The research into genetic algorithms is still in its infancy and so there are as yet no guidelines for selection of the population sizes, number of generations, crossover methods or mutation methods. The values used here have been determined on a trial-and-educated-guess method, so could therefore be open to improvement.

The stability of the model to minor changes in the stream trajectory was tested by Hakala (1995). He found little or no change to the brightness profiles that were being obtained when the radii of the stream arcs was varied. This was the case only if the arc was not too small or too long to produce the observed stream ingress duration (i.e. so long as the y -extent was approximately correct, see Figure 2.9). It is unlikely therefore that strong constraints on the stream trajectory can be found by this method. Hakala also found the fitting algorithm to be highly robust; changes to the initial stream brightness elements do not cause a change in the eventual solution obtained. This often not the case for other fitting algorithms.

Results

The model was applied to the four eclipses observed during the AAT observation of HU Aqr in June 1993. Similar stream brightness profiles were derived for each eclipse; one such profile is displayed in Figure 3.11, along with the best fit to the eclipse profile. The brightness profile is distinctly non-uniform. There is no evidence for emission from the stream over much of the interval $R_i = (0.2 - 1.0)S$, where R_i is the distance of the i^{th} element of the stream from the white dwarf and S is the white dwarf surface/ L_1 point separation. The exception to this is a brightening of the stream over a short interval at $R_i \simeq 0.7$. Ferrario et al. (1989*b*) have suggested that the stream becomes heated as it threads onto the magnetosphere at about this distance. The emission detected here could be the result of such heating.

Close to the white dwarf ($R_i \simeq 0.22$) the stream brightness increases sharply and remains bright down to the white dwarf surface. Such a sudden increase in brightness is difficult to interpret since it suggests an equally sudden heating of the stream. The likely heating mechanisms for the stream, such as X-ray heating from underneath by the pole or collisional excitation, ought to display a more gradual dependence upon radius from the white dwarf. These results are discussed in more detail in conjunction with the line emission brightness distributions derived in the next section.

3.4.2 Emission line model

The model for the accretion stream was extended by including the velocity information for each point along the predicted stream trajectory. This stream velocity information is readily available since the model for the stream trajectory provided by Wynn et al. already uses the particle velocity to find the drag force. By converting the calculated radial velocity of each point along the stream to its Doppler-shifted wavelength, the emission line profile predicted by the model can be created. The model line profile at each orbital phase can then be fitted to the actual line profiles by changing the brightness of the individual points along the stream in exactly the same fashion as for the eclipse profile model.

In order to test the code at an intermediate stage in the development of the model, a simplified scenario was used whereby the only portion of the system included was the stream. No self-

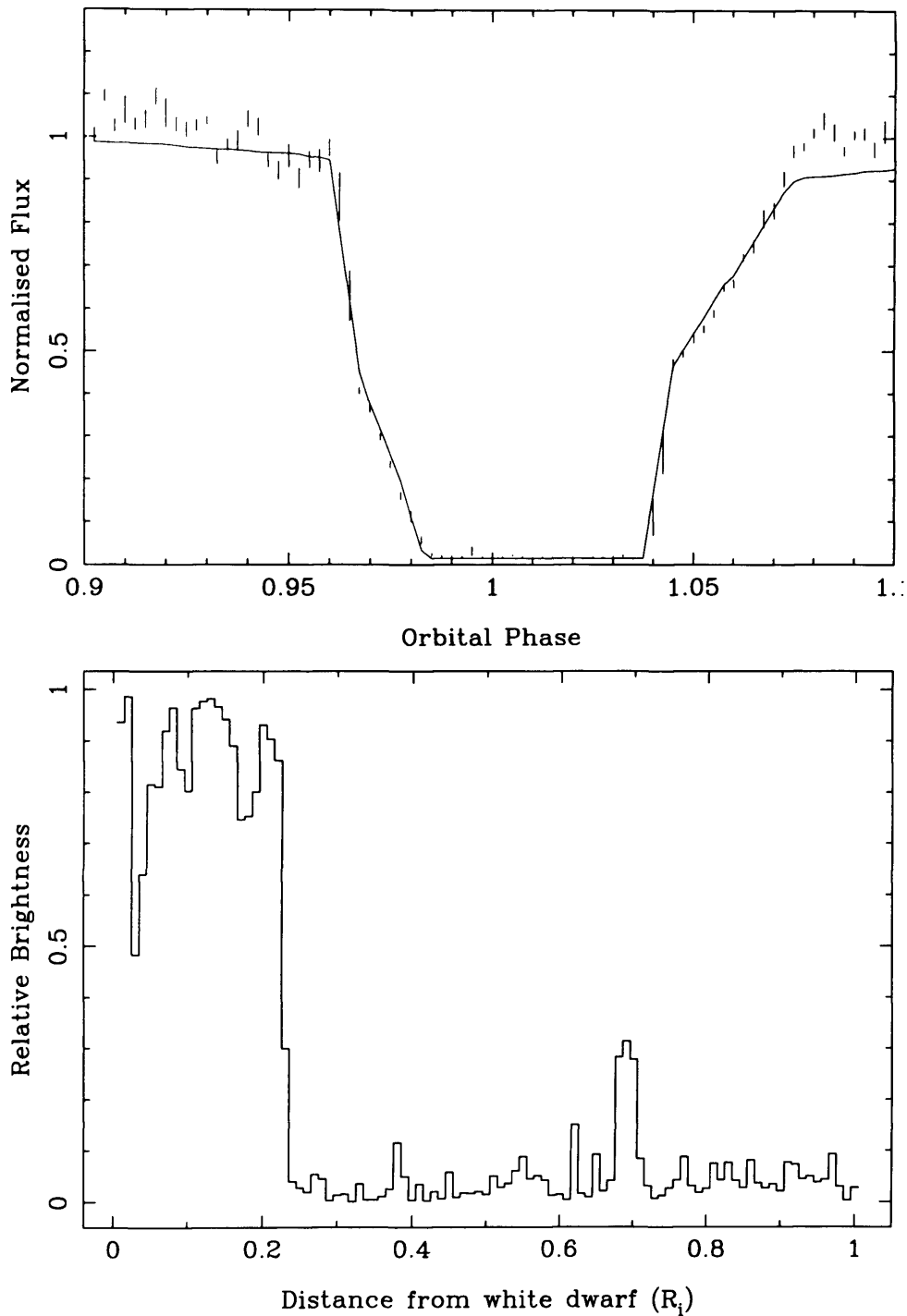


Figure 3.11: Example of the results from the fits to the eclipse profiles of HU Aqr obtained at the AAT in June 1993. The upper panel shows one eclipse (error bars) and the best fit to that profile (solid line). The lower panel shows the corresponding brightness distribution as a function of position along the stream, with the white dwarf at the left and the first Lagrange point at the right.

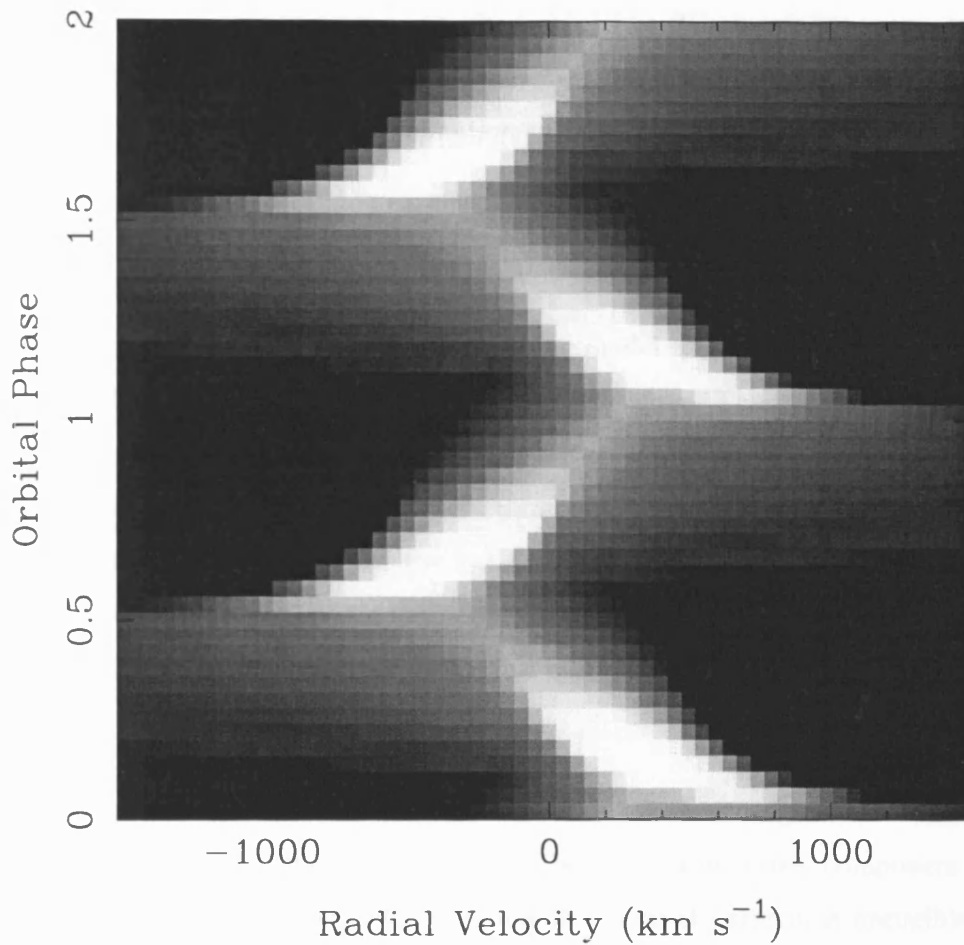


Figure 3.12: Simple trailed spectrogram produced by rotating a uniformly bright accretion stream. Note the apparent decrease in the broad component flux at phase 0.5.

occultation by the stream or occultation from the secondary was included, nor is there any actual fitting of the data; the stream is uniformly bright along its entire length. The trailed spectrogram from this very crude model surprisingly provided a simple explanation for a feature in the trailed spectrogram which had not been understood up to that point. This feature was the significant decrease in the flux of the broad component at conjunction of the primary star ($\phi = 0.5$, see Figures 3.3 and 3.4). The predicted trailed spectrograms from the simple 'rotating stream' model (shown in Figure 3.12) also display a marked decrease at this phase.

Since occultations have not been included in the model, the flux decrease must be caused by geometric factors alone. At phase 0.25 and 0.75 the accretion stream is viewed at its closest to side-on. Since most of the motion is perpendicular to the line of sight, the mean velocity will

be approximately zero with a minimum spread in velocity. As the stream rotates the spread of velocities will increase to a maximum at phase 0.5. The BC therefore *appears* to display a decrease in flux simply because it is smeared out over its largest range of velocities. Such an effect will clearly be strongest in high inclination systems like HU Aqr.

Results

The best-fit trailed spectrogram for the fully working model is shown in Figures 3.13 and 3.14, as applied to both the HeII and H β lines from the AAT data. The spectra have been binned so that the phase resolution of these trailed spectrograms is 0.04ϕ . The best-fit spectrograms display a good match with the data, but with a number of subtle differences which are discussed below. The brightness distributions for the line emission shown in Figure 3.15 do not resemble the brightness distributions derived for the photometry. This result was predicted from evidence provided by the absorption dip and eclipse ingress in the trailed spectrograms, as discussed in Section 3.3.3.

The region closest to the secondary ($R_i = 0.90 - 1.00$) is 2–3 times brighter than any other part of the stream. This portion of the stream clearly gives rise to the narrow component of the line profile. Over the interval $R_i = 0.65 - 0.90$ the line flux from the stream is negligible. Between $R_i = 0.60$ and the white dwarf surface at $R_i = 0.0$ there is significant line flux. This is clearly the origin of the broad component.

In comparison with the results of the fit to the eclipse profile, it is evident that the line emission extends further from the white dwarf than the continuum emission. Clearly this provides us with information about the different generation mechanisms for the two types of emission, but a full interpretation of this result awaits completion of the model. However, it is interesting to note that the line emission brightens at about the same distance from the white dwarf as the short peak in the R-band/BG39 flux. This would suggest that these two emission regions may be linked in some way; perhaps both are associated with the threading process.

Although the BC and NC can be reliably located in the brightness distribution, the HVNC has not revealed itself clearly. The phasing of the HVNC suggested that it might be located in a region between the BC and NC. The portion of the stream around $R_i = 0.50 - 0.65$ is slightly

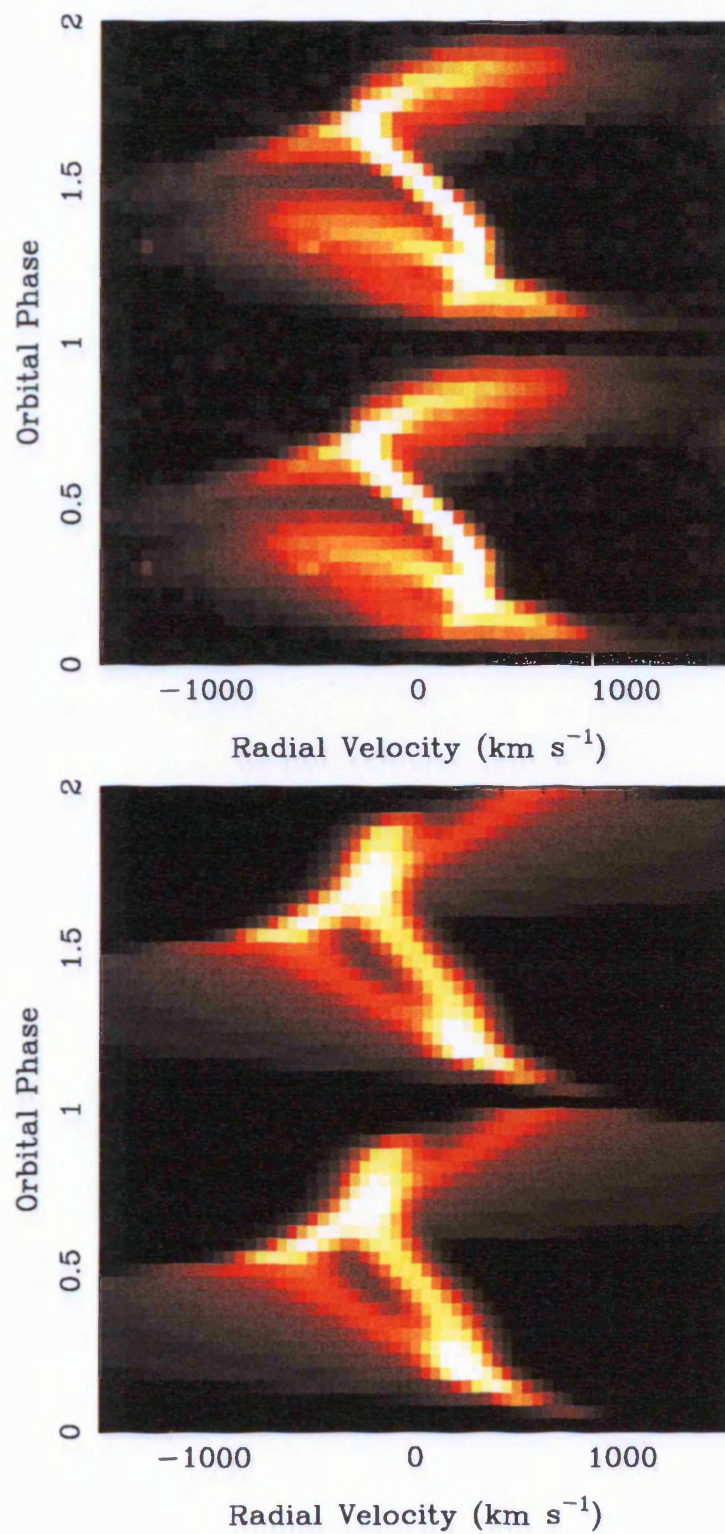


Figure 3.13: Results of fitting to the trailed spectrogram of the HeII $\lambda 4686\text{\AA}$ emission line. The upper plot shows the data, the lower panel shows the best fit. Residuals for this fit are shown in Figure 3.16 below.

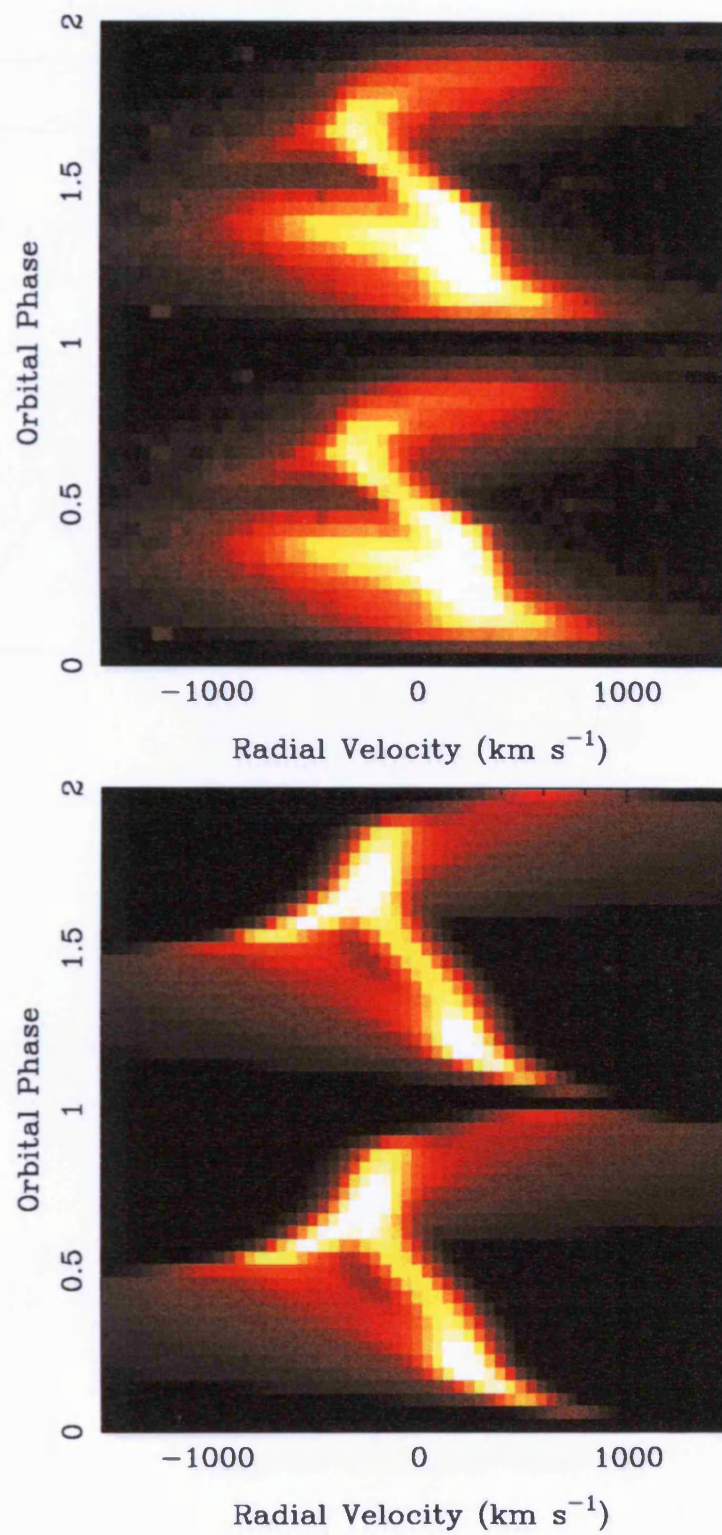


Figure 3.14: Results of fitting to the trailed spectrogram of the $H\beta$ ($\lambda 4861\text{\AA}$) emission line. The upper plot shows the data, the lower panel shows the best fit.

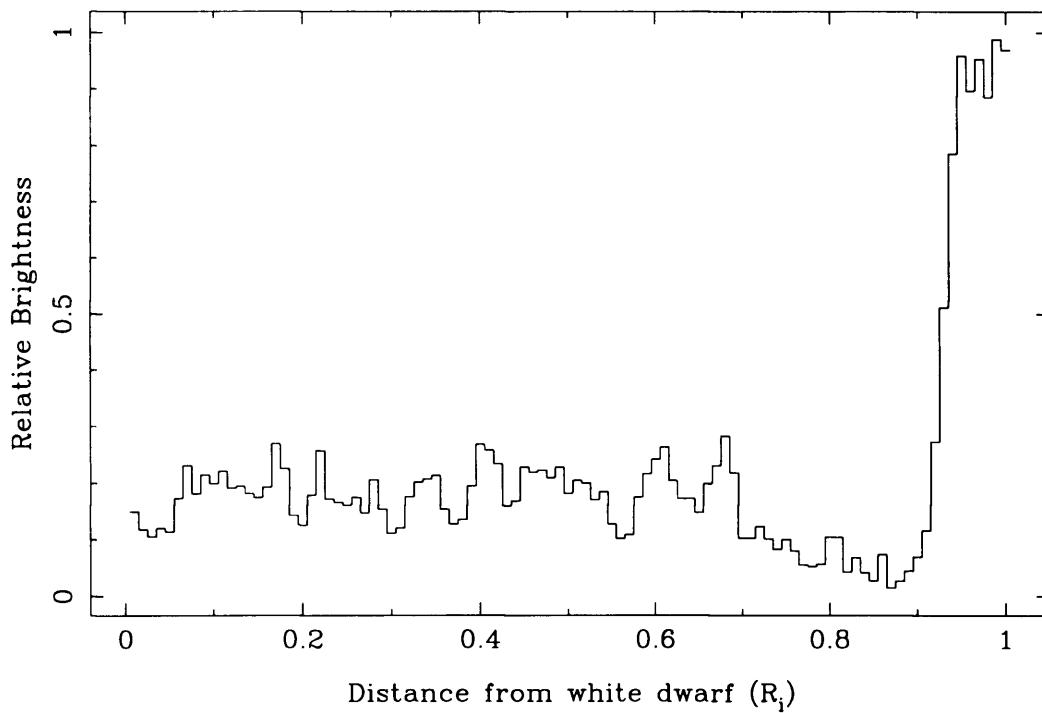
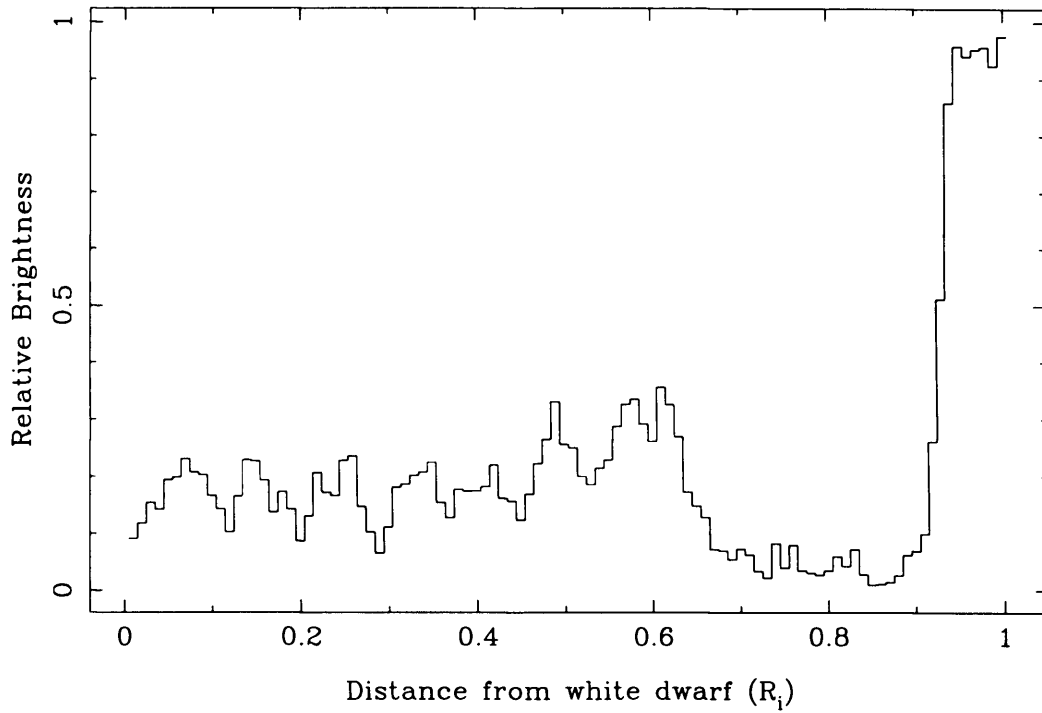


Figure 3.15: Brightness distribution of the accretion stream corresponding to the fit to the HeII emission line (top), shown in Figure 3.13, and to the $H\beta$ line (bottom), shown in Figure 3.14. As with the corresponding result for the eclipse data (Figure 3.11), the white dwarf is at left and the first Lagrange point is at right.

brighter (for the HeII fit) than the portions of the stream closer to the white dwarf. It may be that this is the location of the HVNC emission region. Confirmation of this is straightforward; the trailed spectrogram produced by just a portion of the stream can be created by setting the brightness of the rest of the stream to zero (i.e. by masking out the contributions from the rest of the stream). For instance, by setting the brightness of points outside the range $0.8 < R_i < 1.0$ to zero a spectrogram of the narrow component alone should be produced. Although this has yet to be undertaken, it is anticipated that the HVNC will probably emerge as a brighter portion of the BC mid-way along the stream and not really a separate emission region itself.

Subtle differences have been found between the model spectrogram and that obtained from the data, associated with the narrow component. Figure 3.16 shows the residuals in the fit (model–data) for the HeII line (the $H\beta$ residuals are similar). It can be seen that the narrow component in the model does not have a large enough radial velocity for the majority of the light curve. Because the velocity of the NC is dominated by its orbital velocity rather than the infall velocity, this suggests that the NC needs to be located further from the white dwarf. In the current models this is not possible since the secondary has not been included. By adding the secondary to the model it is confidently predicted that the bulk of this emission region will be located on the secondary star surface.

At phase 0.7–0.8 the narrow component can still be seen in the model spectrogram slightly blueward of the HVNC, but it is not apparent in the data spectrogram. Once again this can be understood if the NC emission region is located on the secondary star surface. It has already been commented that the line emission from the secondary is not symmetric about the line of centres of the two stars (Southwell et al. 1995). If the leading side of the secondary is shadowed by the stream then a reduction in the narrow component flux after phase 0.75 is a straightforward consequence of this. There is now a compelling weight of evidence for this asymmetry in the line emission.

Schwabe et al. (1996) have presented an alternate means of modelling and analysing time resolved spectroscopic data. Their method is based on a tomographic inversion technique known as ‘filtered backprojection’. This transposes the (v, ϕ) data from the spectra into the (v_x, v_y) plane by assuming all emission away from the rest wavelength is shifted due to the Doppler effect. For this reason, when spectroscopic data are represented in this way it is commonly known as

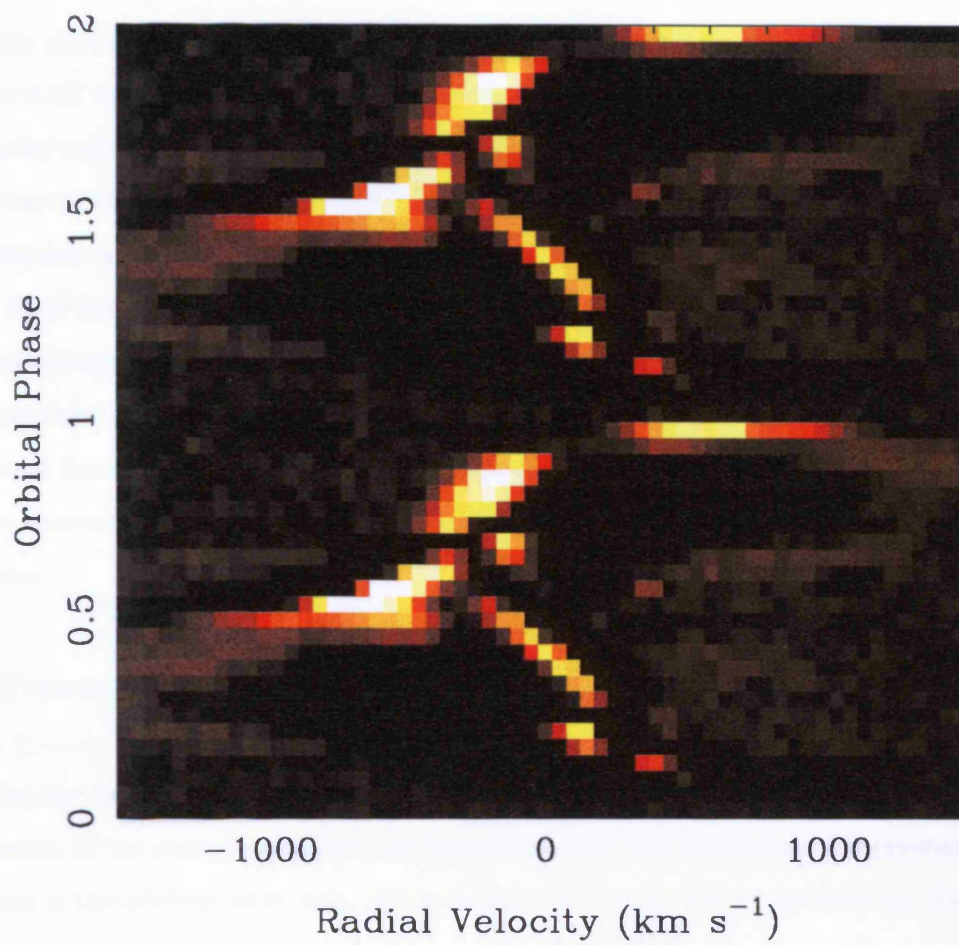


Figure 3.16: Residuals (model-data) for the fit to the HeII emission line.

a ‘Doppler tomogram’. Interpretation of such a representation is undertaken by comparison with simulated tomograms generated from estimations of the likely line emission regions in the binary. Note that this does not include any consideration of the physics involved, and so is more of a method for visualising and interpreting the complex information provided by these datasets. On the other hand, the trajectory-based model described above attempts to derive direct measurements of the properties of the stream.

The results obtained by Schwöpe et al. are, in general, consistent with what emerges from modelling the AAT data. They too find an emission component close to or on the secondary and a high velocity region associated with the infalling stream. However, the Doppler tomograms display a component that extends away from the secondary in a tail-like structure, which Schwöpe et al. associate with the horizontal section of the stream. No complementary component has emerged from the above model, but the high velocities in the tail suggest it ought to be HVNC. A thorough comparison of our results with those of Schwöpe et al. awaits the additions to the model described below. Once the NC has been accurately located and most of the residuals are removed from the fit, the results will be investigated (by the masking method described above) to uncover how the HVNC relates both to the brightness distributions and the Doppler Tomograms.

3.4.3 Future work

Several further lines of enquiry have been suggested by the modelling work undertaken so far. The inclusion of the secondary to test the hypothesis that this will reduce the residuals in the fit to the data is the obvious next step. If the location of the narrow component on the secondary can be accurately determined, it may be possible to return to the mass estimate presented in Section 3.3.5 and add a constraint to the location of the line emission, γ . This will reduce the size of the allowed region in Figure 3.8 and thereby improve the white dwarf mass measurement.

Further improvements to this work will include; (i) increasing the phase resolution to exploit the excellent data available, (ii) more detailed comparisons between the best-fit stream brightness profiles of the two emission lines in an effort to determine the ionisation structure along the stream and (iii) experimenting with different stream trajectories with the aim of constraining the system parameters (the magnetic orientation, for example). In addition, a major goal is to

apply the model to data from other AM Her systems in an effort to determine the dependence of the stream properties on factors such as the mass accretion rate, q and stellar separation.

3.5 Summary

The phase-resolved spectra presented in this Chapter have revealed a great deal about both HU Aqr as a whole and its accretion stream in particular. The optical emission lines from HU Aqr are optically thick and display equivalent width variations on the orbital period that are suggestive of asymmetric heating of the stream. The lines comprise three components with different radial velocities that are consistent with line emission regions located in disparate sections of the stream. The narrow component emission region displays a clear sinusoidal variation with an amplitude of 312 km s^{-1} , and being associated with the secondary star this leads to constraints upon the mass ratio for HU Aqr. The broad and high velocity components arise in the accretion funnel.

The low-resolution red spectra display cyclotron emission features indicating that the magnetic field on the primary is $34 \pm 1 \text{ MG}$. The spectrum from the eclipse minimum has provided a measurement of the secondary's spectral type of M4.5–M5, and distance, $175 \pm 25 \text{ pc}$.

Extensive modelling of the continuum light curves and the radial velocity variations of the emission lines has allowed the first measurement of the optical luminosity as a function of position along the accretion stream. Although only preliminary results are available, this has already demonstrated that the continuum emission region is not located in the same regions as the line emission regions. Furthermore, differences between the emission regions for the $\text{H}\beta$ and $\text{HeII } \lambda 4686 \text{ \AA}$ lines may hold the key to measurements of the ionisation structure along the stream. Evidence for a region of enhanced emission mid-way between the two stars is suggestive of the threading region where it has been postulated that shock heating of the stream may occur. The fits to the narrow component have not only shown that the emission region is located on the secondary, but also indicate that the leading, primary facing quarter of its surface dominates the flux. It is hoped that by improving this measurement of the location of the narrow component it will be possible to better constrain the mass estimate for HU Aqr.

Chapter 4

ROSAT observations of HU Aqr

The ROSAT satellite (Trümper 1984) conducted the first all-sky survey at soft X-ray and extreme ultraviolet wavelengths, increasing the number of known polars by over thirty to the current census of about sixty systems (Beuermann & Burwitz 1995). HU Aqr was one of these discoveries. In addition, pointed observations of polars by the satellite have deepened our understanding of these systems. X-ray observations are a direct probe of the accretion process as the stream impacts on the primary as well as providing more indirect information about the accretion stream itself and the secondary star. The following three chapters deal with the ROSAT soft X-ray observations of a number of AM Her systems. Chapter 4 details results from ROSAT PSPC and HRI observations of HU Aqr. Chapter 5 describes the results from a PSPC observation of UZ For, a system with an orbital period close to that of HU Aqr. HU Aqr and UZ For display many similar properties and the implications of the likenesses and contrasts between these two systems are also discussed in Chapter 5. In Chapter 6 the temporal and spectral properties of a number of polars selected from the ROSAT pointed observations are presented, in order to investigate the collective and individual X-ray properties of the AM Her class of cataclysmic variables.

4.1 Introduction: the ROSAT mission

The *Röntgensatellit*, more commonly known by its acronym ‘ROSAT’, is a joint German, British and American X-ray observatory. The satellite carries an imaging soft X-ray telescope (XRT)

and an extreme ultraviolet telescope, the Wide Field Camera (WFC). The X-ray telescope consists of four primary components; the X-ray mirror assembly (XMA), two Position Sensitive Proportional Counters (PSPC) and the High Resolution Imager (HRI). The XMA focuses incident photons onto the focal plane using a set of four nested grazing incidence mirrors in the Wolter Type 1 configuration. The mirrors are made of Zerodur, gold coated for better X-ray reflectivity. The aperture diameter and focal length are 84 cm and 240 cm respectively. Figure 4.1 is a cross-section of the XRT showing the location of the major components. The three focal plane detectors (two redundant PSPCs and the HRI) are mounted so that they may be individually rotated into and out of the field of view though only a single detector is in use at any one time.

The PSPC is a multiwire proportional counter containing a mixture of argon, methane and xenon gas. X-rays are able to penetrate the chamber through a polypropylene entrance window. The window is coated with carbon and lexan to reduce the UV transmission but this also produces a deep minimum in the quantum efficiency at 0.28 keV due to carbon edge absorption. The FWHM energy resolution of the PSPC is effectively that of a single wire proportional counter and is given by:

$$\Delta E/E = 0.43(E/0.93)^{-1/2} \quad (4.1)$$

The bandpass of the XMA and PSPC combined is 0.1–2.4 keV, and so $\Delta E/E$ has values between 0.3 at 2.4 keV and 1.3 at 0.1 keV. The PSPC has a filter wheel with four filters; open, closed, a spectral calibration filter and a boron filter. The boron filter may be selected to increase the effective spectral resolution of the PSPC at lower energies.

The gas within the PSPC is at a pressure of over one bar and so to contain this gas against the vacuum of space the entrance window has to be reinforced. The window support structure consists of a fine wire mesh, a coarse wire mesh and a rigid circle of diameter 40 arcmin with eight radial struts surrounding it (Figure 4.2). Table 4.1 gives the size and spacings of the fine and coarse wire mesh. The transmission through the support structure as a whole is 79%, but it should be noted that this is an average applicable only over a large area. In the centre of the field of view, the size of the focused X-ray beam at the detector is 2 arcsec FWHM. The data in Table 4.1 show that the coarse wire mesh can completely occult a source, and the fine wire mesh can cause significant, if not total, attenuation of the flux. The exact effect of the wires on a given source in the field of view is difficult to assess precisely unless sub-arcsecond

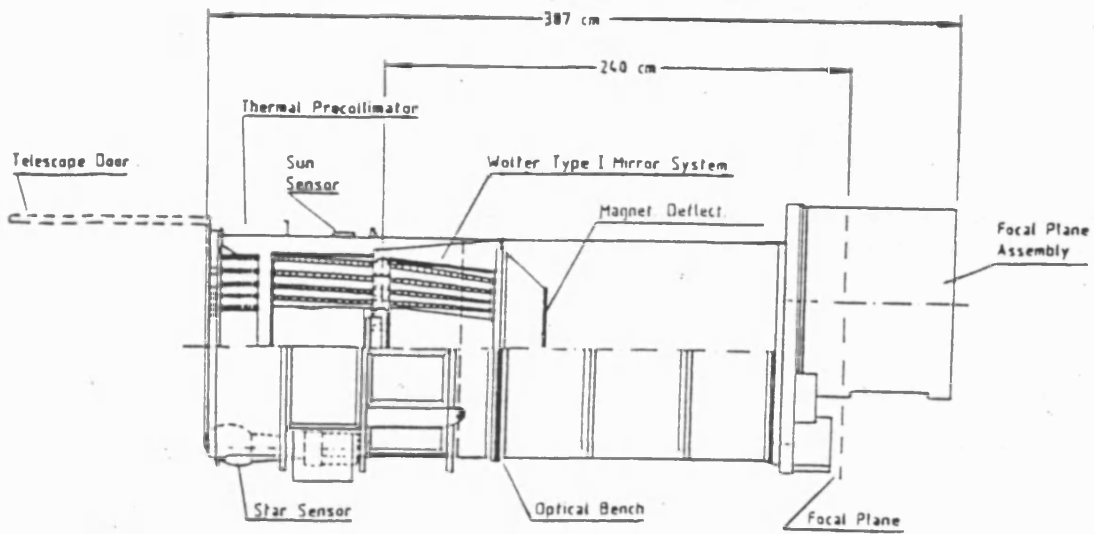


Figure 4.1: Schematic diagram of the ROSAT X-ray Telescope (XRT).

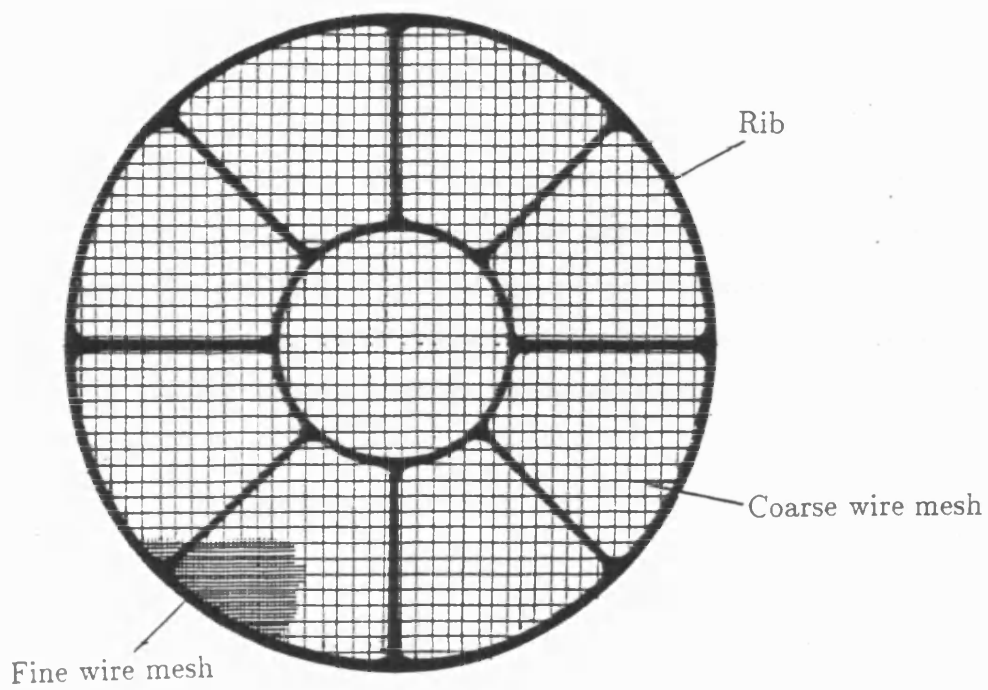


Figure 4.2: The ROSAT window support structure.

structure. Due to a scheduling error this was not done for this observation of HU Aqr, and therefore if any statements about changes in flux observed in the light curve are to be made, it will have to be considered whether the change is real or an artifact of the wires. These problems are discussed in more detail below. A second ROSAT observation of HU Aqr was made in the period October 26 to November 21 1994 using the HRI with a total exposure time of 37,360 s.

Two other independent ROSAT studies of HU Aqr have been conducted, using the HRI instrument. The first, in May 1994, has been obtained from the public archive but is not presented here for two reasons. A quick reduction of the observation reveals that the data are largely similar to the HRI data obtained later that year. Secondly, the data had been proprietary to A. Schwöpe and is soon to be published. The second HRI observation only took place in late 1995 and so became public only after the completion of this work. There were also two short PSPC observations of HU Aqr in 1992 and 1993. These datasets have been reduced but do not reveal anything new and for the sake of brevity are not presented here.

The ROSAT datasets were reduced using ASTERIX, which is the standard Starlink X-ray data analysis package (Saxton 1992). In Section 2.3 a process for optimising the radius of a source integration circle was described for use when reducing optical photometric data. A similar method was applied to the PSPC and HRI datasets to obtain circular source regions for all subsequent data extraction. This gave source regions of 3.0 and 0.5 arcminutes radius for the PSPC and HRI data respectively. A circular source-free region 11 arcmin (PSPC) and 4 arcmin (HRI) away from the source was chosen for determining the background. The regions were selected to be as close to HU Aqr as possible while still ensuring that no sources were in the background box. The background data were then subtracted from the source with appropriate scaling for the different vignetting and solid angles of the two regions. For the most part the choice of background is not a crucial factor since HU Aqr is a bright X-ray source and the flux exceeds the background by a factor of several hundred. It is only when looking at the eclipse that the background becomes critical and for this the background has been dealt with differently, see Section 4.3.5.

4.3 Results

4.3.1 The X-ray light curve

Figure 4.3 shows light curves for both the PSPC and HRI observations folded on the ephemeris quoted in Section 4.3.2. For these plots the data have been collected into ten second bins. The light curve of HU Aqr is dominated by a very clear bright-faint state variation over the orbital period. The bright phase is interrupted by two distinct features, the eclipse of the accretion region on the white dwarf by the secondary between phase 0.96 and 1.04 and a dip-like feature one tenth of a cycle before the eclipse. The eclipse in X-rays is flat bottomed, but not total (see §4.3.5), with sharp transitions lasting less than ten seconds. Unfolded light curves confirm that the eclipse is a stable feature for the duration of the two observations, a total of just over one year. The count rate during the PSPC eclipse is 0.022 ± 0.008 ct s⁻¹. The origin of this residual flux is discussed in Section 4.4.5.

The faint phase count rate was 0.34 ± 0.01 ct s⁻¹, significantly higher than the flux during eclipse, which indicates that one or more X-ray sources are still visible during the faint state. This is evidence for the existence of X-ray emission regions on the primary in addition to the main accreting pole, as will be discussed in Section 4.4.4. In addition to the eclipse and narrow dip, a broader and shallower dip is also present in the light curve of HU Aqr, centred on $\phi = 0.68$. The nature and possible cause of this dip are discussed in Section 4.4.2.

To measure the location of the mid-point of the bright phase, data from the egress (at $\phi \simeq 0.2$) were reversed and overlaid onto the ingress. The egress data were then progressively shifted over the ingress data until the minimum deviation between the two was found. The position at which the light curve is folded to achieve this minimum defines the centre of the bright phase. This method could only be used with the PSPC data because the ingress to the faint phase was not observed by the HRI. Figure 4.4 shows the PSPC egress reversed and overlaid on the ingress at the best fit position. The phase at which both the ingress and egress exceeded 5σ above the mean faint phase flux was used to define the beginning and end of the bright phase, and is marked on this plot. The long duration of the transitions (~ 600 s) means that the support wires will not affect the timings. The duration of the bright phase was found to be 0.723 ± 0.004 orbital cycles, centred on phase 0.851 ± 0.002 . No significant difference between the ingress and

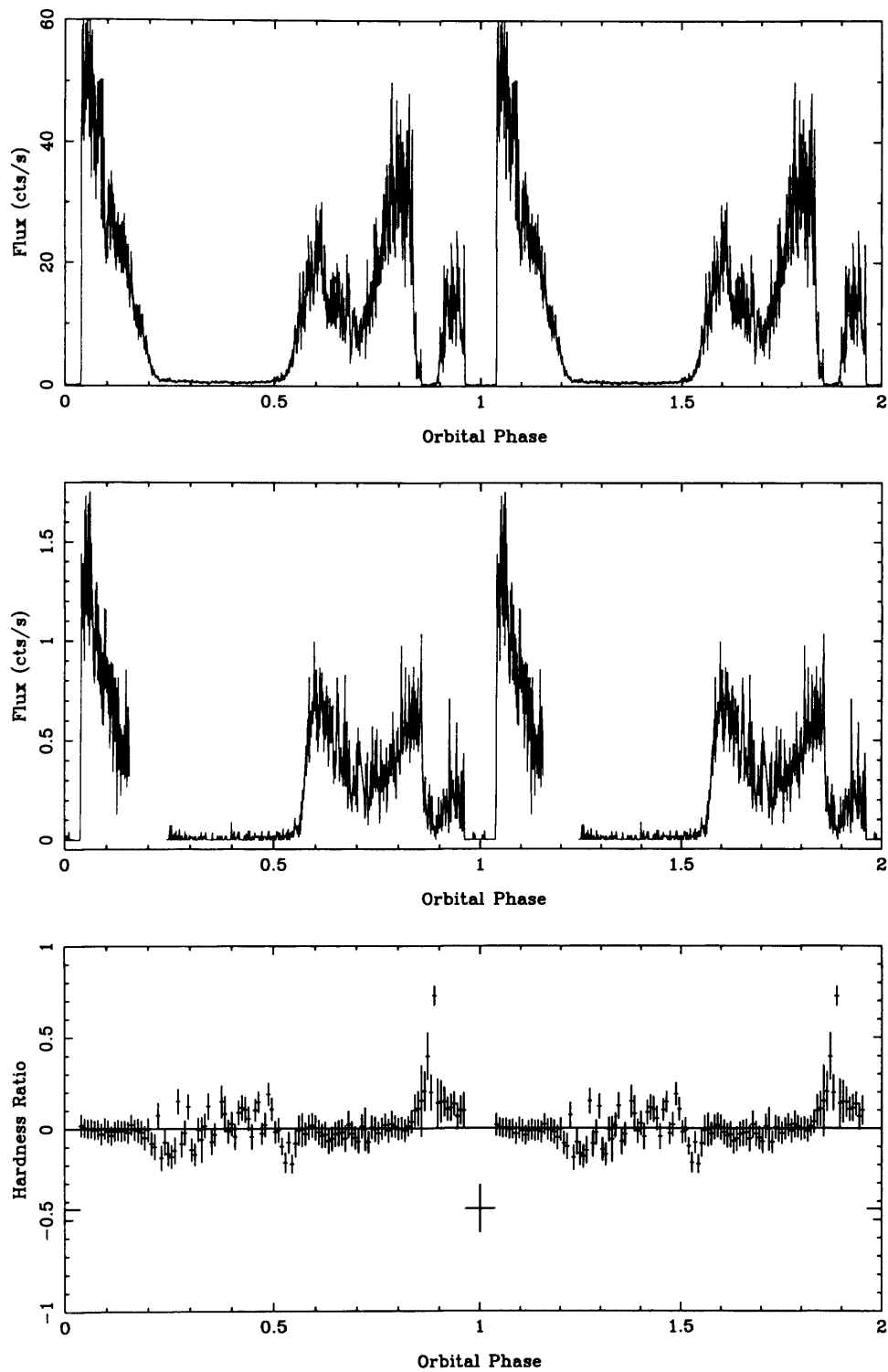


Figure 4.3: Top: Folded ROSAT PSPC light curve of HU Aqr from November 1993. Middle: Folded ROSAT HRI light curve from November 1994. Bottom: The hardness ratio light curve derived from the PSPC data. The resolution of both flux light curves is 10 s, while the hardness ratios are at 60 s resolution.

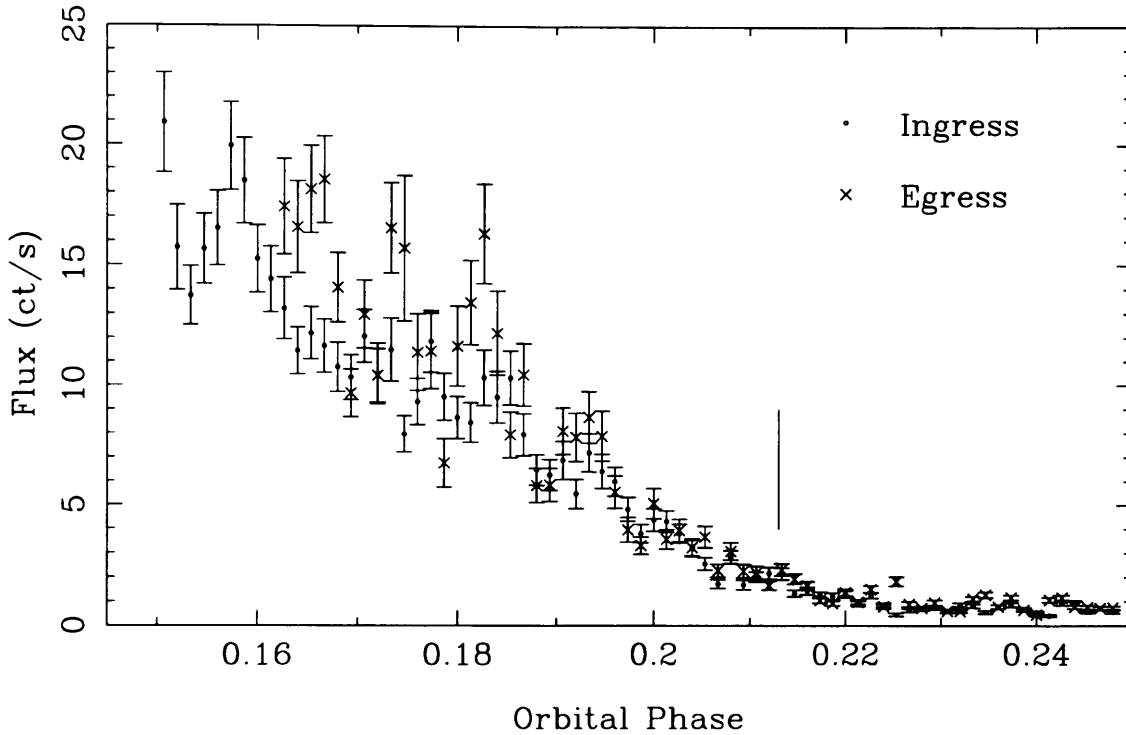


Figure 4.4: The egress from the faint phase of the HU Aqr light curve reversed onto the ingress. The vertical line marks the phase at which both the ingress and egress exceed 5σ above the mean faint phase flux.

egress durations was found, the curves are symmetric about the bright state mid-point.

This information can be employed to estimate the position of the X-ray emission region as was done for the optical photometric data in Section 2.4.2. The equation given there can be used to relate the viewing angle α , the inclination i , the colatitude of the magnetic pole β and the magnetic phase ϕ :

$$\cos \alpha = \cos i \cos \beta - \sin i \sin \beta \cos \phi. \quad (4.2)$$

A number of assumptions are involved in this calculation as described in Section 2.4.2. For a bright phase duration of 0.684 and an inclination of 85° the co-latitude from Equation 4.2 is $9.4^\circ \pm 0.9^\circ$. It will be shown later (§4.4.2) that an X-ray emission region with a significant height would be useful to explain other features in the light curve. At least one of the assumptions in this calculation is therefore likely to be invalid and the co-latitude obtained should be treated as a lower limit.

In AM Her systems, a measurement of the longitude of the main pole can be obtained from

X-ray, optical and circular polarisation bright phases, or from linear polarisation data. The position of the secondary star is well determined in eclipsing systems, and can also be revealed spectroscopically in non-eclipsing systems. Comparison of these two measurements shows that the pole rarely lies along the line of centres joining the two stars. The azimuths of the main pole are found to cluster in a sector $\leq 90^\circ$ wide with a mean value of $\approx 20^\circ$ (Cropper 1988). In HU Aqr, the X-ray eclipse is off-centre with respect to the X-ray bright phase; the eclipse occurs 0.149 ± 0.002 cycles after the mid-point of the bright phase at $\phi = 0.851$. This means that the emission region on the white dwarf leads the line of centres of the stars by $53.3^\circ \pm 0.7^\circ$, and is therefore typical of AM Hers.

4.3.2 Eclipse ephemeris

Early eclipse ephemerides for HU Aqr were quoted by both Hakala et al. (1993) and Schwöpe et al. (1993). These were updated in Glenn et al. (1994) for a baseline of 2.5 yr, giving a period of 125.021 min for HU Aqr. A further six X-ray eclipses have been observed by the PSPC and HRI in addition to the four optical eclipses observed at high time resolution on the AAT (Chapter 2). These data allow an updated ephemeris to be obtained with a baseline that extends over four years.

For the optical data the eclipse centres have been defined as the mid-point between the sharp ingress and egress. The rapid ingress and egress to the X-ray eclipse provide good reference points for determining the centre of eclipse. The ingress and egress were defined by the point at which the flux fell below or rose above a flux level 3σ above the mean residual eclipse flux, and eclipse centre was defined as the mid-point between these two. A light curve with a bin size of five seconds was used for determining the ephemeris. It is estimated that the X-ray ingress and egress could each be measured to within one time bin of their true position, giving an error on the final eclipse times of ± 7 seconds.

The heliocentric eclipse timings from the AAT, PSPC and HRI data are listed in Table 4.1. All ten eclipses match the earlier ephemeris without any phase ambiguity and so the 13 X-ray and optical eclipse timings quoted in Schwöpe et al. (1993) and Glenn et al. (1994) have been included in the calculation of the ephemeris. The eclipse ephemeris calculated as the weighted

| Published eclipse times | | | | Additional eclipse times | | | |
|-------------------------|-------|---------------------------------|--------------|--------------------------|-------|---------------------------------|--------------|
| Source | Cycle | Eclipse centre HJD 2440000 + | O-C (sec) | Source | Cycle | Eclipse centre HJD 2440000 + | O-C (sec) |
| Schwope | -8064 | 8196.42357 | + 3.5 | AAT | 3012 | 9158.046859 | - 1.6 |
| | 0 | 8896.54345 | - 19.0 | | 3013 | 9158.133680 | - 1.6 |
| | 1 | 8896.63057 | + 6.8 | | 3014 | 9158.220495 | - 2.5 |
| | 13 | 8897.67224 | - 8.4 | | 3015 | 9158.307338 | + 0.02 |
| | 23 | 8898.54079 | + 21.5 | | PSPC | 4590 | 9295.049577 |
| | 24 | 8898.62742 | + 5.0 | 4593 | | 9295.310000 | - 1.4 |
| | 35 | 8899.58242 | + 2.9 | 4599 | | 9295.830960 | + 1.8 |
| | 36 | 8899.66942 | + 18.4 | HRI | 8780 | 9658.827260 | + 0.2 |
| | 196 | 8913.56081 | + 28.5 | | 8953 | 9673.847193 | - 0.2 |
| | 209 | 8914.68915 | + 0.4 | | 8956 | 9674.107674 | - 1.5 |
| Glenn | 231 | 8916.59920 | + 0.4 | | | | |
| | 232 | 8916.68602 | + 0.3 | | | | |
| | 2677 | 9128.96204 | + 1.2 | | | | |

Table 4.2: Eclipse centre timings; the table on the left lists the published times used in the calculation, the table on the right gives the times derived from the optical and X-ray datasets presented in this thesis. The error on each AAT measurement is 3 seconds and on each PSPC/HRI measurement is 7 seconds. The columns labelled O-C give the discrepancy between each eclipse centre time and the ephemeris of Equation 4.3.

linear fit to these eclipse timings is:

$$HJD = 2,449,482.147633(7) + 0.086820454(4)E. \quad (4.3)$$

Numbers in parentheses give the 1σ uncertainties in the last digit.

As pointed out in the previous section, the three PSPC timings could be affected by the wire grid of the window support structure. If a transition of a wire by the X-ray beam coincides with the edge of an eclipse, then the eclipse could appear to be slightly off-set and wider than it actually is. The duration of any wire crossings is of the order fifteen seconds, based on the speed of the wobble, the X-ray beam size and the wire diameter. None of the three eclipses appears to be influenced by the wires and the PSPC data are just as accurate to the ephemeris as the HRI data. It is concluded that the wires are not a factor in this case so the PSPC timings were included in the fit.

4.3.3 The hardness ratio of HU Aqr

In order to look for spectral variation over the orbital cycle, a hardness ratio light curve of HU Aqr was produced from the PSPC data. As stated earlier, it is not possible to do this with the HRI data due to its poor spectral capabilities. The hardness ratio is defined as:

$$HR = \frac{H - S}{H + S} \quad (4.4)$$

where S and H denote the X-ray fluxes in the softer (0.10-0.20 keV) band and harder (0.21-2.4 keV) band respectively. These energy ranges were chosen so that the mean hardness ratio of HU Aqr was $\simeq 0$. A significant amount of variability is seen in the hardness ratio, which is shown plotted against phase in Figure 4.3. The flux gets harder during the dip (phase range 0.84–0.96), softer during the transitions to and from the bright phase (phase 0.50–0.56 and 0.20–0.28 respectively) and is harder during the faint phase (0.28–0.50) than in the bright phase (0.56–0.80).

4.3.4 The phase resolved spectra

The hardness ratio light curve clearly demonstrates that the X-ray spectrum of HU Aqr is changing during the orbital cycle. In order to confirm this fact and to quantify the spectral changes involved it is possible to produce a series of time-resolved X-ray spectra of the system. The X-ray spectra from the four different characteristic phase intervals evident in the hardness ratio light curve were produced. These are referred to as the dip phase, transition phase, faint phase and bright phase of the orbital cycle; for the phase range of each of these periods see Section 4.3.3 and Table 4.3. The PHA data extracted for each spectrum were rebinned such that there was a minimum of 15 counts per bin.

The fits to each spectrum were undertaken using XSPEC, an interactive X-ray spectral fitting programme. As with most software designed for X-ray spectral fits, the best fit parameters of a given model are found by generating a model spectrum and folding this through the detector response, thereby creating model data which can be meaningfully compared to the data. The energy resolution of most current X-ray detectors is poor and as a result it is often possible to obtain several models which produce acceptable fits to the data. If this is the case then *a priori*

| | Bright | Dip | Faint | Transition |
|-------------------------------------|-------------------------|-------------------------|-------------------------|-------------------------|
| Phase | 0.56–0.80 | 0.84–0.96 | 0.28–0.50 | 0.20–0.28 0.50–0.56 |
| Flux (ct s ⁻¹) | 9.85 ± 0.05 | 2.28 ± 0.03 | 0.34 ± 0.01 | 1.00 ± 0.02 |
| kT _{bb} (eV) | 37.2 | 45.3 | 45.4 | 37.7 |
| Norm _{bb} | 8.94 × 10 ⁻⁴ | 2.63 × 10 ⁻⁴ | 1.38 × 10 ⁻⁵ | 5.2 × 10 ⁻⁵ |
| N _H (cm ⁻²) | 4.28 × 10 ¹⁹ | 9.95 × 10 ¹⁹ | 0.0 × 10 ¹⁹ | 0.0 × 10 ¹⁹ |
| Norm _{brems} | 5.54 × 10 ⁻⁴ | 3.70 × 10 ⁻⁴ | 2.07 × 10 ⁻⁴ | 3.87 × 10 ⁻⁴ |
| χ _ν ² | 1.43 | 1.11 | 1.25 | 1.39 |
| L _{bb} /L _{brems} | 43.5 | 22.7 | 2.1 | 1.5 |

Table 4.3: Results of the spectral fits to the four regions of the light curve of HU Aqr. The bremsstrahlung temperature has been fixed to 30 keV in all of these fits.

knowledge of the physical processes within the source must be used to select the appropriate models to apply to a given dataset.

For polars, a bremsstrahlung plus absorbed blackbody spectral model can adequately describe the hard X-ray emission region in the column and the reprocessed soft X-ray from the surface respectively, and therefore such models were applied to the HU Aqr data. It was found that the data could be successfully fit by a bremsstrahlung model with a temperature anywhere in the range 10–40 keV without greatly affecting the absorbed blackbody fit to the softer flux. This is a typical result that arises because the bandpass of the ROSAT PSPC does not extend to high enough energies to measure the turnover in the bremsstrahlung spectrum and fix the temperature accurately. All of the spectral fits have therefore had the bremsstrahlung temperature fixed to 30 keV, a value typical of AM Her systems (Cropper 1990).

The spectra from each of the phase ranges are shown in Figure 4.5 with the best-fit model superimposed. Figure 4.6 shows the 68%, 90% and 95% confidence contours in the kT_{bb}/N_H plane for each of the spectra, and the corresponding best-fit parameters for each spectrum are given in Table 4.3.

Both the hardness ratio light curve and the results of the phase-resolved spectral fits show that the spectrum of HU Aqr varies over the orbital period and should not be fit by a single spectral model. The best-fit model to the bright phase spectrum is typical of AM Her variables; an absorbed 35–42 eV blackbody with a 30 keV bremsstrahlung component. During the dip the

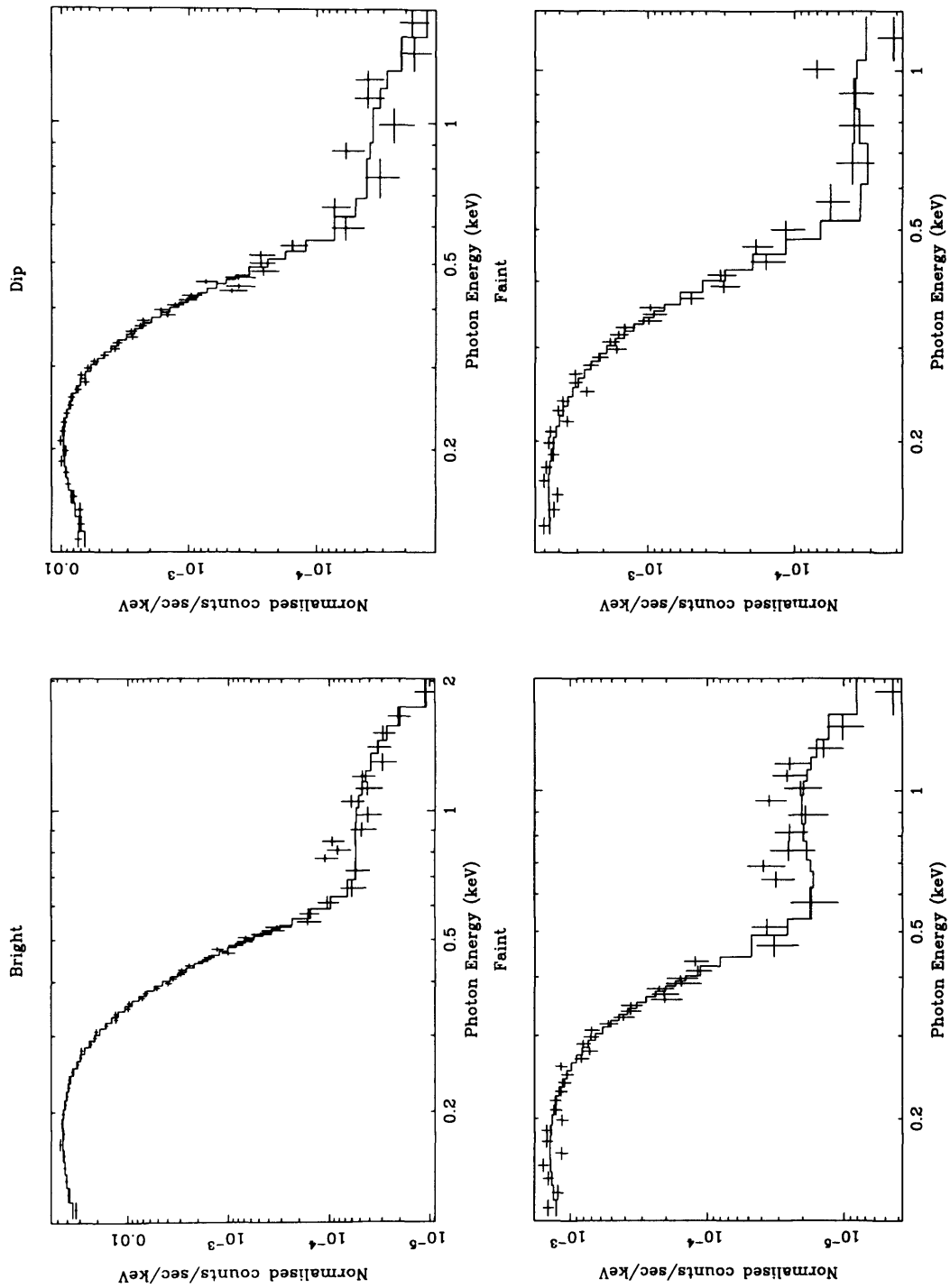


Figure 4.5: The ROSAT PSPC spectra from the bright, faint, transition and dip phases as defined in Table 4.3. The best fit spectra corresponding to the parameters given in Table 4.3 are shown overlaid onto the data (solid line).

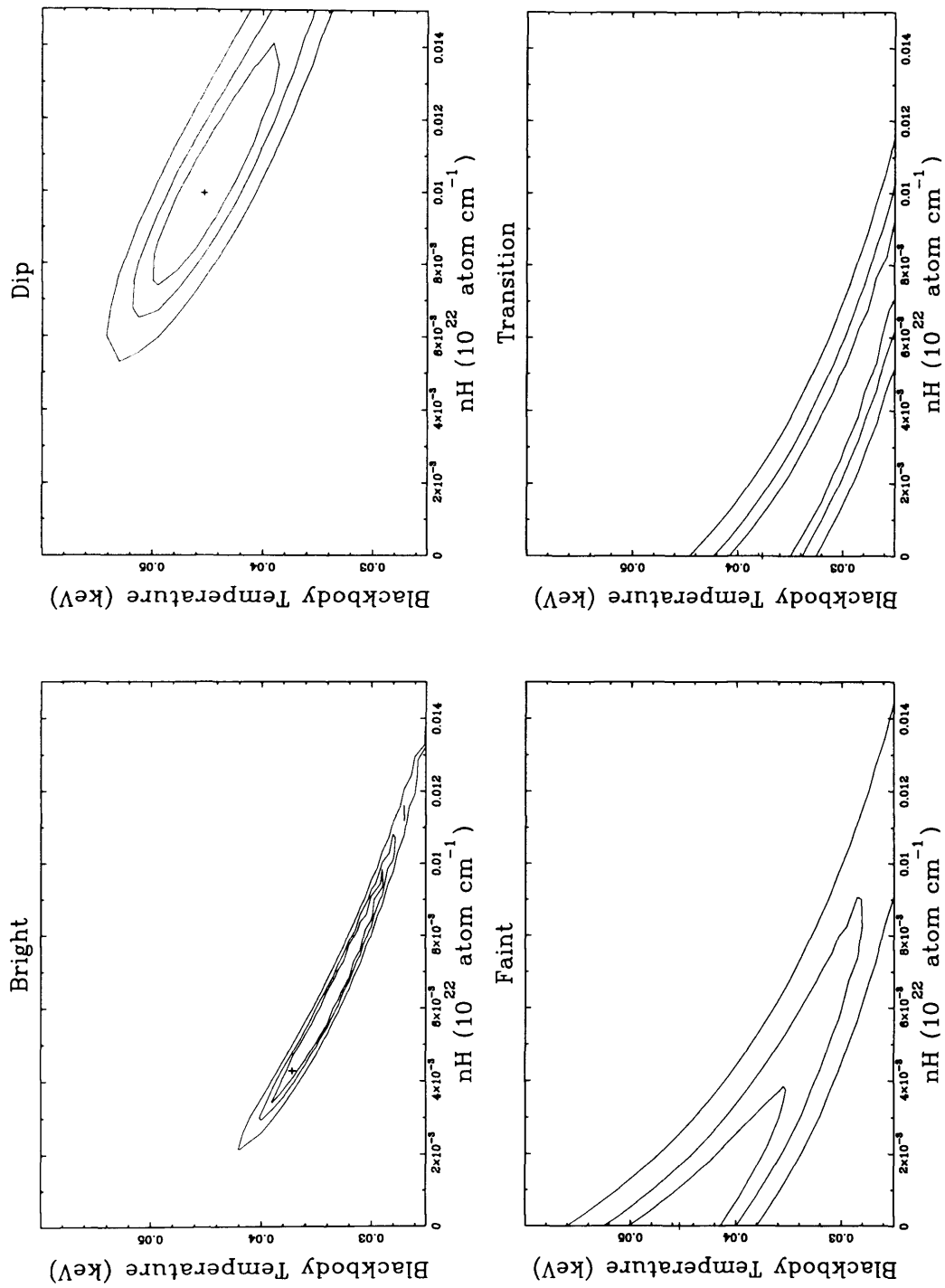


Figure 4.6: Confidence contours in the blackbody temperature versus hydrogen column density plane for the best fits to the spectra shown in Figure 4.5. The 68%, 90% and 99% contours are shown.

column density of the best-fit increases by $8\text{--}12 \times 10^{19} \text{ cm}^{-2}$ while the blackbody temperature is the same as that for the bright spectrum (90% confidence, see Figure 4.6). The model was also fitted to a spectrum from the core of the absorption dip ($\phi = 0.85\text{--}0.90$) and it was found that the best-fit column density rises to $1.3 \pm 3 \times 10^{20} \text{ cm}^{-2}$ at dip minimum. The spectral differences between the other regions of the light curve are not as clear. The 90% confidence contours for the bright and faint phase spectra overlap, even though the hardness ratio indicates the faint phase is slightly harder than the bright phase. The faint phase statistics are, of course, much poorer than the bright phase and a change in either the blackbody temperature or column density cannot be ruled out. There is little overlap of the 90% contours between the transition and bright spectra indicating that the transition regions do have softer spectra. It is unclear if this is due to a smaller column or to lower temperature regions being visible, either possibility fits the data.

4.3.5 Flux in eclipse

The PSPC observation was conducted on-axis, as stated earlier. While causing problems for analysis of the light curve, this does provide the opportunity of observing HU Aqr at higher signal-to-noise than for an off-axis observation. Optical spectroscopy of HU Aqr (§3.3.7) indicates that the distance to HU Aqr may be slightly smaller than was thought from earlier studies (e.g. Glenn et al. 1994). This suggested that the PSPC observations of HU Aqr during eclipse might provide a means of detecting X-ray flux from the secondary itself, because at mid-eclipse all the optical flux is from the secondary alone with little or no contributions from the rest of the system. The on-axis observation provides the opportunity to investigate this possibility.

The X-ray data were extracted limiting the integration times to eclipse phases only ($0.965 \leq \phi \leq 1.035$). The total integration time during the eclipse was 1665 seconds. Circular source boxes with gradually increasing radius were used to collect the data, and a peak in the signal-to-noise was found for a source radius of 3.25 arcmin. This represents a positive detection of a source at the location of HU Aqr with a count rate of $0.022 \pm 0.008 \text{ ct s}^{-1}$ (3σ above the background). Figure 4.7 shows a smoothed PSPC image of HU Aqr during the eclipse with the location of HU Aqr marked by a cross.

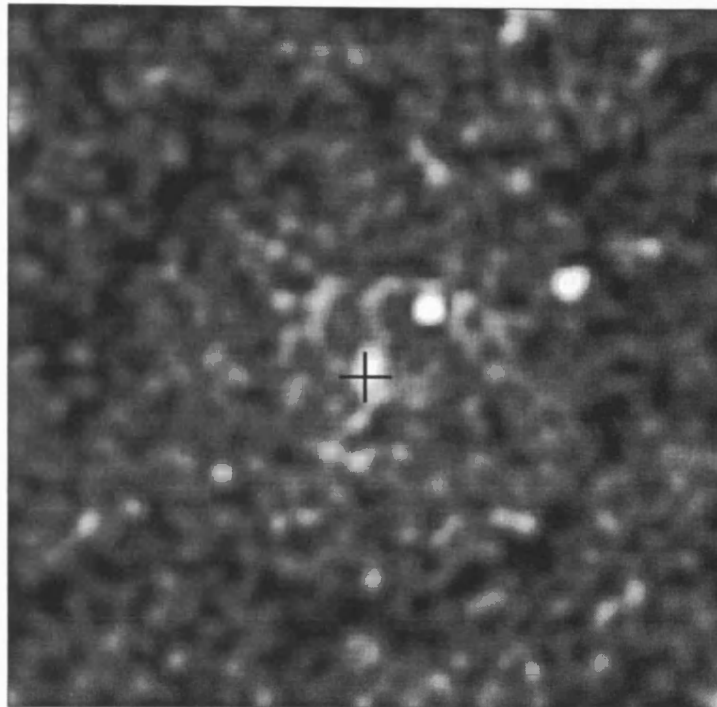


Figure 4.7: PSpC image of HU Aqr, obtained when exposure is limited to eclipse phases only. The central $1^\circ \times 1^\circ$ region of the image is shown, with the location of HU Aqr marked by a cross.

4.4 Discussion

4.4.1 The narrow dip

The narrow dip occurs at the same phase as a dip seen at optical wavelengths which was attributed to free-free absorption in the accretion stream (§2.4.2). Such X-ray dips have been observed in several other polars, for example EF Eri (Watson et al. 1989, Beuermann et al. 1987), VV Pup (Patterson et al. 1984), AN UMa (Mason 1985) and UZ For (Warren et al. 1995 and this thesis). In some cases these are accompanied by near-infrared and optical dips (e.g. EF Eri). While free-free absorption is thought to be responsible for the dips in the optical and infra-red, the strong energy dependence of the dips suggests photoelectric absorption at X-ray wavelengths. The dip also occurs just after the mid-point of the bright phase which is consistent with the notion that the dip is caused by the accretion stream as it rises out of the orbital plane. There are marked differences in the character of this dip between the two HU Aqr observations. In 1993 the PSpC shows a near-total dip while in 1994 the HRI shows a partial dip 0.03 cycles

later than in the PSPC observation (Figure 4.3).

If the conclusion about the optical dip is that it arises due to absorption by the stream, it is therefore logical to suppose that the X-ray dip is also caused by the stream. However, it is still necessary to assess the possible mechanisms for this absorption. In Section 4.3.4 it was demonstrated that the absorption process during the dip causes an increase in the column density from $4 \pm 3 \times 10^{19}$ to $1.3 \pm 0.3 \times 10^{20} \text{ cm}^{-2}$. Similar or much larger column increases have also been detected in most of the other AM Her systems which show dips (e.g. EF Eri; Patterson, Williams & Hiltner 1981, Watson et al. 1989, AN UMa and V834 Cen; Mason 1985). Photoelectric absorption within the stream is highly energy dependent ($\tau_X \propto \sigma(E)N_H$ and $\sigma(E) \sim E^{-3}$), so softer photons will suffer stronger absorption and hence increase the hardness ratio during the dips. It is concluded that photoelectric absorption by distant ($\geq 10^{10} \text{ cm}$) parts of the accretion stream is the likely cause of the X-ray dips in HU Aqr (see King & Williams 1985 and Watson et al. 1989 for a general discussion of X-ray absorption dips).

It is difficult to accurately measure the spectral change occurring within dips because they are often total with short ingress and egress times and because the spectral response of the ROSAT detectors is modest. As a result it is hard to prove conclusively that the dip is caused by the accretion stream. However, there is strong evidence to be found in the structure of the dip. Figures 4.8 and 4.9 shows the absorption dip in detail for each of the nine times this feature was observed with the PSPC and HRI. The onset of the dip is characterised by a change in the light curve from a mean flux of 20-50 cts s^{-1} interrupted by occasional flares to a similar mean flux interrupted by occasional intervals of low/zero flux with a typical timescale of ~ 10 -50 seconds. In all of the observations this structure is visible from the edge of the dip right through to the beginning of the eclipse.

Although this is thought to be the result of structure within the occulting object, one must first consider the possibility that it is an artifact of the support wires (in the case of the PSPC data). The duration of the spacecraft 'wobble' is 400 s (0.053ϕ) and during this time the spacecraft moves back and forth by ± 3 arcmin. The spacing of the wires means that the wobble can only account for four dips in flux in any 400 s interval, which is much less than the amount of observed structure. Also much of the structure seen is on a timescale of 30-60 s and hence is longer than the expected duration of a coarse wire crossing (15 s).

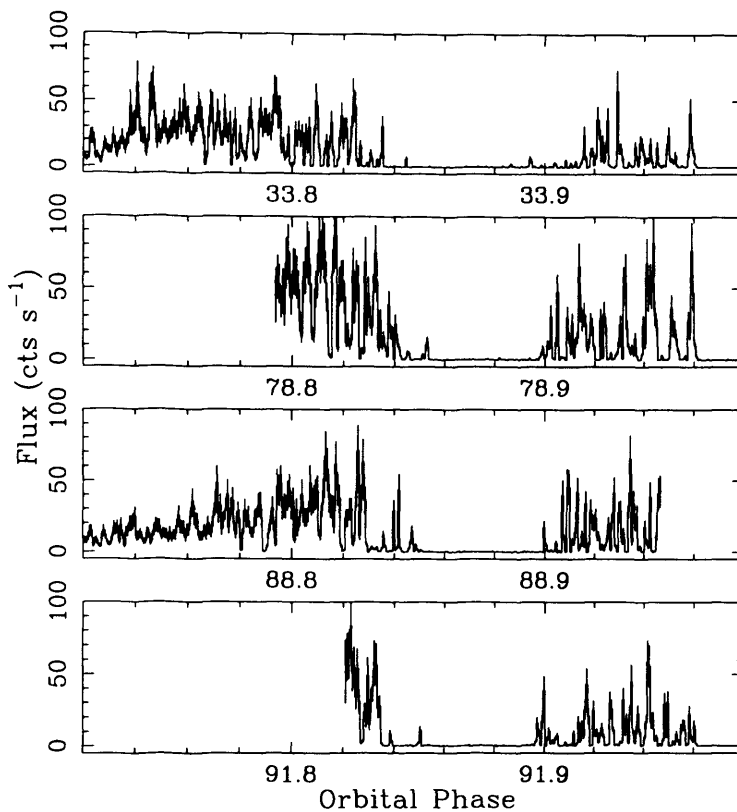


Figure 4.8: Detail of the four individual PSPC observations of the absorption dip.

It is concluded that most of the observed variability is real, although some of the narrower dips in flux must be the result of wire crossings. Real structure at the edge of the dip indicates that the occulting object is not uniform and fits the idea of an inhomogeneous stream (Watson et al. 1989). Discrete filaments within the stream that are dense enough to be optically thick could cause brief intervals of zero flux. The long periods of totality in each dip would then be caused by the line of sight intercepting many of these filaments and the changes to the dip that occur between observations would be the result of movement of the filaments.

Between the dip and the eclipse the X-ray flux is highly variable and never returns to its pre-dip level, suggesting that portions of the stream are still in the line of sight until the eclipse. Further confirmation of this is provided by the hardness ratio which remains high over this phase range. This can only be caused by the accretion stream if it does not thread onto field lines at a single point but instead threads at a number of points with different longitude. For threading to occur, the magnetic pressure must be greater than the ram pressure of the gas, which in turn is proportional to the density of the gas (Frank, King & Raine 1992, pg. 39). If a range of

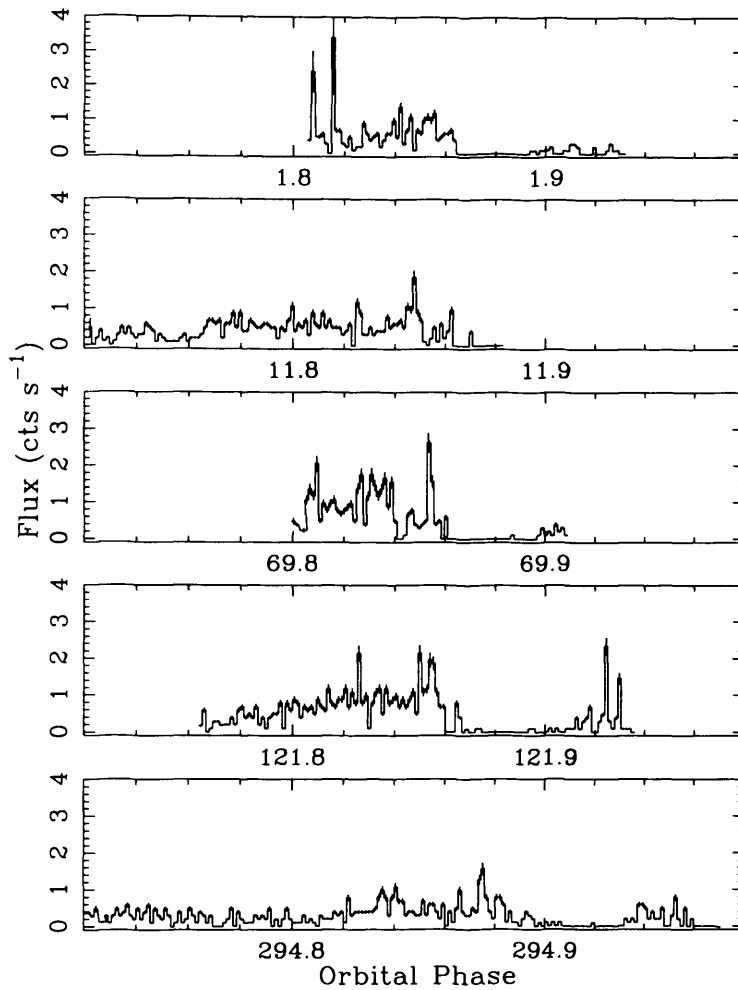


Figure 4.9: Detail of the five individual HRI observations of the absorption dip.

densities is present within the stream then the least dense gas in the stream will thread first and the densest last. This is in contrast to previous representations of the stream, which for simplicity used a single well collimated flow in models of stream line emission, absorption dips etc. (e.g. Ferrario et al. 1989*b* and this thesis, Chapter 3).

Such continuous threading by the stream also agrees with the observation that the surface of the secondary in many polars is not isotropically heated by the pole on the white dwarf. The side of the secondary which leads the orbital motion is often found to be less irradiated, as if it were being shadowed by the accretion stream (Davey & Smith 1996 and references therein). A single, well collimated accretion stream would seem an unlikely candidate for such a large effect. If the threading extends over a wider range of longitudes then significant shadowing of

the secondary by the accretion stream becomes more likely.

The question arises as to why there is a well defined egress from the dip at all, instead of a more gradual rise until the eclipse. If density structure within the stream is to account for a clear egress then the stream must be partly tenuous material and partly very dense material with very little of the gas at intermediate densities. The thin material would thread early on creating the phenomena observed between the dip and eclipse, and the dense material would thread later, creating the discrete dip. However, such a bimodal density structure seems unlikely. A more plausible explanation arises when the physics of the field-stream interaction is considered. Both the ram pressure of the gas in free fall and the magnetic pressure are inversely proportional to the distance from the white dwarf, S ; $P_{RAM} \propto V^2 \propto S^{-1}$ and $P_{MAG} \propto B^2 \propto S^{-4}$. The increase in the ram and magnetic pressure as the stream falls is shown in Figure 4.10. Also marked on the figure is approximately where the gas at different densities will thread. Clearly a larger spread of higher densities will thread over a short range compared to the lower densities, so if the gas has a near uniform range of densities it follows that much of the material will thread over a short range and cause a discrete dip. This could account for the dip profile of HU Aqr.

Another feature of the absorption dip that is evident in Figures 4.8 and 4.9 is the change to the dip profile from epoch to epoch. Changes can be seen to occur to the structure on timescales of hours to days and to the dip phase on timescales of days to months. These two figures show that the structure during the dip ingress and egress is different for each of the nine X-ray observations of the dip. The PSPC dips are all at about the same phase (0.85–0.89 ϕ) which is slightly earlier than the HRI dips. However, there is a more striking change *during* the HRI observation. The first four dips observed by the HRI all occur at approximately the same phase (0.86–0.89 ϕ) but during the long interval between the fourth and fifth absorption dip (173 cycles = 14.4 days) the dip phase undergoes a large shift to phase 0.91–0.94. This explains why the absorption dip seen in the folded HRI light curve of Figure 4.3 is not as pronounced as the PSPC dip observed one year earlier, it is smoothed out by the anomalously late final dip. A second light curve was produced from the HRI data excluding the last absorption dip and is shown in Figure 4.11. This resembles the PSPC dip much more than the original HRI dip; it is deeper with steeper sides although it is narrower.

Figure 4.12 shows the variation of the phase of the absorption dip with time over a four year

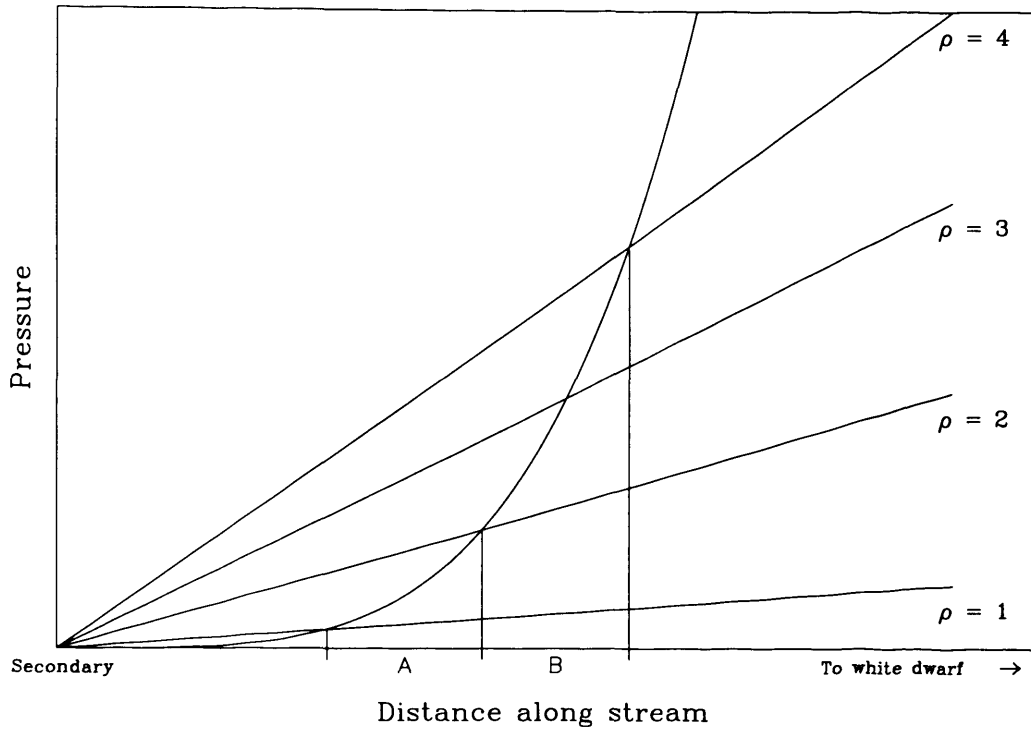


Figure 4.10: Comparison of the rates of increase in the magnetic and ram pressures as an accretion stream free-falls towards the white dwarf. The curve is magnetic pressure while the four straight lines denote the ram pressure for four gas densities. Region 'A' marks the radii at which gas at densities between 1 and 2 will thread. Region 'B' marks the radii at which gas a densities between 2 and 4 will thread.

interval. Also marked are the observations where no dip was observed. The last dip observed by the HRI occurs at a later orbital phase than in any of the other observations of the dip in HU Aqr. It is an interesting fact that this coincides with the final observation made of the dip in HU Aqr before the accretion state changed and the dip disappeared altogether (§2.5). It could be that this sudden phase shift is an indication that the system had begun to enter the new accretion state in November 1994. There also appears to be a trend whereby the dip phase becomes progressively later while HU Aqr is in this accretion state.

In conclusion, what emerges from the ROSAT observations of the X-ray dip in HU Aqr is a picture of the characteristics of the accretion stream at large distances from the white dwarf. Clearly the stream is not a static object, the trajectory of the bulk of the stream changes on measurable timescales; nor is its cross-section uniform, the flickering observed demonstrates that the stream has a filamentary or blobby structure even far from the white dwarf. Finally, there

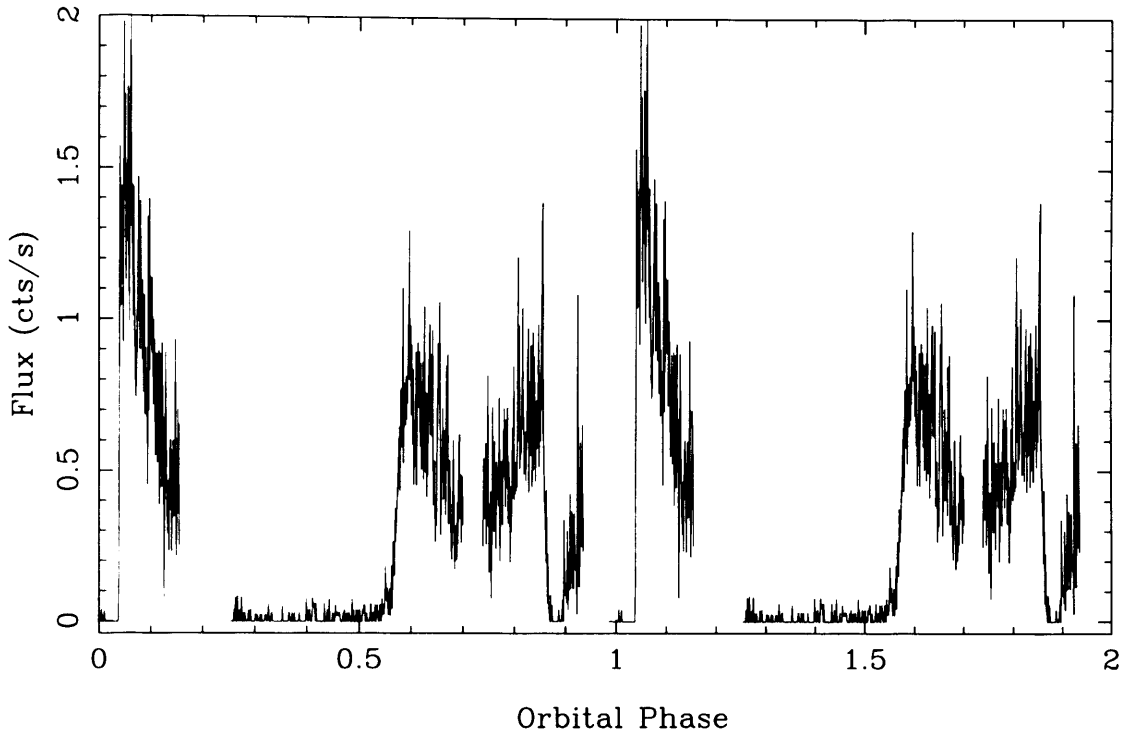


Figure 4.11: The folded light curve from the HRI observation excluding the final observation of the absorption dip. This last dip was significantly shifted in phase with respect to the other four dips.

is evidence that the stream is not even a single entity after threading. A series of streams of varying density arise because each thread the field and leave the ballistic portion of the stream at a different radius from the white dwarf. This is a far more complex situation than the earliest interpretations of X-ray dips suggested.

4.4.2 The broad dip

The broad dip visible in the X-ray light curve (Figure 4.3) is far more of an enigma than the narrower absorption dip at phase 0.90. It is not possible for the accretion stream to produce a dip at $\phi \approx 0.7$ in the same way as the dip at $\phi = 0.9$ because the geometry of the system precludes this. A similar dip feature has been observed in the EUVE light curve of UZ For by Warren, Sirk & Vallergera (1995). It is interesting to note that there is no such feature in the soft X-ray light curve of UZ For from the ROSAT observations presented in Section 5.3.1. Warren et al. suggest that absorption by the accretion stream close to the white dwarf may be the cause for the EUV broad dip. There is no ready explanation for the lack of a similar dip

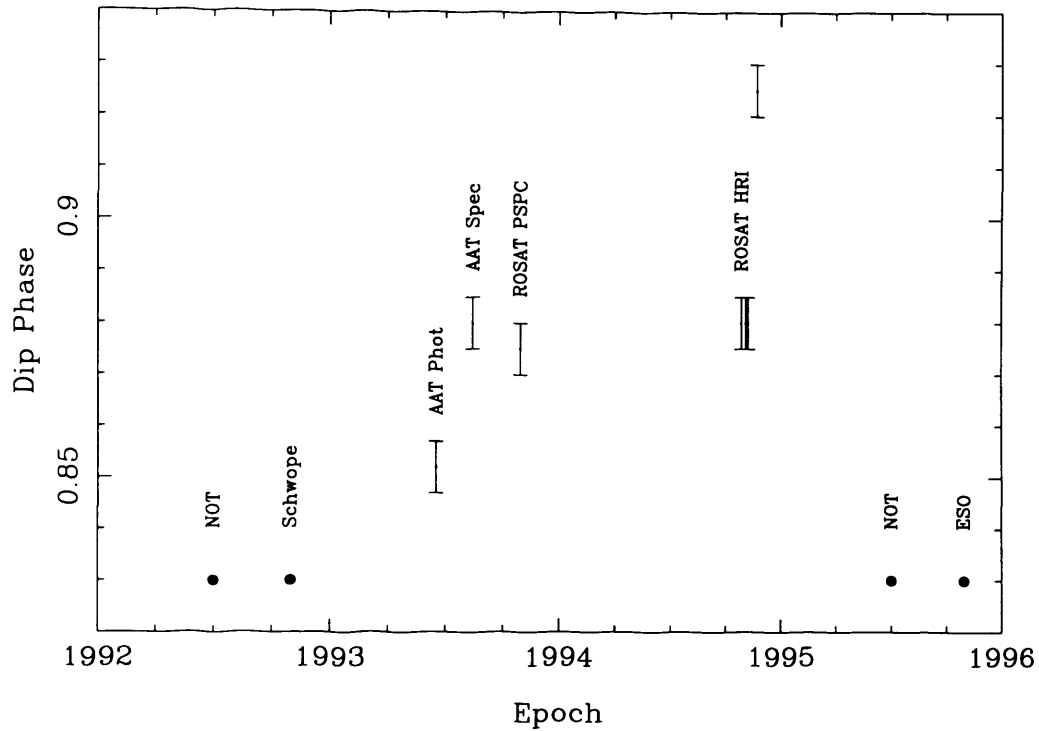


Figure 4.12: The phase of the mid=point of the absorption dip plotted as a function of time. The source of each data point is labeled. Bullets denote observations where no dip was observed.

in the soft X-ray light curve. The spectral band of the ROSAT PSPC is very close to that of EUVE and hence if absorption is seen in the EUV it would be expected that absorption would also be present at soft X-ray energies as well.

Material in the column close to the surface can only obstruct the X-ray region at this phase if the accretion is non-radial. In the case of most polars the accretion region is not located at the magnetic pole but is displaced by 10-20° from it and so the column will not form a right angle with the surface. Should the acute angle between the surface and the column lead the orbital motion (as predicted by the stream trajectory) then obstruction of the pole may occur at a similar phase to the broad dip. This is supported in the case of UZ For by the detection of a short reversal of the circular polarisation at the end of the bright phase (Berriman & Smith 1988, Bailey & Cropper 1991). Such a reversal might be the effect of observing a non-radial column from underneath when it is at the limb of the white dwarf.

This explanation could be applied to HU Aqr but for the fact that no spectral changes are seen

during the broad dip. If the broad dip is associated with photoelectric absorption, which is the most likely X-ray absorption process within the stream, then the hardness ratio is expected to increase as was observed with the narrow dip. Figure 4.3 shows the hardness ratio to be -0.05 throughout the broad dip, only rising at the commencement of the narrow dip, and the hardness ratio after the eclipse is in fact slightly higher than in the broad dip. Both of these features are contrary to what is expected if photoelectric absorption causes the broad dip.

As an alternative, the broad dip could be generated using projection effects alone without invoking absorption by the accretion stream, if the X-ray flux is assumed to arise in a cylinder of gas aligned normally to the white dwarf photosphere. For an optically thick emission region the flux can be regarded as coming from the curved surface of the cylinder alone. From this the relative flux at a given phase can be determined by measuring the projected surface area as seen by the observer. Figure 4.13b shows the light curve produced by this scenario (compare this to the light curve produced by a spot on the white dwarf surface with no height, Figure 4.13a). When looking down the cylinder during the middle of the bright phase the projected surface area of the curved outer surface is at a minimum, and hence a reduction of the X-ray flux is observed. This leads to a bright phase with a broad dip in the middle, the depth of which is determined by how close the observer is to looking straight down the cylinder (i.e. it depends upon i and β). If the inclination were to equal the magnetic co-latitude then the dip would be total. For a cylinder oriented normal to the surface it is impossible for the dip created by this effect to be anywhere other than in the centre of the bright phase.

To off-set the dip from the centre of the bright phase it is necessary only to tilt the accretion column in the direction of orbital motion. Thus the phase at which the observer is closest to looking straight down the cylinder is brought forward. Only a small angle of inclination for the column ($10\text{--}20^\circ$) is required to account for the observed off-set of 0.17ϕ . In addition to placing the broad dip before the centre of the bright phase, this provides an explanation for the apparent asymmetry of the bright phase (comparing the flux at the beginning of the bright phase, $\phi = 0.6$, with that at the end, $\phi = 1.1$, there is almost a two-fold increase in the X-ray flux). At egress the side of the cylinder in view is shorter than at ingress and hence there is less surface area for emission and lower flux. The use of inclined accretion columns may be useful for explaining asymmetric bright phases in other systems, either as an alternative or as a complement to the complex-shaped accretion zones that are often used, as in Cropper (1986). A light curve based

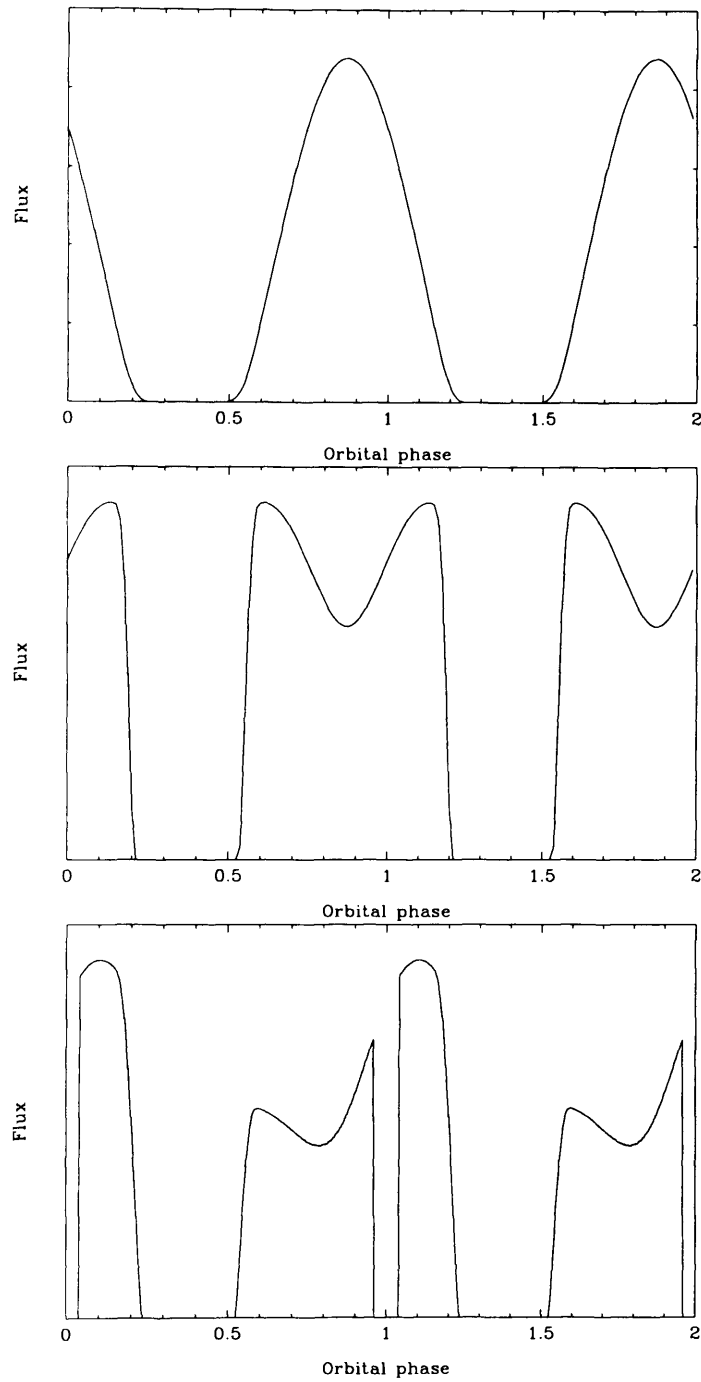


Figure 4.13: Examples of light curves generated using different shapes of emission region on the white dwarf. a) Light curve obtained from a flat spot on the surface of the white dwarf. b) Light curve from a cylindrical emission region. c) Light curve of an inclined cylindrical emission region. As an aid to comparison with the data (Figure 4.3), a representation of the eclipse has been artificially added to this light curve.

| Parameter | Value | Parameter | Value |
|-------------|-------|---------------------------|-----------------|
| Inclination | 85° | Co-latitude | 45° |
| Azimuth | 46.4° | Column height | 0.03 × R_{WD} |
| | | Column Inclination | 10° |
| | | Fractional accreting area | 0.003 |

Table 4.4: Parameters of the X-ray emission used to produce the model light curve shown in Figure 4.13c. Parameters in the first column are based on independent measurements, those on the right were selected to obtain the best match to the observed light curve (Figure 4.3)

on this scenario was produced and is shown in Figure 4.13c. This curve is not a fit to the data, it is just an example based on the parameters listed in Table 4.4. From Figure 4.13c one can see that projection effects can be used to produce a dip at the correct phase with about the right depth and breadth without invoking an absorption effect, and in the process explain the asymmetry of the bright phase. The broad dip detected in the EUVE observation of UZ For was observed to vary in both depth and phase over an interval of some 30 orbits of the system (Warren et al. 1995, Colour Plate 1). Based on this model for the broad dip, such variations can be explained as slight changes in the inclination of the emitting column.

4.4.3 The soft X-ray excess of HU Aqr

The standard model of polar accretion predicts $L_{bb}/(L_{brems} + L_{cyc}) \approx 0.56$ (King & Watson 1987). This ratio has been observed to be as high as 50 in some systems and this confrontation between observation and theory has become known as the soft X-ray problem. From the spectral fitting to the PSPC data, the blackbody-to-bremsstrahlung luminosity ratio for HU Aqr during the bright phase is 43.5 (Table 4.3). The changes to this ratio through the orbital phase are discussed in the next section. Although L_{cyc} cannot be estimated from this study, it is unlikely to be large enough to bring the luminosity ratio down to the predicted level. The presence of a soft excess in HU Aqr confirms that the simple radiative models for the source of emission do not agree with observation.

The ROSAT observation of HU Aqr therefore renders additional support for the inhomogeneous accretion models of Kuijpers & Pringle (1982). Such a need for ‘blobby’ material fits well with the earlier results on the structure of the accretion stream. Evidence has been found in the

structure of both the optical and X-ray absorption dips (§2.6, §4.4.1) for inhomogeneity in the accretion stream at large distances from the white dwarf. This inhomogeneity could be the precursor of the blobs that cause the soft X-ray excess in HU Aqr and flares detected in the X-ray light curve. Although there is currently no direct evidence for this, in the future it may be possible to compare the size of the blobs derived from structure in the absorption dips and from the size of the X-ray flares, and thereby answer the question of whether they have the same origin.

A strong relationship between the luminosity ratio and the magnetic field of the primary was discovered in a study of 11 polars observed with ROSAT (Ramsay et al. 1994, Beuermann & Burwitz 1995). Low dispersion optical spectra have enabled us to estimate the magnetic field of HU Aqr (§3.3.8). A magnetic field of 34 MG and a L_{bb}/L_{brems} ratio of 43.5 is fully consistent with the predictions of both studies.

4.4.4 The X-ray emission regions

Using the distance estimate of 175 ± 25 pc obtained in Section 3.3.7 and the results of the spectral fitting (§4.3.4), the luminosity of HU Aqr at each interval of the orbital cycle can be calculated. The bright and faint phase luminosities over the 0.1–2.4 keV range were found to be $1.0 \pm 0.3 \times 10^{32}$ erg s⁻¹ and $4.8 \pm 1.4 \times 10^{30}$ erg s⁻¹ respectively. Other polars are known to have significant flux during the faint phase (e.g. ST LMi, see Figure 6.1) and a straightforward explanation is that a second, weaker pole on the white dwarf surface is responsible. The spectral analysis undertaken in §4.3.4 demonstrates the key difference between the bright and faint phases; the L_{bb}/L_{brems} ratio is 20 times lower during the faint phase. The hardness ratio light curve in Figure 4.3 does not contradict this result, the faint phase flux is hard. This is entirely consistent with X-ray emission from a second pole.

There is strong evidence to argue against this interpretation. The optical photometry and polarimetry have shown that a second pole is visible from the eclipse to phase 0.26 at some epochs (§2.4.2), which does not match the phase range over which the residual X-ray flux is seen (i.e. the whole faint phase). Although the X-ray and optical observations are separated by five months, both observations took place in a high state, and high states appear to coincide with periods of two-pole accretion in this system (K. Harrop-Allin, private communication).

Indeed, an excess of flux has been detected in the early faint phase; up to $\phi \simeq 0.3$ the mean flux is 0.60 ± 0.01 ct s⁻¹, for the remainder of the faint phase the flux is 0.41 ± 0.01 ct s⁻¹. This is likely to be a marginal detection of a second X-ray pole which is roughly coincident with the second optical pole identified by photometry and polarimetry.

Two origins for the remaining faint phase X-ray flux ($0.30 < \phi < 0.48$) can be envisaged. The flux detected could arise at the main pole and be scattered into the line of sight by the accretion stream. The optical depth for electron scattering, τ_{es} , is given by:

$$\tau_{es} = \sigma_{es} \int_0^s \frac{\rho}{m_H} ds \quad (4.5)$$

where σ_{es} is the *wavelength independent* cross section for electron scattering ($\simeq 6.65 \times 10^{-25}$ cm²) and ρ is the density of the material. The integral is simply the column density, so Equation 4.5 can be rewritten:

$$\tau_{es} = \sigma_{es} N_H. \quad (4.6)$$

A critical column density, above which significant scattering will occur, can be found by setting τ_{es} to 1, hence

$$N_H^{crit} = \frac{1}{\sigma_{es}} = 1.5 \times 10^{24} \text{ cm}^{-2} \quad (4.7)$$

The column densities for the accretion stream, obtained by fits to the absorption dip spectra, lie four orders of magnitude below this value, which suggests electron scattering is a weak effect at best. This indicates that scattering by the stream is probably not the cause of the faint phase flux.

The other possible origin is a more extended emission region on the white dwarf surface, rather than a discrete pole. The wider range of viewing angles would mean that little or no modulation of the flux could occur. This is analogous to recent results by S. Potter which have shown that a fraction of the accretion luminosity at optical wavelengths may arise in many small regions spread over much of the white dwarf's surface, based upon modelling of the optical flux and polarisation variations from polars (presented at the 1997 Keele One-day Workshop on Interacting Binaries). Similar emission regions for HU Aqr could account for the observed faint phase X-ray luminosity.

Another origin for the flux which cannot be completely ruled out is the corona of the late-type secondary. However, the flux detected during the faint phase is over a factor of ten greater

than that during the eclipse (which must come from the secondary, see §4.4.5). If the flux during both the eclipse and the faint phase arises from the secondary then one side of it must be much brighter in X-rays than the other. This is a possibility; the primary facing side of the secondary could have enhanced field structure leading to more activity on the primary side. This activity may arise from the flow of material towards the L1 point, from the effect of the primary's magnetic field on that of the secondary or other factors.

The softening of the PSPC flux detected during the transitions to and from the faint phase cannot arise from the admixture of flux from the main pole and any secondary poles. The flux during the transitions is definitely softer than both the bright and faint phase flux which makes this impossible. The observed softening is therefore indicative of spectral structure within the main emission region itself. A region of softer emission must surround a harder emission region because the softening effect is observed at both ingress and egress to the faint phase. The data are also consistent with softer emission originating *above* the harder emission.

The approximate size and brightness of these emission regions can be determined from a detailed inspection of the egress, which displays the more pronounced softening effect. The egress ends at the same phase (0.60) for both the PSPC and HRI observations. The softening is only seen from phase 0.50–0.56 and therefore a significant portion of the harder emission region has become visible by phase 0.56. If it is assumed that the emission regions are flat spots on the surface of the white dwarf, then the semi-angle δ , subtended at the centre of the primary by that region is given by (Cropper 1986)

$$\delta = [\cos^{-1}(\cos i \cos \beta - \sin i \sin \beta \cos \phi_1) - \cos^{-1}(\cos i \cos \beta - \sin i \sin \beta \cos \phi_2)]/2 \quad (4.8)$$

where i and β are the inclination and the magnetic co-latitude respectively, ϕ_1 is the phase interval between the onset of egress from the faint phase (or the end of the ingress) and the mid-point of the faint phase, and ϕ_2 is the phase interval between the end of the egress (or beginning of the ingress) and the mid-point.

From this it is found that the projected size of the softer region is an annulus with an outer radius of 30° around a harder region of radius 15° . At phase 0.56, the PSPC flux has recovered to 50% of its final flux (at $\phi = 0.60$), implying that at most half the soft X-ray flux arises in the outer, softer emission region. The effect of the broad dip on the shape of the egress is unknown since the exact cause of the broad dip is itself unknown, and this could have an effect upon these estimates.

What physical processes could lead to this spectral structure within the polecap? A softer emission region on the surface of the white dwarf may arise due to hard X-ray irradiation of the photosphere by the accretion column which is then reprocessed into soft X-rays. This would be in accordance with the standard model of accretion (Lamb & Masters 1979). A shock with a height of 15% of the radius of the white dwarf can illuminate a large enough area to account for the softening effect and shock heights of this size are not implausible (Frank, King & Raine 1992).

How could the spectral structure be explained using inhomogeneous accretion models? Discrete blobs of accreting material that penetrate the photosphere do not heat a large enough area on the white dwarf surface to account for the softening in the bright/faint transitions. The only way to account for the spectral change is if the accretion flow consists of blobs with a range of densities. The denser blobs penetrate the photosphere and contribute the strong soft X-ray flux, while the less dense shock above the surface and irradiate a surrounding region. Soft X-rays arise in this region by reprocessing of the hard X-ray flux, and are the cause of the softening in the transitions. This kind of density structure within the stream was also inferred from the structure of the X-ray absorption dips.

The spectral fitting results presented in Table 4.3 show that the major difference between the bright phase and the transition spectra lies in the relative luminosities of the blackbody and bremsstrahlung components, not the blackbody temperature. During the transitions, the blackbody luminosity has been reduced by a factor of 17, while the bremsstrahlung luminosity has only fallen by a factor of 1.5. This suggests that the region that is occulted first (at ingress) is the source of the bulk of the soft X-ray flux. In the first scenario described above, the centre of the emission region contributes mostly hard X-ray bremsstrahlung, while the outer parts emit the reprocessed soft component, and so this scenario is not consistent with the spectral fit results. For the inhomogeneous scenario, the core of the emission region is dominated by the soft X-ray emission from the dense blobs of accreting material while the outer region contributes all the reprocessed soft X-ray flux. This scenario is in much better agreement with the spectral fitting, and is therefore strongly favoured.

4.4.5 Detection of secondary in eclipse

In Section 4.3.5 it was demonstrated that significant soft X-ray flux from HU Aqr is detected during eclipse. What is the origin of this residual flux? During the eclipse the white dwarf is completely obscured and therefore cannot account for the flux. The obvious sources that remain are the accretion stream and the corona of the secondary star. The optical light curves prove that the accretion stream is still visible during the X-ray eclipse. The X-ray flux detected could be scattered into the line of sight by the accretion stream. If such a process were occurring then the X-ray flux detected should increase if more of the stream is visible. In other words, more X-ray flux ought to be detected in the first part of the eclipse, when the pole has been eclipsed but a significant part of the stream is still visible. There is no difference in the X-ray flux between region $\phi = 0.965\text{--}0.985$ and region $\phi = 0.985\text{--}1.035$, within the limited statistics available. Scattering by the stream is therefore ruled out and one must therefore concentrate on the possibility that the X-ray flux in eclipse arises in the corona of the secondary. If confirmed, this would represent the first detection of coronal X-ray emission from the red dwarf companion in a polar, although the possibility of such emission has been suggested in the past.

The activity of late-type stars is directly dependent upon the strength of the dynamo effect in the star, which in turn is determined by the rotation rate. The rotational period of isolated, short period dwarfs is typically eight hours or more, compared to 1.5 to 8 hours for polars, so the activity of the late-type companion in polars should be comparable to that of isolated dwarf stars at least. However, this assumes that the structure of the Roche-filling dwarf in AM Her systems is the same as that for the single red dwarfs, a fact that is by no means certain. When the X-ray luminosity of late-type dwarfs is plotted as a function of the rotational period (Figure 4.14), it is found that the luminosity reaches a maximum of $\approx 5 \times 10^{29}$ erg s⁻¹ below a period of about 5 days (e.g. Stauffer et al. 1994). The X-ray emission for rapidly rotating dwarf stars clearly becomes saturated in some way.

It is uncertain what the exact cause of this saturation is, but it must be due to a limit in the efficiency of the X-ray generation mechanism; for instance the number of active regions on the surface of the star. For HU Aqr the rotational period is 0.087 days, and the X-ray luminosity during eclipse is $4.5 \pm 1.3 \times 10^{29}$ erg s⁻¹ which places the companion in HU Aqr well above the rotational velocities of the fastest rotating single red dwarfs, yet with the same luminosity.

because the higher infall velocities of the accretion stream dominate the emission line profiles. Mass measurements thus often require a further assumption, that the secondary follows the main sequence mass-radius relation. For a review of the considerations involved in mass determination, see Bailey (1995). Such an assumption may not be valid because the effect of filling a Roche lobe upon the star is unknown. If the similarity between the X-ray emission from the dwarf star in HU Aqr and the emission from isolated dwarfs indicates that the internal structures are the same, then the assumption that the main sequence mass-radius relation can be applied to the secondaries in polars may also be valid.

4.5 Summary

The soft X-ray light curve of HU Aqr is rich with structure caused by the rotation of the various portions of the system into and out of the line of sight. Strong and systematic spectral variability has been found, associated with the bright/faint transitions and absorption dip. Straightforward measurement of the bright phase duration and eclipse phase have provided constraints on the geometry of the system and an updated ephemeris.

The X-ray absorption dip of HU Aqr has revealed a great deal about the nature of the accretion flow. Structure at the edges of the dip have suggested that the stream is fragmented into filaments or blobs at large distances from the white dwarf. The trajectory of the stream has been found to be highly variable. These results fit in well with the conclusions drawn from the optical datasets presented in Chapters 2 and 3.

The discovery of a broad dip in the early portion of the bright phase in HU Aqr has been interpreted as arising from an inclined, optically thick accretion column. As a direct consequence of this, the asymmetry of the bright phase is explained. Such inclined columns will have further application, to UZ For and other AM Hers, as will be seen in the next two chapters. A first detection has also been made of coronal X-ray emission from the secondary in an AM Her system by measuring the feeble but significant residual eclipse flux. The luminosity measured is anticipated to be consistent with that predicted for isolated M-dwarf stars at the rotation rate of HU Aqr, although a comparison has so far only been possible with isolated K-dwarfs.

The most interesting and potentially important discovery has been the detection of softening

during the transitions between the bright and faint phases. These are suggestive of a structured emission region on the surface of the white dwarf, comprising a softer region surrounding a harder core. Based on this result, the large collecting area and spectral capabilities of future X-ray missions, like XMM, promise to reveal the emission regions to be highly complex, with structure in all three dimensions.

Chapter 5

ROSAT and quasi-simultaneous optical observations of UZ For

5.1 Introduction

UZ For was first detected by EXOSAT as a serendipitous source in the satellite's low-energy X-ray telescopes (LE1 and LE2) in 1983 and 1986 (Giommi & Angelini 1987). The X-ray flux was strongly modulated; the count rate varied from 0 to 2 ct s^{-1} with a periodicity of ~ 128 minutes (Osborne et al. 1988). The folded light curve of the system displayed a bright phase and faint phase each lasting ~ 0.5 orbital cycles. The bright phase is interrupted by an 8 minute total eclipse. At the time UZ For was the third and brightest AM Her system to have a secondary star eclipse. The orbital period was the longest all AM Hers below the period gap and current theory on AM Her evolution would suggest that the system is just emerging from the gap, the red star having recently reestablished contact with its Roche lobe. In addition, Hameury, Lasota & King (1988) have argued that UZ For must have a higher mass than other AM Her systems to explain its existence at a period greater than the 114 minute period spike.

Follow-up observations by Berriman & Smith (1988) confirmed that UZ For was an AM Her system by the detection of strong optical circular polarisation that varied between +10% and -2% on the orbital cycle. This was also confirmed by Ferrario et al. (1989*a*). Strong optical modulation including the optical counterpart to the X-ray eclipse was found which enabled the period to be refined to 126.5 minutes. Low dispersion optical spectroscopy by Beuerman, Thomas & Schwope (1988) demonstrated that the spectral type of the secondary was M4.5.

This, coupled with the measurement of the radial velocity variations of the emission lines ($K_2 = 395 \pm 67$ km/s), provided a mass estimate for the primary of $0.93 M_\odot$. This is in accordance with the prediction of a high mass primary for UZ For by Hameury et al. (1988). The detection of cyclotron harmonics also enabled the authors to estimate the magnetic field on the primary to be 55 MG, at that time the largest magnetic field measurement of any AM Her system. Ferrario et al. (1989a) found further evidence for a high mass primary in the optical light curve of UZ For. They also argued for the existence of a second emission region on the white dwarf with a magnetic field strength of 28 MG, based on the detection of a peak in the spectrum at 4750\AA that was presumed to be cyclotron emission.

Allen et al. (1989) later refuted that claim because the feature at 4750\AA is seen in isolation at $\phi = 0.25$, and a second pole would have to have a much stronger field than that of the main pole to create such an isolated emission feature in the spectrum. They discuss further possibilities but can provide no explanation for the 4750\AA feature. Allen et al. present the first high-dispersion spectra of UZ For allowing the radial velocity variations of the individual components within the emission lines to be followed. The variations seen were typical of AM Her systems and a model developed by the authors demonstrated that the line emission arises from two regions *within* the accretion stream. High time-resolution optical photometry of UZ For revealed the profiles of the ingress into and egress from the eclipse for the first time. The eclipse begins with a steep ingress followed by a much gentler decline to flux minimum and ends with a gentle rise followed by a steep egress to flux maximum. The duration (<5 s) and depth (75% out-of-eclipse flux) of the rapid transitions indicates that they are associated with a polecap on the white dwarf $\sim 2.6 \times 10^8$ cm in diameter, while the gradual transitions are consistent with an object of diameter 2.6×10^9 cm or greater surrounding the polecap which is probably the white dwarf photosphere. Detailed modeling of the optical eclipse profiles was undertaken by Bailey & Cropper (1991). From their models they derived a mass estimate for the primary ($0.61M_\odot < M_1 < 0.79M_\odot$), an estimate for the inclination (81°) and an estimate for the magnetic co-latitude (150°). The mass obtained in this way is much lower than the spectroscopic value of $M_1 > 0.93 M_\odot$ derived by Beuermann et al. (1988), but the 99 percent confidence limit of the earlier study is $M_1 > 0.63 M_\odot$ which is not inconsistent with the results of Bailey & Cropper (1991)

The results of an early ROSAT observation of UZ For were presented by Ramsay et al. (1993). These confirmed many of the results from the previous EXOSAT CMA observations; strong

modulation in the X-ray flux (count rate variations between 0 and 8 cts s⁻¹), bright/faint phase behaviour and a deep X-ray eclipse. By fitting an absorbed blackbody plus bremsstrahlung spectral model to the bright phase spectrum of the system it was found that 19 eV < kT_{bb} < 25 eV and 7 × 10¹⁹ cm⁻² < N_H < 1.7 × 10²⁰ cm⁻². The soft X-ray excess was also found to be at least a factor of 7 from this fit. A lengthy EUVE observation by Warren et al. (1995) shows the EUV flux to vary between 0 and 0.8 cts s⁻¹ (58–174Å) with similar features in the light curve to the soft X-ray light curve. The eclipse ingress and egress are unresolved even at the 1 s sampling of the EUV light curve. A curious broad dip feature, similar to that seen in the X-ray light curve of HU Aqr (§ 4.4.2), is observed in addition to a narrow absorption dip. The X-ray data are used by Warren et al. to constrain the spot size to <5°. Further modeling of the profiles of the bright-faint transitions showed the spot to be raised vertically by ~ 5% of the white dwarf radius.

Most recently, *Hubble Space Telescope* observations presented by Stockman & Schmidt (1996) demonstrate that the optical/UV eclipse profile has significantly altered since earlier epochs. A longer ingress now follows the steep ingress, and the steep egress no longer reaches the out-of-eclipse flux level, but is followed by a gradual transition (Figure 5.8). This is a similar eclipse profile to that in the optical observation presented in this chapter. An interpretation of this new profile will be presented in § 5.4.5.

The ROSAT observations of UZ For presented in this chapter were primarily motivated by the eclipsing nature of the system. Eclipses by the secondary star in AM Her systems enable the geometry of the system to be defined accurately. This helps to constrain the more detailed models used to describe such features as the bright-faint transitions in the X-ray light curve, the emission line variations arising from emission in the accretion stream, the absorption dip profile and cyclotron emission harmonics. UZ For was the brightest known eclipsing system at the time of the observations and hence was a prime target for undertaking such a programme. UZ For is presented here due to its similarity to HU Aqr. It was already known that both systems have many features in common, for instance they are both eclipsing systems, both display bright-faint phase variations and their orbital periods are similar. In addition to these it turns out that the systems are similar in their more subtle X-ray properties as well, as will be demonstrated in this chapter. Much of the analysis presented here follows the method applied to HU Aqr and the reader is referred to the previous chapter for further details.

5.2 Observations

UZ For was observed by ROSAT on Aug 14, 1991. The total on-target time was 49,496 s, the equivalent of 6.5 orbital cycles of the system. ROSAT observed UZ For continuously, apart from periods of earth occultation and intervals of high particle count. The total baseline of the observation is therefore only 85 ksec (11.2 orbital cycles). UZ For was located off-axis to minimise the flickering due to the wire grid. This will slightly downgrade the spectral quality of the observations, since the spectral response calibration is not well established off-axis (Osborne, private communication). A circular source region of radius 4.9 arcmin. was selected for the data extraction using the method laid out in § 2.3. The nearest source-free region to the target that could be used for determining the background was 25 arcminutes away because of the radial ribs of the window support structure. The large separation should not adversely affect the quality of the background subtraction. ASTERIX, the standard Starlink software for ROSAT data processing was used to perform the reduction of the data.

UZ For was also observed using the Auxiliary Focus Photometer on the 3.9 metre Anglo-Australian Telescope on the nights of Jul 20, Aug 16 and Aug 18, 1991. This observation was intended to coincide as closely as possible with the ROSAT observation. The photometer used an unfiltered GaAs photomultiplier giving a broad wavelength coverage from the atmospheric UV cutoff at about 3400Å to about 8600Å. The HSP3 high speed photometry system was used to record data with a time resolution of 100 ms. The data have been placed on an approximate flux scale using observations of standard stars from Graham (1982). Because of the very broad band the accuracy of the absolute zero point is likely to be only about 20%. These optical observations, the data reduction and a portion of the interpretation of the optical results was carried out by J. Bailey.

5.3 Results

5.3.1 The X-ray light curve

The ROSAT PSPC light curve of UZ For is presented in Figure 5.1. The data from all orbital cycles have been folded and binned into 10 s intervals, using the most recent ephemeris,

obtained from the optical observations presented in this chapter ($T = \text{HJD}2445567.17622 + 0.0878654444E$, J. Bailey, private communication). The light curve of UZ For bears a striking resemblance to that of HU Aqr (Figure 4.3), characterised by a very clear bright phase covering roughly one half of the orbital cycle, interrupted by both an eclipse of the white dwarf (and pole) by the secondary and a dip just prior to the eclipse. The eclipse in X-rays is flat bottomed and total, no significant residual flux is detected during the eclipse. The likelihood of detecting any such residual flux is much smaller for this observation than it was for the on-axis observation of HU Aqr because the larger PSF at large off-axis angles seriously degrades the signal-to-noise. The broad dip feature seen prior to the narrow dip in EUVE observations of UZ For (Warren, Sirk & Valerga 1995) is not evident in the ROSAT light curve.

Using the technique described in section 4.3.1 of reversing the egress and overlaying it on the ingress to determine the mid-point of the bright phase, it was found that the duration of the bright phase is 0.57 ± 0.01 orbital cycles, centred on phase 0.852 ± 0.001 . When overlaid, the ingress and egress to the faint phase match well, indicating that the ingress and egress durations are the same. Figure 5.2 shows the egress reversed and overlaid onto the ingress at the best-fit position. From the duration of the faint phase an estimate of the location of the X-ray emission region on the white dwarf has been made, using Equation 2.1. The magnetic co-latitude was found to be $138^\circ \pm 9^\circ$. The assumptions implicit in this calculation are that accretion is taking place at the magnetic pole, that this accretion is radial and that the emission arises in a flat regions on the surface of the white dwarf (i.e. with zero height). These are reasonable assumptions to make for UZ For at this point, but it should be remembered that they are likely to be invalid since X-ray emission regions with significant height are often required to explain details in the shape of the light curve. The inclination of UZ For was taken to be $81^\circ \pm 2^\circ$, as derived by Bailey & Cropper (1991) from optical data, and this value is used throughout this chapter. The eclipse is off-centre with respect to the middle of the bright phase by $0.148 \phi \pm 0.001 \phi$ and from this the longitude of the pole is estimated to be $53.3^\circ \pm 0.3^\circ$.

The dip that occurs just before the eclipse is analogous to the dip found in the light curve of HU Aqr which was associated with occultation of the pole by the accretion stream. This feature has been detected in several previous observations of UZ For but there have also been a number of others where this feature was not present. The occasional disappearance of absorption dips was also seen in HU Aqr and is discussed in relation to UZ For below.

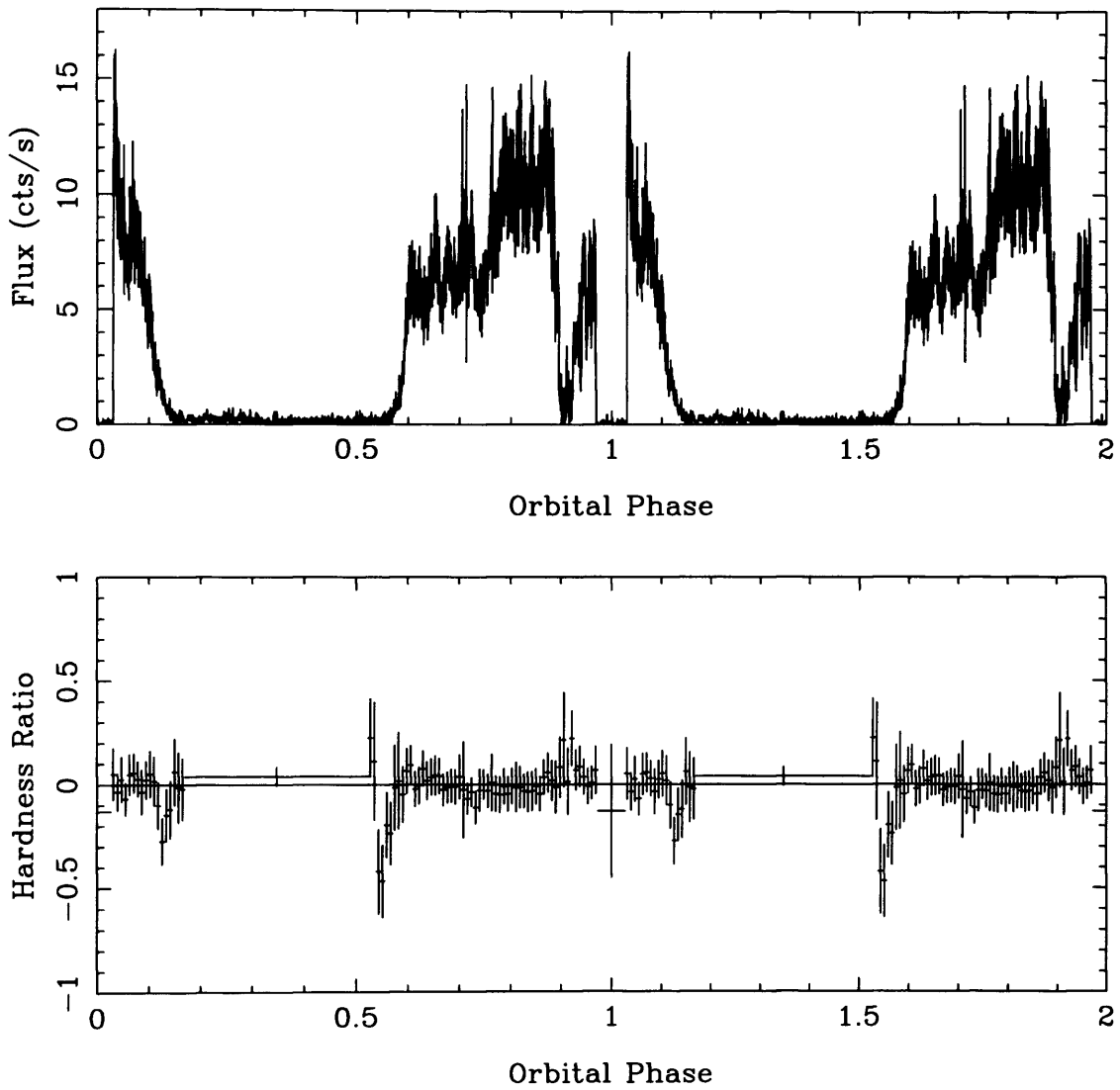


Figure 5.1: The soft X-ray light curve of UZ For. The data have been folded and binned up to a resolution of 10 sec. The lower figure shows the hardness ratio light curve for the data, at a resolution of 60 sec.

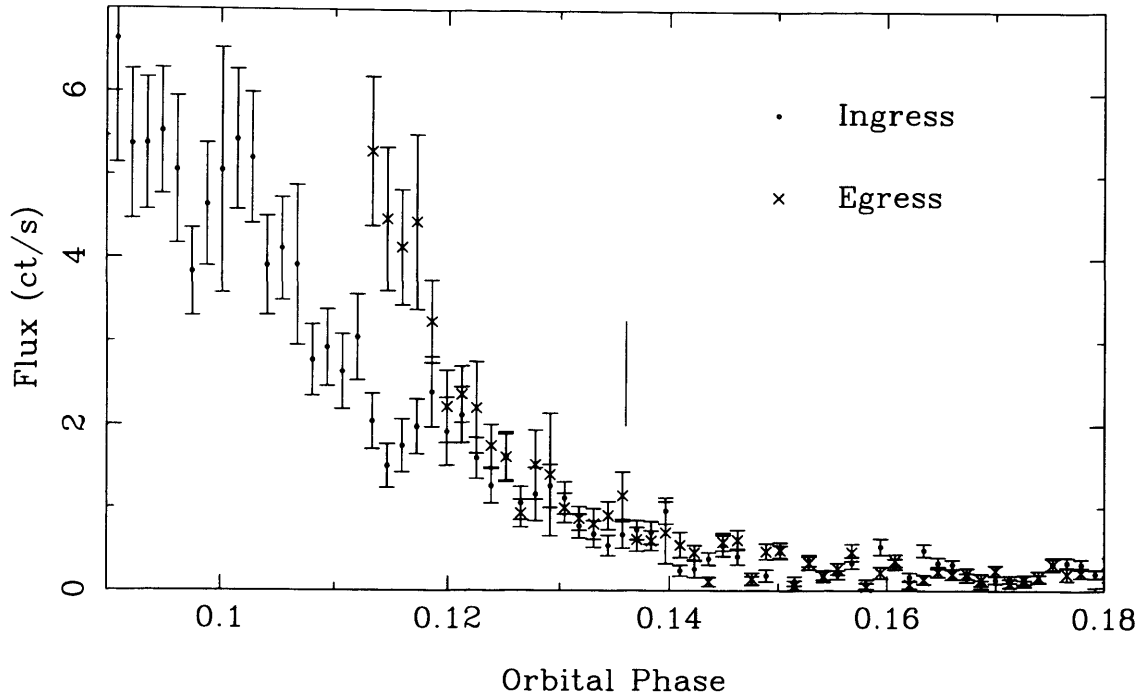


Figure 5.2: The egress from the faint phase of the UZ For light curve reversed onto the ingress. The vertical line marks the phase at which both the ingress and egress exceed 5σ above the mean faint phase flux.

5.3.2 The hardness ratio of UZ For

A hardness ratio light curve for the PSPC observation of UZ For was created, using Equation 4.4 to define the hardness ratio. The softer (0.10-0.19 keV) and harder (0.20-2.4 keV) energy bands were chosen such that the mean hardness ratio was zero. The light curve obtained is shown in Figure 5.1 and displays significant spectral variation on the orbital period. The light curve can be divided into four characteristic phase intervals similar to those chosen for HU Aqr; the bright phase (phase range 0.60–0.86), dip phase (0.89–0.95), the transition phase (0.53–0.59 and 0.11–0.16) and the faint phase (0.16–0.53). Once again, the soft X-ray flux gets softer during the transitions to and from the faint state and harder during the dip.

5.3.3 The phase resolved spectra

In order to study the changes to the spectrum of UZ For through the orbital cycle in more detail, a series of time-resolved spectra were created by collecting the data from the transition

| | Bright | Dip | Faint | Transition |
|-------------------------------------|-------------------------|-------------------------|-------------------------|-------------------------|
| Phase | 0.60–0.86 | 0.89–0.95 | 0.16–0.53 | 0.11–0.16 0.53–0.59 |
| Flux (ct s ⁻¹) | 3.99 ± 0.02 | 1.70 ± 0.03 | 0.095 ± 0.003 | 0.37 ± 0.01 |
| kT _{bb} (eV) | 35.5 | 37.6 | 39.5 | 28.5 |
| Norm _{bb} | 3.18 × 10 ⁻⁴ | 1.42 × 10 ⁻⁴ | 5.3 × 10 ⁻⁶ | 4.46 × 10 ⁻⁵ |
| N _H (cm ⁻²) | 1.14 × 10 ¹⁸ | 10.9 × 10 ¹⁸ | 0.0 × 10 ¹⁸ | 5.98 × 10 ¹⁸ |
| Norm _{brems} | 1.52 × 10 ⁻⁴ | 1.70 × 10 ⁻⁴ | 1.30 × 10 ⁻⁴ | 9.24 × 10 ⁻⁵ |
| χ _ν ² | 1.045 | 0.721 | 0.897 | 0.829 |
| L _{bb} /L _{brems} | 18.4 | 8.8 | 0.49 | 1.85 |

Table 5.1: Results of the spectral fits to the phase resolved spectra of UZ For. The bremsstrahlung temperature has been fixed to 30 keV in all of these fits.

phase, dip phase, bright phase and faint phase intervals listed above. The data was re-binned to improve the statistics, then fit with a bremsstrahlung plus absorbed blackbody model. XSPEC was used to undertake the spectral fitting (see section 4.3.4 for a brief description of XSPEC). It was confirmed that the data could be fit by a range of bremsstrahlung temperatures because of the limited bandpass of the PSPC and so the temperature of this component was fixed to 30 keV for all of the spectral fitting. This is the same bremsstrahlung temperature selected by Ramsay et al. (1993) for their spectral fits to the 1990 observation of UZ For. The resulting best-fit spectral parameters are listed in Table 5.1. Figure 5.3 shows the spectra for each of the phase intervals, with the best fit model superimposed. The 68%, 90% and 95% confidence contours in the blackbody temperature (kT_{bb}) versus column density (N_H) plane are given in Figure 5.4 for each phase interval.

UZ For emerges as another AM Her system that cannot be described by a single spectral model. The hardness ratio light curves and the results of the phase-resolved spectral fitting demonstrate that the spectrum varies significantly over the orbital period. The mean bright phase spectrum is well fit by a bremsstrahlung plus absorbed blackbody model. The fit obtained to the dip phase data has both a higher column density and a slightly higher blackbody temperature. Inspection of the contour plots in Figure 5.4 shows that the two fits overlap only at the 99% confidence level. When fitting the model to a spectrum from the core of the absorption dip, the best-fit column density rises to $2.6 \pm 0.4 \times 10^{19} \text{ cm}^{-2}$. Ramsay et al. (1993) performed spectral fits to the 1990 ROSAT observation of UZ For, their Figure 4 shows the confidence contours in the blackbody temperature versus hydrogen column density plane for their fit to the data.

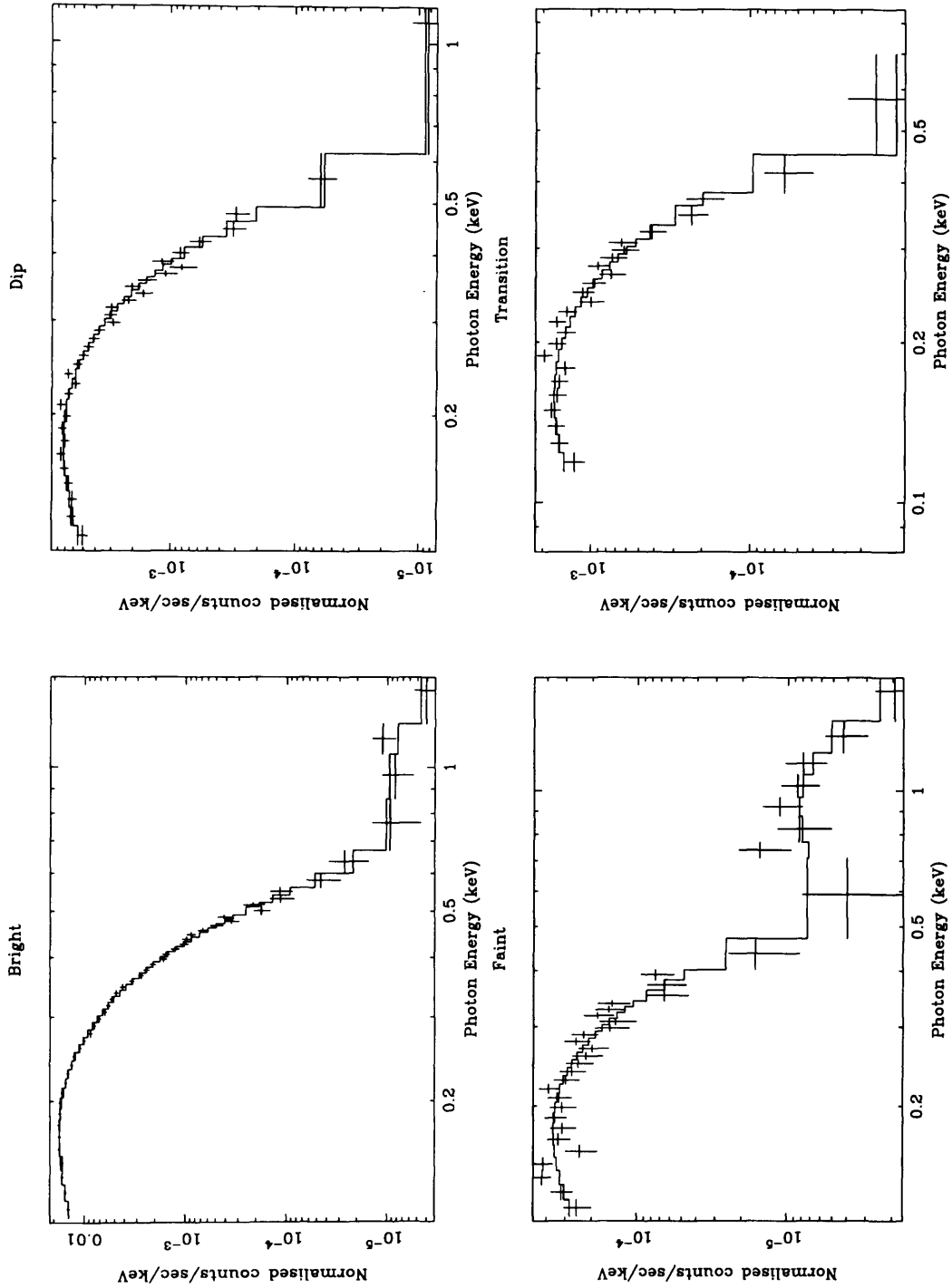


Figure 5.3: The ROSAT PSPC spectra from the four phase intervals listed in Table 5.1. The best fit spectra corresponding to the parameters given in Table 5.1 are shown overlaid onto the data as a solid line.

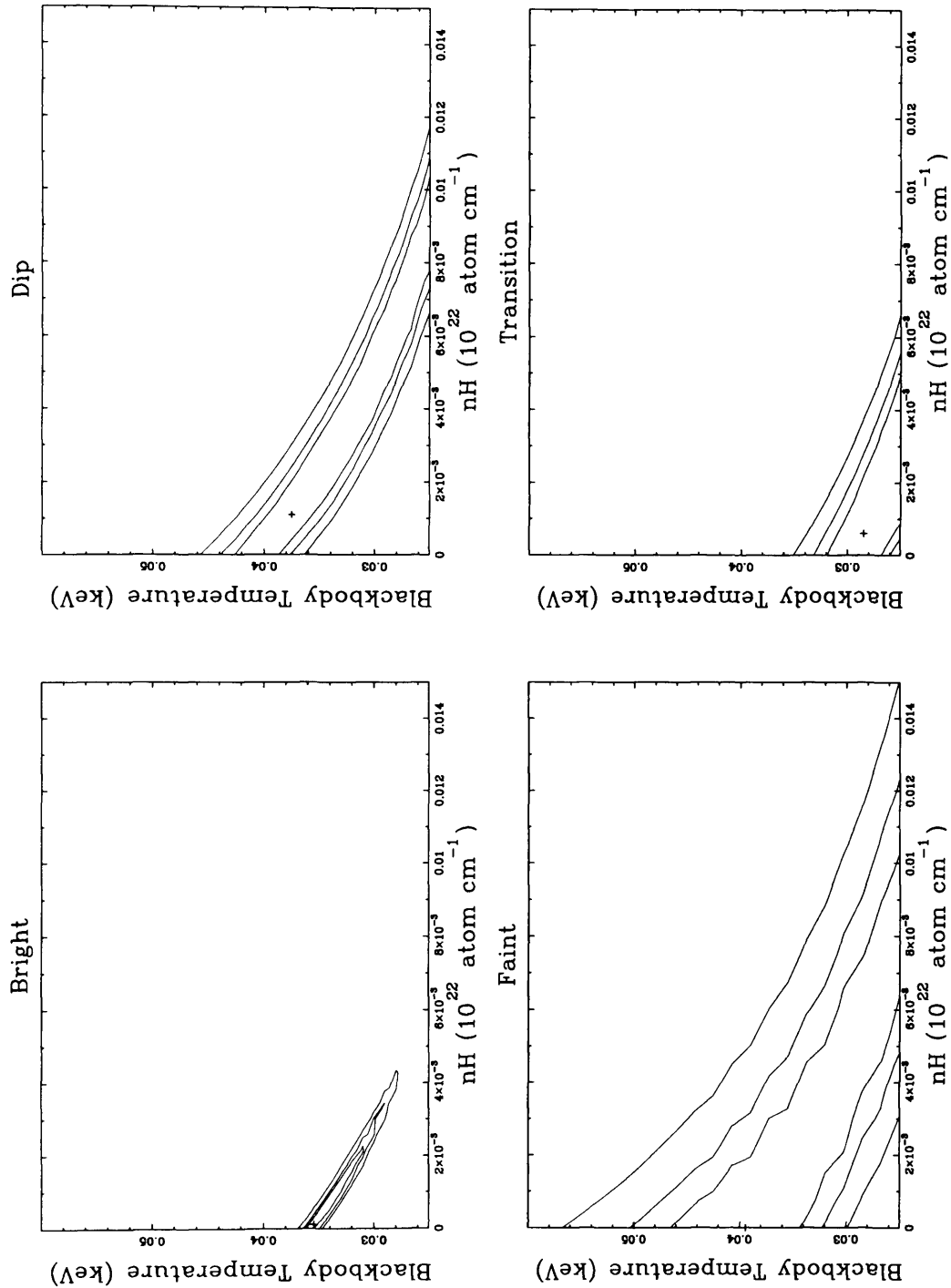


Figure 5.4: Confidence contours in the blackbody temperature versus hydrogen column density plane for the best fits to the spectra shown in Figure 5.3. The 68%, 90% and 99% contours are shown.

Comparison of this figure with Figure 5.4 demonstrates both that the fitting in 1990 is not as well constrained as the fitting presented here (the exposure time in 1990 was only 15 ksec) and that the fitting results are consistent with each other, since the 90% confidence contours from both datasets overlap completely. The poorly constrained fits to the faint phase spectrum do not indicate any spectral difference between the bright and faint phase intervals. The fit to the transition spectrum does reveal that a spectral change is occurring, probably to the blackbody temperature rather than the column density.

5.3.4 The optical light curve

Figure 5.5 plots the optical light curves from the three nights of observation in 1 s bins and the X-ray data in the soft and hard bands in 2 s bins. Only the region around the eclipse is shown. UZ For was in a bright state during these observations with a broad band flux outside eclipse of about 1.1 mJy corresponding to a V magnitude of 16.3. This is brighter than most previous observations, and the eclipse light curves differ substantially from previous high resolution data (Allen et al. 1989, Bailey & Cropper 1991). The previous eclipses showed a very fast component (<5 s) in the ingress and egress which was identified with the accretion spot, and a slower component (about 40 sec.) identified with the white dwarf photosphere. The slower component follows the fast component on ingress and precedes the fast component on egress. Although these components are still visible in the 1991 data, there are additional features. The most notable is that there is an even slower component visible at ingress up to phase 0.995 and at egress from phase 0.03 to 0.07.

5.4 Discussion

5.4.1 The narrow dip

The dip just prior to the eclipse in the light curve of UZ For displays most of the characteristics of the absorption dip seen in HU Aqr. It is therefore logical to suppose that the X-ray dip in UZ For can also be attributed to photoelectric absorption by the accretion stream. The dip is associated with an increase in the column density; from $8 \pm 3 \times 10^{18} \text{ cm}^{-2}$ during the bright phase to $26 \pm 4 \times 10^{18} \text{ cm}^{-2}$ in the core of the dip. This is consistent with the energy dependence

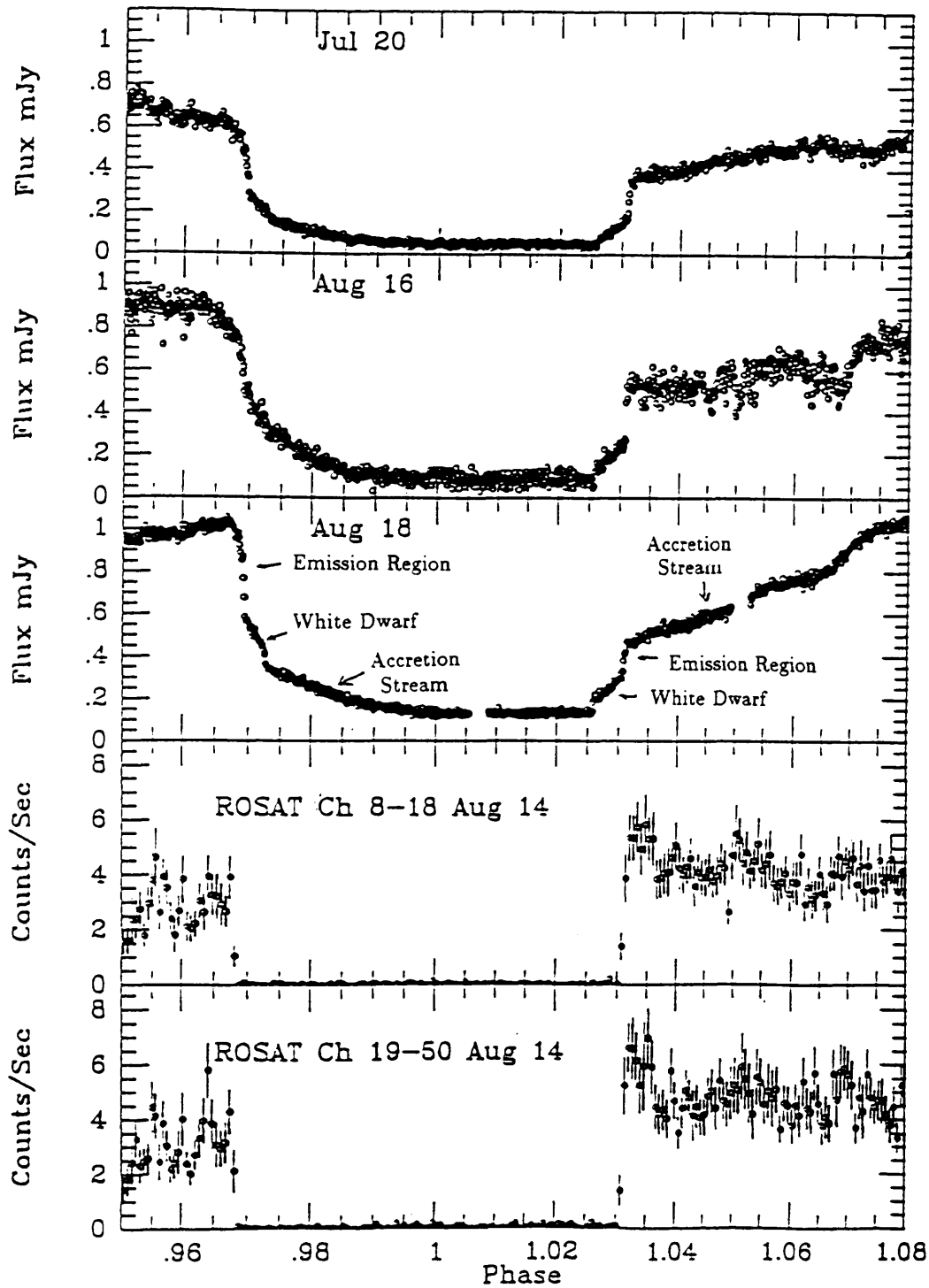


Figure 5.5: The optical light curve from the three nights of observation at the AAT. Only the region around the eclipse is shown. The portions of the ingress and egress associated with the various elements of the system are indicated on the Aug 18 light curve. The two lower panels display the soft and hard band X-ray light curves from the ROSAT observation on Aug 14 at 5s resolution.

of photoelectric absorption ($\tau_X \propto E^{-3}$, see §4.4.1).

The edges of the dip are also highly structured and variable. Figure 5.6 shows the dip from each of the individual observation slots where it was detected. The structure is evident as short (30-80 sec) intervals of zero flux interspersed within a mean flux level of ~ 8 cts s^{-1} . The shape of the individual dips changes markedly in spite of the short baseline of the observation (only 7 cycles separate the first and last absorption dip observed). The fourth dip observed (in orbital cycle 7) is barely detectable as a slight increase in the duration of the intervals of zero flux, whereas the second and third dips are quite well defined. There is no chance that any of this structure is associated with the wire grid since this observation was conducted with the source off-axis. The flickering is evidence that a non-uniform body is causing the occultation, and that this body also varies over time. Such an object could only be the stream, and so it is concluded both that the accretion stream in UZ For causes the dip in the light curve and that it is comprised of inhomogeneous blobs or filaments within a more tenuous medium.

Between the absorption dip and the eclipse the light curve of HU Aqr displayed evidence that the accretion stream was still causing absorption effects. This evidence was continued flickering, a failure of the flux to recover to its pre-dip level, and a continuously high hardness ratio up to the eclipse. UZ For does not exhibit all of these features at these phases in its light curve. There are still the intervals of zero flux that indicate that parts of the stream may still be occulting the pole on the white dwarf. However, the mean flux level recovers more than HU Aqr did between the dip and the eclipse, and the hardness ratio does not remain high between the dip and eclipse. This implies that the nature of the absorption by the stream in UZ For is different to that seen in HU Aqr. The accretion process occurring in UZ For and HU Aqr may appear the same in terms of their general characteristics, but they clearly differ in detail.

Table 5.2 is a log of UZ For observations since 1983, and lists whether an absorption dip was detected or not for each. The intermittent disappearance of the dip is further indication that the dip is caused by a non-stable object that can only be the accretion stream. Note that no optical dips have been detected from UZ For. None of the optical observations were completely simultaneous with an X-ray observation, but the lack of an optical dip in the 1991 AAT observation that is separated by only two days from a ROSAT observation (where a dip *was* present) suggests that an optical counterpart to the X-ray dips may not exist at any epoch. Only a

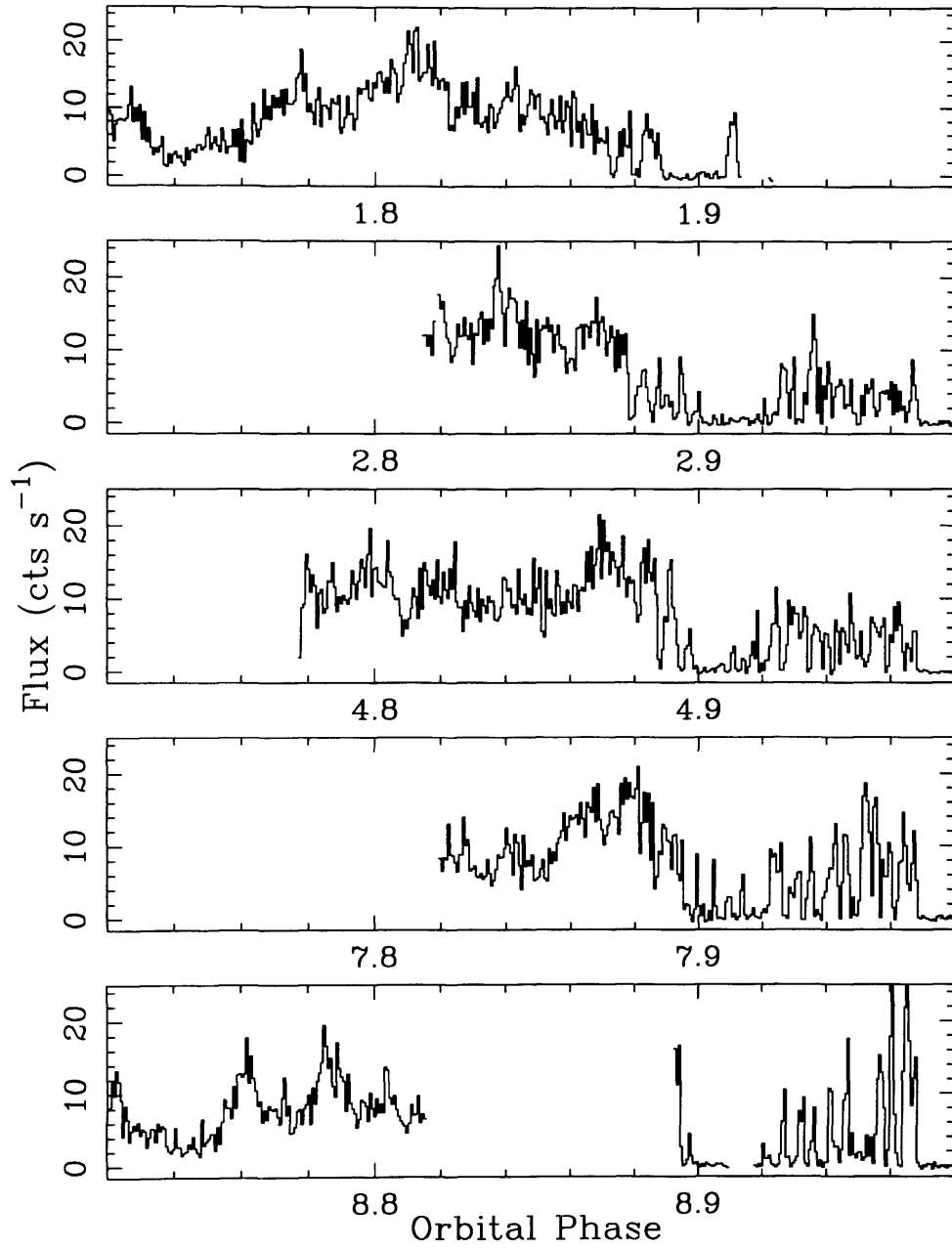


Figure 5.6: Detail of the five individual PSPC observations of the absorption dip.

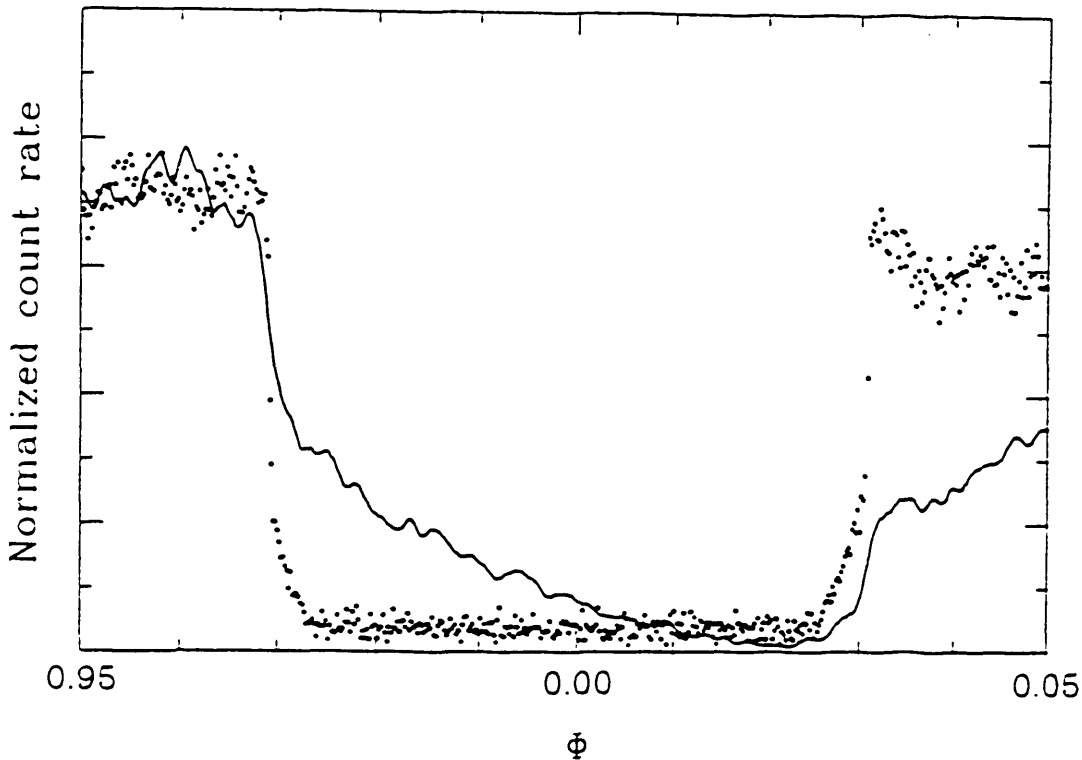


Figure 5.7: Near-UV *HST* data (lines) with the BG39 observations of Bailey & Cropper (1991) (dots) overlaid. Taken from Figure 6 of Stockman & Schmidt (1996).

very small column density increase is measured from the X-ray dip (it is an order of magnitude smaller than that for HU Aqr), so a low optical opacity is expected.

Stockman & Schmidt (1996) present optical and UV light curves of UZ For from an *HST* observation in 1992. This light curve is like that of the 1991 AAT observation in that it displays a long ingress and egress associated with the accretion stream. These eclipse profiles are different to that observed by Bailey & Cropper (1991). Figure 5.7 displays the optical light curve from Bailey & Cropper with the near-UV light curve from Stockman & Schmidt (figure taken from Stockman & Schmidt 1996). The two profiles are markedly different.

In §2.5 it was noted that the changing shape to the optical eclipse profile of HU Aqr appeared to be related to the presence or absence of an absorption dip. This was explained by changes to the trajectory of the accretion stream; when dips are absent the accretion stream becomes more

| Date | Observatory | Dip? | Reference |
|----------|-------------|------|----------------------------------|
| 1983 Aug | EXOSAT | Y | Osborne et al. (1988) |
| 1986 Jan | EXOSAT | Y | Osborne et al. (1988) |
| 1987 Oct | La Silla | N | Beuermann et al. (1988) |
| 1987 Nov | Steward | N | Berriman & Smith (1988) |
| 1987 Dec | AAT | N | Ferrario et al. (1989 <i>a</i>) |
| 1989 Oct | AAT | N | Bailey & Cropper (1991) |
| 1990 Jul | ROSAT | N | Ramsay et al. (1993) |
| 1991 Aug | ROSAT | Y | This thesis |
| 1991 Aug | AAT | N | This thesis |
| 1992 Jun | HST | N | Stockman & Schmidt (1996) |
| 1993 Aug | EUVE | Y | Warren et al. (1995) |

Table 5.2: Log of UZ For observations. The presence or absence of a dip is indicated.

extended in the y -direction (perpendicular to the line of centres in the orbital plane) thereby causing the long optical ingress. Unfortunately, it is impossible to say whether this is also the case for UZ For because of the lack of optical photometric observations simultaneous with X-ray observations. Changes to the duration of the long optical ingress in UZ For have been observed; in 1991 and 1992 a long accretion stream ingress is evident, but not at some other epochs. Such sparse data are insufficient to comment on the link between the optical eclipse profile and X-ray absorption dips. This demonstrates the importance of obtaining simultaneous optical photometry when making X-ray observations of AM Her systems. Further observations of both HU Aqr and UZ For may confirm the correlation between dips and the duration of stream ingress and hence provide a valuable insight into the way the accretion stream trajectory can vary.

Warren et al. (1995) reported a broad dip feature prior to the absorption dip and eclipse in a 1993 EUVE observation of UZ For. A soft X-ray counterpart to this broad dip was evident in the 1990 ROSAT observations (Ramsay et al. 1993), but not in 1991 (this thesis). It was argued for HU Aqr that the broad dip arises due to projection effects from an optically thick, inclined accretion column and the same argument can apply to the UZ For broad dip in the EUV. Based on this interpretation, the lack of a broad dip in the soft X-ray light curve suggests that the tilt of the column has changed such that the dip no longer occurs. Warren et al. observed both the depth and the phase of the broad dip to change on a timescale of several orbits. Because changes to the way accretion is taking place are clearly altering the depth and phase of the

broad EUV dip there is no reason why they could not also account for the absence of a broad soft X-ray dip at some epochs. Simultaneous EUV and X-ray observations would be useful to confirm that the broad dip is not present at X-ray wavelengths when it is at EUV wavelengths. Such observations may enable the origin of the broad dip to be established conclusively.

5.4.2 The X-ray emission regions

The bright phase and faint phase X-ray luminosities derived from the spectral fitting are $2.5 \pm 1.1 \times 10^{31} \text{ erg s}^{-1}$ and $1.69 \pm 0.7 \times 10^{30} \text{ erg s}^{-1}$ respectively (assuming a distance of $208 \pm 40 \text{ pc}$ quoted in Ferrario et al. 1989a). Clearly significant soft X-ray emission has been detected from UZ For during the faint phase. The spectral fitting reveals that the L_{bb}/L_{brems} ratio is almost 40 times lower in the faint phase than in the bright phase (note that this factor is twice that measured for HU Aqr). As with HU Aqr, possible origins for this flux include the secondary, emission from the white dwarf surface (possibly a second pole) and scattering by the accretion stream.

It was shown in Section 4.4.4 (Equation 4.7) that a critical density exists, below which electron scattering is not likely to be a strong mechanism ($N_H^{crit} = 1.5 \times 10^{24} \text{ cm}^{-2}$). The column densities for the stream in UZ For are $\sim 10^{18} \text{ cm}^{-2}$, so scattering by the stream is likely to be a weak effect. This argues against the stream as a source of the faint phase flux.

The faint phase flux is unlikely to arise on the secondary because it exceeds the eclipse flux by at least two orders of magnitude (though there are arguments in favour of enhanced X-ray emission from the primary-facing side of the secondary, see Section 4.4.4). Evidence for a second pole in UZ For has been found from the optical studies of Ferrario et al. (1989a) and Schwöpe et al. (1990). In section 5.4.5 it is also shown that the optical eclipse profile obtained four days after this ROSAT observation displays a new feature which can only be associated with a second pole. Given that the main accreting pole is located below the orbital plane (in the farther hemisphere), this second emission region probably lies in the upper hemisphere and is visible for much of the orbital cycle. the lack of modulation of the optical flux during the faint phase, suggests that any secondary emission region is spread over a large area.

The hardness ratio light curve (Figure 5.1) and the results of the spectral fits to the bright and

transition phase spectra demonstrate conclusively that the spectrum of UZ For changes at either end of the bright phase. This is consistent with a structure to the main emission region on the white dwarf comprising a core of emission with a harder spectrum than its surroundings. The softening observed cannot be the product of the admixture of the flux from the main pole with that from any secondary poles because the flux from both the bright and faint phases is harder than the transition flux. In the 1990 ROSAT observation of UZ For (Ramsay et al. 1993) an increase in the 8–18/19–40 channel ratio (softness ratio) from 1.02 ± 0.06 in the bright phase to 1.5 ± 0.3 during the egress from the faint phase was detected (the ingress was not observed). This demonstrates that such softening represents a long term feature of the system.

Ramsay et al. (1993) have fit a light curve to the faint state egress from the 1990 data, based upon an emission spot on the surface of the white dwarf rotating into view over the limb. They comment that the light curve shape is consistent with a large region of emission around a more luminous and probably hotter core, where the bulk of the accretion is occurring. Therefore the light curve shape is itself consistent with the picture of the accretion region that was deduced from the spectral changes alone. An analysis carried out by M. Watson and P. Hakala on the 1991 ROSAT data from UZ For modelled the shape of the bright/faint transitions, shown in Figure 5.2, with emission regions of various shapes. It was found that the shape cannot be fit simply by a flat region, more success was achieved using a region with significant vertical height.

The duration of the softening effect allows an estimate to be made of the size of the emission regions involved. The ingress to the faint phase begins at 0.07ϕ and the softening during the ingress occurs between 0.11ϕ and 0.15ϕ . Correspondingly, the softening during egress lasts from 0.54ϕ to 0.57ϕ while the overall egress ends at 0.60 . The semi-angle δ subtended by the core and soft region can then be obtained using Equation 4.8 (Equation 9 from Cropper 1990):

$$\delta = [\cos^{-1}(\cos i \cos \beta - \sin i \sin \beta \cos \phi_1) - \cos^{-1}(\cos i \cos \beta - \sin i \sin \beta \cos \phi_2)]/2 \quad (5.1)$$

From this it is found that the core of emission has a radius of $\sim 6^\circ$ and the softer region surrounding it has a radius of $\sim 10^\circ$. A very rough estimate of the relative brightness of the core and surrounding regions associates half of the bright phase flux with each.

The favoured explanation for the softening seen in HU Aqr, given in Section 4.4.4, is that it arises due to irradiation of a large area on the white dwarf by a shocks standing up to 15% of the white dwarf radius above the photosphere. These shocks arise from the less dense portions

softening during the transitions. UZ For is in line with this prediction because it has a smaller soft X-ray excess than HU Aqr and displays a stronger softening effect during the transition phases (see Figures 4.3 and 5.1).

5.4.4 The optical eclipse profile

The complex profiles of the ingress and egress to the optical eclipse in the 1991 AAT observation of UZ For in Figure 5.5 can be interpreted as follows. The ingress begins with a rapid loss of flux at phase $\phi = 0.967$, in which the optical flux decreases by $\sim 40\%$ in a very short interval. This implies an extremely bright and compact object, which can only be the pole on the white dwarf. There is less than a 5 s difference between this rapid optical ingress and the ingress to eclipse in the X-ray light curve. The X-ray ingress indicates the eclipse of the X-ray emitting pole, which is expected to be at the same location as (or very close to) the optical pole. Thus the X-ray light curve provides confirmation that the rapid change in the optical arises from the eclipse of the pole.

Between phase 0.9685 and 0.9725 a more gradual transition occurs which is the eclipse of the white dwarf. The relative size and brightness of the white dwarf and pole match those observed at other epochs, which supports this interpretation. Finally, there is a long, even slower decline down to flux minimum at about phase 0.995. Because of the size of this component it must be the eclipse of the accretion stream. This component was not detected in previous observations of UZ For (e.g. Bailey & Cropper 1991), which took place when the system was in a faint state. This is consistent with a reduced brightness of the stream at these epochs. It could be argued that the white dwarf eclipse is actually part of the accretion stream eclipse, and the gradient change arises from a change in the brightness along the accretion stream. The egress profile rules this out as will be explained below.

The order in which the optically bright elements of the system emerge from eclipse is different to the order that they are detected at ingress. The white dwarf egress occurs first, then the pole egress follows. The pole is again distinguishable by a large change in flux in a short interval, and by the X-ray egress. There can be no doubt that an object undergoes egress before the pole does, because the X-ray egress fixes the position of the pole egress absolutely. Due to the geometry of the system it is impossible for the stream to emerge before the pole and white dwarf. This

softening during the transitions. UZ For is in line with this prediction because it has a smaller soft X-ray excess than HU Aqr and displays a stronger softening effect during the transition phases (see Figures 4.3 and 5.1).

5.4.4 The optical eclipse profile

The complex profiles of the ingress and egress to the optical eclipse in the 1991 AAT observation of UZ For in Figure 5.5 can be interpreted as follows. The ingress begins with a rapid loss of flux at phase $\phi = 0.967$, in which the optical flux decreases by $\sim 40\%$ in a very short interval. This implies an extremely bright and compact object, which can only be the pole on the white dwarf. There is less than a 5 s difference between this rapid optical ingress and the ingress to eclipse in the X-ray light curve. The X-ray ingress indicates the eclipse of the X-ray emitting pole, which is expected to be at the same location as (or very close to) the optical pole. Thus the X-ray light curve provides confirmation that the rapid change in the optical arises from the eclipse of the pole.

Between phase 0.9685 and 0.9725 a more gradual transition occurs which is the eclipse of the white dwarf. The relative size and brightness of the white dwarf and pole match those observed at other epochs, which supports this interpretation. Finally, there is a long, even slower decline down to flux minimum at about phase 0.995. Because of the size of this component it must be the eclipse of the accretion stream. This component was not detected in previous observations of UZ For (e.g. Bailey & Cropper 1991), which took place when the system was in a faint state. This is consistent with a reduced brightness of the stream at these epochs. It could be argued that the white dwarf eclipse is actually part of the accretion stream eclipse, and the gradient change arises from a change in the brightness along the accretion stream. The egress profile rules this out as will be explained below.

The order in which the optically bright elements of the system emerge from eclipse is different to the order that they are detected at ingress. The white dwarf egress occurs first, then the pole egress follows. The pole is again distinguishable by a large change in flux in a short interval, and by the X-ray egress. There can be no doubt that an object undergoes egress before the pole does, because the X-ray egress fixes the position of the pole egress absolutely. Due to the geometry of the system it is impossible for the stream to emerge before the pole and white dwarf. This

| Object | Ingress | Egress |
|-------------|---------|--------|
| Stream | 0.40 | 0.50 |
| White Dwarf | 0.25 | 0.20 |
| Pole | 0.20 | 0.15 |
| Residual | 0.15 | 0.15 |

Table 5.3: The contribution to the optical flux by the various elements of the system, in mJy , at both ingress and egress. See the text and Figure 5.5 for a description of each element. ‘Residual’ refers to the flux observed at eclipse minimum, which arises mostly from the secondary star.

leaves the white dwarf photosphere as the only candidate for the first egress. Having detected the white dwarf in the egress with a significant brightness it is also expected to be present in the ingress. This is confirmation that the ingress at $\phi = 0.9685$ is due to the white dwarf and not a part of the stream.

There is an additional rapid drop on ingress at phase 0.9725 and a corresponding rise on egress at phase 0.0260, most visible in the August 18 data. These are most likely associated with something on the white dwarf rather than the stream, as they occur at the same phase with respect to the white dwarf at both ingress and egress. It is reasonably certain that this feature is associated with a second accretion region, probably located near the second magnetic pole on the white dwarf. The existence of such an emission region had been suspected from earlier spectroscopic and photometric data (Ferrario et al. 1989*a*, Schwöpe et al. 1990).

The brightness of all the contributors to the optical flux at both ingress and egress are listed in Table 5.3. The accretion stream contributes a surprisingly large amount of the optical flux, in much the same way as the stream in HU Aqr was found to do. The flux detected from the pole decreases from ingress to egress which could be consistent with limb darkening and projection effects as the pole rotates around the surface of the white dwarf.

5.5 Summary

The soft X-ray properties of UZ For have been shown to resemble those of HU Aqr in many ways. Apart from small differences in the geometry, the soft X-ray light curve of UZ For has produced identical results to HU Aqr; a variable, highly structured absorption dip with a strong increase

in hardness and a structured emission region that causes softening during the transitions to and from the faint phase. Notable differences include a completely different optical eclipse profile, arising because the accretion stream in UZ For is fainter while the white dwarf is relatively brighter, and a lack of a broad dip, although a similar structure has been detected at Extreme UV wavelengths.

UZ For therefore provides confirmation that some of the most interesting features found in HU Aqr are not unique to that system. This has motivated, in part at least, the X-ray study presented in Chapter 6 wherein the soft X-ray light curves and hardness ratios of a large set of AM Hers will be investigated.

Chapter 6

ROSAT pointed observations of AM Her systems

The light curves and hardness ratio data that can be derived from the ROSAT observations of AM Hers provide a wealth of information about the nature of these systems. As has been demonstrated in the two preceding chapters on HU Aqr and UZ For, the light curves are dependent on the accretion geometry and system geometry while changes to the spectrum of the soft X-ray flux reveal the structure of the emission regions on the white dwarf and of the accretion stream. The availability of archival ROSAT data via the LEDAS data archive at the University of Leicester provides the opportunity to inspect the light curve morphology and spectral variability of all AM Hers observed with the ROSAT PSPC. Previous studies have concentrated on the phase-averaged spectra of the AM Her systems, mostly in an effort to understand the soft X-ray excess (e.g. Ramsay et al. 1994). Analysis of the X-ray light curves of the polar population would complement such analyses. In this chapter the results of a study of the light curves from ROSAT PSPC pointed observations of 30 AM Her systems are presented.

6.1 Selection criteria

The systems selected for inclusion in this study were taken first from Table 6.1 of Warner (1995). This table lists the 42 systems confirmed as polars at the time of going to press, in late 1994. The 20 systems listed by Warner as probable polars (see his Table 6.2) were later added to the study. Further references (Beuermann & Thomas 1993, Kolb & de Kool 1993, Beuermann et al. 1995)

that include lists of confirmed or probable polars provided one additional system not listed by Warner (RE J1846+55). A search was made for public PSPC observations of these 63 systems in the ROSAT Data Archive. Selection of the systems was based upon the maximum orbital coverage available (i.e. the exposure time/orbital period). Table 6.1 lists all AM Her systems considered, their positions, orbital periods and why they were excluded from the study if that was the case. In general, the reason for most of the exclusions was because the system was not observed by ROSAT or the observation was too brief to be useful (typically <1 orbital cycle). Of the candidate systems in Table 6.2 of Warner (1995), seventeen were excluded for one of these two reasons and are not included in Table 6.1. BY Cam was not included in the study because of its asynchronicity and generally complex behaviour which would be difficult to incorporate into an interpretation of the properties of the class as a whole. RE1940-10, another asynchronous system with similar characteristics to BY Cam, was left in the sample because there is some debate as to the identification of a dip as either a stream or secondary star occultation. Despite being observed for over four orbital cycles, the signal-to-noise of the ROSAT light curve from the polar candidate GQ Mus was too low to warrant inclusion in the study.

6.2 Reduction method

The reduction of the data followed similar lines to that followed for HU Aqr and UZ For. Circular source regions encompassing $\sim 95\%$ of the source flux and appropriate background regions were used for data extraction. For each system an X-ray light curve encompassing the full ROSAT bandwidth (0.1-2.4 keV) and a hardness ratio light curve were produced. The energy ranges for the harder and softer bands were selected individually for each system to give a mean hardness ratio of zero. Equation 4.4 was again used to define the hardness ratio:

$$HR = \frac{H - S}{H + S} \quad (6.1)$$

Light curves from multiple observations of the same system were combined to improve the statistics and orbital coverage. This was not done if the morphology of the light curve had obviously changed during the interval between the two observations or if the mean flux had changed significantly (as happened in the case of AM Her, for example). In these cases all available light curves have been shown separately and interpreted independently. Portions of the hardness ratio light curves where the individual bins are clearly dominated by noise have

Table 6.1: The 42 systems confirmed as polars at the time of writing, in ascending order of period. Four candidate AM Her systems are also included. Each system was taken from Table 6.1 of Warner (1995) unless indicated. The periods given are obtained from the references listed in Table 6.2, or from Table 6.2 of Warner (1995).

^a Taken from Table 6.2 of Warner (1995).

^b Taken from from Beuermann et al. (1995).

^c Two candidate orbital periods for RE0453-42 exist.

| Star | Co-ords (J2000) | | P_{orb} (days) | Comment |
|--------------------------|-----------------|-------------|----------------------|----------------|
| | RA | Dec | | |
| RX J0132-65 | 01 32 43 | -65 55 36 | 0.05417 | Obs. too short |
| RX J1307+53 | 13 07 53.9 | +53 51 30 | 0.05534 | In sample |
| RX J1015+09 | 10 15 34 | +09 04 43 | 0.05547 | In sample |
| EF Eri | 03 14 13.1 | -22 35 42.1 | 0.05627 | In sample |
| GQ Mus ^a | 11 52 02.4 | -67 12 20.1 | 0.05937 | In low state |
| CP Pup ^a | 08 11 46.0 | -25 21 05.1 | 0.06143 | In sample |
| RX J0153-59 | 01 54 00 | -59 48 12 | 0.06181 | In sample |
| DP Leo | 11 17 16.1 | +17 57 37.1 | 0.06236 | In sample |
| RX J1844-74 | 18 44 47.8 | -74 18 33 | 0.06255 | In sample |
| RE J1149+28 | 11 49 55.7 | +28 45 07.5 | 0.06260 | In sample |
| RX J0453-42 | 04 53 25.5 | -42 13 41 | 0.07080 ^c | In sample |
| | | | 0.06516 | |
| RX J1957-57 | 19 57 10 | -57 38 20 | 0.06880 | Obs. too short |
| VV Pup | 08 15 06.8 | -19 03 18.1 | 0.06975 | In sample |
| V834 Cen | 14 09 07.6 | -45 17 18.1 | 0.07050 | Obs. too short |
| EP Dra | 19 07 06.9 | +69 08 40.1 | 0.07266 | In sample |
| RX J1002-19 | 10 02 12 | -19 25 40 | 0.07360 | Obs. too short |
| CE Gru | 21 37 56.5 | -43 42 14.1 | 0.07537 | In sample |
| V2301 Oph | 17 52 | +08 | 0.07845 | Not observed |
| RX J1802+18 | 18 02 06.4 | +18 04 48 | 0.07882 | In sample |
| MR Ser | 15 52 47.3 | +18 56 27.1 | 0.07880 | Obs. too short |
| BL Hyi | 01 41 00.4 | -67 53 29.1 | 0.07892 | In sample |
| ST LMi | 11 05 39.8 | +25 06 28.1 | 0.07909 | In sample |
| EK UMa | 10 51 35.1 | +54 04 36.8 | 0.07948 | In sample |
| AN UMa | 11 04 25.8 | +45 03 14.1 | 0.07975 | In sample |
| WW Hor | 02 36 11.6 | -52 19 15.1 | 0.08020 | In sample |
| AR UMa | 11 15 47 | +42 58 50 | 0.08050 | Not observed |
| HU Aqr | 21 07 58.3 | -05 17 39.1 | 0.08682 | In sample |
| EU Cnc ^a | 08 51 27.6 | +11 46 45 | 0.08713 | In sample |
| UZ For | 03 35 28.7 | -25 44 23.1 | 0.08787 | In sample |
| RX J1846+55 ^b | 18 46 59 | +55 38 23 | 0.08958 | In sample |
| RX J0531-46 | 05 31 35.8 | -46 24 07 | 0.09236 | In sample |
| QS Tel | 19 38 35.6 | -46 12 57.2 | 0.09719 | In sample |
| DR V211B | 20 08 56.5 | -65 27 22.1 | 0.1109 | Not observed |
| RX J0525+45 | 05 25 | +45 | 0.1111 | Not observed |
| RX J0501-03 | 05 01 46 | -03 59 28 | 0.1187 | Obs. too short |
| AM Her | 18 16 13.4 | +49 52 03.1 | 0.1289 | In sample |
| V1500 CYG | 21 11 36.6 | +48 09 02.1 | 0.1396 | Obs. too short |
| BY Cam | 05 42 49.0 | +60 51 31 1 | 0.1384 | Asynchronous |

Table 6.1: Continued.

| Star | Co-ords (J2000) | | P_{orb} (days) | Comment |
|--------------|-----------------|-------------|---------------------|----------------|
| | RA | Dec | | |
| RX J1940-10 | 19 40 11.4 | -10 25 25.1 | 0.1402 | In sample |
| RX J0929-24 | 09 29 07 | -24 04 50 | 0.1412 | In sample |
| RX J1007-20 | 10 07 35 | -20 16 59 | 0.1444 | In sample |
| RX J2316-05 | 23 16 03 | -05 27 08 | 0.1451 | In sample |
| QQ Vul | 20 05 42.0 | +22 39 58.1 | 0.1545 | In sample |
| EXO 0329-260 | 03 32 04.6 | -25 56 57.1 | 0.1583 | Obs. too short |
| RX J1313-32 | 13 13 16 | -32 59 19 | 0.1771 | Obs. too short |
| RX J0203+29 | 02 03 48 | +29 59 25 | 0.1913 | Obs. too short |

been represented by a single data point. The ephemerides have been obtained from various sources; each ephemeris and reference are listed in Table 6.2. In some cases only a period for the system is available, for those systems an arbitrary epoch has been selected.

The ROSAT observations of each of these 30 systems are summarised in Table 6.3. All ROSAT observations used for each system are shown. For each observation, the date, exposure, the mean 0.1-2.4 keV count rate, the energy range for the ‘soft band’ and time bin size are given. The ‘soft band’ refers to one of the two bands used to calculate the hardness ratios. The corresponding hard band extends from the upper limit of each soft band to 2.4 keV. The two bin sizes given for each system refer to the flux and hardness ratio light curve binning respectively.

6.3 Theoretical expectations

Before presenting the results of this work it is important to consider what features the soft X-ray light curves of AM Herculis systems are expected to display and how often these features are expected to appear. Both HU Aqr and UZ For introduced most of the common features of X-ray light curves; bright and faint phases, absorption dips and eclipses. In addition to these, continuous (as opposed to bright/faint) light curves and flaring systems are also considered. The expected frequency with which spectral (hardness ratio) variations are expected to be associated with features in the light curves are discussed.

Table 6.2: Ephemerides for the 30 AM Her systems included in this study. A reference for the ephemeris is also given. Numbers in brackets represent error values in the last digits.

| Star | Epoch (MJD) | Period (days) | Reference |
|-------------|-------------------|-----------------|----------------------------------|
| RX J1307+09 | 48 748.9421(5) | 0.05533838(26) | Osborne et al. 1994 |
| RX J1015+09 | 49 487.85649(26) | 0.055471287(11) | Burwitz et al. 1995 |
| EF Eri | 43 944.4522 | 0.056265925(5) | Pirola, Reiz & Coyne 1987 |
| CP Pup | – | 0.06143 | O’Donoghue et al. 1989 |
| RX J0153-59 | – | 0.06181 | Warner 1995 |
| DP Leo | 44 214.052929(43) | 0.0623628440(7) | Robinson & Córdoba 1994 |
| RX J1844-74 | 48 474.7933(2) | 0.06255330(2) | Ramsay et al. 1996 |
| RE J1149+28 | 49 042.16985(7) | 0.06260(1) | Howell et al. 1995 |
| RX J0453-42 | 49 336.1131 | 0.07080(14) | Burwitz et al. 1996 |
| | | 0.06516(15) | |
| VV Pup | 27 889.1474 | 0.0697468256 | Vennes et al. 1995 |
| EP Dra | 47 681.22916(10) | 0.07265625(17) | Remillard et al. 1991 |
| CE Gru | 46 698.4765(47) | 0.07537(35) | Tuohy et al. 1988 |
| RX J1802+18 | – | 0.07882 | Szkody et al. 1995 |
| BL Hyi | 44 883.7176(6) | 0.07891518(4) | Schwöpe et al. 1995 <i>a</i> |
| ST LMi | 45 059.2024(3) | 0.07908908(8) | Cropper 1986 |
| EK UMa | 48 756.0965(11) | 0.079544032(16) | Morris et al. 1987 |
| AN UMa | 43 190.5255(24) | 0.07975282(4) | Bonnet-Bidaud et al. 1992 |
| WW Hor | 47 125.62782 | 0.080199035 | Beuermann et al. 1990 |
| HU Aqr | 49 481.647633(7) | 0.086820454(4) | This thesis. |
| EU Cnc | – | 0.08713 | Gilliland et al. 1991 |
| UZ For | 45 566.67622 | 0.0878654444 | J. Bailey, private comm. |
| RX J1846+55 | – | 0.08958 | Beuermann et al. 1995 |
| RX J0531-46 | 48 984.2407 | 0.09268(9) | Reinsch et al. 1994 |
| QS Tel | 48 894.0568(15) | 0.09718707(16) | Schwöpe et al. 1995 <i>d</i> |
| AM Her | 43 014.26614(4) | 0.128927041(5) | Heise & Verbunt 1988 |
| RX J1940-10 | 49 217.4234(5) | 0.1402350(1) | Watson et al. 1995 |
| RX J0929-24 | 49 007.0879(14) | 0.14124(26) | Sekiguchi, Nakada & Bassett 1994 |
| RX J1007-20 | – | 0.1444 | Warner 1995 |
| RX J2316-05 | – | 0.1451 | Warner 1995 |
| QQ Vul | 45 234.3364(4) | 0.15452105(6) | Osborne et al. 1987 |

Table 6.3: Data on the ROSAT observations for each AM Her system. For each observation the date, exposure time (in seconds), mean count rate (in ct s^{-1}), soft band energy range, and time resolution are given. The energy range used for the ‘soft band’ was selected as described in the text, and the corresponding the hard band extends from the upper limit of the soft band to 2.4 keV. The size of the time bins for both the flux and hardness ratio light curves are given.

| System | Date | Exp. | Count Rate | Soft Band | Bin Size (s) |
|-------------|-------------|--------|------------|-----------|--------------|
| RX J1307+09 | 10 Nov 1993 | 10,061 | 0.046 | 0.12-0.59 | 100/100 |
| RX J1015+09 | 9 Nov 1993 | 4,683 | 4.60 | 0.12-0.22 | 50/50 |
| EF Eri | 18 Jul 1990 | 16,499 | 5.05 | 0.12-0.22 | 50/50 |
| CP Pup | 1 May 1993 | 7,917 | 0.058 | 0.12-1.09 | 200/400 |
| RX J0153-59 | 1 Jul 1992 | 4,244 | 0.091 | 0.12-0.22 | 150/300 |
| DP Leo | 30 May 1992 | 7,365 | 0.239 | 0.12-0.18 | 50/100 |
| | 30 May 1993 | 23,018 | 0.262 | | |
| RX J1844-74 | 18 Oct 1992 | 3,626 | 1.58 | 0.12-0.20 | 100/200 |
| | 26 Mar 1993 | 5,083 | 2.96 | | |
| RE J1149+28 | 25 May 1993 | 15,946 | 0.700 | 0.12-0.18 | 40/80 |
| RX J0453-42 | 21 Sep 1992 | 11,750 | 0.99 | 0.12-0.19 | 75/150 |
| VV Pup | 17 Oct 1991 | 14,747 | 4.20 | 0.12-0.19 | 25/50 |
| EP Dra | 1 Jul 1993 | 12,768 | 0.024 | 0.12-0.29 | 200/400 |
| CE Gru | 28 Apr 1993 | 7,610 | 0.014 | 0.12-0.31 | 200/400 |
| RX J1802+18 | 11 Sep 1993 | 11,307 | 2.02 | 0.12-0.22 | 200/400 |
| BL Hyi | 15 Apr 1991 | 13,064 | 1.81 | 0.12-0.19 | 100/200 |
| | 10 Oct 1993 | 3,488 | 1.83 | | |
| ST LMi | 20 May 1993 | 41,790 | 0.053 | 0.12-0.27 | 200/400 |
| EK UMa | 12 May 1992 | 12,117 | 1.05 | 0.12-0.21 | 50/100 |
| | 28 Nov 1992 | 4,083 | 1.83 | | |
| | 7 May 1993 | 11,454 | 0.73 | | |
| AN UMa | 18 Nov 1991 | 16,794 | 1.02 | 0.12-0.18 | 100/200 |
| WW Hor | 21 Jul 1992 | 14,637 | 0.032 | 0.12-0.80 | 200/400 |
| | 17 Jul 1993 | 23,670 | | | |
| HU Aqr | 27 Oct 1993 | 36,740 | 7.30 | 0.12-0.20 | 10/60 |
| EU Cnc | 15 Nov 1991 | 10,028 | 0.003 | 0.12-0.26 | 200/400 |
| | 25 Apr 1993 | 12,628 | 0.002 | | |
| UZ For | 14 Aug 1991 | 49,496 | 1.62 | 0.12-0.19 | 10/60 |
| RX J1846+55 | 15 Jun 1992 | 7,717 | 0.086 | 0.12-0.24 | 100/200 |
| | 25 Sep 1993 | 23,796 | 0.096 | | |
| RX J0531-46 | 31 Jul 1993 | 32,693 | 0.005 | 0.12-0.28 | 200/400 |
| QS Tel | 13 Oct 1992 | 22,680 | 0.71 | 0.12-0.18 | 75/150 |
| AM Her | 15 Sep 1991 | 17,405 | 0.363 | 0.12-0.43 | 100/200 |
| | 31 Jan 1993 | 4,481 | 77.9 | 0.12-0.20 | |
| | 12 Apr 1993 | 11,610 | 100.4 | | |

Table 6.3: Continued.

| System | Date | Exp. | Count Rate | Soft Band | Bin Size (s) |
|-------------|-------------|--------|------------|-----------|--------------|
| RX J1940-10 | 8 Oct 1992 | 25,000 | 0.203 | 0.12-0.93 | 100/200 |
| | 13 Oct 1993 | 29,640 | 0.238 | | |
| RX J0929-24 | 1 Jun 1994 | 18,350 | 0.409 | 0.12-0.25 | 100/200 |
| RX J1007-20 | 17 Nov 1992 | 9,415 | 0.45 | 0.12-0.22 | 400/800 |
| RX J2316-05 | 25 May 1993 | 13,646 | 0.009 | 0.12-0.90 | 400/800 |
| QQ Vul | 12 Apr 1991 | 12,964 | 3.25 | 0.12-0.20 | 100/200 |
| | 10 Nov 1993 | 2,362 | 4.27 | | |

Overall morphology

The overall morphology of the soft X-ray light curves of the AM Her systems is dependent primarily upon the visibility of the dominant accreting pole. The range of light curves is therefore controlled solely by the inclination, i and the magnetic co-latitude β . For the purposes of this chapter, it is assumed that accretion is occurring at one of the magnetic poles itself. Since accretion is believed to occur in a region not far from the pole, this does not greatly affect the arguments presented here. Most soft X-ray light curves of AM Her systems can be placed into one of two groups; those in which the main pole is occulted by the white dwarf once per orbital period, and those in which the main pole is always in view. The former leads to light curves with a bright phase (pole in view) and a faint phase (pole occulted), while the latter leads to light curves with no faint phases. In this chapter these two morphologies are denoted ‘bright/faint’ light curves and ‘continuous’ light curves respectively.

AM Her systems are commonly labelled ‘one-pole’ and ‘two-pole’ systems, based upon their X-ray light curves. However, systems that have been labelled ‘one-pole’ (i.e. with continuous light curves) could be mis-interpreted. In the light curves of some one-pole systems, both poles make a contribution to the X-ray flux, and this point may be missed by some or cause confusion for others. For this reason the terms ‘one-pole’ and ‘two-pole’ are avoided in favour of the more descriptive ‘bright/faint’ and ‘continuous’ light curves. Furthermore, these two classifications are intended as an aid to the comparison of different systems only; it should be emphasised that the distribution of light curve morphologies is going to be continuous. The separation of types is therefore somewhat artificial, and some light curves could easily be placed into either category.

In what proportion should these two light curve morphologies occur? The duration of the faint

phase is entirely dependent upon the value of the inclination, i and the magnetic co-latitude, β , as defined by Equation 2.1 (it is assumed throughout that the extent of the emission spot is negligible). If $i + \beta < 90$ then the pole is never occulted by the white dwarf and the faint phase duration is zero. If $i + 90 < \beta$ then the pole is never in view and the ‘faint’ phase duration becomes 1.0ϕ (such systems may well be difficult to detect). If neither of these conditions is met then the pole is eclipsed periodically and a bright phase and faint phase is seen. The duration of the faint phase (typically $0.2\text{--}0.5\phi$) increases as both i and β increase. If the distribution of inclinations and magnetic co-latitudes are random, these conditions predict that bright/faint phase variations are seen in 50% of AM Her systems.

However, the distribution of magnetic co-latitudes β is not uniform; Brainerd & Lamb (1985) point out that the magnetic moments of the white dwarfs will tend to be aligned with the spin axes. This reflects the fact that the phase-locking MHD torque is proportional to the component of the magnetic moment that is parallel to the spin axis of the white dwarf. Thus in phase-locked magnetic CVs (polars) the magnetic co-latitude will tend towards lower values. As a result the proportion of systems with bright/faint states will be greater than 50%.

The bearing that observational selection effects might have on this prediction must also be considered. Both Brainerd & Lamb (1985) and Cropper (1988) have shown that polars cluster on the semi-circle in the $\cos i - \cos \beta$ plane defined by $\cos^2 \beta + \cos^2 i = 1$. This bias arises due to the preferential detection of systems where the accretion region spends more of its time close to the limb of the white dwarf. When close to the limb, the optical linear polarisation from the accretion column is maximised, and therefore the likelihood of detection and identification of a polar is increased. However, over 70% of the systems included in this study were discovered by their X-ray emission, either serendipitously or through surveys. It is therefore the X-ray selection effects that will have the greater influence.

Although X-ray emission from the polecap in AM Her systems is not subject to such strong beaming effects as the optical flux is, the complex shape of the optically thick blackbody emission regions can lead to complicated dependencies on i and β . This can be seen from the light curve simulations of Imamura & Durisen (1983) and in the light curve simulations in Section 4.4.2, for example. The unravelling of such a complex relationship is beyond the scope of this thesis. However, in most cases the detectability of a system ought to be independent of i and β , so

long as they allow the pole to rotate into view for some portion of the orbit. It is therefore anticipated that any bias introduced by X-ray selection effects will be small.

There are additional factors that will serve to further complicate the light curves of AM Her systems. Significant accretion onto a second pole may ‘fill in’ the faint phase, making its flux comparable to the bright phase. Eclipses, absorption dips and other phase-dependent features may also be apparent (see below). Lastly, viewing effects as the pole rotates may lead to modulation of the soft X-ray flux, which will add structure to both the continuous light curves and the bright phases.

Of the spectral effects that might be detected, one is the softening detected during the transitions between the bright and faint phases in both HU Aqr and UZ For, attributed to a softer region around the harder core of the emission region. Determining how often such spectral affects are expected to occur can be difficult if not impossible to do accurately. Our ability to detect changes to the soft X-ray spectrum of an AM Her is limited by the capabilities of the instrumentation available. Put simply, only the largest column density changes will be detectable over short timescales, and conversely the smallest column changes will only be detectable over long timescales. In order to fully understand a property, like the softening mentioned above or hardening during the dips, its complete range of behaviour must be available to us; all changes must be slow enough or large enough for detection. This almost certainly does not apply to ROSAT observations of the transition softening effect; some of the spectral variability is likely to be either too subtle or too rapid for detection.

Flaring systems

Some polars will display light curves that are dominated by stochastic (random) flaring. For some only a small number of flares may be seen, in which case the overall light curve morphology will still be apparent. In others the light curve may be dominated by flares which mask or confuse the underlying morphology; this produces a third, ‘flaring’ class of light curve. It may be possible to infer the true soft X-ray light curve morphology of a stochastic system by observations at a different epoch when the system is quieter, or in a different waveband in which the flaring is not evident.

Eclipses

For an eclipse to occur, the limb of the secondary must cross the line of sight to the white dwarf. If the angle subtended at the white dwarf by the secondary's radius is θ , then this provides a limit on the inclination;

$$i < 90 - \theta. \quad (6.2)$$

The range of values for this inclination limit must be known to calculate the probability of an eclipse. To a first approximation, θ depends upon both the binary separation, A and upon the Roche lobe radius R_L by the simple relation;

$$\theta = \tan^{-1}\left(\frac{R_L}{A}\right) \quad (6.3)$$

R_L , as a fraction of the binary separation, can be set by the mass ratio (Eggleton 1983):

$$R_L = \frac{0.49q^{2/3}}{0.6q^{2/3} + \ln(1 + q^{1/3})}, \quad 0 < q < \infty \quad (6.4)$$

The *mean* inclination limit for all systems will therefore depend upon the distribution of the mass ratio for the AM Her population as a whole. An independent determination of this limit will depend on which evolutionary model for polars is selected, the inclination limit is typically between 70° and 75° . For example, a system with a mass ratio of 0.3 has an inclination limit of 74° . Given a random distribution of inclinations, this would suggest that 17–22% of cataclysmic variables ought to display eclipses of the primary by the secondary.

A discussion of eclipses ought be conducted in relation to the systems in Table 6.1 rather than the subset of systems included in the X-ray study because the eclipsing systems were known before this study and because the table provides a larger sample of the AM Her population than the X-ray subset does. Although the eclipsing nature of these systems has been determined from various wavebands, all eclipsing systems will display X-ray eclipses as well. Of the 46 AM Her systems listed in Table 6.1, eight display eclipses (if RE J1940-10 is included amongst the eclipsing systems; see the discussion of this system below for why this may be the case). This proportion (17%) matches well with the above prediction. It should be noted that one system, RX J0515+0105, has been confirmed as an AM Her since Warner (1995) published his list. If this system, which is eclipsing, is also included then the proportion rises to 19%.

Absorption dips

According to Watson et al. (1989), X-ray absorption effects are inevitable if the accretion flow crosses the line of sight to the emission region on the white dwarf. Due to the manner in which the magnetic field lifts the stream out of the orbital plane this is likely to be a common event. There is only one way for the stream to cross the line of sight; the inclination i must exceed the magnetic co-latitude β :

$$i > \beta \quad (6.5)$$

If accretion is taking place in the lower hemisphere (as seen by the observer) then i cannot exceed β because $\beta > 90^\circ$ and i is always $< 90^\circ$. Qualitatively, this is just the logical assertion that the stream is always below the orbital plane for accretion into the lower hemisphere. Since not all systems which accrete into the upper hemisphere can display absorption dips, the overall proportion of systems with dips is clearly less than one half.

For a random distribution of β , the probability distribution is given by the following;

$$P = \frac{2 \int_0^\pi \beta \sin \beta \, d\beta}{\pi \int_0^\pi \sin \beta \, d\beta} \quad (6.6)$$

Note that this means that orientations where β lies close to 90° are favoured. When Equation 6.6 is evaluated, the proportion of systems expected to display absorption dips is found to be only 18%.

The above calculation assumes a uniform distribution of both inclination and magnetic co-latitude. The distribution of inclinations in detected systems is unlikely to be uniform due to selection effects, and this will slightly alter the proportion of dips in *detected* systems (the full consideration of this is not presented here). It has already been noted above that the distribution of magnetic co-latitudes β is also not uniform (Brainerd & Lamb 1985). In phase-locked magnetic CVs (polars) the magnetic co-latitude is predicted to tend towards lower values. As a result the proportion of systems found to have an absorption dip will be larger than that predicted.

Furthermore, at least one system, UZ For, is known to display absorption dips in spite of an accretion geometry that should preclude dips. Bailey & Cropper (1991) established that $i \sim 81^\circ$ and $m \sim 150^\circ$ for UZ For, yet a clear dip is detected. Warren et al. (1995) maintain that broadening of the accretion flow in the stagnation region (where the stream is threaded by the field) causes the dip. However, an alternative explanation is offered by Watson (1995), who

suggests that a second accretion flow to a second and far weaker pole causes the dip instead. The case of UZ For demonstrates that things are not as clear-cut as the above arguments would suggest; factors such as broadening of the flow or multiple streams may cause dips in some systems that geometrically should have none. The value of 18% for the proportion of systems with dips should therefore be taken as a lower limit.

What percentage of absorption dips that *are* detected can be expected to display hardening of the soft X-ray flux as has been observed from HU Aqr and UZ For? If photoelectric absorption is accepted as the mechanism by which the accretion stream attenuates the X-ray flux, the amount of hardening will depend upon the density of the stream and the stream's depth along the line of sight to the pole. It has been demonstrated that these parameters are consistent with photoelectric absorption for at least one AM Her system, EF Eri (Watson et al. 1989). However, once the optical depth along the line of sight through the stream rises above a value of about 4, total attenuation of the X-ray flux will occur. In this case no hardening of the flux will be detectable. Given the likely range of densities in the stream, most if not all dips should cause some hardening of the X-ray flux. What then needs to be considered is whether that hardening is detectable.

The factors involved in detecting spectral effects in soft X-ray light curves, discussed above in relation to the softening during the transitions, apply equally to the detection of hardening during the absorption dips. Some of the spectral variability in the absorption dips of AM Hers is likely to be either too subtle or too rapid for detection. This means that in some systems real absorption dips will display no detectable spectral change. Hence it is impossible to predict the likelihood of detecting hardening during an absorption dip with the ROSAT PSPC.

6.4 Results

For each system the orbital phase-folded flux light curve (0.1-2.4 keV) is presented as well as the hardness ratio light curve. All folded light curves are plotted twice for clarity. The ephemerides used to create these folded light curves are given in Table 6.2. What follows is a brief review of each system, detailing any issues related to the system's classification and any other interesting features found in the light curve. In particular, AM Her and VV Pup are discussed at greater

| Classification | | | |
|----------------|------------|-----------------|--------------|
| Bright/Faint | Continuous | Flare Dominated | Unclassified |
| RX J1015 | WGA J1802 | RX J0929 | RE J0153 |
| RE J1149 | RE J1844 | RE J1940 | RE J0531 |
| RE J1846 | AN UMa | BL Hyi | RE J1007 |
| CP Pup | EF Eri | | RE J1307 |
| AM Her | EP Dra | | RE J2316 |
| DP Leo | QQ Vul | | CE Gru |
| EK UMa | QS Tel | | EU Cnc |
| HU Aqr | | | |
| UZ For | | | |
| ST LMi | | | |
| VV Pup | | | |
| WW Hor | | | |
| RX J0453 | | | |

Table 6.4: Classification of soft X-ray light curves. The 30 systems included in this study are grouped according to the type of light curve displayed. See the text for a description of each of these classes.

length in terms of some of the ideas put forward in the analysis of HU Aqr and UZ For in the preceding chapters.

The light curve of each system has been classified according to the three categories described above; bright/faint, continuous and flaring. Table 6.4 lists the systems which fall into each class. The light curves of all 30 systems included in this study are grouped according to type in Figure 6.1 and Figures 6.3 through 6.5. Figure 6.1 shows the twelve systems which display a clear bright/faint variation, plus a system for which there is strong evidence for inclusion in this class (RE 0453-42). Seven continuous light curve systems are given in Figure 6.3, and the light curves of the three systems dominated by flare events are given in Figure 6.4. Finally, Figure 6.5 shows the seven systems for which it was not possible to make any interpretation of the soft X-ray light curves or hardness ratios.

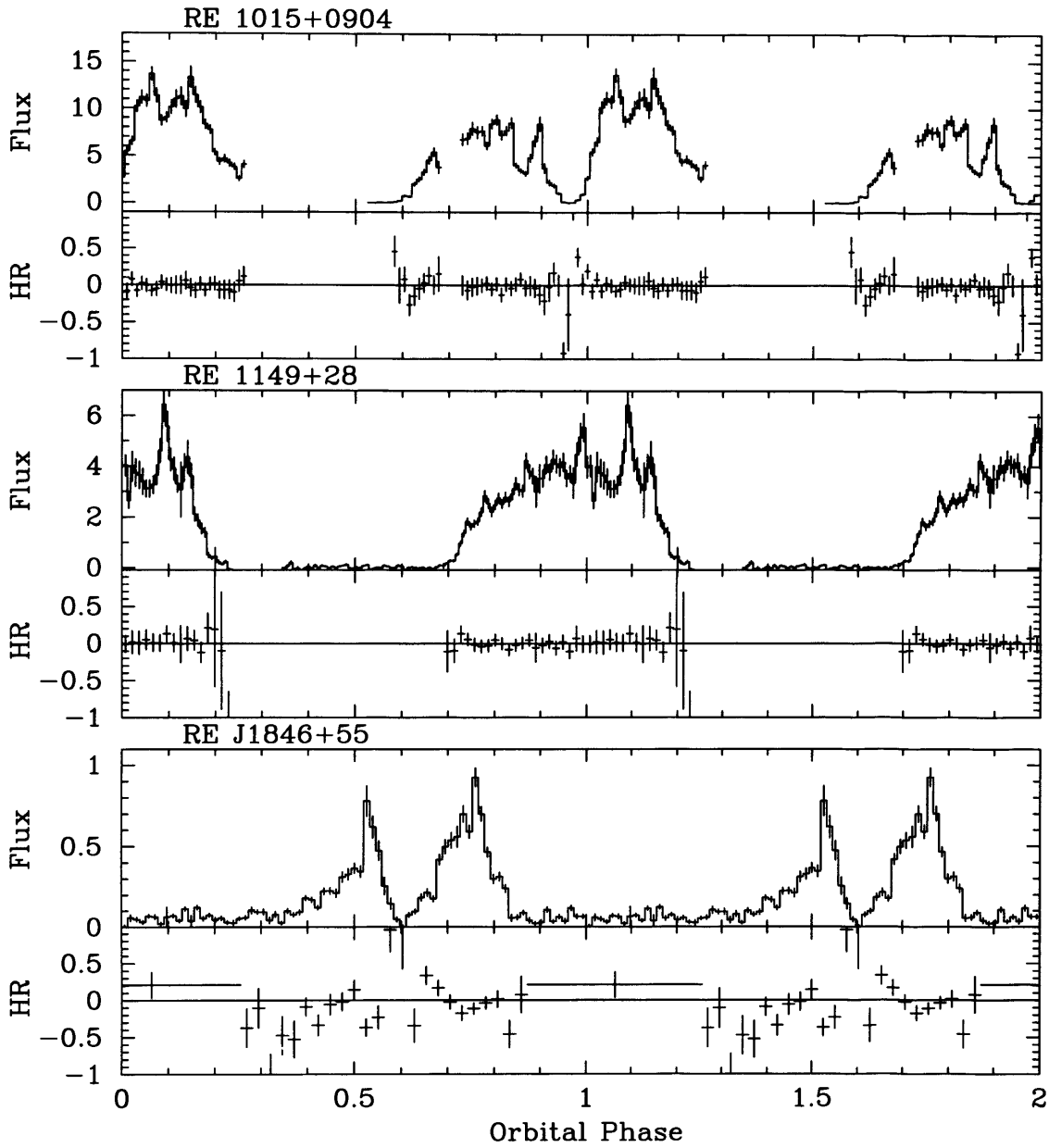


Figure 6.1: Flux and hardness ratio light curves of the polars classified as bright/faint systems.

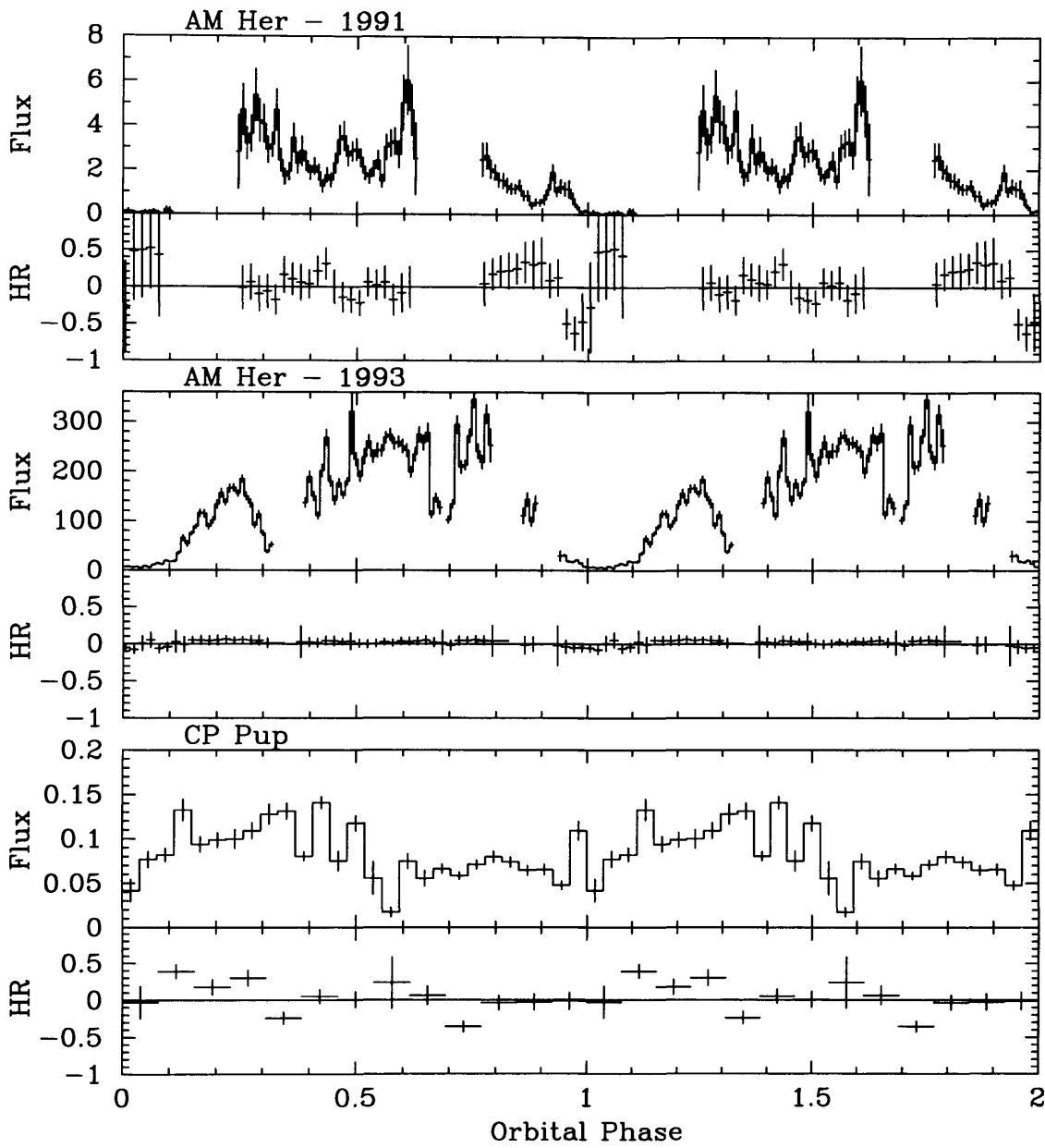


Figure 6.1: Continued.

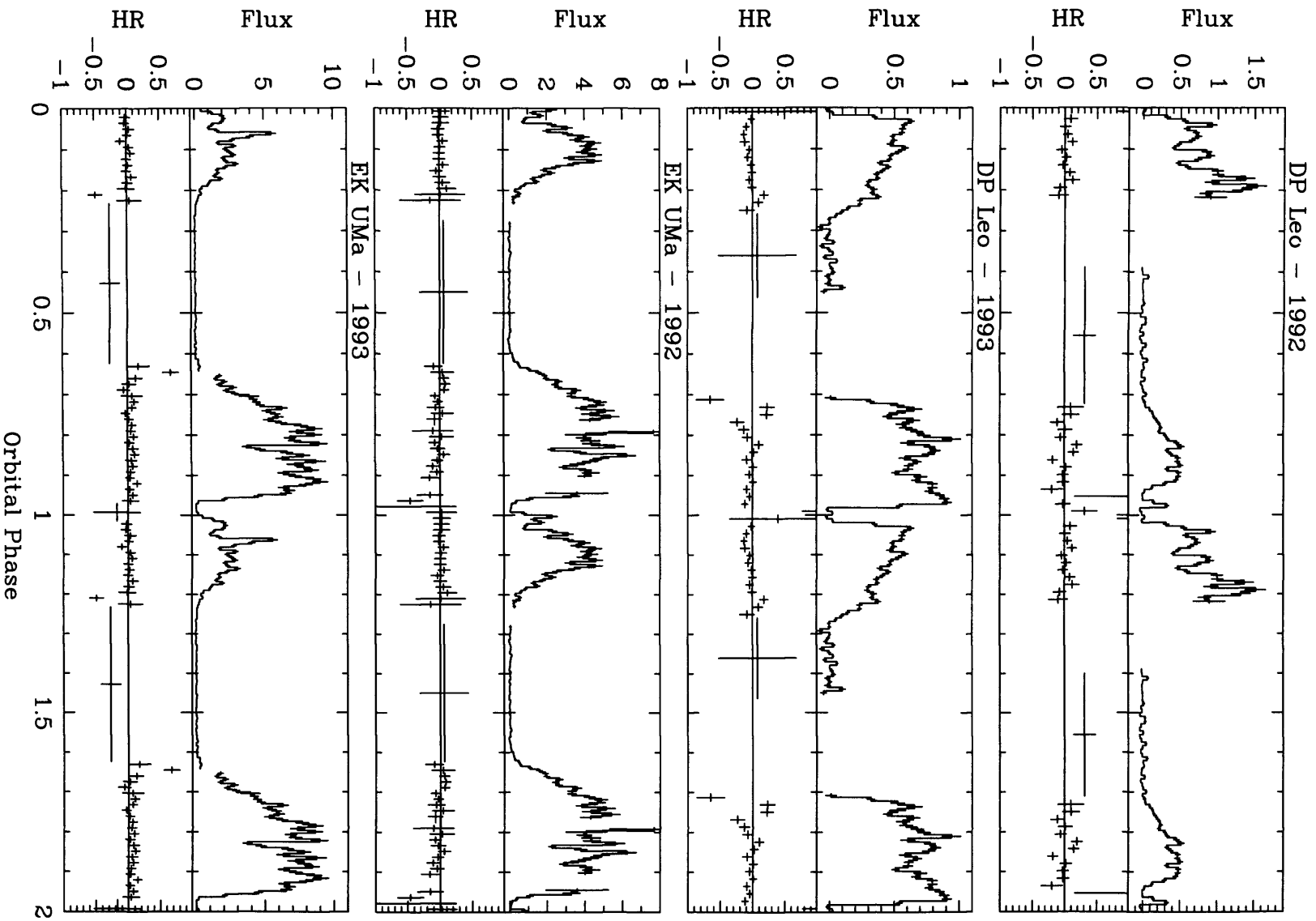


Figure 6.1: Continued.

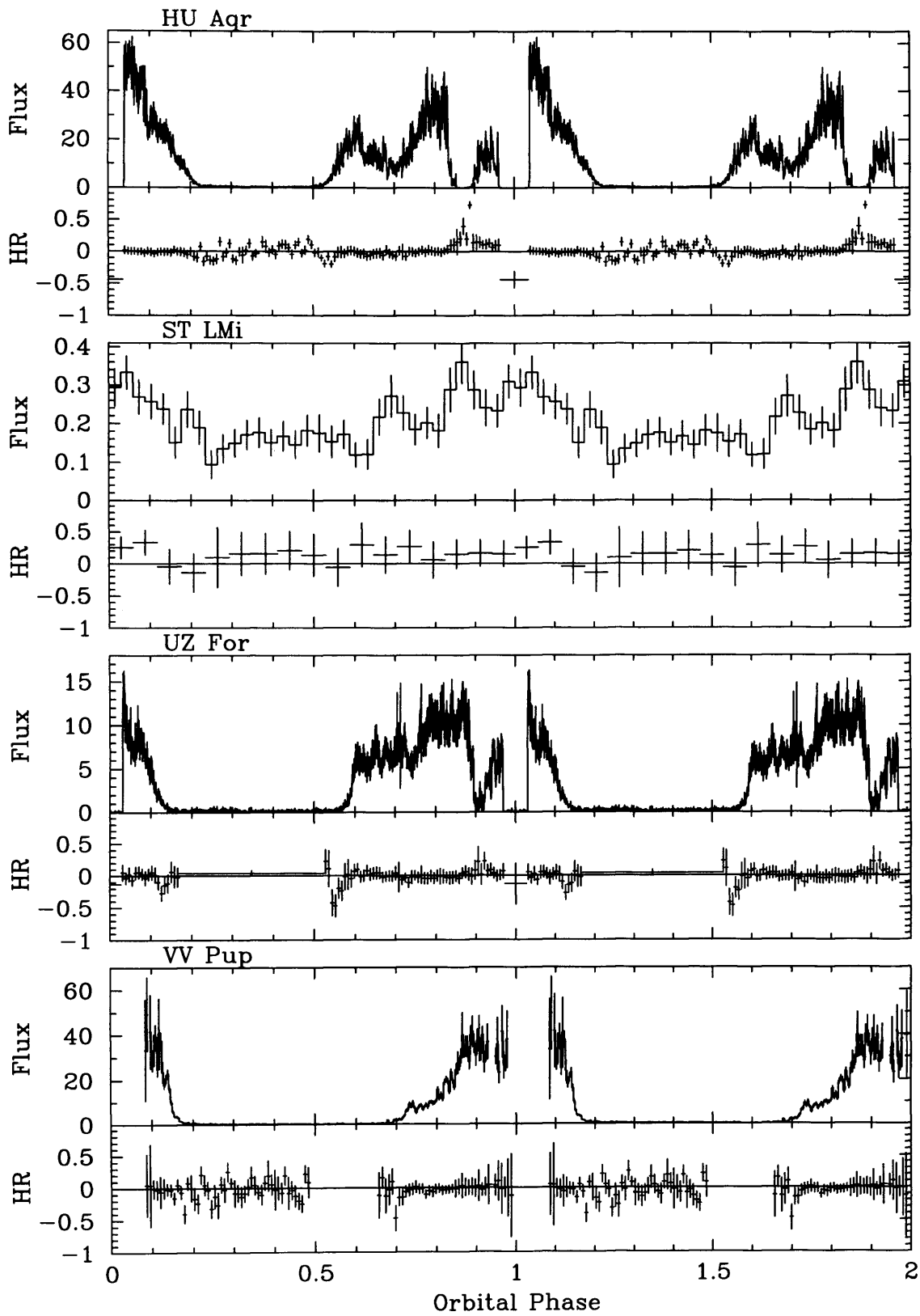


Figure 6.1: Continued.

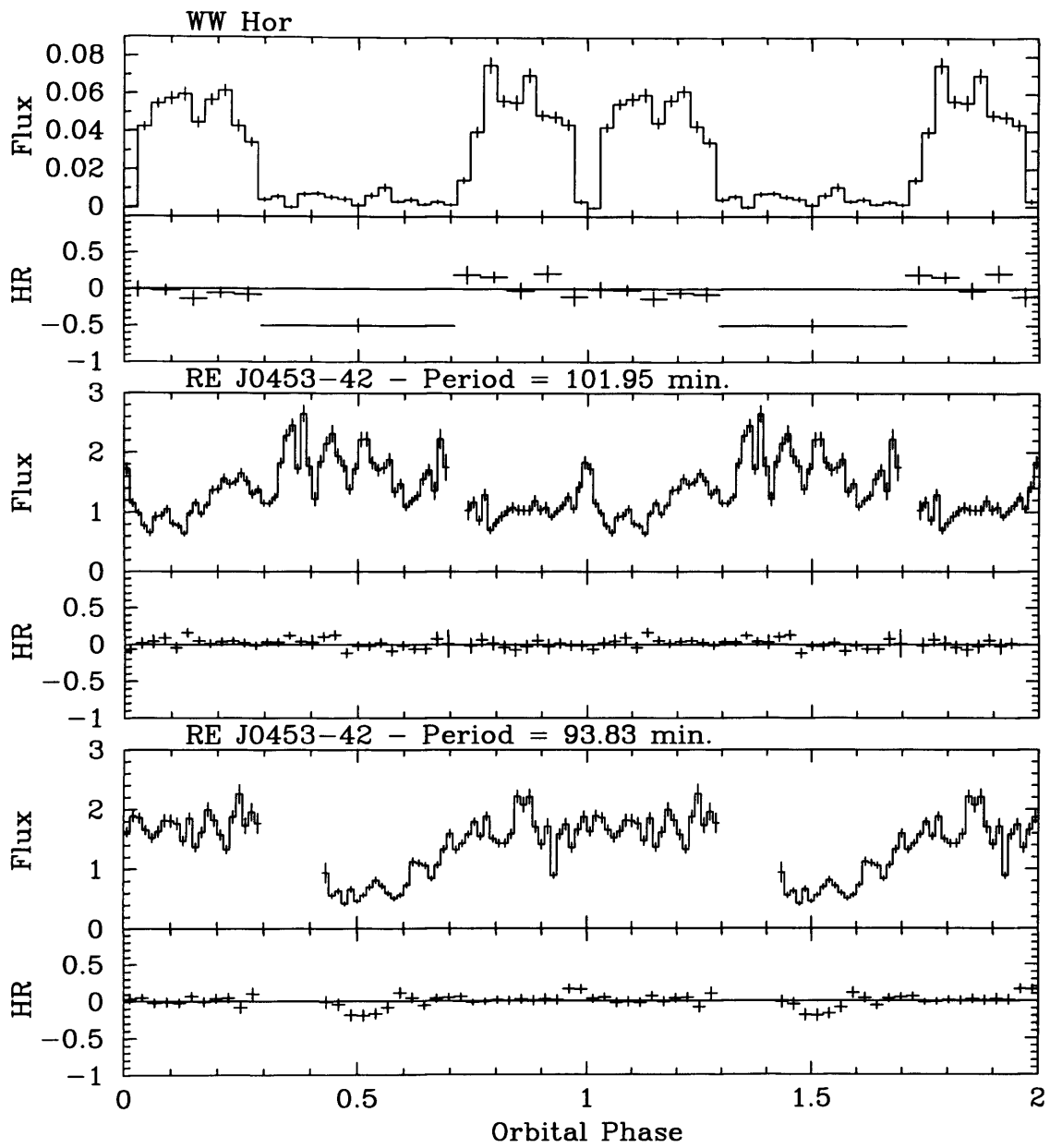


Figure 6.1: Continued.

6.4.1 Bright–faint systems

RX J1015+0904

Although the orbital coverage during the ROSAT PSPC observation of RE1015+09 was just 65% and only the very end of the faint phase was observed, HRI observations confirm that this system does exhibit bright/faint variations (Burwitz et al. 1995). The bright phase is interrupted by a strong, near total dip which Burwitz et al. associate with absorption by the accretion stream, not an eclipse. In Figure 6.1 a 0.2-0.4 increase in the hardness ratio is evident during the dip ingress and egress. This confirms the conclusion of Burwitz et al. that this is indeed an absorption dip.

During the egress from the faint phase at phase 0.6 there is a softening of the X-rays by 0.3. Although the significance of this hardness change is not high, it does occur at the same phase as the softening observed in HU Aqr and UZ For. One is inclined to place greater weight upon the detection of this change in RE1015+535 when compared to the light curves of other AM Her systems than if the light curve of this system were taken alone. There is further support provided by the shape of these soft X-ray pulses, which are discussed further in Section 6.4.3. RE1015+535 therefore exhibits all the properties of an AM Her system like HU Aqr and UZ For, but observed at a lower inclination so that no eclipse by the secondary is found.

RE J1149+28

The soft X-ray bright phase of RE1149+28 appears to be slightly asymmetric; more flux is evident at the end than at the beginning of the bright phase. Howell et al. (1995) found a similar asymmetry based upon data obtained with the EUVE satellite (see their Figure 2b).

Several strong X-ray flares are evident during the peak of the bright phase. The two strongest flares represent a 50% increase in flux over an interval of 150 s, with a decline to the pre-flare flux level in approximately the same time. These sections of the light curve were only observed on a single occasion and so it is not possible to comment on the permanence of these features. They may be caused by large individual blobs of material within the accretion stream as they impact the white dwarf surface. Overall there are no hardness ratio variations during the bright phase. There is very marginal evidence for a softening of the X-ray flux as the main pole crosses

the limb of the white dwarf, particularly at the egress from the faint phase.

(Note: The size of the error in the period is such that by the epoch of the ROSAT observations a substantial ambiguity in the phasing exists. The light curves presented in Figure 6.1 have been shifted such that the centre of the X-ray bright phase is at phase 0.0, matching the phase convention used by Howell et al.)

RE J1846+55

RE1846+55 is listed as a candidate AM Her system. The morphology of the X-ray light curve suggests that the emission is dominated by a single pole visible for 0.4ϕ . In the middle of the bright phase there is a very broad dip feature that could be associated with stream occultation. A hardening of the flux at this phase supports this conclusion.

AM Her

AM Her is notorious for possessing two modes of accretion which lead to two X-ray light curve morphologies. In the 'normal' mode, one pole is inactive and the main accreting pole is seen to undergo a grazing self-eclipse by the white dwarf with a typical duration of 0.2 orbital cycles (Beuermann 1988). Because of the grazing nature of the eclipse this duration is highly sensitive to variations in the location of the emission region and at certain epochs the eclipse cannot be detected at all. In the reversed X-ray mode, the soft X-ray flux becomes anti-phased with respect to its behaviour in the normal mode; a soft X-ray peak occurs at the same phase as the grazing eclipse of the main pole.

Two X-ray light curves of AM Her are presented here, both of which display the normal mode configuration but with vastly different count rates. In 1991 the system was in a low accretion state with a mean count rate of 1.9 cts s^{-1} and in 1993 it was in a high state with a count rate of 141.7 cts s^{-1} . Beardmore et al. (1995a) reported a softening in the *Ginga* X-ray flux *during* the eclipse. No spectral changes are seen in the hardness ratio light curve of the ROSAT high-state observation. In the low-state a strong softening effect is seen just prior to the low state ($0.95 < \phi < 1.02$).

It is possible to understand this based on the inhomogeneous accretion model of Kuijpers &

Pringle (1982) in which the accretion stream consists of dense blobs immersed in a flow of more tenuous gas. These blobs release their accretion energy deep in the photosphere and this energy will emerge as soft X-rays. The tenuous gas will shock above the photosphere generating hard X-rays, some of which will irradiate the white dwarf surface and contribute to the soft X-ray flux by reprocessing. This soft X-ray component will be weaker than that generated by buried shocks with a considerably smaller effective temperature (Hameury & King 1988).

The behaviour of AM Her can therefore be explained as follows. It is assumed that the reduction in flux during the low state arises because the accretion flow is made up of fewer dense blobs than in the high state. This is a reasonable assumption given that the blobs carry the bulk of the accreting material to the white dwarf. The accretion luminosity from the tenuous material will remain more or less unchanged (Hameury & King 1988). Thus in a low state soft X-rays reprocessed from standing shocks will contribute a larger fraction of the overall soft X-ray flux than during a high state. If these reprocessed soft X-rays are the cause of the temperature structure seen across the emission region in polars then it follows that this structure will be more observable during the low state. This is exactly the behaviour displayed by AM Her.

A further conclusion is that the mean blackbody spectrum of AM Her should be both cooler and less dominant during the low state while the bremsstrahlung component should remain more or less unchanged. The mean spectrum of AM Her during both high and low states was extracted and separately fitted with bremsstrahlung plus absorbed blackbody models. As for previous fits, the bremsstrahlung temperature is fixed to 30 keV. The results of the two fits, shown in Table 6.5, fit the pattern outlined above; both the blackbody temperature and normalisation are significantly reduced in the low state observation. This is true in spite of a decrease in the bremsstrahlung normalisation by a factor of 6 during the low state, because the difference is much less than the factor of 23 decrease for the blackbody normalisation. Although this analysis is not proof, it does provide some compelling evidence that the softer emission region around the main emission region is created by irradiation from a standing shock.

CP Pup

The ROSAT light curve of CP Pup is reminiscent of the light curve of ST LMi (see below). Two humps in the soft X-ray light curve are present, between phase 0.0 and 0.6 and between phase

| | High State | Low State |
|-----------------------|----------------------|-----------------------|
| kT_{BB} | 33.7 eV | 16.5 eV |
| Norm_{BB} | 7.8×10^{-6} | 3.35×10^{-7} |
| N_H | 0.2×10^{20} | 1.66×10^{20} |
| kT_{Brems} | 30 keV | 30 keV |
| Norm_{Brems} | 7.8×10^{-6} | 1.32×10^{-6} |

Table 3.5: Results of spectral fitting to the high and low state spectra of AM Her.

0.6 and 1.0 (the weaker of the two). This is a typical bright/faint light curve for a system where both poles are of comparable luminosity. The hardness ratio light curve shows some variation through the orbital cycle, for example the brief intervals of softer flux at phase 0.55 and 0.7. These hardness changes do not appear to relate to the X-ray flux and hence their interpretation is difficult.

DP Leo

Two ROSAT PSPC observations of DP Leo were conducted, separated by one year. The results of the earlier observation have already been presented by Robinson & Córdova (1994). In both light curves a total soft X-ray eclipse is detected at phase 0.0. In 1992 a dip is present before the eclipse, but not in 1993. The hardness ratio light curve in 1992 does not show any systematic variation during the bright phase. There is a single data point which shows an increase in hardness between the dip and eclipse. This may be associated with the dip (as in HU Aqr) but it is not really possible to draw any conclusion from a single datum. This dip is still most likely caused by the accretion stream, despite the lack of a clear hardness increase.

In 1993 the light curve appears somewhat different. The dip is gone, which suggests that the origin of the dip in 1992 was indeed the stream; the stream is the only object that can both cause the dip and change its position within the system. The light curve after the eclipse has also changed; the flux is significantly less variable than was seen in the previous year. Robinson & Córdova asserted that these flares in 1992 represented the impact of individual blobs, based on the ideas put forward by Hameury & King (1988). The change in the nature of this part of the light curve can be linked to the disappearance of the dip if both are strongly associated with the stream. An obvious explanation would be a change in the mass accretion rate that has altered both the blob size and the stream trajectory.

In 1993 the hardness ratio again does not display any changes that can readily be associated with features in the flux light curve, although there are two brief intervals of softening, at phase 0.07 and 0.78. As with RE J1844-74 (see below) these may be associated with changes in the orientation of the pole(s) with respect to the line of sight.

EK UMa

Both the 1992 and 1993 light curves of EK UMa display essentially the same morphology. The light curve is dominated by a bright phase lasting 0.6ϕ which is interrupted a variable number of dips. Two of the dips, at phase 0.95 and 0.05, are stable and have been detected each time this phase interval has been observed. They are probably both associated with accretion stream absorption (Clayton & Osborne 1994) although the lack of spectral change at these phases is surprising. The double-dip profile is an indication that the occulting part of the stream is quite structured. The stream probably does not thread onto field lines at one location, so each rising portion of the stream obscures the pole at a different phase.

The two narrow dips seen in 1992 at phase 0.85 and 0.90 were only observed once and are not permanent features of the light curve. They are most likely associated with flaring or absorption activity during the bright phase (Clayton & Osborne 1994). The flux prior to the dip increased by a factor of ~ 2 between the observations, while the post-dip flux remained constant. No hardness ratio variations are seen, though the second light curve indicates that the residual faint phase flux is significantly softer than the bright phase.

HU Aqr

The light curve of HU Aqr displayed earlier in this thesis is repeated here for comparison with the rest of the sample. HU Aqr displays most of the interesting features seen in the flux and hardness ratio light curves of AM Her systems; an eclipse, a hardening of the X-ray flux associated with an absorption dip, and softening during the bright-faint transitions. For a more detailed look at the ROSAT results from HU Aqr, see Section 4.4.

ST LMi

The ROSAT light curve of ST LMi displays a double-humped morphology with the main and

secondary peaks occurring at phase 0.95 and 0.45. This is consistent with the soft X-ray light curve of ST LMi obtained with the EXOSAT satellite (Cropper & Horne 1994). Each hump arises from one pole; clearly the slightly brighter pole is in view at phase 0.95. This is the classic example of a ‘two-pole’ system with two poles of comparable luminosity which could easily be confused with a continuous, ‘one-pole’ light curve.

The hardness ratio light curve is flat with no highly significant variations. However, it should be noted that the three data points with the softest flux correspond to the phase at which one pole is becoming more dominant than the other (phase 0.2 and 0.6). This is exactly where softening is expected to occur based upon the results obtained with HU Aqr, UZ For etc. In spite of the fact that the significance of the softening is very small in itself, it does fit the pattern emerging in the population of AM Her systems as a whole. Thus greater weight is placed upon this marginal detection than is justified by the data from ST LMi alone.

UZ For

The X-ray light curve and hardness ratio of UZ For is discussed in detail in Section 5.4, but is included here for clarity. As for HU Aqr, this system displays most of the interesting features of polar light curves.

VV Pup

The bright phase of VV Pup is interrupted by a 0.1ϕ interval for which no data is available. This lack of coverage arose due to aliasing of the 100 min. binary period with the ~ 90 min. orbital period of the ROSAT spacecraft. VV Pup has been observed to have an absorption dip at phase ~ 0.95 (e.g. Vennes et al. 1995) which is not evident in this observation. A small data gap exists between 0.925 and 0.950 that could account for the lack of a dip, but as dips are known to disappear at some epochs (§4.4.1) it is more likely that the VV Pup dip was simply not present for the ROSAT observation.

The bright phase itself is markedly asymmetric, and such asymmetry has been observed previously at optical (Patterson et al. 1984, Cropper & Warner 1986), EUV (Vennes et al. 1995) and X-ray wavelengths (Patterson et al. 1984). There is a softening of the X-rays during egress evident in the hardness ratio light curve but there is no softening on ingress. Cropper & Warner

(1986) reported a number of other differences between the beginning and end of the bright phase in their optical photometric and polarimetric light curves. It is clear that VV Pup is displaying very different properties during the ingress to the faint phase than those displayed during the egress. These are summarised below:

1. The bright phase is asymmetric in optical, EUV and X-ray observations.
2. A softening of the X-ray flux occurs during egress which is not evident on ingress.
3. A peak in the optical linear polarisation occurs during ingress, but not egress.
4. There is a negative peak in the optical circular polarisation only during the ingress.

Vennes et al. (1995) stated that the slow rise and abrupt decline in VV Pup could indicate an asymmetric accretion region on the white dwarf. Although this is true, it only explains the shape of the light curve, not the spectral and polarisation differences. It is proposed here that an accretion column tilted in the direction of orbital motion, as was discussed in reference to HU Aqr (described in §4.4.2), could be employed to explain all four differences between the ingress and egress. Each attribute of the VV Pup light curves can then be understood:

1. It has already been discussed how a tilted column could produce an asymmetric bright state (§ 4.4.2). In fact, a detailed look at both the X-ray and EUV light curves reveals that the egress, up to phase ~ 0.75 , occurs at more or less the same rate as the ingress. Figure 6.2 shows the egress from the faint phase reversed and overlaid onto the ingress, following the method applied to both HU Aqr and UZ For (§4.3.1, §5.3.1). The egress clearly deviates from the ingress after $\phi = 0.75$. A stepped egress is exactly the profile produced by an accretion column tilted by a large angle (larger than in the case of HU Aqr). The broad dip becomes shifted to an earlier phase by the greater tilt, and once it overlaps the egress a step is produced.

2. It was discussed in Section 4.4.4 that softening of the X-ray flux during ingress/egress can occur if a softer region of emission surrounds the main emission on the surface or is extended above it. If a softer emission region is located above a tilted column, then during the egress the soft region will emerge well before the rest of the column and the softening will be observable, whereas at ingress the whole column will be occulted at the same time. Another useful way of

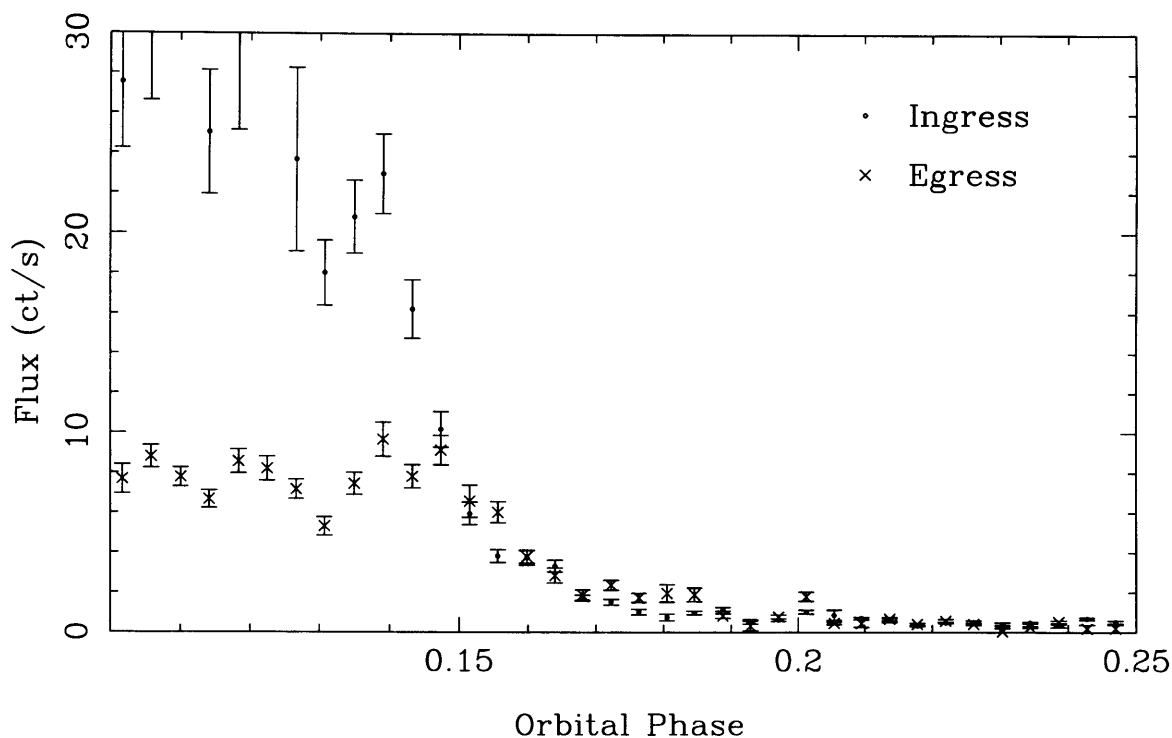


Figure 3.2: The egress from the faint state from the light curve of VV Pup, reversed (about $\phi = 0.44$) and overlaid onto the ingress. The deviation of the shape of egress from that of the ingress can clearly be seen.

looking at this is that the ingress to the faint phase occurs over such a compressed phase range that the softening simply is not resolved in the light curve.

Sirk & Howell (1996) have modelled the ingress and egress to the EUV faint phase of VV Pup. Their model represents the emission region as a small mound on the white dwarf surface which gives an adequate fit to the data, but systematically underestimates the flux at the earliest and latest segments of the rise and fall phases respectively. They attribute the residual flux to radiation from the accretion column immediately above the emission spot itself. Sirk & Howell successfully fit the excess emission by modelling it as an exponential decline in emission with height above the spot. This represents independent confirmation of an extended emission region above the spot as has been argued for here.

3. Linear polarisation peaks occur when the accretion column is being observed at its closest to 90° . For a column that is perpendicular to the white dwarf surface, this occurs at the beginning and end of the bright phase. If the column is tilted in the direction of orbital motion, then these peaks will occur earlier. As a result, the egress peak occurs *before* the column emerges and is

therefore not observed. The second peak is still seen preceding the ingress. This matches the observations of Cropper & Warner (1986) exactly (see their Figure 2).

4. Short reversals of the circular polarisation at the end of the bright phase have been seen in other systems (e.g. UZ For, Bailey & Cropper 1991). The reversal is thought to be the effect of observing an accretion column with significant height from underneath. Although this is possible for a radial column (with a large height) it is much more likely if a tilted column is present. The same argument is used by Warren et al. (1995) to explain a negative polarisation pulse in the light curve of UZ For.

Threading of the accretion stream by the magnetic field occurs at finite distances from the white dwarf and the field lines along which the material then flows will seldom meet the surface radially. Given that a range of different magnetic orientations are possible, and that the stream can penetrate the magnetic field to a range of different depths, it is inevitable that the accretion column can lead the orbital motion by a range of different inclinations. The proportion of systems which will display observable effects of this tilt could be determined from the distribution of such parameters as the magnetic moment, the magnetic co-latitude, the binary separation and the mass accretion rate, but an estimation of this value is well beyond the scope of this thesis.

VV Pup has emerged as another system with an asymmetric bright phase that can be explained by a column tilted in the direction of orbital motion. The benefit of this explanation over others is that a number of other anomalies associated with the system can also be easily explained, without having to make any further assumptions. After similar conclusions for HU Aqr and UZ For, there is now significant observational evidence to indicate that non-radial accretion can be a feature in some AM Her systems.

WW Hor

WW Hor is an eclipsing system; the soft X-ray eclipse is visible in Figure 6.1 at phase 0.0. No significant hardness ratio variations are seen, apart from a faint phase hardness ratio significantly lower than that during the bright phase. The ROSAT observation of WW Hor took place when the system was in a low accretion state and combined with the large distance to the system (430 pc, Bailey et al. 1988) means that the detected count rate is relatively low. The ingress and egress to the faint phase therefore appear not to be very well resolved, which may account for

the lack of spectral features at these phases.

RX J0453-42

The results of the 1992 ROSAT PSPC observation of RX0453-42 have already been presented by Burwitz et al. (1996). Their analysis of the radial velocities of the Balmer and HeII emission lines put forward two candidate orbital periods for the system; 101.95 ± 0.20 min and the alias period of 93.83 ± 0.22 min. The optical data favour the longer period. The ROSAT X-ray data were folded on the two candidate periods and both light curves are shown in Figure 6.1. For the 102 minute period, the morphology of the light curve is unclear; no obvious features are evident, nor is there any apparent spectral change. The 94 minute period, although it has poorer orbital coverage, shows reduced flux between phase 0.4 and 0.6 which may be a short faint state.

Evidence to support the 94 minute period comes from the hardness ratio light curve. Structure in the emission regions (§ 4.4.4) and softer flux from a second pole can lead to a softening effect in the hardness ratio light curve when the main pole is eclipsed. The X-rays from RX0453-42 soften during the flux minimum ($0.4 < \phi < 0.6$), which could be taken as confirmation that the true period is closer to 94 minutes than 102 minutes. If so, then the light curve morphology of RX0453-42 is reminiscent of that of AM Her. For this reason RE 0453-42 has been included in the bright/faint class of systems.

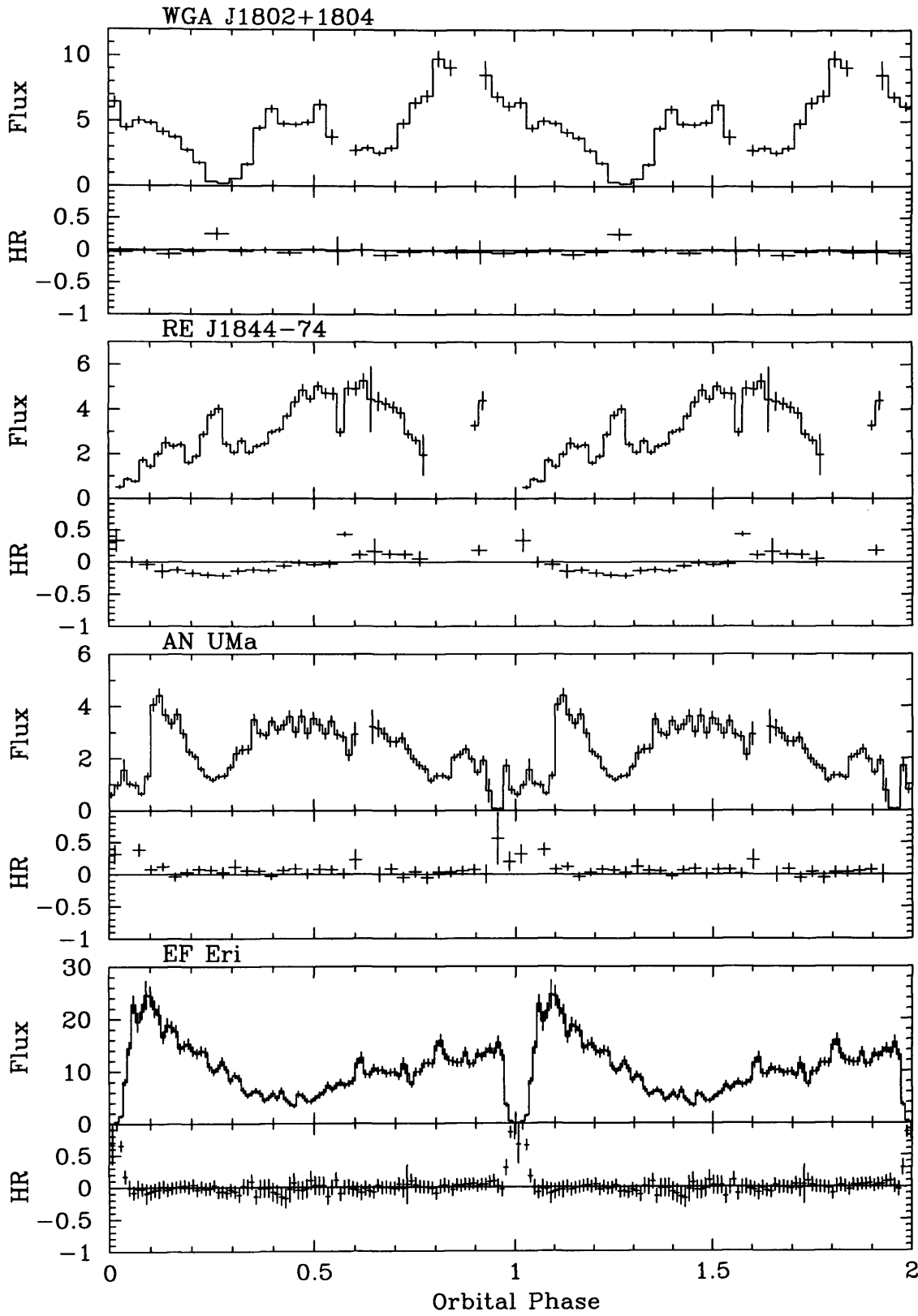


Figure 3.3: Flux and hardness ratio light curves of the polars classified as continuous systems.

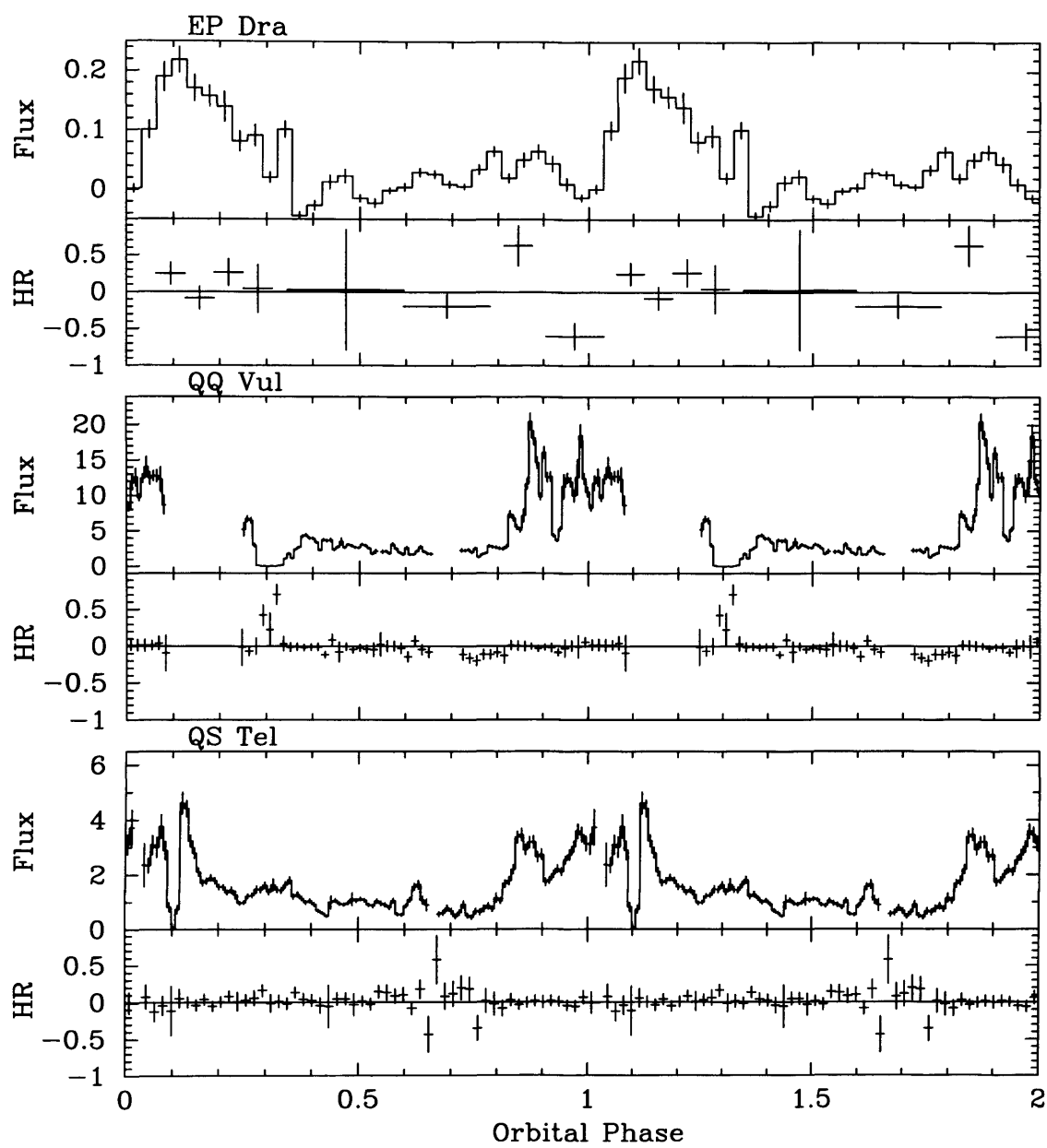


Figure 3.3: Continued.

3.4.2 Continuous systems

WGA J1802+1804

Szkody et al. (1995) have commented that the light curve morphology of WGA1802+1804 resembled that of QQ Vul, based on the presence of two dips at phase 0.25 and 0.65 (the second dip is less distinct in the fold of the data presented here). The hardness ratios show no significant change over the orbital cycle. The conclusion about the dip seen in QQ Vul is that it is an absorption dip (Osborne et al. 1987) and the marginal hardening at phase 0.22-0.31 in Figure 6.3 may support a similar conclusion about the dip in WGA1802+1804.

RE J1844-74

Ramsay et al. (1996) reported that the soft X-ray light curve of RE1844-74 displayed a bright phase lasting ~ 0.5 phase units, consistent with the appearance of a pole for only part of the orbital cycle. This bright phase is evident in the light curve above, centred on phase ~ 0.57 . There is a gradual softening of the X-ray flux between phase 0.1 and 0.3, followed by a gradual hardening until phase 0.5. The information available here is insufficient to provide a firm explanation for this, but it may be due to the admixture of flux from two X-ray emission regions (poles) with different spectra. The systematic variation of the hardness may represent the continuous change in the proportion of flux from each pole as they rotate into and out of view on the white dwarf surface.

AN UMa

The soft X-ray light curve of AN UMa is remarkably stable over long periods of time. The EXOSAT observation in 1984 displayed a light curve that is almost identical to the 1991 ROSAT PSPC data presented here (Osborne 1988, see Ramsay et al. 1994 for the light curve folded on the ephemeris below). This should be compared to systems like RX1844-74 where the light curve can change markedly from one cycle to the next (Ramsay et al. 1996). The light curve of AN UMa shows a broad peak between phase 0.3 and 0.8, and a narrower peak between phase 0.85 and 0.2 interrupted by a highly structured dip. The dip runs between phase 0.93 and 0.10 and the hardness ratio is significantly high throughout this interval, consistent with the interpretation of the dip as the result of accretion stream occultation.

The dip profile is not uniform; it begins with a brief period of near-totality (0.03ϕ) followed by a recovery to a non-zero flux of $\sim 1 \text{ ct s}^{-1}$ for 0.14ϕ . At phase 0.1 the dip ends as the flux return to a level of 4 ct s^{-1} . Ramsay et al. (1994) explain this complex profile as the passage of both the rising and falling portions of the stream across the line of sight. This seems an unlikely explanation given that the stream would have to be twisted to achieve this. No single stream which is following a dipolar field line could produce this profile. A more plausible and straightforward explanation is that the stream itself is structured, as was the explanation given above for the highly structured dip in EK UMa. An accretion stream with a ‘curtain’-like structure will obscure the pole at a range of different phases, thereby creating a highly structured dip.

Note that the hardness ratios calculated from the same data by Ramsay et al. (1994) do not show any hardening during the dip. The energy ranges selected for the hard and soft bands were identical to this study, but Ramsay et al. used the formula $\text{HR} = \text{H}/\text{S}$ for their hardness ratios. When this method was used to calculate the hardness ratio an increase in hardness is still present, albeit at somewhat lower significance. From this it is unclear why Ramsay et al. did not detect any hardening whatsoever. This comparison demonstrates the improved signal-to-noise that Equation 6.1 provides in calculating the hardness ratios.

EF Eri

It has long been known that EF Eri displays the textbook example of an AM Her absorption dip. Systematic hardening of the X-rays through the dip were first detected with the *Einstein* Observatory (Patterson et al. 1981). They proposed that the accretion stream was the only body in the system that could account for all the observed phenomena, and this has now become the established explanation for the dip in this and other systems.

The shape of the ROSAT PSPC light curve of EF Eri agrees well with that observed in previous X-ray studies. A sinusoidal variation in flux is seen with a degree of asymmetry to the peak; the maximum is located at $\phi = 0.10$ while the minimum is less than half a cycle away, at $\phi = 0.45$. One tenth of a cycle prior to maximum flux the absorption dip is detected. As was the case in earlier X-ray studies (Watson et al. 1989), there are no variations in hardness throughout the orbital cycle apart from the striking peak during the absorption dip during which the hardness

ratio rises to a value of ~ 0.9 . The ingress and egress to the dip are so well resolved and the spectral change is so strong that it is possible to detect the gradual increase and decrease in the hardness through the dip.

EP Dra

EP Dra is an eclipsing system and the X-ray eclipse is observable in the ROSAT data at phase 1.0. These data have been presented previously by Schlegel & Mukai (1995). The light curve they produced, folded on the ephemeris of Remillard et al. (1991), had an eclipse at phase 0.85 and hence Schlegel & Mukai concluded that the period was incorrect by some 0.045 s. Both the data and the ephemeris used to create the light curve presented above are the same as those used by Schlegel & Mukai, yet there is no evidence for an error in the period. From the above fold it is estimated that the period is incorrect by at most 0.009 s. Further observations to confirm the period are therefore required. No systematic spectral changes can be seen in the hardness ratio light curve.

QQ Vul

QQ Vul is known to possess two different accretion states which display major differences in their soft X-ray light curves (Osborne et al. 1987). During the ‘simple’ mode the light curve shows two maxima of similar strength and two minima separated by half an orbital cycle. The simple mode is thought to be the product of accretion onto a single pole on the white dwarf. A near-total minimum is present during the ‘complex’ mode, without the smooth sinusoidal variations in flux of the simple mode.

The ROSAT PSPC light curve of QQ Vul exhibits the complex morphology. A near-total dip feature is present at phase 0.3 that is clearly associated with accretion stream absorption, as the hardness increases to a mean value of 0.45 at that phase. After the dip the X-ray flux remains at a constant level until $\phi = 0.82$ where a rapid four-fold increase in flux occurs. Beardmore et al. (1995*b*) reported an increase in the hardness ratio during the bright portion of the light curve. There is an increase in the hardness between phase 0.75 and 0.85 in the ROSAT data which is suggestive of this spectral difference. On the other hand the hardness in the 0.40-0.65 phase range is about the same as at 0.85-1.10, which is contrary to what Beardmore et al. observed. The morphology and spectral changes of the complex mode light curve is

probably due to accretion onto two poles with different spectral characteristics (Beardmore et al. 1995*b*).

QS Tel

The data presented here have been discussed previously in Rosen et al. (1996). In earlier EUV and X-ray observations of QS Tel a clear bright phase to faint phase variation was seen. This ROSAT PSPC observation does not display such behaviour and hence the system may now be accreting onto two poles rather than one. There is still evidence for a broad bright phase between phase 0.8 and 1.25 in the data, interrupted by a narrow dip. This dip is not evident in former observations, and so it was concluded by Rosen et al. that an accretion stream occultation is occurring at this phase. There is a lack of systematic variation in the hardness ratios through the orbital cycle including the dip. The light curve between phase 0.6 and 0.8 was only observed once and so the hardness ratio not well defined at this phase. The absence of any hardening during the dip may be accounted for by the rapid transitions into and out of the dip which do not allow the spectral change to be resolved.

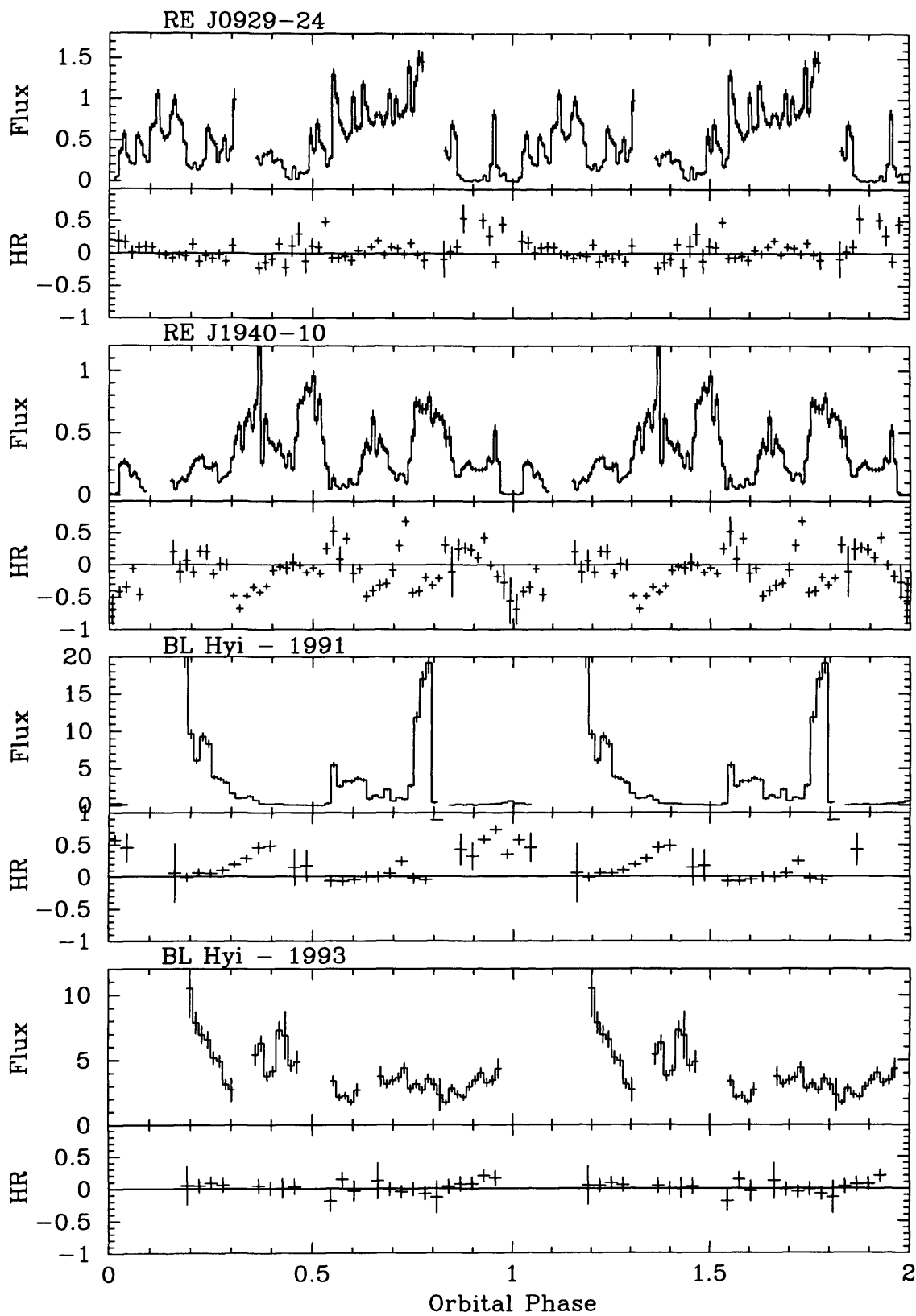


Figure 3.4: Flux and hardness ratio light curves of the AM Her systems for which the soft X-ray light curve morphology is dominated by flares.

3.4.3 Flaring systems

RX J0929-24

The soft X-ray light curve of RX0929-24 is dominated by flaring events throughout the orbital cycle. This becomes more apparent when the light curve is compared to that of another system with a similar count rate, like AN UMa. Each flare may indicate the impact of an individual blob of stream material on the white dwarf surface. The flux minimum at phase 0.0 is the X-ray counterpart to the optical eclipse reported by Sekiguchi, Nakada & Bassett (1994). One tenth of an orbital cycle prior to this eclipse is another flux minimum, interpreted here as an X-ray absorption dip; there is a significant increase in the hardness ratio at this phase. Apart from this, the hardness ratio light curve is essentially featureless. The overall morphology of the X-ray light curve is unclear, although the minimum at phase 0.5 may indicate a double- or single-humped morphology.

RE J1940-10

There is a great deal of structure in the soft X-ray light curve of RE1940-10 which makes it difficult to interpret. The one distinct and stable feature in the light curve is the dip at phase 0.0, the origin which has yet to be resolved. Watson et al. (1995) propose that the accretion stream causes the dip, based in part on the detection of hardening during the dip from a *Ginga* observation of the system. On the other hand Patterson et al. (1995) support the view that the feature is actually an eclipse by the secondary. This study has been unable to resolve the issue; no hardening is found, which would favour the eclipse explanation, but for the fact that a softening is detected during the dip which not easy to interpret with either a dip or an eclipse.

The other, less distinct features in the light curve are a reduction in flux at $\sim 0.6 \phi$ and two peaks in flux at 0.4ϕ and 0.8ϕ . Watson et al. (1995) suggested that the overall modulation of the light curve might be represented by a period other than the dip period. This would reduce the number of stable features present in the current fold.

BL Hyi

Brief reports on the 1991 and 1993 ROSAT observations of BL Hyi have been given in Schwope et al. (1995*b*, 1995*c*). In 1991 BL Hyi was in a unique accretion state. Long periods of zero accretion, characterised by zero X-ray flux, were interrupted by a number of X-ray flares of up to 80 ct s^{-1} . It is not apparent what the cause of this irregular accretion is, nor which of the accreting poles is the origin of the flares. In 1993 the light curve displays a bright and a faint phase, although most of the bright phase was not observed (Schwope et al. 1995*b*). The bright phase lasts approximately between phase 0.0 and 0.5 in this fold of the data. Significant flux is detected during the faint phase which suggests accretion is taking place onto both poles at this epoch.

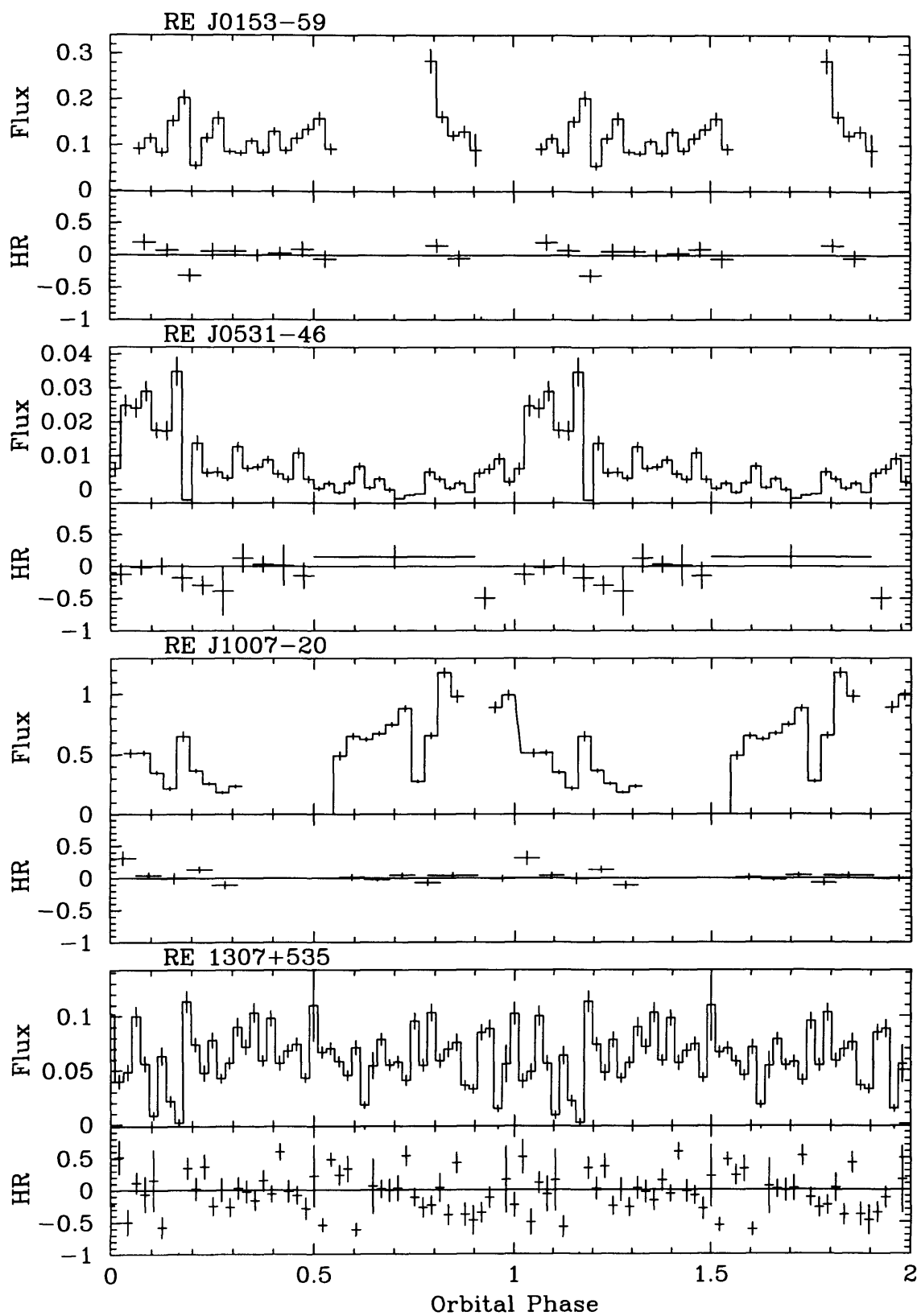


Figure 3.5: Flux and hardness ratio light curves of the AM Her systems for which no classification could be made.

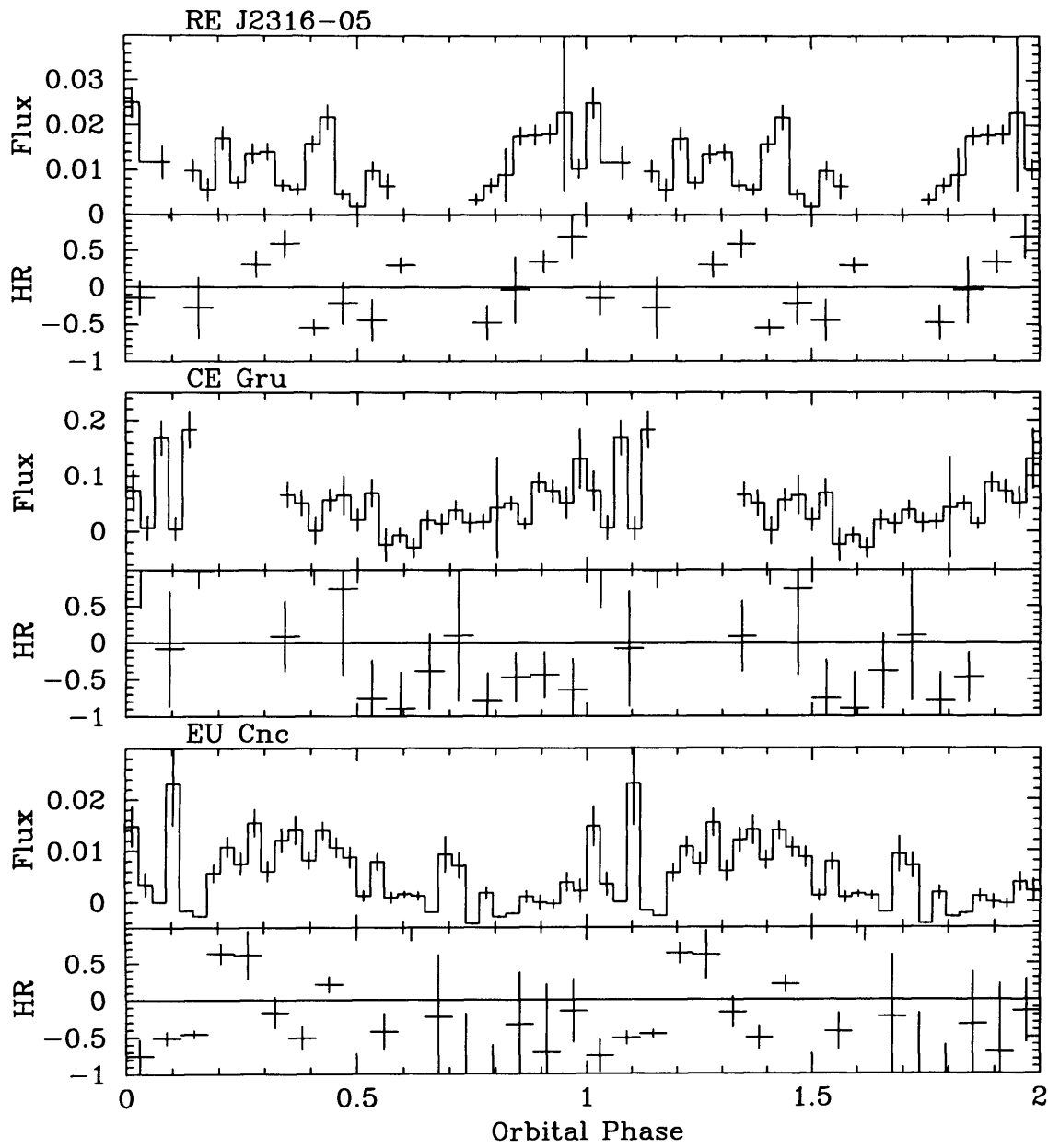


Figure 3.5: Continued.

3.5 Discussion

3.5.1 Classification of the soft X-ray light curves

Table 6.4 shows that of the 30 systems studied, only 20 have provided soft X-ray light curves with enough quality to be classified as either bright/faint systems or continuous systems. The seven systems listed in the fourth column of the table were unable to be classified because of a low detected count rate or poor orbital coverage. Such low X-ray fluxes either represent the long-term behaviour of the system, or are attributable to a temporary low state of accretion. The three systems in the third column of the table are dominated by flaring through most of the orbital cycle, which has hidden the underlying morphology of the light curve.

In Section 6.3 it was predicted that the proportion of bright/faint systems ought to be 50%. The ratio of bright/faint systems to continuous systems in this study is 13:7 (i.e. 65% are bright/faint systems). Furthermore, some of the classifications made here are somewhat subjective and could be contested. For example, QS Tel is classified here as a continuous system, but Rosen et al. (1996) have interpreted the ROSAT light curve as a bright/faint system with significant flux from a second X-ray pole. The systems that are included in the first column of Table 6.4 have been defined as those for which the bright/faint variations are *clear*. It is therefore likely that some of the continuous light curves may be re-interpreted as bright/faint systems for which the bright-to-faint variability is not distinct. EF Eri, EP Dra and QS Tel might be examples of such systems. If some systems are re-evaluated in this way, the actual proportion of bright/faint systems would rise to over 75%.

By finding that the fraction of bright/faint systems is well over 50%, this study has confirmed that geometric factors alone do not determine the distribution of soft X-ray light curve types. It appears that co-alignment of the spin axis with the rotational axis *does* occur during the early evolution of AM Her systems.

| System | Hardening? | System | Hardening? |
|--------------|------------|-----------|------------|
| RE J1015 | Y | WGA J1802 | Y? |
| RE J1846 (?) | Y | AN UMa | Y |
| DP Leo | N | EF Eri | Y |
| EK UMa | N | QQ Vul | Y |
| HU Aqr | Y | QS Tel | N |
| UZ For | Y | RE J0929 | Y |
| | | RE J1940 | N |

Table 3.6: AM Her systems included in this study which display dips. For each system the presence or absence of hardening of the soft X-ray flux during the dip is indicated.

3.5.2 Absorption dips

Frequency of detection

Absorption dips appear to be a very common feature of the soft X-ray light curves of AM Her systems. Dips have been detected in 13 of the 23 systems for which a significant X-ray flux was detected (those systems in columns 1-3 in Table 6.4). These 13 systems are listed in Table 6.6. Clearly, the percentage of systems that display dips in their soft X-ray light curves substantially exceeds the lower limit of 18% which was based on purely geometric arguments. Again it appears that geometric factors alone do not determine the distributions of i and β , and that further evidence for the co-alignment of the magnetic and rotational axis has been found. In addition, it is also likely that some systems are producing dips through more complicated accretion geometries; such as the enlarged stagnation regions and multiple streams mentioned in Section 6.3.

Spectral changes through absorption dips

In Section 6.3 it was established that AM Her absorption dips ought to be associated with hardening of the soft and/or hard X-ray flux (Watson et al. 1989) in a large proportion of systems. This study has confirmed that fact with the detection of hardening in 9 of the 13 absorption dips observed (69%, see Table 6.6). Those dips for which no hardening is found do not necessarily indicate either that the dip is not an absorption dip caused by the stream, or that this absorption is not photoelectric in origin and therefore causing some hardening of the X-ray flux. As was discussed in Section 6.3, any rapid or subtle changes to column density are

simply not detectable by the ROSAT PSPC. The best candidate for a dip affected in this way is the extremely narrow and deep dip in QS Tel.

This study has therefore shown that hardening of the soft X-ray flux is associated with a large fraction of AM Her absorption dips, possibly as many as 90%. Such a result must be considered in the interpretation of all X-ray light curves of AM Her systems. The hardness ratio is clearly a powerful tool for determining the origin of dip features in light curves; an absence of hardening in the X-ray flux is highly suggestive of a non-stream origin for the dip. The only exception to this interpretation should be made when other evidence for accretion stream occultation is found. The converse is also true; the simplest interpretation of a hardness increase during a dip is photoelectric absorption by the accretion stream. These principles were applied when interpreting the broad dip in HU Aqr; no spectral features were associated with this dip, and so an explanation other than accretion stream occultation was sought.

3.5.3 Structured emission regions

In the light curves of 13 of the 23 systems in this study there is a discernible bright/faint variation. Of these 13 systems only five display a strong softening during the ingress and/or egress to the faint phase (HU Aqr, UZ For, VV Pup, AM Her and RE J1015+0904). Three additional systems show slight evidence for a similar softening effect; RE J1149+28, ST LMi, if the marginal detection at the correct phase is accepted, and RX J0453–42, assuming (i) that the 94 min period is correct and (ii) the observed softening is not due to a second pole. This situation should be contrasted with the absorption dip where the spectral effect was found to have a high rate of detection. This suggests that in many cases the softening in the transitions is not strong enough for detection by the PSPC. In addition, some systems may possess emission regions without the structure required to produce this effect. Given that the accretion flow-white dwarf surface interaction is highly complex this is perhaps not surprising. The strong dependence of the softening effect on the accretion mode is well demonstrated in the case of AM Her, for which softening was only found during the low state. It is reasonable to suppose that accretion in other systems may be taking place in a mode similar to AM Her in its high state, in which case the emission structure will not be present.

Closer inspection of the five systems that display softening effects during the transitions reveals

| | Method | Ingress | Egress |
|--------|------------------|-------------------|-------------------|
| HU Aqr | Flux $> 5\sigma$ | 0.213 ± 0.005 | 0.529 ± 0.005 |
| | Hardness ratios | 0.240 ± 0.008 | 0.520 ± 0.008 |
| UZ For | Flux $> 5\sigma$ | 0.136 ± 0.005 | 0.570 ± 0.005 |
| | Hardness ratios | 0.146 ± 0.006 | 0.539 ± 0.006 |

Table 3.7: Orbital phase at which the ingress and egress to the bright phase occurs in HU Aqr and UZ For. These are defined as the phase at which the flux exceeds 5σ of the mean faint phase flux and as the phase at which softening occurs in the hardness ratios, associated with the appearance of the edge of the emission region.

a consistent shape to the hardness ratio light curves in all but AM Her. The soft ‘pulses’ are asymmetric; the hardness decreases suddenly on egress followed by a gradual increase to the mean bright phase level. On ingress the reversed shape is seen. The explanation for this is obvious; when the systems is observed closer to the faint phase, less of the harder core to the emission region is in view, so the spectrum becomes softer. The existence of a consistent shape to the soft pulses from one system to another confirms that a real effect is being observed and not just a statistical fluctuation. It also lends weight to marginal detections where the pulse shape matches the pattern, as in the case of RX J1015+0904.

The phase at which the rapid changes in softness occur represents the time at which the edge of the emission region moves over the limb of the white dwarf and these rapid changes could be used as an alternate definition of the beginning or end of the bright phase. Table 6.7 compares the phase of ingress and egress obtained by the method described in Sections 4.3.1 to the phase obtained from the spectral change for HU Aqr and UZ For. In spite of these differences, the correct way to define the limits of the bright phase is probably not the time of rapid spectral change, as it is not entirely clear what object is being detected passing over the limb, the base of the column or extended emission above it or surrounding it.

In the future detailed investigations of these transitions could provide useful information on the X-ray spectrum at different locations within the emission region itself. Such techniques will be a valuable tool for confirming and refining our understanding of the physical processes occurring in the accretion region. The improved sensitivity and spectral capability of future X-ray missions should provide the opportunity of making the high time- and spectral resolution measurements that would be required to achieve this.

Inclined accretion columns

The possible use of inclined emission regions with a significant height have been discussed a number of times and have been used to explain the broad dips and asymmetric bright phases of HU Aqr, UZ For (EUV data) and VV Pup. The need for three-, rather than two-dimensional emission regions is well established (e.g. Sirk & Howell 1996), but not the use of a tilted accretion column. It has been stated earlier that inclined columns may arise because the accretion flow is along field lines which do not meet the white dwarf surface orthogonally. This being the case then the occurrence of inclined columns could be quite high and most of the systems with a bright phase have the potential to show some evidence of this. However, only three systems have required their use to explain the shape of the light curve. This therefore suggests that, in general, the range of such parameters as the magnetic moment, co-latitude and threading distance do not favour accretion columns that are inclined in the direction of orbital motion, or that the quality of data available is not sufficient to reveal the presence of inclined columns.

The hardness ratios

One fact this study has demonstrated clearly is that the hardness ratio of most AM Her systems is remarkably constant. Apart from known features like dips, eclipses, transitions and so on, the hardness ratio light curves of most bright/faint and continuous systems are flat to within the errors on the data. AM Her and EF Eri are perhaps the best examples of this (see Figures 6.1 and 6.3). These systems should be contrasted with the light curves of RE1940-10 and BL Hyi, and possibly RE1844-74 as well, all of which show large and systematic hardness ratio changes over large portions of the orbital cycle. What remains unclear is whether these changes are intrinsic to the source or arise due to the instrumentation or data processing. This will have to be investigated further, but is included here as an interesting and unexpected result to emerge from this analysis.

References

- Allen, R. G., Berriman, G., Smith, P. S. & Schmidt, G. D., 1989, *Astrophys. J.*, **347**, 426
- Bailey, J. A., 1988, in Coyne, G. V., et al., eds, *Polarised Radiation of Circumstellar Origin*, p. 105
- Bailey, J. A., 1995, in Buckley, D. A. H., Warner, B., eds, *Cape Workshop on Magnetic Cataclysmic Variables*, p. 10
- Bailey, J. & Cropper, M., 1991, *Mon. Not. R. astr. Soc.*, **253**, 27
- Bailey, J. A., Watts, D. J., Sherrington, M. R., Axon D. J., Giles, A. B., Hanes, D. A., Heathcote, S. R., Hough, J. H., Hughes, S., Jameson, R. F. & McLean, I., 1985, *Mon. Not. R. astr. Soc.*, **215**, 179
- Bailey, J. A., Wickramasinghe, D. T. Hough, J. H. & Cropper, M., 1988, *Mon. Not. R. astr. Soc.*, **234**, 19P
- Barrett, P. E. & Chanmugam, G, 1984, *Astrophys. J.*, **278**, 298
- Beardmore, A. P., Done, C., Osborne, J. P. & Ishida, M., 1995a, *Mon. Not. R. astr. Soc.*, **272**, 749
- Beardmore, A. P., Ramsay, G., Osborne, J. P., Mason, K. O., Nousek, J. A. & Baluta, C., 1995b, *Mon. Not. R. astr. Soc.*, **273**, 742
- Beasley, D., Bull, D. R. & Martin, R. r., 1993a, *University Computing*, 15(2), 58
- Beasley, D., Bull, D. R. & Martin, R. r., 1993b, *University Computing*, 15(4), 170
- Berriman, G. & Smith, P. S., 1988, *Astrophys. J.*, **329**, L97
- Beuermann, K., 1988, in *Polarised Radiation of Circumstellar Origin*, p. 125
- Beuermann, K. & Burwitz, V., 1995, in Buckley, D. A. H., Warner, B., eds, *Cape Workshop on Magnetic Cataclysmic Variables*, p. 99

- Beuermann, K. & Thomas, H.-C., 1993, *Adv. Sp. Res.*, **13**, 115
- Beuermann, K., Stella, L. & Patterson J., 1987, *Astrophys. J.*, **316**, 360
- Beuermann, K., Thomas, H.-C. & Schwope, A. D., 1988, *Astr. Astrophys.*, **195**, L15
- Beuermann, K., Burwitz, V., Reinsch, K., Schwope, A. D. & Thomas, H.-C., 1995, in Bianchini, A. et al. (eds.), *Cataclysmic Variables*, p. 381-388
- Beuermann, K., Thomas, H.-C., Schwope, A. D., Giommi, P. & Tagliaferri, G., 1990, *Astr. Astrophys.*, **238**, 187
- Biermann, P., Schmidt, G. D., Liebert, J., Stockman, H. S., Tapia, S., Kühr H., Strittmatter, P.A., West, S., & Lamb, D.Q., 1985, *Astrophys. J.*, **293**, 303.
- Boeshaar, P. C., 1976, PhD Thesis, Ohio State University
- Bonnet-Bidaud, J. M., Mouchet, M., Somova, T. A. & Somov, N. N., 1992, IAU Circ. 5673
- Brainerd, J. J. & Lamb, D. Q., 1985, in Lamb, D. Q. & Patterson, J., eds, *Cataclysmic Variables and Low-Mass X-ray Binaries*, p. 247
- Brett, J. M. & Smith, R. C., 1993, *Mon. Not. R. astr. Soc.*, **264**, 641
- Burwitz, V., Reinsch, K., Schwope, A. D., Beuermann, K., Mengel, S., Notni, P., van Teeselin, A. & Thomas, H.-C., 1995, in Evans, A, Wood, J. H. eds, *Proceedings IAU Colloquium 158*, p. 229
- Burwitz, V., Reinsch, K., Schwope, A. D., Beuermann, K., Thomas, H.-C. & Greiner, J., 1996, *Astr. Astrophys.*, **305**, 507
- Córdova, F., 1995, in Lewin, W. H. G., Van Paradijs, J. & Van den Heuvel, E. P. J., eds, *X-ray Binaries*, p. 331
- Caillault, J. -P. & Patterson, J., 1990, *Astron. J.*, **100**, 825.
- Campbell, C. G., 1989, *Mon. Not. R. astr. Soc.*, **236**, 475

- Canalle, J. B. G. & Opher, R., 1988, *Astr. Astrophys.*, **189**, 325
- Chanmugam, G. & Dulk, G. A., 1981, *Astrophys. J.*, **244**, 569
- Clayton, K. L. & Osborne, J. P., 1994, *Mon. Not. R. astr. Soc.*, **268**, 229
- Cropper, M., 1986, *Mon. Not. R. astr. Soc.*, **222**, 853
- Cropper, M., 1987, *Mon. Not. R. astr. Soc.*, **228**, 389
- Cropper, M., 1988, *Mon. Not. R. astr. Soc.*, **231**, 597
- Cropper, M., 1990, *Space Sci. Rev.*, **54**, 195
- Cropper, M. & Horne, K., 1994, *Mon. Not. R. astr. Soc.*, **267**, 481
- Cropper, M. & Warner, B., 1986, *Mon. Not. R. astr. Soc.*, **220**, 633
- Cropper, M., Bailey, J. A., Wickramasinghe, D. T. & Ferrario, L. 1990. *Mon. Not. R. astr. Soc.*, **224**, 34P.
- Czerny, M. & King, A. R., 1986, *Mon. Not. R. astr. Soc.*, **221**, 55P
- Davey, S. C. & Smith, R. C., 1996, *Mon. Not. R. astr. Soc.*, **280**, 481
- Eggleton, P. P., 1983, *Astrophys. J.*, **268**, 368.
- Fabbiano, G., Hartmann, L., Raymond, J., Steiner, J., Branduardi-Raymont, G. & Matilsky, T., 1981, *Astrophys. J.*, **243**, 911
- Ferrario, L. & Wickramasinghe, D. T., 1990, *Astrophys. J.*, **357**, 582
- Ferrario, L., Wickramasinghe, D. T., Bailey, J., Tuohy, I. R. & Hough, J. H., 1989a, *Astrophys. J.*, **337**, 832
- Ferrario, L., Wickramasinghe D. T., Tuohy, I. R., 1989b, *Astrophys. J.*, **341**, 327
- Frank, J., King, A. R. & Lasota, J.-P., 1988, *Astr. Astrophys.*, **193**, 113

- Frank, J., King, A. R. & Raine, D. J., 1992, *Accretion Power in Astrophysics*, CUP, 2nd ed.
- Fujimoto, R. & Ishida, M., 1995, in Buckley, D. A. H., Warner, B., eds, *Cape Workshop on Magnetic Cataclysmic Variables*, p. 136
- Fujimoto, R. & Ishida, M., 1997, *Astrophys. J.*, **474**, 774
- Gilliland, R. L., Brown, T. M., Duncan, D. K., Suntzeff, N. B., Lockwood, G. W., Thompson, D. T., Schild, R. E., Jeffrey, W. A. & Penprase, B. E., 1991, *Astron. J.*, **101**, 541
- Giommi, P. & Angelini, L., 1987, *EXOSAT Express*, **18**, 45
- Glenn, J., Howell, S. B., Schmidt, G. D., Liebert, J., Grauer, A. D. & Wagner, R. M., 1994, *Astrophys. J.*, **424**, 967.
- Graham, J. A., 1982, *Pub. astr. Soc. Pac.*, **94**, 244
- Greenstein, J. L., Sargent, W. L. W., Boroson, T. A. & Boksenberg, A., 1977, *Astrophys. J.*, **218**, L121
- Hakala, P. J., 1995, *Astr. Astrophys.*, **296**, 164
- Hakala, P. J., Watson, M. G., Vilhu, O., Hassall, B. J. M., Kellett, B. J., Mason K. O. & Piirola, V., 1993, *Mon. Not. R. astr. Soc.*, **263**, 61.
- Hameury, J. M. & King, A. R., 1988, *Mon. Not. R. astr. Soc.*, **235**, 433
- Hameury, J. M., King, A. R. & Lasota, J.-P., 1986, *Astr. Astrophys.*, **162**, 71
- Hameury, J. M., King, A. R., Lasota, J.-P. & Ritter, H., 1987, *Astrophys. J.*, **316**, 275
- Hameury, J. M., Lasota, J.-P. & King, A. R., 1988, *Astr. Astrophys.*, **195**, L12
- Heise, J., 1985, *Astr. Astrophys.*, **148**, L14
- Heise, J. & Verbunt, F., 1988, *Astr. Astrophys.*, **189**, 112

- Heise, J., Brinkman, A. C., Gronenschild, E., Watson, M. G., King, A. R., Stella, L. & Kieboom, K., 1985, *Astr. Astrophys.*, **148**, L14
- Hellier, C., 1991, *Mon. Not. R. astr. Soc.*, **251**, 693
- Horne, K. & Schneider, D. P., 1989, *Astrophys. J.*, **343**, 888.
- Howell, S. B., Sirk, M. M., Malina, R. F., Mittaz, J. P. D. & Mason, K. O., 1995, *Astrophys. J.*, **439**, 991
- Imamura, J. N., 1984, *Astron. J.*, **285**, 223
- Imamura, J. N. & Durisen, R. H., 1983, *Astrophys. J.*, **268**, 291
- Imamura, J. N., Durisen, R. H., Lamb, D. Q. & Weast, G. J., 1987, *Astrophys. J.*, **313**, 298
- Ishida, M. & Fujimoto, R., 1995, in Buckley, D. A. H., Warner, B., eds, *Cape Workshop on Magnetic Cataclysmic Variables*, p. 132
- King, A. R., 1988, *Quartl. Jl. R. astr. Soc.*, **29**, 1
- King, A. R., 1989, *Mon. Not. R. astr. Soc.*, **241**, 365
- King, A. R., 1993, *Mon. Not. R. astr. Soc.*, **261**, 144
- King, A. R., 1994, in Shafter, A. W., ed, *Interacting Binary Stars*, p. 189
- King, A. R., 1995, in Buckley, D. A. H., Warner, B., eds, *Cape Workshop on Magnetic Cataclysmic Variables*, p. 21
- King, A. R. & Lasota, J.-P., 1979, *Mon. Not. R. astr. Soc.*, **188**, 653
- King, A. R. & Watson, M. G., 1987, *Mon. Not. R. astr. Soc.*, **227**, 205
- King, A. R., & Williams, G., 1985, *Mon. Not. R. astr. Soc.*, **215**, 1P
- King, A. R., Frank, J. & Whitehurst, R., 1990, *Mon. Not. R. astr. Soc.*, **244**, 731

- Kirkpatrick, J. D. & McCarthy, D. W., 1994, *Astron. J.*, **107**, 333.
- Kirkpatrick, J. D., Henry, T. J. & McCarthy, D. W., 1991, *Astrophys. J. Suppl.*, **77**, 417.
- Kitchin, C. R., 1991, *Astrophysical Techniques*, IOP Publishing, 2nd ed.
- Koester, D. & Weidemann, V., 1980, *Astr. Astrophys.*, **81**, 145
- Kolb, U. & de Kool, 1993, *Astr. Astrophys.*
- Kuijpers, J., Pringle, J. E., 1982, *Astr. Astrophys.*, **114**, L14
- Kylafis, N. D. & Lamb, D. Q., 1979, *Astrophys. J.*, **228**, L105
- Kylafis, N. D. & Lamb, D. Q., 1982, *Astrophys. J. Suppl.*, **48**, 239
- Lamb, D. Q., 1985, in Lamb, D. Q. & Patterson, J., eds, *Cataclysmic Variables and Low-Mass X-ray Binaries*, p. 179
- Lamb, D. Q. & Masters, A. R., 1979, *Astrophys. J.*, **234**, L117
- Lamb, D. Q. & Melia, F., 1988, in Coyne, G. V., et al. , eds, *Polarised Radiation of Circumstellar Origin*, p. 45
- Landolt, A. V., 1983, *Astron. J.*, **88**, 439.
- Liebert, J. & Stockman, H. S., 1985, in Lamb, D. Q. & Patterson, J., eds, *Proceedings of the 7th North American Workshop on Cataclysmic Variables and X-ray Binaries*, Reidel, Dordrech, p. 151
- Mason, K. O., 1985, *Space Sci. Rev.*, **40**, 99
- Meggitt, S. M. A. & Wickramasinghe, D. T., 1984, *Mon. Not. R. astr. Soc.*, **207**, 1
- Middleditch, J., 1982, *Astrophys. J.*, **257**, L71
- Morris, S. L., Schmidt, G. D., Liebert, J., Stocke, J., Gioia, I. M. & Maccacaro, T., 1987,

Astrophys. J., **314**, 641

Mukai, K., 1988, *Mon. Not. R. astr. Soc.*, **232**, 175

O'Donoghue, D., Warner, B., Wargau, W. & Grauer, A. D., 1989, *Mon. Not. R. astr. Soc.*, **240**, 41

Osborne, J. P., 1988, *Mem. Astron. Soc. Italy*, **59**, 117

Osborne, J. P., Beardmore, A. P., Wheatley, P. J., Hakala, P., Watson, M. G., Mason, K. O., Hassall, B. J. M. & King, A. R., 1994, *Mon. Not. R. astr. Soc.*, **270**, 650

Osborne, J. P., Beuermann, K., Charles, P., Maraschi, L., Mukai, K. & Treves, A., 1987, *Astrophys. J.*, **315**, L123

Osborne, J. P., Giommi, P., Angelini, L., Tagliaferri, G. & Stella, L., 1988, *Astrophys. J.*, **328**, L45

Paerels, F., Heise, J. & van Teeseling, A., 1994, *Astrophys. J.*, **426**, 313

Panek, R. J. & Eaton, J. A., 1982, *Astrophys. J.*, **258**, 572

Patterson, J., 1994, *Publs. astr Soc. Pacif.*, **106**, 209

Patterson, J., Beuermann, K., Lamb, D. Q., Fabbiano, G., Raymond, J. C., Swank, J. & White, N. E., 1984, *Astrophys. J.*, **279**, 785

Patterson, J., Skillman, D. R., Thorstensen, J. & Hellier, C., 1995, *Publ. astr. Soc. Pacific*, **107**, 307

Patterson, J., Williams, G. & Hiltner, W. A., 1981, *Astrophys. J.*, **245**, 618

Pirola, V., Reiz, A. & Coyne, S. J., 1987, *Astr. Astrophys.*, **186**, 120

Pottasch, S. R., 1984, *Planetary Nebulae*, Reidel, Dordrecht

Priedhorsky, W. C., Krzeminski, W. & Tapia, S., 1978, *Astrophys. J.*, **225**, 542

- Ramsay, G., Cropper, M., Wu, K. & Potter, S., 1996, *Mon. Not. R. astr. Soc.*, **282**, 726
- Ramsay, G., Mason, K. O., Cropper, M., Watson, M. G. & Clayton, K. L., 1994, *Mon. Not. R. astr. Soc.*, **270**, 692
- Ramsay, G., Rosen, S. R., Mason, K. O., Cropper, M. S. & Watson, M. G., 1993, *Mon. Not. R. astr. Soc.*, **262**, 993
- Raymond, J. C., Black, J. H., Davies, R. J., Dupree, A. K., Gusky, H., Hartmann, L. & Matilsky, T. A., 1979, *Astrophys. J.*, **230**, L95
- Reinsch, K., Burwitz, V., Beuermann, K., Schwobe, A. D. & Thomas, H.-C., 1994, *Astr. Astrophys.*, **291**, L27
- Remillard, R., Stroozas, B., Tapia, S. & Silber, A., 1991, *Astrophys. J.*, **379**, 715
- Ritter H., & Kolb U. 1997, *Astr. Astrophys. Suppl.*, in press
- Robinson, C. R. & Córdova, F. A., 1994, *Astrophys. J.*, **437**, 436
- Rosen, S. R., Mason, K. O. & Córdova, F. A., 1987, *Mon. Not. R. astr. Soc.*, **224**, 987
- Rosen, S. R., Mittaz, J. P. D., Buckley, D. A., Layden, A. C., Clayton, K. L., McCain, C., Wynn, G. A., Sirk, M. M., Osborne, J. P. & Watson, M. G., 1996, *Mon. Not. R. astr. Soc.*, **280**, 1121
- Saxton R., 1992, *PPARC Starlink User Note*, 98
- Schlegel, E. M. & Mukai, K., 1995, *Mon. Not. R. astr. Soc.*, **274**, 555
- Schechter, P. L., Mateo, M. & Saha, A., 1993, *Publs. astr Soc. Pacif.*, **105**, 1342
- Schmidt, G. D., Stockman, H. S. & Margon, B., 1981, *Astrophys. J.*, **243**, L157
- Schrijver, C. J., 1985, *Space Sci. Rev.*, **40**, 3
- Schwobe, A. D., 1990, *Rev. Mod. Astr.*, **3**, 44

- Schwobe, A. D. & Beuermann, K., 1990, *Astr. Astrophys.*, **238**, 173
- Schwobe, A. D. & Mengel, S., 1997, *Astron. Nacht.*, **318**, 25
- Schwobe, A. D., Beuermann, K. & Jordan, S., 1995a, *Astr. Astrophys.*, **301**, 447
- Schwobe, A. D., Beuermann, K. & Thomas, H.-C., 1990, *Astr. Astrophys.*, **230**, 120
- Schwobe, A. D., Mantel, K.-H. & Horne, K., 1996, *Astr. Astrophys.*, **319**, 894
- Schwobe, A. D., Thomas, H.-C. & Beuermann, K. 1993, *Astr. Astrophys.*, **271**, L25
- Schwobe, A. D., Beuermann, K., Burwitz, V., Mantel, K.-H. & Schwarz, R., 1995b, in Bianchini, A. et al. (eds.), *Cataclysmic Variables*, p. 389-396
- Schwobe, A. D., Schwarz, R., Mantel, K.-H., Horne, K. & Beuermann, K., 1995c, in Buckley, D. A. H., Warner, B., eds, *Cape Workshop on Magnetic Cataclysmic Variables*, p. 166
- Schwobe, A. D., Thomas, H.-C., Beuermann, K., Burwitz, V., Jordan, S. & Haefner, R., 1995d, *Astr. Astrophys.*, **293**, 764
- Sekiguchi, K., Nakada, Y. & Bassett, B., 1994, *Mon. Not. R. astr. Soc.*, **266**, L51
- Shortridge, K. & Meyerdierks, H., 1996, *PPARC Starlink User note*, 86
- Sirk, M. M. & Howell, S. B., 1996, *IAU Colloquium # 152*, p. 343
- Southwell, K. A., Still, M. D., Smith, R. C. & Martin, J. S., 1995, *Astr. Astrophys.*, **302**, 90
- Stauffer, J. R., Caillault, J.-P., Gagné, M., Prosser, C. F., Hartmann, L. W., 1994, *Astrophys. J. Suppl.*, **91**, 625
- Stockman, H. S. & Lubenow, A. F., 1987, *Astrophys. Space Sci.*, **131**, 607
- Stockman, H. S. & Schmidt, G. D., 1996, *Astrophys. J.*, **468**, 883
- Szkody, P., Silber, A., Hoard, D. W., Fierce, E., Singh, K. P., Barrett, P., Schlegel, E. & Piirola,

- V., 1995, *Astrophys. J.*, **455**, L43
- Tapia, S., 1977, *Astrophys. J.*, **212**, L125
- Thompson, A. M. & Cawthorne, T. V., 1987, *Mon. Not. R. astr. Soc.*, **224**, 425
- Trümper, J., 1984, *Physica Scripta*, **T7**, 209
- Tuohy, I. R., Ferrario, L., Wickramasinghe, D. T. & Hawkins, M. R. S., 1988, *Astrophys. J.*, **328**, L59
- Tuohy, I. R., Lamb, F. K., Garmire, G. P. & Mason, K. O., 1978, *Astrophys. J.*, **226**, L7
- Unger, S. W., Taylor, K., Pedlar, A., Ghataure, H. S., Penston, M. V. & Robinson, A., 1990, *Mon. Not. R. astr. Soc.*, **242**, 33P.
- Vennes, S., Szkody, P., Sion, E. M. & Long, K., 1995, *Astrophys. J.*, **445**, 921
- Warner, B., 1987, *Mon. Not. R. astr. Soc.*, **227**, 23
- Warner, B., 1995, *Cataclysmic Variable Stars*, CUP, 1st ed.
- Warren, J. K., Sirk, M. M. & Vallergera, J. V., 1995, *Astrophys. J.*, **445**, 909
- Watson, M. G., 1986, in Mason, K. O., Watson, M. G. & White, N. E., eds, *Lecture Notes in Physics: Proceedings of Workshop on 'The Physics of Accretion onto Compact Objects'*, p. 97
- Watson, M. G., 1994, in Schlegel, E. M. & Petre, R., eds, *The Soft X-ray Cosmos*, p. 64
- Watson, M. G., 1995, in Buckley, D. A. H., Warner, B., eds, *Cape Workshop on Magnetic Cataclysmic Variables*, p. 179
- Watson, M. G., King, A. R., Jones, M. H. & Motch, C., 1989, *Mon. Not. R. astr. Soc.*, **237**, 299
- Watson, M. G., Rosen, S. R., O'Donoghue, D., Buckley, D. A. H., Warner, B., Hellier, C., Ramseyer, T., Done, C. & Madejski, G., 1995, *Mon. Not. R. astr. Soc.*, **273**, 681

- Wheatley, P. J., 1995a, *Mon. Not. R. astr. Soc.*, **274**, L51
- Wheatley, P. J., 1995b, *PhD Thesis*, University of Leicester
- Whitehurst, R., 1988, *Mon. Not. R. astr. Soc.*, **233**, 529
- Wickramasinghe, D. T., 1988, in Coyne, G. V. et al., eds, *Polarized Radiation of Circumstellar Origin*, Vatican Observatory, p. 3
- Wickramasinghe, D. T. & Meggitt, S. M. A., 1985, *Mon. Not. R. astr. Soc.*, **214**, 605
- Wickramasinghe, D. T. & Wu, K., 1994, *Astrophys. Space Sci.*, **211**, 61
- Woelk, U. & Beuermann, K., 1992, *Astr. Astrophys.*, **256**, 498
- Wynn, G. A. & King, A. R., 1992, *Mon. Not. R. astr. Soc.*, **255**, 83
- Wynn, G. A. & King, A. R., 1995, *Mon. Not. R. astr. Soc.*, **275**, 9
- Young, P. & Schneider, D. P., 1979, *Astrophys. J.*, **230**, 502

Acknowledgements

I owe a huge debt of gratitude to my supervisor, Mike Watson, for his support and advice which have been invaluable to me ever since I began working with him on my undergraduate dissertation five years ago. He has always found the time in his busy schedule to answer my questions, and has always been patient with me when I was slow to understand. Thanks Mike.

I express my deepest gratitude to those who kindly allowed me to use their data in this thesis; Mike Watson, Jeremy Bailey, Darragh O'Donoghue, Pasi Hakala and Simon Rosen. I also thank Pasi and Simon for taking me with them on observing runs at the NOT and at CTIO, particularly for showing me how to order beer in Spanish and how to travel in style through Chile. My thanks go to those involved with the stream brightness modelling; to Pasi for the initial model code, and to Graham Wynn, Kevin Pearson and Andrew King for the stream particle code.

During the past four years I have been through five different offices, and shared them with the most diligent, quiet and mature bunch of postgrads and postdocs you can find (yea right). Those who deserve special mention are Matt 'never complains' Burleigh, John 'Bat Out of Hell' Morley, Tim 'Alex Ferguson' Roberts, Jon 'the Jester' Rainger, Dennis 'Barry White' Stavros, Kathryn 'blue spot day' Clayton, Gareth 'rugby' Griffiths, Paul 'curry' Dobbie, and Richard 'RTFM' West. Special thanks go to Pete Wheatley, partly for the discussions about CVs he and I have had, but mostly for the entertainment the stories of his 'Travels as an Astronomer' have provided. Because of Pete I'm sure I will now never hit a kangaroo on the way to the AAT!

The sub-wardens of Villiers and G-M have always provided a welcome diversion at the end of a long day spent toiling over my thesis. I especially thank Elizabeth for feeding me endless cups of coffee and for staying up to the early hours of the morning with me while we discussed our lives and gossiped about everybody else's! I am sure that Simon Reglar knows how much I appreciate our friendship, but I wanted to grab this chance to thank him for the early morning Doom sessions in the Bennett, for those nights in Equinox, and, of course, for the time spent talking about, playing the games from, and watching *those* films!! Thanks also to Big H and Col. My life right now would be radically different had I not met Lucy; I am deeply grateful to her for inspiring me to finally sort things out, and for the fun we have had over the past year. I couldn't possibly describe how important her unwavering love and support (not to mention the occasional kick up the ****!) have been to me over the past months as I laboured on my thesis.

No small thanks go to my mother and sister for always being behind what I do (and thanks for introducing me to Friends, Heath!). I'd especially like to recognise my mother's uncanny ability to know when to guide me through the pitfalls of life, and when it's best to just let me get on with it myself. You're the best, Mom.

And lastly I must thank a certain person from Modesta, California for providing the initial inspiration that put me on the path towards a career in astronomy. Thanks George.

Keith Sohl
March 1998

This thesis was supported jointly by the University of Leicester and by a PPARC studentship. The majority of the data analysis was carried out using Starlink software and hardware.